

# NOTE TO USERS

This reproduction is the best copy available.

**UMI**<sup>®</sup>



**University of Alberta**

NANOSTRUCTURED THIN FILMS FOR HUMIDITY SENSING

by

JOHN JEREMIAH STEELE



A thesis submitted to the Faculty of Graduate Studies and Research  
in partial fulfillment of the requirements for the degree of

DOCTOR OF PHILOSOPHY

Department of Electrical and Computer Engineering

Edmonton, Alberta

Fall 2007



Library and  
Archives Canada

Bibliothèque et  
Archives Canada

Published Heritage  
Branch

Direction du  
Patrimoine de l'édition

395 Wellington Street  
Ottawa ON K1A 0N4  
Canada

395, rue Wellington  
Ottawa ON K1A 0N4  
Canada

*Your file* *Votre référence*  
*ISBN: 978-0-494-33072-2*  
*Our file* *Notre référence*  
*ISBN: 978-0-494-33072-2*

**NOTICE:**

The author has granted a non-exclusive license allowing Library and Archives Canada to reproduce, publish, archive, preserve, conserve, communicate to the public by telecommunication or on the Internet, loan, distribute and sell theses worldwide, for commercial or non-commercial purposes, in microform, paper, electronic and/or any other formats.

The author retains copyright ownership and moral rights in this thesis. Neither the thesis nor substantial extracts from it may be printed or otherwise reproduced without the author's permission.

**AVIS:**

L'auteur a accordé une licence non exclusive permettant à la Bibliothèque et Archives Canada de reproduire, publier, archiver, sauvegarder, conserver, transmettre au public par télécommunication ou par l'Internet, prêter, distribuer et vendre des thèses partout dans le monde, à des fins commerciales ou autres, sur support microforme, papier, électronique et/ou autres formats.

L'auteur conserve la propriété du droit d'auteur et des droits moraux qui protègent cette thèse. Ni la thèse ni des extraits substantiels de celle-ci ne doivent être imprimés ou autrement reproduits sans son autorisation.

---

In compliance with the Canadian Privacy Act some supporting forms may have been removed from this thesis.

Conformément à la loi canadienne sur la protection de la vie privée, quelques formulaires secondaires ont été enlevés de cette thèse.

While these forms may be included in the document page count, their removal does not represent any loss of content from the thesis.

Bien que ces formulaires aient inclus dans la pagination, il n'y aura aucun contenu manquant.

  
**Canada**

To my family.

# Abstract

Humidity sensors are found in a variety of applications with differing requirements. The sensitivity, range of humidity operation, and response time of a humidity sensor are important in determining suitable applications. The performance of a humidity sensor is largely determined by the properties of the sensing medium including porosity, surface area, and morphology. Glancing angle deposition (GLAD) is a physical vapour deposition (PVD) technique capable of fabricating highly porous thin films with controlled morphology on the 10 nm length scale. The high porosity, large surface area, controlled morphology, and ability to use virtually any source material that can be deposited via PVD make GLAD films ideal for humidity sensing studies.

The research presented in this thesis investigates the use of GLAD films for capacitive and optical based humidity sensors. Capacitive sensors were fabricated by coating interdigitated capacitor (IDC) substrates with metal oxide GLAD films. Optimized sensors exhibited a three orders of magnitude change in the capacitance over the entire relative humidity range, and had response times in the 400 ms range. The capacitive response was found to diminish with time and attempts to regenerate the response via heat treatments had some success. The geometry of the IDC substrates was observed to have a significant impact on sensitivity.  $\text{TiO}_2$  GLAD films were found to be the most sensitive in comparison to similarly fabricated sensors utilizing  $\text{SiO}_2$  and  $\text{Al}_2\text{O}_3$  films. The overall capacitance change and high humidity sensitivity was discovered to be a result of the first few hundred nanometres

of GLAD film. The response time was found to be determined predominantly by film thickness and ranged from a couple hundred milliseconds to over one second for TiO<sub>2</sub> films 0.28–8.5 μm thick. The capacitive response and response time were also affected by the incident vapour flux angle ( $\alpha$ ) used during film deposition.

An optical humidity sensor was fabricated from a TiO<sub>2</sub> film with periodic nano-scale porosity variations designed to yield a narrow-bandpass optical interference filter with a humidity sensitive transmittance spectrum. Comparisons to capacitive sensors were made and advantages identified.

# Acknowledgements

Thank you to my wife and family for their amazing support. To my son Raine, I thank for always being able to make me smile even during the most stressful times, and for flushing my wireless mouse down the toilet when he needed to spend time with daddy.

Thank you Dr. Michael Brett for your easygoing and supportive supervision. Your constant encouragement and advice kept me motivated and was appreciated.

I would like to thank Michael Taschuk for his instrumental role in the development of Chapter 4 and for his general help and guidance in writing this thesis. Thank you Andy van Popta for the great discussions we've had on my research directions. You helped me to focus on important issues and probably saved me months of unnecessary work. To Mark Summers I thank you for the many hours you spent operating the NINT SEM to get the amazing images presented in this thesis. Thank you to Michael Fleischauer, Shufen Tsoi, Matthew Hawkeye, James Gospodyn, and Sumudu Fernando for their contributions to my research.

To current and previous members of the GLAD group including Dr. Jeremy Sit, Jason Sorge, Nick Wakefield, Doug Gish, Louis Bezuidenhout, Katie Krause, Graeme Dice, Bryan Szeto, Peter Hrudey, Anastasia Elias, Ken Harris, Martin Jensen, Doug Vick, Jim Broughton, Ben Bathgate, and Karin Hayward, thank you for making my time here so very enjoyable.

Finally, and mostly, thank you to my Lord and Saviour Jesus Christ for, well, everything!



# Contents

<b>1</b>	<b>Introduction</b>	<b>1</b>
1.1	Introduction to Humidity Sensing . . . . .	1
1.2	History of Humidity Sensing Technology . . . . .	3
1.3	Materials for Humidity Sensors . . . . .	6
1.4	Current Research . . . . .	7
1.5	Motivation and Scope of Thesis Research . . . . .	9
<b>2</b>	<b>Water Adsorption on Metal Oxides</b>	<b>13</b>
2.1	Adsorption Mechanisms . . . . .	13
2.1.1	Chemisorption . . . . .	14
2.1.2	Physisorption . . . . .	16
2.2	Water Adsorption on Metal Oxide Surfaces . . . . .	17
2.2.1	Acid-Base Chemisorption and Hydrogen Bonding . . . . .	17
2.2.2	Redox Based Chemisorption . . . . .	19
2.3	Conductivity and Permittivity Alteration . . . . .	21
2.3.1	Conductivity . . . . .	21
2.3.2	Permittivity . . . . .	23
2.4	Conclusions . . . . .	25
<b>3</b>	<b>Sensor Fabrication</b>	<b>27</b>
3.1	Glancing Angle Deposition . . . . .	27

3.1.1	Oblique Angle Deposition to GLAD . . . . .	28
3.2	Capacitive Humidity Sensors . . . . .	34
3.3	IDC Fabrication . . . . .	36
3.3.1	Large Geometry IDCs . . . . .	37
3.3.2	Counter-Sunk Electrode IDCs . . . . .	37
3.4	Thin Film Deposition . . . . .	38
3.5	Summary . . . . .	40
<b>4</b>	<b>Experimental Methodology</b>	<b>43</b>
4.1	Humidity Generation and Control . . . . .	43
4.1.1	Capacitive Response Measurement with LabVIEW . . . . .	44
4.2	Capacitance Measurement and Calibration . . . . .	46
4.2.1	Capacitance Calibration . . . . .	48
4.3	Resistance Measurement and Calibration . . . . .	54
4.3.1	Resistance Calibration . . . . .	54
4.4	Vaisala Relative Humidity Probe Calibration . . . . .	59
4.4.1	Vaisala RH Accuracy Error . . . . .	61
4.4.2	Vaisala RH Precision Error . . . . .	64
4.4.3	Vaisala RH Absolute Error . . . . .	64
4.5	Sensor Response Time Measurement . . . . .	66
4.6	Commercial Sensor Testing . . . . .	70
4.7	Conclusions . . . . .	77
<b>5</b>	<b>Sensor Characterization</b>	<b>79</b>
5.1	Impedance Parameters . . . . .	79
5.2	Hysteresis . . . . .	81
5.3	Ageing . . . . .	84
5.4	IDC Geometry . . . . .	88
5.5	Effect of Flow Rate on Response Time . . . . .	95

5.6	Summary . . . . .	99
<b>6</b>	<b>Composition and Morphology Effects</b>	<b>101</b>
6.1	Sensing Material . . . . .	101
6.1.1	Capacitive Response . . . . .	102
6.1.2	Response Time . . . . .	111
6.2	Film Thickness . . . . .	112
6.2.1	Low Humidity . . . . .	112
6.2.2	Mid Range Humidity . . . . .	115
6.2.3	High Humidity . . . . .	115
6.2.4	Response Time . . . . .	115
6.2.5	Conclusions . . . . .	118
6.3	Deposition Angle $\alpha$ . . . . .	118
6.4	Discussion . . . . .	123
6.5	Conclusions . . . . .	124
<b>7</b>	<b>Optical Humidity Sensor</b>	<b>125</b>
7.1	Introduction . . . . .	125
7.2	Theory . . . . .	126
7.3	Filter Fabrication . . . . .	128
7.4	Sensor Characterization . . . . .	129
7.5	Results and Discussion . . . . .	131
7.6	Conclusions . . . . .	138
<b>8</b>	<b>Conclusions and Future Work</b>	<b>139</b>
8.1	Summary of Results . . . . .	139
8.2	Contributions to the Field . . . . .	141
8.3	Proposed Future Work . . . . .	143
8.3.1	Ageing . . . . .	143
8.3.2	Modeling . . . . .	143

8.3.3	Porosimetry Measurements . . . . .	143
8.3.4	Device Fabrication . . . . .	144
8.3.5	Response Time . . . . .	144
8.3.6	Sensing Material . . . . .	144
8.3.7	Hysteresis . . . . .	144
	<b>References</b>	<b>145</b>
	<b>A Analytic Fitting of Linear Data with Large Range</b>	<b>159</b>
	<b>B Visual Basic Code</b>	<b>163</b>

# List of Tables

2.1	Definitions of terms used throughout chapter. Taken from [1]. . . . .	14
2.2	Heat of adsorption ( $q_a$ ) for water vapour adsorption mechanisms on metal oxide surfaces [2]. $q_L$ is the heat of liquefaction for water. . . .	20
2.3	Dominant conduction mechanism for ionic type humidity sensors at different surface coverage. . . . .	22
3.1	IDCs used for thesis research. IDC-25-20-10 substrates were fabricated using standard photolithography techniques. All other IDCs were fabricated by Micralyne, Inc. . . . .	38
4.1	Fit values ( $C_{meas} = mC_{nom}$ ) for the 4 sets of capacitance measurements and the QuadTech calibration certificate. . . . .	50
4.2	Fit values ( $R_{meas} = mR_{nom}$ ) for the 3 sets of resistance measurements and the QuadTech calibration certificate. . . . .	56
4.3	Polynomial fit constants $A_i$ and RH at 25°C with 99.7% confidence level uncertainty for lithium chloride, magnesium chloride, sodium chloride, and potassium sulfate. [3] . . . . .	60

4.4	Weighted least squares regression analysis ( $y = mx + b$ ) for data plotted in Figure 4.10. . . . .	62
4.5	Precision data from last 100 RH measurements of saturated salt solutions calibration experiments. The relative standard deviation (RSD) is calculated by dividing the standard deviation ( $\sigma$ ) by the mean value ( $RH_{mean}$ ). . . . .	65
5.1	Measured high RH values of eight scans with different high RH setpoints, but the same low RH setpoint (2%) used to test sensor hysteresis and repeatability. . . . .	85
5.2	Minimum and maximum sensitivity, $S$ , of the sensors that produced the capacitive responses shown in Figure 5.13. . . . .	95
5.3	Response times for the data shown in Figure 5.14 calculated using exponential fitting with SigmaPlot. . . . .	96

# List of Figures

2.1	Surface hydroxylation of metal oxide surfaces. Water molecules in the vicinity of the surface (a) will initially form a dative bond with coordinatively unsaturated metal cations, M (b). With time the water will dissociate and form two hydroxyl groups (c) resulting from deprotonation of the water with the hydroxyl bonding to the metal cation and the proton bonding with a neighbouring oxygen anion, O.	18
2.2	Water vapour adsorption on metal oxide surface. The coordinatively unsaturated metal cations, M, and oxygen anions, O, at the surface facilitate the dissociation of water vapour in the vicinity of the surface (a) into a hydroxyl group, which binds to a metal cation site, and a proton, which binds to an oxygen anion site (b). Once surface hydroxylation is present, water vapour is physisorbed through double hydrogen bonds shared with two surface hydroxyl groups (c). Upon completion of this first physisorbed layer, subsequent layers are adsorbed via single hydrogen bonds (d). The broken lines represent hydrogen bonds.	20
3.1	Geometrical shadowing and columnar growth. In the initial stages of film growth adatoms condense and form nuclei which results in geometrical shadowing of regions of the substrate (a), preventing film growth in those regions (b). The resulting film consists of columns that grow off the nuclei and are inclined in the direction of the vapour source (c). [4]	30

3.2	Physical vapour deposition apparatus for GLAD. Engineering of thin film nanostructure is achieved through in situ adjustments of the angles $\alpha$ and $\phi$ during a deposition. Substrate motion control is based on deposition rate feedback from a quartz crystal microbalance (QCM).	32
3.3	Examples of GLAD nanostructured thin films. The slanted post film (a) was fabricated by holding both $\alpha$ and $\phi$ constant throughout the deposition. A chevron film (b) is fabricated by increasing $\phi$ by $180^\circ$ between slanted post segments. A helical film (c) is fabricated by continually increasing $\phi$ at a slow rate such that the column growth can trace the substrate motion, if the $\phi$ rotation rate is too fast the helical structure will degenerate in to a vertical post structure like that shown in (d).	33
3.4	Capacitor humidity sensors are based on either parallel-plate or IDC structures. IDC based sensors are faster as water vapour is not impeded by an electrode. However, parallel-plate based sensors are more sensitive as they confine the electric field to the sensing medium as opposed to half the field passing through the substrate, as is the case with IDC based sensors.	35
3.5	IDC geometry, top view. Not to scale.	36
3.6	Cross-sectional illustration of Micralyne Inc. fabricated CSE-IDC. Not to scale.	39
3.7	Photograph of a CSE-IDC. The dimensions of the die are roughly $2 \times 2$ cm.	39
3.8	Cross-sectional SEM image of a single digit from an IDC-100-3-5 coated with a $1.5 \mu\text{m}$ thick $\text{Al}_2\text{O}_3$ vertical post GLAD film deposited at $\alpha = 81^\circ$ .	41



4.1	Humidity control setup. The flow through the mass flow controllers (MFCs) is varied to set the mixing ratio of dry nitrogen and moist air. The mixed gas enters the testing chamber where the humidity is monitored by a commercial humidity probe. Atmospheric pressure is maintained with a 1-way valve. . . . .	44
4.2	Nulling type bridge circuit used in LCR meter. When the current through the detector equals zero, the impedance of the DUT can be calculated based on bridge elements $Z_1$ , $Z_2$ , and $Z_3$ . The QuadTech meter utilizes different combinations of inductive, capacitive, and resistive bridge elements, depending on the measured quantity. . . .	46
4.3	Equivalent circuit for a capacitor. . . . .	47
4.4	Nominal versus measured capacitance from QuadTech calibration certificate and 4 sets of capacitors (125 in total) from various manufacturers. . . . .	50
4.5	Histogram of relative residuals of measured capacitance values from best fit line and corresponding Gaussian fit from SigmaPlot version 10.0 (Marquardt-Levenberg algorithm). Gaussian parameters were $x_0 = 0.2 \pm 0.4\%$ and $\sigma = 5.4 \pm 0.4\%$ with a correlation coefficient of $R^2 = 0.940$ . The good fit to a Gauss distribution indicates that the relative residuals are normally distributed and that the capacitors used are uncorrelated. . . . .	52
4.6	Relative standard deviation of a minimum 200 capacitance measurements using the fast and slow integration time setting on the LCR meter. The fit was obtained using Equation 4.10. . . . .	53
4.7	Nominal versus measured resistance from QuadTech calibration certificate and 3 sets of resistors (86 in total). . . . .	56

4.8	Histogram of relative residuals of measured resistance values from best fit line and corresponding Gaussian fit from SigmaPlot. Gaussian parameters were $x_0 = 0.07 \pm 0.04\%$ and $\sigma = 0.4 \pm 0.04\%$ with a correlation coefficient of $R^2 = 0.937$ . The good fit to a Gauss distribution indicates that the relative residuals are normally distributed and that the resistors used are uncorrelated. . . . .	57
4.9	Relative standard deviation of a minimum 100 resistance measurements on resistors with different nominal values. . . . .	58
4.10	Reference RH versus measured RH for Vaisala humidity probe calibration experiments. The data from the Vaisala calibration certificates for both probes have been included for comparison. The line was obtained from fitting all data sets together using weighted least squares regression. . . . .	62
4.11	95% confidence level ( $2\sigma$ ) absolute error for RH measurements. . . . .	65
4.12	Response time setup using diverting solenoid valves. Desorption is depicted here where solenoid #1 is energized causing dry nitrogen to flow onto the sensor while the humid air in solenoid #2 (de-energized) is diverted. . . . .	68
4.13	Timing circuitry for asatable switching of solenoid valves. . . . .	69
4.14	GE G-CAP2 capacitive humidity sensor response. The close agreement between the measured data and the data provided by GE indicates the ability to accurately obtain the capacitive response of humidity sensors. . . . .	71
4.15	GE G-CAP2 response time data for 1 LPM flow rates. Adsorption and desorption response times were calculated to be $81 \pm 3$ s and $111 \pm 2$ s, respectively, from exponential fitting with SigmaPlot. . . . .	73
4.16	Vaisala MultiMeterMate RHT probe capacitive humidity sensor response. . . . .	74

4.17	Vaisala MultiMeterMate RHT probe response time data for 1 LPM flow rates. The average adsorption and desorption response times were calculated to be $1.3 \pm 0.1$ s and $2.5 \pm 0.1$ s, respectively, from a best fit exponential. . . . .	75
4.18	Nafion coated IDC resistive humidity sensor response. . . . .	76
4.19	Nafion coated IDC resistive sensor response time data for 2.5 LPM flow rates. The adsorption and desorption response times were $37 \pm 3$ ms and $153 \pm 4$ ms, from best fits to an exponential. . . . .	77
5.1	The DUT is modeled by the LCR meter as either a series or parallel equivalent circuit. For inductive circuits the capacitors $C_s$ and $C_p$ are replaced by inductors $L_s$ and $L_p$ , respectively. . . . .	80
5.2	Series capacitance (a) and parallel capacitance (b) response of a sensor comprised of a $1.5 \mu\text{m}$ thick $\text{TiO}_2$ vertical post GLAD film deposited onto a IDC-100-3-5. . . . .	82
5.3	First and second scan capacitive response for $1.5 \mu\text{m}$ thick $\text{TiO}_2$ vertical post film deposited at $\alpha = 81^\circ$ onto a IDC-100-3-5. Hysteresis is substantially reduced after initial exposure to high humidity. . . . .	83
5.4	Fourth scan capacitive response for $1.5 \mu\text{m}$ thick $\text{TiO}_2$ vertical post film deposited at $\alpha = 81^\circ$ onto a IDC-100-3-5. . . . .	85
5.5	Sixth scan capacitive response for $1.5 \mu\text{m}$ thick $\text{TiO}_2$ vertical post film deposited at $\alpha = 81^\circ$ onto a IDC-100-3-5. . . . .	86
5.6	Eighth scan capacitive response for $1.5 \mu\text{m}$ thick $\text{TiO}_2$ vertical post film deposited at $\alpha = 81^\circ$ onto a IDC-100-3-5. . . . .	86
5.7	Capacitive response over several days for a $1.5 \mu\text{m}$ thick $\text{TiO}_2$ vertical post film deposited at $\alpha = 81^\circ$ onto a IDC-100-3-5. . . . .	87

5.8	Regeneration attempt using 400°C 1 hour heat treatment for a 1.5 $\mu\text{m}$ thick $\text{TiO}_2$ vertical post film deposited at $\alpha = 81^\circ$ onto a IDC-100-3-3.	89
5.9	X-ray diffraction patterns for a 1.5 $\mu\text{m}$ thick $\text{TiO}_2$ vertical post film deposited at $\alpha = 81^\circ$ onto a standard boron doped p-type silicon (100) test wafer. As deposited, the film is amorphous, however, after heating at 400°C for 1 hour the film exhibits crystalline properties of the anatase (A) phase. The average grain size was calculated to be $21 \pm 2$ nm.	89
5.10	IDC-25-20-10 coated with a 2 $\mu\text{m}$ thick $\text{TiO}_2$ film deposited at $\alpha = 81^\circ$ . Substrate shadowing at electrode boundaries results in film irregularities, which reduces surface area available for water vapour adsorption.	91
5.11	1.5 $\mu\text{m}$ thick $\text{TiO}_2$ film ( $\alpha = 81^\circ$ ) deposited onto a CSE-IDC (IDC-100-3-5). Elimination of film irregularity at electrode boundary facilitates the use IDCs with reduced digit periods and therefore thinner GLAD films.	93
5.12	Capacitive response comparison between IDC-25-20-10 (large geometry IDC) and IDC-25-3-3 (CSE-IDC) both coated with a 2 $\mu\text{m}$ thick $\text{TiO}_2$ vertical post film deposited at $\alpha = 81^\circ$ .	94
5.13	Effect of varying IDC geometry on capacitive response. All IDCs were coated with a 1.5 $\mu\text{m}$ thick $\text{TiO}_2$ vertical post film deposited at $\alpha = 81^\circ$ .	94
5.14	Effect of flow rate on response time measurement. A large contribution of the observed response times for 0.5 and 1.0 LPM are from air mixing and the gas delivery system.	96
6.1	As deposited XRD patterns for 1.5 $\mu\text{m}$ thick $\text{TiO}_2$ , $\text{SiO}_2$ , and $\text{Al}_2\text{O}_3$ GLAD films deposited at an angle of $\alpha = 81^\circ$ onto silicon wafers (100).	103

6.2	Comparison of the capacitive response for sensors made with TiO <sub>2</sub> , SiO <sub>2</sub> , and Al <sub>2</sub> O <sub>3</sub> GLAD films. All films were 1.5 ± 0.1 μm thick and deposited at an angle of α = 81° onto IDC-100-3-5 capacitors. . . . .	103
6.3	Repeatability of capacitive response for different sensors using TiO <sub>2</sub> and Al <sub>2</sub> O <sub>3</sub> GLAD films deposited on different days. All sensors were tested within 24 hours after film deposition. . . . .	104
6.4	Sensitivity plotted as a function of relative humidity for sensors made with TiO <sub>2</sub> , SiO <sub>2</sub> , and Al <sub>2</sub> O <sub>3</sub> GLAD films. The sensitivity changes with RH due to the exponential response of the sensors. . . . .	105
6.5	Cross-sectional and top down SEM images of TiO <sub>2</sub> , SiO <sub>2</sub> , and Al <sub>2</sub> O <sub>3</sub> films used in humidity sensors producing the capacitive responses shown in Figure 6.2. All images were taken at 50,000× magnification.	106
6.6	TEM image of TiO <sub>2</sub> column. . . . .	107
6.7	TEM image of SiO <sub>2</sub> column. . . . .	108
6.8	TEM image of Al <sub>2</sub> O <sub>3</sub> column. . . . .	109
6.9	Effect of depositing SiO <sub>2</sub> in high pressure oxygen environment on the capacitive response. . . . .	110
6.10	Response times for TiO <sub>2</sub> , SiO <sub>2</sub> , and Al <sub>2</sub> O <sub>3</sub> based sensors obtained by taking a weighted average of three adsorption and three desorption response time measurements. . . . .	112
6.11	Cross-sectional SEM images of IDC-100-3-5 substrates coated with TiO <sub>2</sub> films of varying thickness. The image of the 1.1 μm thick film was excluded. All images were obtained at 8,000× magnification. . .	113

6.12	Top down SEM images of IDC-100-3-5 substrates coated with TiO <sub>2</sub> films of varying thickness. The image of the 1.1 μm thick film was excluded. All images were obtained at 25,000× magnification. . . . .	114
6.13	(a) Capacitive response for IDC-100-3-5 substrates coated with TiO <sub>2</sub> films of different thickness. (b) Sensor sensitivity (capacitive response local slope) as a function of RH. . . . .	116
6.14	Change in capacitance between 2–93% RH as a function of film thickness. The line fit is a guide for the eye. This figure shows that the overall capacitance change is primarily a result of the first few hundred nanometres of GLAD film and that as the thickness of the film extends past the electric field of the IDC the change in capacitance begins to diminish. . . . .	117
6.15	Weighted average response times as a function of film thickness. Linear regression R <sup>2</sup> values were 0.983 and 0.996 for the adsorption and desorption response time data, respectively. . . . .	117
6.16	Cross-sectional SEM images of TiO <sub>2</sub> films used to investigate the impact of α on sensor performance. All films were deposited on IDC-25-3-5 substrates and were ~1.5 μm thick. All images were obtained using 45,000× magnification. . . . .	120
6.17	Top down SEM images of TiO <sub>2</sub> films used to investigate the impact of α on sensor performance. All films were deposited on IDC-25-3-5 substrates and were ~1.5 μm thick. All images were obtained using 100,000× magnification. . . . .	121
6.18	(a) Capacitive response for IDC-25-3-5 substrates coated with 1.5 μm thick TiO <sub>2</sub> films deposited at different α. (b) Sensitivity as a function of RH. . . . .	122
6.19	Weighted average response time for sensors fabricated using 1.5 μm thick TiO <sub>2</sub> films deposited at different α. The best fit lines are a guide for the eye. . . . .	123

7.1	Refractive index profile used to obtain a narrow-bandpass optical interference filter. A $\pi$ -phase shift is introduced after 5 periods of a 9.5 period sinusoidal oscillation of the refractive index to create the bandpass. . . . .	127
7.2	Response time setup for optical humidity sensor. . . . .	130
7.3	Cross-sectional SEM images of narrow-bandpass filter at 40k (a) and 180k (b) magnification. The alternating bright/dark horizontal layers correspond to the regions of high/low index respectively. . . . .	132
7.4	Normal incidence transmittance spectra of the film shown in Figure 7.3. In (a), the spectrum from 300 nm to 1100 nm is shown, revealing a bandpass located at 679 nm (peak wavelength) within the 550 nm to 830 nm stop band. In (b), the bandpass spectra obtained at different RH levels (percentages given at bandpass peaks) are shown.	133
7.5	(a) Bandpass location as a function of increasing and decreasing humidity. (b) Transmittance at 668.5 nm wavelength as a function of humidity obtained from the spectrophotometer and laser diode setup.	135
7.6	Adsorption (a) and desorption (b) response time data for the GLAD produced optical humidity sensor (solid line) and the Vaisala MultiMeterMate RHT probe (broken line). The humidity changed from 13% RH to 71% RH for adsorption and 71% RH to 17% RH for desorption. Response times were calculated from exponential best fits provided from SigmaPlot. For the optical sensor they were $315 \pm 35$ ms and $196 \pm 12$ ms for adsorption and desorption, respectively. The Vaisala probe adsorption response time was calculated to be $2.27 \pm 0.16$ s, while desorption was $2.86 \pm 0.19$ s. . . . .	137

# List of Symbols and Abbreviations

$\alpha$	Angle of vapour incidence	Degrees
A	Interdigitated capacitor planar area	mm <sup>2</sup>
$A_0$	Greenspan polynomial fit parameter	% RH
$A_1$	Greenspan polynomial fit parameter	%/°C
$A_2$	Greenspan polynomial fit parameter	%/°C <sup>2</sup>
$A_3$	Greenspan polynomial fit parameter	%/°C <sup>3</sup>
$\beta$	BJT common emitter current gain	
b	Intercept of linear regression	
BJT	Bipolar junction transistor	
C	555 timer capacitance	F
c(t)	Transient concentration	
$c_1$	Initial concentration	
$c_2$	Final concentration	
$C_p$	Parallel capacitance	F
$C_s$	Series capacitance	F
$C_{meas}$	Measured capacitance	F
$C_{nom}$	Nominal capacitance	F
COPD	Chronic obstructive pulmonary disease	
CSE-IDC	Counter-sunk electrode interdigitated capacitor	
$\delta_b$	Error in intercept	
$\delta_m$	Error in slope	



$\delta_x$	Error in x-axis data	
$\Delta n$	Refractive index modulation	
$\Delta n_{max}$	Maximum refractive index	
$\Delta n_{min}$	Minimum refractive index	
$\Delta RH$	Incremental/decremental RH value between setpoints	%
DOD	Dynamic oblique deposition	
DUT	Device under test	
$\epsilon_{C,acc}$	Accuracy error for capacitance measurements	
$\epsilon_{C,pre}$	Precision error for capacitance measurements	
$\epsilon_C$	Absolute error for capacitance measurements	
$\epsilon_{R,acc}$	Accuracy error for resistance measurements	
$\epsilon_{R,pre}$	Precision error for resistance measurements	
$\epsilon_R$	Absolute error for resistance measurements	
$\epsilon_{RH,acc}$	Accuracy error for relative humidity measurements	
$\epsilon_{RH,pre}$	Precision error for relative humidity measurements	
$\epsilon_{RH}$	Absolute error for relative humidity measurements	
EPR	Equivalent parallel resistance	$\Omega$
ESR	Equivalent series resistance	$\Omega$
$f$	Flow rate	L/min
FET	Field effect transistor	
FWHM	Full width at half maximum	
GLAD	Glancing angle deposition	
IDC	Interdigitated capacitor	
$\lambda$	Wavelength	m
$\lambda_{BP}$	Bandpass wavelength at maximum transmittance	m
$\lambda_{SB}$	Stop band centre wavelength	m
L	Digit length	mm
$L_p$	Parallel inductance	H

$L_s$	Series inductance	H
LFM	Linear feet per minute	ft/min
LPM	Litres per minute	L/min
m	Slope	
$\bar{m}$	Mean slope	
$n_{ave}$	Average refractive index	
N	Number of cycles to complete	
NIR	Near infrared	
$\Omega$	Physical periodicity	m
OAD	Oblique angle deposition	
$\phi$	Substrate rotation angle	Degrees
ppm <sub>v</sub>	parts per million by volume	
ppm <sub>w</sub>	parts per million by wight	
$P_w$	Partial pressure of water vapour	Pa
$P_s$	Saturation vapour pressure for water	Pa
PVD	Physical vapour deposition	
$q_a$	Heat of adsorption	KJ/mol
$q_L$	Heat of liquifaction of water	KJ/mol
$R^2$	Coefficient of determination	
$R_A$	555 timer resistance	$\Omega$
$R_B$	555 timer resistance	$\Omega$
$R_{IB}$	BJT switch base resistance	$\Omega$
$R_{IC}$	BJT switch collector resistance	$\Omega$
$R_s$	Series resistance	$\Omega$
$R_p$	Parallel resistance	$\Omega$
$R_{meas}$	Measured resistance	$\Omega$
$R_{nom}$	Nominal resistance	$\Omega$
RH	Relative humidity	%

$RH_i$	Start RH setpoint	%
$RH_f$	End RH setpoint	%
$RH_{ref}$	Reference humidity	%
$RH_{meas}$	Measured humidity	%
RSD	Relative standard deviation	%
$\sigma$	Standard deviation	
$\sigma_b$	Standard deviation of intercept	
$\sigma_m$	Standard deviation of slope	
$\sigma_{meas}$	Standard deviation of measurements	
$\sigma_{noise}$	Noise error	
$\sigma_{pre}$	Precision error	
$s$	Digit separation	$\mu\text{m}$
S	Sensitivity	nF/%RH
$S_{max}$	Maximum sensitivity	nF/%RH
$S_{min}$	Minimum sensitivity	nF/%RH
SBD	Serial bideposition	
sccm	Standard cubic centimeters per minute	$\text{cm}^3/\text{min}$
$\sim$	Approximately	
$\theta$	Surface coverage	
$\tau$	Time constant	s
t	Time	s
$t_{90}$	90% response time	s
$t_{e.x}$	Extrinsic response time	s
$t_{in,ads}$	Intrinsic adsorption response time	s
$t_{in,des}$	Intrinsic desorption response time	s
$t_H$	Time at high voltage	s
$t_L$	Time at low voltage	s
T	Period of time	s

$T_{wait}$	Wait time at each RH setpoint	min
UV	Ultra violet	
V	Exchange volume	L
$V_C$	BJT switch collector voltage	V
$V_H$	555 timer high voltage	V
$V_L$	555 timer low voltage	V
$V_S$	Source voltage	V
VIS	Visible	
W	Digit width	$\mu\text{m}$
x	Interdigitated capacitor width	mm
$x_0$	Gaussian fit centre value	
$X_C$	Capacitor reactance	$\Omega$
XRD	X-ray diffraction	

# Chapter 1

## Introduction

This thesis presents research in humidity sensing. This introductory chapter will begin with a definition of humidity and selected sensing applications. The history of humidity sensor technology will be discussed followed by a review of the field including the various architectures, sensing materials, and limitations of humidity sensors. The motivation and scope of the research presented in this thesis will be discussed.

### 1.1 Introduction to Humidity Sensing

The humidity of a gas is a measure of the water vapour content. There are several measures that quantify the water vapour content including dew point, frost point, mixing ratio in parts per million by weight ( $\text{ppm}_w$ ) and parts per million by volume ( $\text{ppm}_v$ ), absolute humidity, relative humidity, and saturation deficit. These measures are related to each other and once one is known, the others can be calculated if the temperature and pressure of the gas are known [5]. The most common measurement of water vapour content is the relative humidity ( $RH$ ) defined as:

$$RH = \frac{P_w}{P_s} \times 100\% \quad (1.1)$$

where  $P_w$  is the partial pressure of water vapour and  $P_s$  is the saturation vapour pressure, which is dependent on the temperature and pressure of the gas [5].

The measurement and control of humidity finds applications in a variety of fields. The following examples were taken from [5], additional references are cited as needed. Helium cooled nuclear reactors require control of the humidity in the helium gas as even trace amounts of water vapour can degrade the graphite moderator rods and change the process heat balance. In the medical industry humidity sensors are used for perspiration measurements, incubators, artificial heart fabrication, and medical gases. In museums, preserving centuries-old art requires control of ambient humidity levels. The efficiency of industrial dryers is greatly enhanced through humidity level monitoring to determine when drying is complete, as opposed to operating for a set amount of time. In the semiconductor industry, humidity level control is critical in device fabrication as failure rates are dependent on the relative humidity. In food processing, the equilibrium relative humidity of food is important for packaging and controlling micro-organism growth. Meteorological applications are numerous and include weather forecasting, airplane lift calculations critical to safe take off and landings, cloud studies, and ozone depletion research. Indoor air quality and human comfort are greatly influenced by the humidity level where deviations from the recommended 35-65% RH range (from the International Standards Organization and the American Society of Heating, Refrigerating and Air-Conditioning Engineers) can cause enhanced outgassing of volatile chemicals from furniture and/or promote the growth of molds, algae, and mildew [6]. These applications only probe a small fraction of those requiring humidity sensors, however, they serve to identify the diverse environments and situations where humidity sensors are currently used.

The immense range of applications of humidity sensors results in a similarly vast range of operating conditions. A variety of sensor architectures and sensing material combinations have been developed, as no single sensor is capable of meet-

ing the requirements of all applications. In general, the properties of a humidity sensor which limit its use are [7,8]:

1. Operational humidity range
2. Operational temperature range
3. Response time
4. Sensitivity
5. Selectivity
6. Accuracy
7. Repeatability / interchangeability
8. Contamination resistance
9. Durability
10. Lifetime
11. Size
12. Cost

## **1.2 History of Humidity Sensing Technology**

The following account of the history of humidity sensing technology can be found in [5]. Additional references are cited as needed.

The first hygrometer (humidity meter) was invented by Nicholas Cryfts in 1450 where he tied segments of wool to one end of a scale and balanced them with rocks. As the humidity changed the water content in the wool, and therefore its weight, would correspondingly change, thus providing a measure of the water content in the air. This concept was later improved upon by Leonardo da Vinci in 1550 where he substituted the wool with a sponge, increasing sensitivity.

In 1614, Santorio Santorre invented a new type of hygrometer that involved the contraction and elongation of a lyre string attached between two fixed points

and a weight suspended at its centre. The cord contracted from increased humidity causing the weight to rise. A decrease in humidity would cause the weight to lower.

In 1660 the dew point hygrometer was discovered from water condensing on the outside of an ice-packed container on rainy days. The temperature at which air condenses (i.e., the dew point) is a direct measure of the humidity.

The onset of modern humidity sensor technology occurred in the twentieth century with the development of the field of electronics. In the 1930's the Dunmore cell, the Pope cell, and the dew cell were created. In the 1950's the electrolytic, infrared, and the Lyman-Alpha hygrometers came to market. The development of most modern sensing techniques occurred in the 1960's including the automatic chilled mirror and aluminum oxide hygrometers. Due to the range of performance characteristics, most sensors found a niche market.

Modern sensors can be classified as capacitive, resistive/impedance, gravimetric, hygrometric or optical based sensors [7,9]. Capacitive based sensors operate on the principle that adsorption of water vapour increases the dielectric constant of a humidity sensitive material. Using a non-conductive humidity sensitive material as the dielectric in a capacitive structure produces a device with a capacitance proportional to the ambient humidity level. Capacitive based humidity sensors account for approximately 75% of the market [7,9]. This dominance is in large part due to the low power consumption, high sensitivity, and low cost of capacitive based sensors [9].

Resistive/impedance sensors measure conductivity changes resulting from water vapour adsorption/desorption and are otherwise very similar to capacitive based sensors. There are several adsorption mechanisms that contribute to conductivity changes and will be discussed in Chapter 2 as they play an important role in both resistive/impedance and capacitive based sensors.

Gravimetric sensors are based on mass changes that result from water vapour adsorption/desorption. A popular type of gravimetric humidity sensor uses a



quartz crystal microbalance (QCM) coated with a humidity sensitive material. The water vapour induced mass changes of the humidity sensitive material cause a shift in the oscillation frequency of the QCM [7]. Other gravimetric based sensors use cantilever beams and surface acoustic wave (SAW) devices [7].

Hygrometric sensors utilize mechanical changes such as elongation/contraction or swelling/shrinking of a humidity sensitive material. The lyre string hygrometer invented by Santorio Santorre is a perfect example of a hygrometric based sensor. A modern example is found from Gerlach and Sager who coated a silicon/polysilicon membrane with a polymer (polyimide) that swells with increased water adsorption and strains the membrane, which is quantified via on-chip piezoresistors [10].

Optical based sensors are diverse and can obtain humidity information through the amplitude, polarization, frequency, or phase of a light source as it interacts with a humidity sensitive material. The chilled mirror hygrometer (CMH) is an optical based sensor known to provide the most accurate, reliable, and fundamental measurement of humidity and is therefore widely used as a calibration standard [5]. The CMH operates on the principal that condensed water on the surface of a thermoelectrically cooled mirror scatters incident light from a light emitting diode and reduces the electrical signal of a photo-transistor / optical detector positioned to collect reflected light off the surface of the mirror [5]. The temperature of the mirror is monitored and reduced until the reflectance signal drops, indicating the dew point of the ambient gas. The use of optical fibers is widespread where a humidity sensitive material is used as the cladding over a small segment of the fiber, or is deposited on the cleaved end of the fiber [11–13]. For cladding sensors the water content in the humidity sensitive coating (function of RH) alters the refractive index of the cladding and therefore the transmitted power [11, 12]. For sensors with the humidity sensitive material on the end of a fiber it is the reflected signal that is altered as a result of humidity induced refractive index changes [13]. Other optical based humidity sensors have utilized waveguides where TM polarized wave prop-

agation is modified by humidity [14], luminescent humidity sensitive films where the quenching or shifting of the luminescence spectrum is humidity dependent [15], and nondispersive infrared detectors which relate the humidity to the amplitude of water vapour's optical absorption peaks at 1.4 and 1.9  $\mu\text{m}$  [6].

### 1.3 Materials for Humidity Sensors

Porous ceramics and polymers are the most common materials used in commercial humidity sensors [16]. A range of porous ceramics have been used in humidity sensors including anodized alumina, perovskites, spinel compounds, and various other metal and semiconductor oxides [9, 16, 17]. These materials are fabricated using various techniques such as vacuum deposition, bulk sintering, sol-gel, anodization, and screen printing [17]. For humidity sensing applications, porous ceramics have the advantages of mechanical strength, thermal stability, and ability to operate at high humidity for prolonged periods [7, 16]. The primary disadvantage of porous ceramics is their sensitivity to contamination from dust, dirt, oil, smoke, alcohol, and other solvents. These impurities adsorb on the surface and degrade sensor response. Thus, it is typical for porous ceramic based sensors to include heating elements for periodic regeneration by heating the ceramic to hundreds of degrees Celcius to outgas contaminants [16, 18, 19].

Polymers frequently used in humidity sensors include cellulose acetate, polyimide, polymethyl methacrylate, polyethersulphone, polysulfone, divinyl siloxane benzocyclobutene, and hexamethyldisilazane [9, 17, 20]. In general, polymer based sensors are either resistive or capacitive and are therefore based on conductivity and permittivity changes resulting from water vapour absorption [17, 21, 22]. However, some humidity sensors utilize absorption induced swelling of polymers such as polyethyleneoxide-sorbitol and hydroxyethyl-cellulose [22]. Advantages of polymers include a linear response and compatability with silicon based microfab-

rication processes [7]. In general, disadvantages of polymers are their instability at high humidity and high temperature, hysteresis, and sensitivity to organic vapours [7, 17, 20]. However, techniques such as cross-linking and graft-polymerization can be used to improve these shortcomings [20].

## 1.4 Current Research

The majority of research conducted involves changing the humidity sensitive material and/or its properties and observing the impact on one or more of the important properties of humidity sensors listed in Section 1.1 on page 3. Papers on varying the type of material [11, 23–27] and material properties such as thickness, porosity, and pore size distribution [11, 27–30] are frequently found. Other groups are also researching the effect of sensor architecture properties (e.g., electrode geometry) on sensor performance [28, 31–33].

In general, many authors do not address a limitation or problem of humidity sensors that requires a solution. Instead they report the fabrication and characterization of humidity sensors with subtle differences from those already reported. The notable exception to this are papers addressing the slow response time of commercial sensors, which is on the order of several seconds and longer [7, 34, 35]. Many applications exist that would substantially benefit from further reduced response times. Portable spirometers for the diagnosis of asthma and chronic obstructive pulmonary disease (COPD) is one such application [35–39]. Asthma and COPD affect 10-20% of the world population [36, 39]. Current spirometers use mechanically operating peak expiratory flow meters, which suffer from large discrepancies, limited accuracy, and lack of data storage [36]. The development of a portable spirometer requires a humidity sensor with a response time less than half a second [36]. No current commercial humidity sensor is this fast.

Monitoring human respiration is another application that requires high speed

humidity sensors. Apnea is the state of suspension of external breathing and is currently monitored using both intubated (tube in airway) and non-intubated techniques. Inductance plethysmography and electromyography are non-intubated techniques currently used for long term monitoring. However, these measurements are unreliable as they suffer from motion artifacts [40]. Rapid humidity sensors (less than 1 second response time) show promise as non-intubated apnea monitors using cyclic humidity levels in patient airflow [40]. The need for a rapid humidity sensor is especially apparent for neonates (less than 4 weeks old) as they have respiration rates in the 45 breaths per minute range [41]. When the respiration rate of a neonate exceeds 60 breaths per minute it can be a sign of illness and in particular, group B streptococcal infection [41]. Detection of airway obstruction in neonates using fast humidity sensors is also receiving attention as current monitoring techniques based on sensing the movement of the chest wall may not detect airway obstruction [42].

Rapid measurements of humidity in human breath may find applications in the management of patients undergoing anesthesia and critical care medicine. The humidity level during respiration can be used, along with other information such as temperature and air flow, to obtain a measurement of the oxygen consumption per breath [43]. Oxygen consumption is an important monitor of normal cardiopulmonary and tissue function and is useful for body temperature control and lung hydration during anesthesia and critical care medicine [43].

The measurement of humidity in the troposphere where large humidity gradients are present requires sensors with sub-second response times [44]. Although humidity is frequently measured through the launch of radiosondes, the spatial and temporal nature of these measurements do not capture the complexity of the three-dimensional structure that governs atmospheric heating and cooling, especially for cloud development and dissipation [44]. A fast humidity sensor mounted on an aerial vehicle would be able to obtain water vapour concentration profiles over distances of tens of metres, which is desirable for better understanding of fundamental

mechanisms in the areas of atmospheric chemistry, hydrology, severe weather prediction, climate research, and polar region studies [44].

Several groups have attempted to reduce response times using different techniques. Kang and Wise developed a capacitive sensor with multiple polyimide columns to increase the sensing surface area and the rate of moisture uptake [34]. They were able to obtain a one second adsorption response time (response time during an increasing humidity change), however, no desorption (decreasing humidity change) response time was reported. Laville and Pellet fabricated a capacitive sensor with a 200 ms adsorption response time by heating a thin layer of benzocyclobutene to 40°C during operation [35]. Unfortunately, this device had an 11 second desorption response time. Other studies have shown that pore size distribution in porous ceramic based sensors [29,45], film thickness [46,47], and the surface functional groups of polymer based sensors [48,49] can affect response time.

## **1.5 Motivation and Scope of Thesis Research**

The response time and general performance of a humidity sensor is largely determined by the properties of the sensing medium including porosity, surface area, morphology, and thickness [6–9, 16, 17, 22, 29, 34, 46, 50]. Glancing angle deposition (GLAD) is a physical vapour deposition (PVD) technique capable of fabricating highly porous thin films with control over film morphology on the 10 nm length scale [51,52]. The GLAD process will be described in Chapter 3. The high porosity, large surface area, controlled morphology, and ability to use virtually any source material that can be deposited via PVD make GLAD films ideal for humidity sensing studies.

As previously discussed, there are immediate commercial opportunities for high speed humidity sensors with sub-second response times. Initial studies performed by Harris et al. have shown that capacitive based humidity sensors fabricated with

GLAD films are extremely fast with response times on the order of 100 ms [53]. To date, very few others have been able to fabricate humidity sensors with such short response times. Kalkan et al. developed a resistive humidity sensor with a 200 ms response time by depositing a GLAD-like columnar silicon film onto an interdigitated electrode structure [54]. The silicon film was deposited using a silane-based high-density plasma deposition process with low substrate temperature (100°C) [55]. Kuban et al. utilized thin (~200 nm) films of Nafion perfluorosulfonate ionomer deposited onto interdigitated rhodium electrodes to achieve response times of 30-50 ms [47]. The high-speed response was attributed to the use of very thin sensing layers and electrode voltages high enough to cause electrolysis of water at the sensor surface. The use of thin sensing layers to achieve a rapid response was also reported by Briglin and Lewis, who showed the dependence of sensor response time on the square of film thickness in accordance with Fickian diffusion [46]. Briglin and Lewis were able to fabricate volatile organic vapour sensors with a 17 ms response time through the use of very thin (< 200 nm) carbon black-poly(ethylene-co-vinyl acetate) composite films. Their results also showed, however, that this high-speed response came at the cost of reduced sensitivity, which is also proportional to film thickness. GLAD offers the advantage of a rapid response without the need of extremely thin coatings (the films utilized by Harris et al. were 1.4  $\mu\text{m}$  to 2.3  $\mu\text{m}$  thick) and therefore without sacrificing sensitivity.

The research presented in this thesis investigates the use of metal oxide GLAD films for humidity sensors. The objectives are to discover which properties of GLAD films account for their rapid detection capability and to optimize sensor performance in terms of sensitivity, response time, and range of humidity operation.

In Chapter 2, background information on water vapour interaction with metal oxide surfaces is presented. The corresponding conductivity and permittivity alterations as a result of these interaction is identified in terms of sensing applications.

In Chapter 3, a description of the fabrication process for the capacitive based humidity sensors presented in this thesis is given.

In Chapter 4, the experimental methodology used to characterize the sensors is developed. Particular attention is paid to instrument calibration and error estimates.

Chapter 5 establishes a framework for meaningful interpretation of the data obtained from GLAD produced humidity sensors. This is imperative as several factors can alter the performance of the sensors, and without this framework, comparisons between sensors can not be drawn.

The results from several studies are presented in Chapter 6. In particular, the impact of GLAD film composition and morphology on sensor performance is investigated. The composition of the GLAD films was altered by selecting different source materials ( $\text{TiO}_2$ ,  $\text{SiO}_2$ ,  $\text{Al}_2\text{O}_3$ ) for thin film deposition. Morphological changes to the GLAD films were achieved through variations of the film thickness as well as the deposition angle used to grow the films.

The fabrication and characterization of an optical based humidity sensor using a gradient index thin film is described in Chapter 7. The performance and potential advantages in comparison to the capacitive based sensors are given.

Lastly, Chapter 8 provides a summary of the research and conclusions presented in this thesis. Contributions to the field and suggestions for future work are also given.

## Chapter 2

# Water Vapour Adsorption on Metal Oxide Surfaces

The humidity sensors studied in this thesis are based on the interaction of water vapour with metal oxide thin films. This chapter provides background information on the mechanism of water vapour adsorption on metal oxide surfaces. A general discussion of adsorption mechanisms including chemisorption and physisorption will be given prior to addressing the specific case of water vapour adsorption on metal oxides. The final section describes the resulting changes to the conductivity and permittivity of the oxide due to water adsorption, in regards to sensing applications.

### 2.1 Adsorption Mechanisms

Table 2.1 lists some definitions of terms used throughout this chapter. Adsorption occurs through either chemical bonding (chemisorption) or non-bonding (physisorption) interactions between the adsorbent and adsorptive. The following sections will discuss the mechanisms of both types of adsorption as they pertain to metal oxide surfaces.



**Table 2.1.** Definitions of terms used throughout chapter. Taken from [1].

Term	Definition
Adsorptive	Adsorbable substance in the fluid phase
Adsorbate	Adsorptive in the adsorbed state
Adsorbent	Solid material on which adsorption occurs
Chemisorption	Adsorption through chemical bonding
Physisorption	Adsorption through non-bonding intermolecular forces
Monolayer capacity	Either chemisorbed amount needed to occupy all surface sites or physisorbed amount needed to cover surface
Surface coverage	Ratio of amount of adsorbate to monolayer capacity

### 2.1.1 Chemisorption

Chemisorption on metal oxide surfaces is either dissociative or molecular (i.e., non-dissociative) and occurs through either acid-base (also referred to as donor-acceptor) or redox based reactions [56]. The following will briefly discuss each type of chemisorption and the metal oxide properties that influence the process.

#### 2.1.1.1 Acid-Base Type Chemisorption

Coordinatively unsaturated metal cations and oxygen anions exist at the surface of metal oxides and promote acid-base type reactions. The Lewis acidity is dependent on the metal cations having empty orbitals and positive charges, which can interact with the filled orbitals, negative charges, and/or dipoles of Lewis basic molecules. The Lewis acidity strength of metal oxide surfaces is therefore dependent on the metal cation charge (e.g.,  $\text{Ti}^{4+}$  vs.  $\text{Al}^{3+}$ ), the degree of coordinative unsaturation, and the availability of empty orbitals. Lewis basicity of metal oxide surfaces is dependent on the availability of a pair of 2p electrons associated with oxygen ions. Thus, Lewis basicity strength is dependent on coordination as well as cation charge and radius, where low cation charge and large cation radius results in weaker bonding and therefore more basic surfaces [56].

Molecular chemisorption through acid-base type reactions results in a coordinate (dative) bond forming between the Lewis acid and Lewis base. Dissociative

chemisorption occurs through heterolytic cleavage ( $AB$  gives  $A^+$  and  $B^-$  ions) of the adsorbate, with the resulting anion and cation bonding to a metal cation and neighbouring oxygen anion at the surface, respectively [56]. Water is an example of an adsorbate that can chemisorb through both molecular and dissociative mechanisms as will be discussed below in Section 2.2.

### 2.1.1.2 Redox Based Chemisorption

Redox based chemisorption occurs through either direct electron transfer between the adsorbate and adsorbent, or through the addition or removal of surface oxygen species [56]. The net result for either case is the change in oxidation state of surface species, or the formation of free electrons. Redox based chemisorption through direct electron transfer typically results in the former, however, when surface oxygen is involved either can occur [56]. An adsorbate can react with oxygen anions at the surface resulting in the addition of a neutral oxygen atom to the adsorbate and the release of electrons [56]. These electrons can be free carriers or used to reduce the oxidation state of metal cations.

The electronic properties of metal oxides largely determine their redox properties. The bandgap of the oxide is often mentioned in redox properties since the difficulty in forming electrons and holes in large bandgap oxides (e.g., pre-transition metals) means that they are neither easily reduced nor oxidized. However, the bandgap is not solely responsible in determining redox properties as the presence of surface defects or unidentified pre-adsorbed or co-adsorbed molecules can have an impact [56]. In general, pre-transition metal oxides are relatively inert to redox based chemisorption, whereas most transition and post-transition metal oxides can chemisorb through redox based reactions as their electron configurations are easier to alter [56].

Like acid-base type chemisorption, redox based chemisorption can be either dissociative or molecular. Examples of dissociative chemisorption are  $H_2$  and  $Cl_2$

which homolytically dissociate into H and Cl atoms which then reduce/oxidize to  $H^+/Cl^-$  ions through their chemisorption onto cations/anions at the surface [56]. An example of molecular chemisorption is found in carbon monoxide, which chemisorbs onto an oxygen anion site forming carbon dioxide and excess electrons [56].

### 2.1.2 Physisorption

Physisorption is a result of non-bonding intermolecular forces in which there are six basic types. In order of strength they are:

1. Ion-dipole
2. Hydrogen bond
3. Dipole-dipole
4. Ion-induced dipole
5. Dipole-induced dipole
6. Instantaneous dipole-induced dipole (London dispersion)

All intermolecular forces arise from electrostatic attractive forces between opposite charges [57]. The ion-dipole force between an ion and the oppositely charged end of a dipole is the strongest non-bonding intermolecular force. The hydrogen bond is slightly weaker and is a special type of dipole-dipole bond between molecules with a hydrogen atom bonded to a small, highly electronegative atom with lone electron pairs such as nitrogen, oxygen, and fluorine. The high electronegativity of the N, O, and F atoms result in highly polar H-N, H-O, and H-F bonds with the hydrogen end being partially positive. The hydrogen end is attracted to a lone electron pair on N, O, or F of another molecule, forming the hydrogen bond. Polar molecules experience dipole-dipole forces between their oppositely charged ends. Ion-induced dipole forces arise from the electric field of an ion

which polarizes a non-polar molecule and induces a dipole, which is then attracted to the ion. Dipole-induced dipole forces are similar in that the electric field of a polar molecule can induce a dipole in a non-polar molecule, which is subsequently attracted to the polar molecule. Instantaneous dipole-induced dipole forces are also referred to as London dispersion forces and arise from the momentary oscillation of electron charge in an atom/molecule forming an instantaneous dipole that induces a dipole in a neighbouring molecule resulting in their attraction.

The nature of intermolecular forces reveals that both the polarity and polarizability of the adsorbent and adsorptive play critical roles in physisorption processes.

## 2.2 Water Adsorption on Metal Oxide Surfaces

The mechanisms of water vapour adsorption on metal oxide surfaces are well studied and several sources are available on the topic [2, 16, 17, 56, 58, 59]. In general, water vapour adsorption occurs via acid-base type chemisorption followed by hydrogen bonded physisorption [56]. However, certain oxides can chemisorb water vapour through redox reactions [16]. The following will consider each interaction type.

### 2.2.1 Acid-Base Chemisorption Followed by Hydrogen Bonded Physisorption

The water molecule has two lone-pairs of electrons and acts as a Lewis base, which can interact with the acidic cation sites. Water molecules in the vicinity of a metal oxide surface will initially molecularly chemisorb through a dative bond with a metal cation at the surface [2]. With time, the molecularly chemisorbed water will heterolytically dissociate into a proton and hydroxyl ion with the proton bonding to a neighbouring oxygen anion and the hydroxyl ion remaining bonded to the

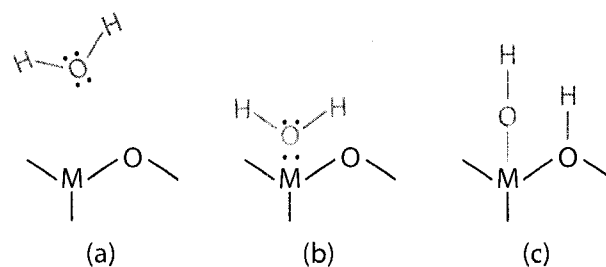


**Figure 2.1.** Surface hydroxylation of metal oxide surfaces. Water molecules in the vicinity of the surface (a) will initially form a dative bond with coordinatively unsaturated metal cations, M (b). With time the water will dissociate and form two hydroxyl groups (c) resulting from deprotonation of the water with the hydroxyl bonding to the metal cation and the proton bonding with a neighbouring oxygen anion, O.

metal cation [2,56]. The net result of water vapour chemisorption is the formation of two surface hydroxyl groups per every chemisorbed water molecule. Figure 2.1 illustrates this surface hydroxylation process on metal oxides. Once hydroxyls are formed they are thermally stable up to temperatures in the 400-500°C range where they begin to desorb from the surface [16, 58]. Complete surface hydroxylation (covered with a monolayer of hydroxyl groups) of metal oxides is dependent on the ambient conditions (humidity level, temperature, pressure) and material properties (crystallinity, surface defects, thermal history, contamination) [56, 60, 61].

Once surface hydroxyls are present, water vapour physisorbs via double hydrogen bonding, where one water molecule binds to two neighbouring surface hydroxyls [58]. This was demonstrated in 1969 by Morimoto et al. by observing the difference between the first (dehydroxylated) and second (hydroxylated) water vapour adsorption isotherms of titanium and iron oxides [58]. Adsorption isotherms describe the amount of gas adsorbed as a function of vapour pressure (relative to saturation) at a constant temperature [1]. They are obtained by first heat treating samples under vacuum to clean the surface by outgassing any adsorbed species. Once the samples are cooled to the desired temperature, which depends on the probe gas (e.g., nitrogen, krypton, water) and what is under investigation (e.g., surface area analysis, adsorption mechanisms), the vapour pressure is incremented by

introducing small amounts of probe gas to the chamber [1]. The volume of gas adsorbed is determined from pressure changes resulting from adsorption. Morimoto et al. discovered that the ratio of the capacity of first physisorbed layer of water vapour to the total number of underlying hydroxyl groups was nearly equal to 1:2, indicating that a water molecule is adsorbed on two surface hydroxyl groups [58]. This type of double hydrogen bonded physisorption continues with increasing humidity until a monolayer forms. The humidity at which this monolayer forms can be determined from the shape of the adsorption isotherm (the “knee” of the volume adsorbed vs. relative pressure plot where the volume adsorbed plateaus with respect to the pressure) as well as calorimetric data (relative humidity where heat of adsorption has reduced to a level comparable to the heat of liquifaction, see Table 2.2 below) [1,22,60]. Increasing the humidity above this point results in further physisorption on top of this monolayer through single hydrogen bonds [16,17,22]. This single hydrogen bonding continues with increasing humidity to multiple layers of adsorbed water. Figure 2.2 illustrates the adsorption mechanism from initial surface hydroxylation through to multi-layer physisorption.

In 1989 Fubini et al. reported typical heats of adsorption ranges for the different types of adsorption mechanisms on oxides at 303 K [2]. Table 2.2 lists these values with reference to Figures 2.1 and 2.2.

### 2.2.2 Redox Based Chemisorption

Metal oxides with small bandgaps (i.e., semiconducting) and/or inter bandgap defect states (resulting from doping, co-adsorbed molecules, surface defects, etc.) can chemisorb water vapour through redox reactions [16].  $\text{SnO}_2$ ,  $\text{ZnO}$ ,  $\text{In}_2\text{O}_3$ , and perovskites are examples of oxides that chemisorb water through redox reactions [17]. At room temperature, these materials can adsorb water vapour through redox, acid-base, and physisorption (hydrogen bonding) reactions [17]. As the temperature is increased, the redox adsorption mechanism is expected to dominate, espe-

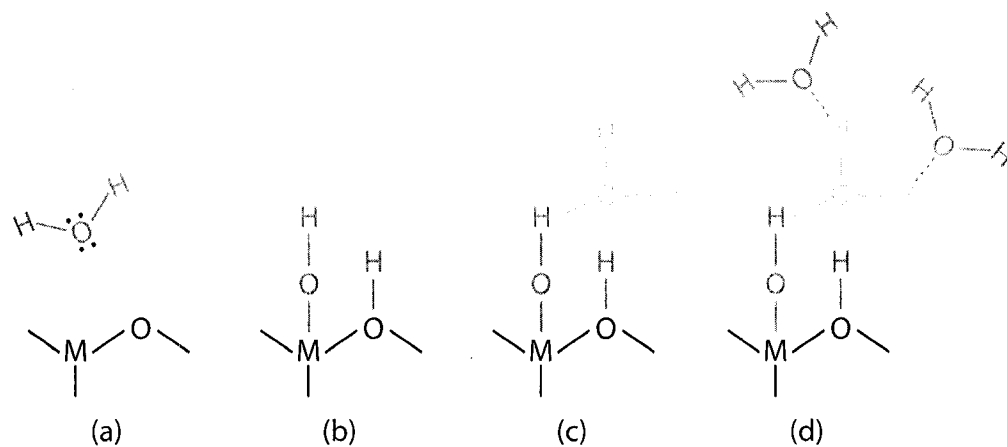


**Figure 2.2.** Water vapour adsorption on metal oxide surface. The coordinatively unsaturated metal cations,  $M$ , and oxygen anions,  $O$ , at the surface facilitate the dissociation of water vapour in the vicinity of the surface (a) into a hydroxyl group, which binds to a metal cation site, and a proton, which binds to an oxygen anion site (b). Once surface hydroxylation is present, water vapour is physisorbed through double hydrogen bonds shared with two surface hydroxyl groups (c). Upon completion of this first physisorbed layer, subsequent layers are adsorbed via single hydrogen bonds (d). The broken lines represent hydrogen bonds.

**Table 2.2.** Heat of adsorption ( $q_a$ ) for water vapour adsorption mechanisms on metal oxide surfaces [2].  $q_L$  is the heat of liquefaction for water.

Adsorption Mechanism	Fig. Ref.	$q_a$ [kJ/mol]
Coordinative chemisorption	2.1b	70-120
Dissociative chemisorption	2.1c	>120
Double hydrogen bonded physisorption	2.2c	50-70
Single hydrogen bonded physisorption	2.2d	$\sim 44 = q_L$

### 2.3. Conductivity and Permittivity Alteration

---

cially for temperatures  $> 100^{\circ}\text{C}$  where physisorption of water vapour is not possible [16].

Unlike the acid-base and hydrogen bonded adsorption mechanisms, the exact nature of redox based reactions with oxides is not well understood and controversy exists [16,17]. Water vapour acts as a reducing gas and therefore results in electron transfer to the surface upon adsorption. Different electron transfer mechanisms have been proposed including direct transfer between the water and surface, indirect transfer as a result of the replacement of previously adsorbed oxygen anions ( $\text{O}^-$  and  $\text{O}^{2-}$ ) with water vapour, and the liberation of trapped electrons at surface defects upon water vapour adsorption [16,17,56]. In any case, the net effect is the apparent transfer of electrons to the surface [16,17]. This transfer accounts for the conductivity changes utilized in high-temperature ( $> 100^{\circ}\text{C}$ ) humidity sensors.

## 2.3 Conductivity and Permittivity Alteration

Metal oxide conductivity and permittivity changes that result from water vapour adsorption are exploited to sense ambient humidity. Both of these changes will now be addressed.

### 2.3.1 Conductivity

Resistive/impedance based humidity sensors utilize conductivity changes and are classified as either ionic or electronic type sensors depending on the mechanism(s) of water vapour adsorption.

#### 2.3.1.1 Conduction Mechanism for Ionic Humidity Sensors

Ionic type sensors adsorb water vapour primarily through the acid-base and hydrogen bonding mechanisms described in Section 2.2.1. The conduction mechanism is dependent on the surface coverage,  $\theta$  (see Table 2.1 for a definition). A



**Table 2.3.** Dominant conduction mechanism for ionic type humidity sensors at different surface coverage.

Coverage	Dominant Conduction Mechanism
$\theta \approx 0$	H <sup>+</sup> hopping along surface hydroxyls
$0 < \theta < 1$	H <sub>3</sub> O <sup>+</sup> diffusion + clustered Grotthuss + electron tunneling
$\theta \geq 1$	Grotthuss in continuous layer(s) of water

monolayer ( $\theta = 1$ ) is taken to be a monolayer of physically adsorbed (i.e., double hydrogen bonded) water, since hydroxylation is irreversible at room temperature and for sensing applications it is the reversible response that is important.

At very low surface coverage ( $\theta \approx 0$ ), an externally applied field results in proton (H<sup>+</sup>) hopping between surface hydroxyl groups [16, 22]. When physically adsorbed water is present, but monolayer formation is incomplete ( $0 < \theta < 1$ ) hydronium (H<sub>3</sub>O<sup>+</sup>) diffusion along the hydroxylated surface and proton transfer between adjacent water molecules in clusters are the dominant conduction mechanisms [16, 22]. Khanna and Nahar have shown that in this sub-monolayer regime, an additional mechanism of phonon assisted electron tunneling can take place where an adsorbed water molecule donates an electron to the oxide leaving a hole, which is subsequently filled from an electron tunneling from a neighbouring water molecule, thus leaving behind a hole and facilitating the continuation of the conduction mechanism [62]. When a monolayer is present, the dominant conduction mechanism is proton transfer between adjacent water molecules [16, 22]. This conduction mechanism is the same as that in liquid water and is called the Grotthuss chain reaction [16, 17]. Table 2.3 lists the dominant conduction mechanisms for different surface coverage.

### 2.3.1.2 Conduction Mechanism for Electronic Humidity Sensors

Electronic type sensors employ semiconducting oxides as their sensing medium and therefore exploit the electron transfer to the oxide resulting from redox based

chemisorption of water vapour. For n-type semiconductors, this results in an increase in conductivity with increasing humidity, whereas for p-type semiconductors, the conductivity will decrease. This conduction mechanism is dependent on the operating temperature and the doping, crystallinity, grain size, and microstructure of the oxide material [16].

#### **2.3.2 Permittivity**

Permittivity is a measure of the ease of polarization of a material exposed to an electric field (larger permittivity means easier to polarize). With dielectric materials there are four types of polarization [63]:

1. Electronic
2. Orientational
3. Ionic/atomic
4. Interfacial

Electronic polarization occurs when the electronic charge distribution is displaced relative to the nucleus/nuclei, resulting in a dipole moment dependent on the strength of the applied electric field and the electronic polarizability (atom/molecule constant). Orientational polarization occurs in polar materials where permanent dipoles experience a torque and orient themselves such that their electric field is in opposition to the applied field. Ionic polarization occurs in ionically bonded materials where the application of an electric field displaces the ions relative to each other and results in a net dipole moment (with no applied field the random orientation of the permanent dipoles results in no net dipole moment). Non-ionic materials experience atomic polarization where the nuclei of atoms forming a molecule are displaced. This is in contrast to electronic polarization, which is a result of electron displacement, however, it is similar to ionic polarization in that it involves the displacement of charge centres. Thus, ionic and atomic polarization are often grouped

together as one type of polarization, but referred to as either ionic or atomic depending on the ionic character of the material. Interfacial polarization is a result of the local accumulation of charge carriers as they drift through the material and is a result of conductivity changes occurring at an interface between two materials, boundaries between crystalline and amorphous regions, imperfections such as cracks and defects, regions of differing moisture content, and electrode-material interfaces [63, 64]. Unlike the previous three mechanisms, which involve bound charge, interfacial polarization is a result of free charge and is therefore dependent on conductivity [63].

All polarization processes are time dependent and have a temperature dependent relaxation time unique to the process [63, 64]. The permittivity of a material is therefore dependent on the temperature and the frequency of the applied electric field, with different polarization mechanisms being dominant over different frequency/temperature ranges. In general, interfacial polarization is dominant at low frequency (e.g., DC – kHz), orientational polarization is strongest in the radio to microwave range, ionic/atomic in the infrared, and electronic in the optical frequencies [63].

Iwaki and Morimoto have shown that the dielectric properties between 0.1 Hz – 5 MHz and 77 – 273 K of adsorbed water vapour on several oxides are due to three primary mechanisms [65–69]:

1. Interfacial polarization
2. Orientational polarization of surface hydroxyl groups
3. Orientational polarization of physisorbed water

At room temperature, interfacial polarization is dominant and is dependent on the conduction mechanisms described in Section 2.3.1.1. Thus, as the relative humidity is increased, both the conductivity and permittivity of metal oxides will increase [65–71]. As the temperature is decreased below room temperature, orientational

polarizations of surface hydroxyls and physisorbed water play an increasing role in the permittivity of the oxide, however, interfacial polarization is still dominant [66,68]. Furthermore, orientational polarization of hydroxyl groups is only present under sub-monolayer conditions [66,68].

In summary, the same conduction mechanisms utilized in resistive/impedance humidity sensors are responsible for the interfacial polarization and humidity dependent permittivity of metal oxides. The frequency of the applied voltage along with the temperature are critical in determining the capacitive response of metal oxide based humidity sensors.

## 2.4 Conclusions

Different adsorption mechanisms for metal oxide surfaces were discussed along with the specific case of water vapour adsorption. The adsorption of water vapour can alter the conductivity and permittivity of a metal oxide, thus providing a transduction mechanism for humidity sensing applications. Conduction mechanisms depend on surface coverage and involve protons, hydronium ions, and electron tunneling. The dominant mechanism responsible for permittivity changes in the DC–MHz frequency range is interfacial polarization.

The humidity sensors studied in this thesis utilize nanostructured  $\text{TiO}_2$ ,  $\text{Al}_2\text{O}_3$ , and  $\text{SiO}_2$  thin films. It is believed that these films adsorb water vapour through the acid-base type chemisorption and hydrogen bonded physisorption mechanisms described in Section 2.2.1 [17]. In the next chapter the fabrication of humidity sensors is discussed.

## Chapter 3

# Sensor Fabrication <sup>1</sup>

This chapter describes the fabrication of capacitive based humidity sensors used in this thesis. Each sensor was comprised of an interdigitated capacitor (IDC) coated with a humidity sensitive porous metal oxide thin film deposited by a technique known as glancing angle deposition (GLAD). The following will be discussed:

1. History and methodology of GLAD
2. Capacitive humidity sensors and justification for using IDCs
3. IDC fabrication
4. Thin film deposition

### 3.1 Glancing Angle Deposition

GLAD is a thin film fabrication technique that combines oblique angle deposition with substrate motion control, enabling the growth of thin films with engineered nanostructures [52, 73]. These films are extremely porous and consist of isolated columns that can take the form of, for example, helices, vertical posts and polygonal spirals [51, 74]. Applications of GLAD films include field emitters, supercapacitors, solar cells, thermal barrier coatings, high-speed gas sensors, and polarized

---

<sup>1</sup>Part of this chapter has been published in: J.J. Steele and M.J. Brett. Nanostructure engineering in porous columnar thin films: recent advances. *Journal of Materials Science: Materials in Electronics*, 18(4):367-379, April 2007. [72]

photoluminescence devices [75–81].

Properties of thin films largely depend on their composition, crystal structure, and morphology. Under certain growth conditions it is possible to fabricate thin films with a columnar morphology that can be engineered to provide specific characteristics. For example, a thin film with a microstructure that is shaped into a helical morphology will exhibit circular birefringence [82], silicon thin films composed of periodically arranged square spiral columns form 3-D photonic crystals [83], and a metallic chevron microstructure produces films with electrical conductivity anisotropies [84].

GLAD has been utilized to fabricate humidity sensitive thin films with different compositions and morphology. The high degree of control over film microstructure possible with the GLAD technique allows control of sensor performance. A brief review of the history of oblique angle deposition leading up to the development of GLAD will now be given followed by an account of the primary techniques used to fabricate basic film structures.

### 3.1.1 Oblique Angle Deposition to GLAD

The substantial history of oblique angle deposition includes works dating back to 1886 [85]. Initial studies entailed physical vapour deposition onto static substrates held in a position such that incident vapour flux arrives at non-normal, or oblique angles. This work showed that tilting the substrate during deposition changed the properties of the film. In 1953, Holland observed an anisotropic selective transmittance of light for aluminum films deposited with vapour incidence angles of  $80^\circ$  and  $85^\circ$  with respect to the substrate normal [86]. Smith, as well as Knorr and Hoffmann, demonstrated strong magnetic anisotropies in iron and nickel films deposited at vapour incidence angles exceeding  $70^\circ$  [87, 88]. At the time, it was thought that these effects could be a result of film morphology and in particular, the tendency of the ‘grains’ of the film to grow in the direction of the vapour source.

In 1959, Young and Kowal utilized this directional growth to, for the first time, engineer material properties by combining oblique angle deposition with periodic rotation of the substrate [89]. In their study they deposited fluorite films onto rotating substrates held at oblique angles and showed that the films exhibited optical activity as a result of the substrate rotation during oblique angle deposition.

In 1966, Nieuwenhuizen and Haanstra directly viewed the columnar morphology of obliquely deposited aluminum films with a scanning electron microscope (SEM) [90]. They presented images showing that the columns of an obliquely deposited film are tilted and grow in the direction of the vapour source. Directional columnar growth is key to the GLAD process and a brief discussion of the process will now be given. Detailed information on the physical and chemical mechanisms governing thin film growth can be found in [91, 92]. During the initial stages of vapour deposited film growth (for any angle of vapour incidence) adatoms condense onto the substrate and form individual separated islands, or nuclei [92, 93]. When the substrate is tilted such that incident vapour arrives at oblique angles, the topography of adatom nuclei shadows regions of the substrate. Thus, gaps between the nuclei are not filled in, preventing the coalescence of nuclei into a continuous thin film layer. Instead, the nuclei capture the vapour flux that would have landed in the shadowed regions, resulting in the formation of columns growing in the direction of the vapour source. The shadowing mechanism and directional column growth is illustrated in Figure 3.1.

This type of columnar growth is only possible from a directional vapour source with a small angular distribution; otherwise the vapour can fill in the shadowed regions of the substrate. Highly collimated vapour sources are easily attained with various physical vapour deposition (PVD) techniques such as evaporation (both thermal and electron beam) and long-throw, low-pressure sputtering [94–97]. Another requirement of columnar growth is that the temperature of the substrate must be less than  $\sim 0.3$  times that of the melting point of the source material [74]. At

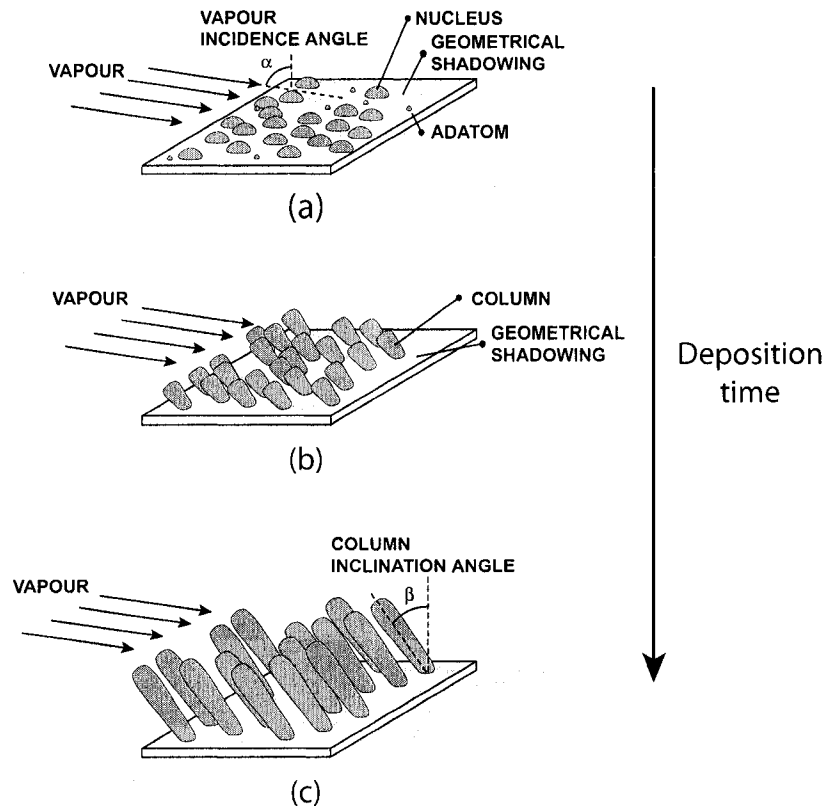


**Figure 3.1.** Geometrical shadowing and columnar growth. In the initial stages of film growth adatoms condense and form nuclei which results in geometrical shadowing of regions of the substrate (a), preventing film growth in those regions (b). The resulting film consists of columns that grow off the nuclei and are inclined in the direction of the vapour source (c). [4]

higher temperatures, the surface diffusivity of adatoms increases and a point will be reached where their diffusion length is large enough that they are able to fill in the shadowed regions of the substrate [98,99].

Nieuwenhuizen and Haanstra utilized the directional columnar growth of obliquely deposited films to fabricate the first film with a chevron, or zig-zag, column morphology [90]. By rotating the substrate  $180^\circ$  between two subsequent oblique angle depositions they were able to reverse the direction of column growth. In 1989, Motohiro and Taga improved upon the concept using in situ substrate motion control to instantaneously change the direction of column growth on the nanometre



length scale [100].

The next major development in oblique angle deposition came in 1995 when Robbie and Brett reported the glancing angle deposition (GLAD) technique [96, 101]. The GLAD process make use of extremely oblique ( $>80^\circ$  with respect to substrate normal) deposition to achieve an isolated and very porous columnar film morphology, and utilizes computerized control of substrate motion to change the relative vapour flux direction to manipulate the column growth and engineer the nanostructure of the resulting thin film. A key component of GLAD is the computerized substrate motion control based on deposition rate feedback from a quartz crystal microbalance (QCM). Figure 3.2 shows a schematic representation of a GLAD evaporation system. During a deposition, the angles  $\alpha$  (angle of vapour incidence) and  $\phi$  are adjusted according to a pre-defined motion control algorithm designed to yield a specific film nanostructure. Figure 3.3 shows SEM images of GLAD films demonstrating the various shapes the columns can take. The slanted post film shown in Figure 3.3(a) is the most basic film structure and was fabricated by holding both  $\alpha$  and  $\phi$  constant throughout the deposition. The chevron film shown in Figure 3.3(b) was fabricated by holding  $\alpha$  constant and periodically increasing  $\phi$  by  $180^\circ$ .

Instead of abruptly changing the direction of column growth, continuous changes can be obtained with a slow  $\phi$  rotation rate, resulting in a helical structure as shown in Figure 3.3(c). If the  $\phi$  rotation rate is too fast, however, the column growth will not respond to changes in direction of impinging vapour molecules and will degenerate into a vertical post as shown in Figure 3.3(d).

GLAD is a powerful platform for thin film research and is exploited by several groups. Hodgkinson et al. developed a variant of GLAD, called serial bideposition (SBD), capable of fabricating highly birefringent biaxial thin films [102, 103]. Others have adapted the GLAD technique to suit their particular application such as two-phase substrate rotation reported by Ye et al. [104], oblique angle deposition

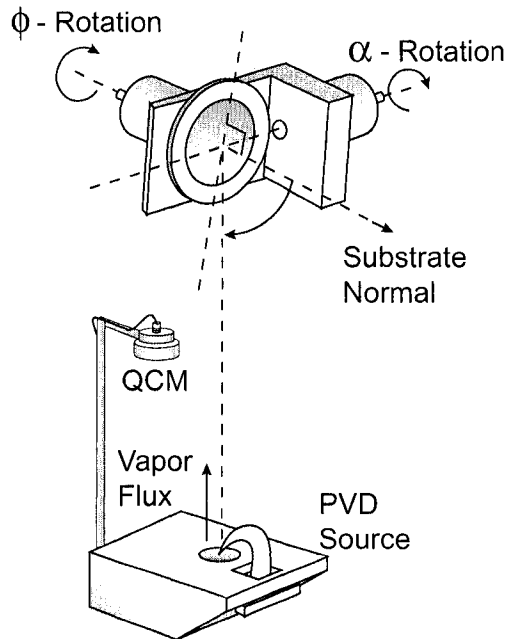


**Figure 3.2.** Physical vapour deposition apparatus for GLAD. Engineering of thin film nanostructure is achieved through in situ adjustments of the angles  $\alpha$  and  $\phi$  during a deposition. Substrate motion control is based on deposition rate feedback from a quartz crystal microbalance (QCM).

(OAD) used by Zhao et al. [105], and dynamic oblique deposition (DOD) reported by Suzuki et al. [106].

GLAD is a versatile process. Most materials that can be deposited via PVD methods can be used to fabricate GLAD films, including numerous metals, semiconductors, and insulators. The nanostructure of GLAD films can be engineered to suit the application and can range from the simple nanostructures shown in Figure 3.3, to exotic nanostructures such as polygonal spirals, periodically bent nematics and superhelices [94, 107, 108].

GLAD films are extremely well suited for humidity sensing studies as their composition and morphology can be fine tuned through the deposition process. Thus, properties of the sensing material such as surface area, pore size distribution, and thickness, all of which have a profound impact on sensor performance [6–9, 16, 17, 22, 29, 34, 46, 50], can be optimized.

### 3.1. Glancing Angle Deposition

---

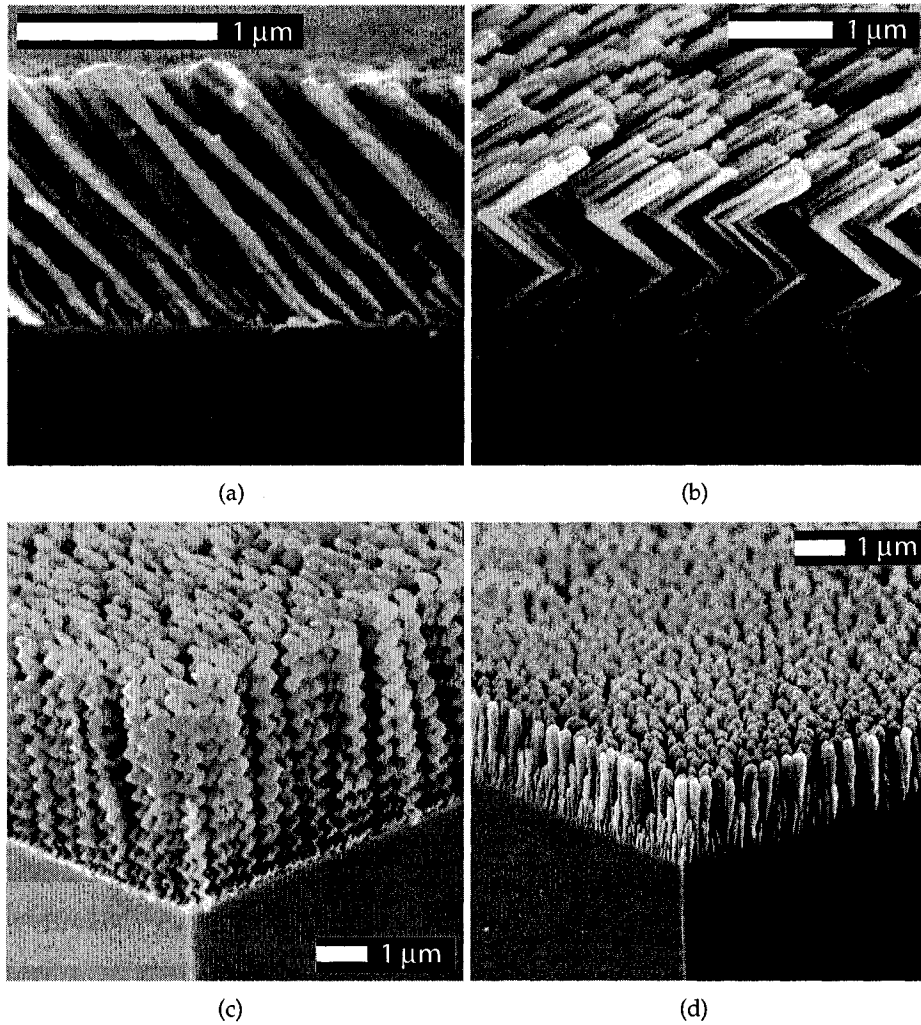


**Figure 3.3.** Examples of GLAD nanostructured thin films. The slanted post film (a) was fabricated by holding both  $\alpha$  and  $\phi$  constant throughout the deposition. A chevron film (b) is fabricated by increasing  $\phi$  by  $180^\circ$  between slanted post segments. A helical film (c) is fabricated by continually increasing  $\phi$  at a slow rate such that the column growth can trace the substrate motion, if the  $\phi$  rotation rate is too fast the helical structure will degenerate in to a vertical post structure like that shown in (d).

## 3.2 Capacitive Humidity Sensors

Capacitive humidity sensors are based on permittivity changes of an insulating hydrophilic material as a result of water vapour adsorption/desorption. When such a material is used as the dielectric in a capacitive structure the result is a device with a humidity dependent capacitance. As mentioned in Chapter 1, capacitive humidity sensors dominate the market (75%) in large part due to their low power consumption, high sensitivity, and low cost [9].

There are two types of capacitive structures used in humidity sensors: parallel plate, and IDC. Figure 3.4 illustrates the differences between the two structures. Parallel plate structures are formed by depositing a bottom electrode onto a substrate (or use a conductive substrate as the bottom electrode), followed by the deposition of the sensing medium, then depositing a second electrode on top of the sensing medium. The top electrode is typically only 10's of nanometres thick making it porous, which facilitates water vapour access to the sensing medium resulting in reduced response times [109]. As this top electrode must remain electrically continuous, it will always impede water vapour transfer between the environment and the sensing medium. Using an interdigitated electrode for the top electrode to increase the exposed area of the sensing medium and further enhance response time is also common, however, humidity sensors based on parallel-plate capacitive structures are always slower than IDC based humidity sensors (for a given sensing medium) due to the top electrode obstructing water vapour transfer between the environment and sensing medium [28,36]. It is therefore more common to find IDC based sensors where there sensing medium is deposited on top of an IDC, giving water vapour complete, unobstructed access to the sensing medium [7, 109, 110]. Although IDC based sensors are faster, they are typically less sensitive as half the electric field passes through the substrate, whereas parallel plate structures confine the field to the sensing medium [28].

Sensor response time is a focus of this thesis; therefore using IDC based sen-

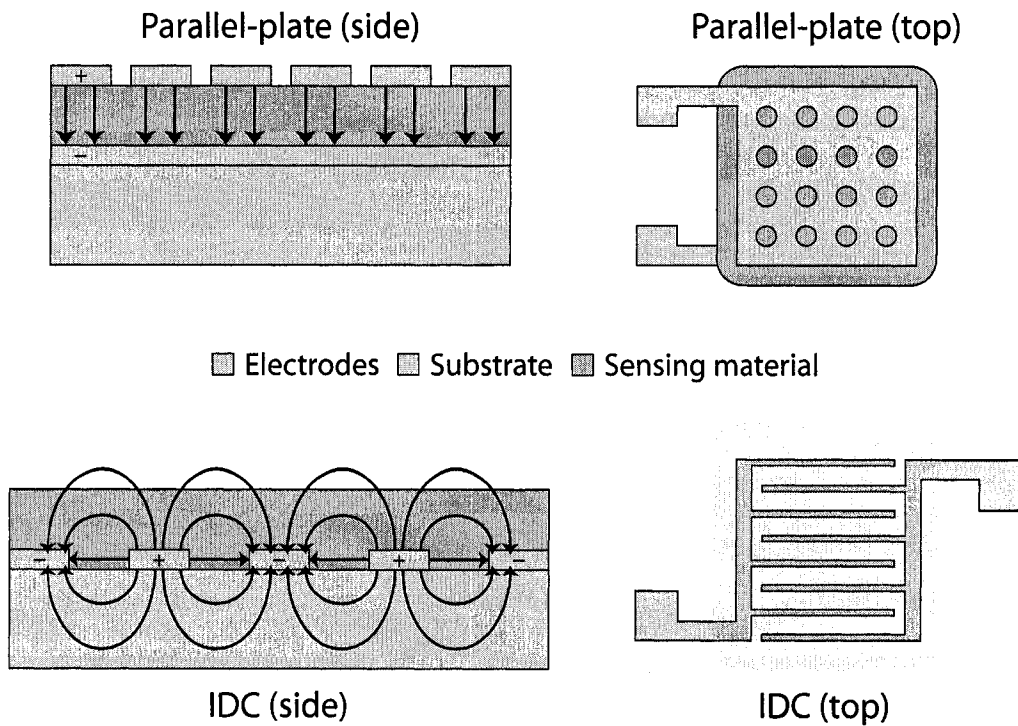


**Figure 3.4.** Capacitor humidity sensors are based on either parallel-plate or IDC structures. IDC based sensors are faster as water vapour is not impeded by an electrode. However, parallel-plate based sensors are more sensitive as they confine the electric field to the sensing medium as opposed to half the field passing through the substrate, as is the case with IDC based sensors.

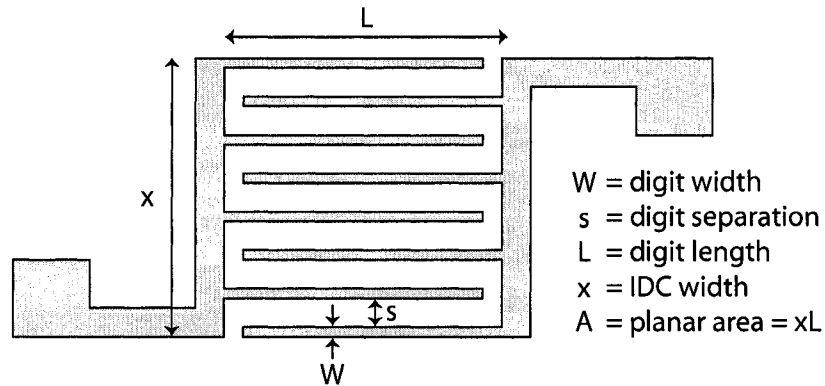


Figure 3.5. IDC geometry, top view. Not to scale.

sors was more appropriate. Another imperative reason for using IDCs is ease of fabrication. Parallel-plate based sensors are less suitable for the GLAD process as they require the film to be “capped” by slowly decreasing the deposition angle ( $\alpha$ ) to near normal incidence to make the top of the film dense enough to support an electrically continuous top electrode [53,111]. For these reasons, IDC based sensors were used.

### 3.3 IDC Fabrication

With IDC based sensors, the geometry alters the electric field density/profile within the sensing medium and significantly impacts the sensitivity of the device [31,32,110,112,113]. Figure 3.5 shows a top view illustration of IDC geometry with the important features being the digit width ( $W$ ), digit separation ( $s$ ), digit length ( $L$ ), IDC width ( $x$ ), and planar area ( $A = xL$ ).

Two types of IDCs were fabricated: IDCs with relatively large digit widths and separations in the tens of micrometres range, and IDCs where the electrodes were counter-sunk into a silicon dioxide layer and had digit widths and separations in the micrometre range. The large geometry IDCs were fabricated using standard photolithography techniques, whereas the counter-sunk electrode IDCs

(CSE-IDCs) were fabricated using a proprietary procedure from Micralyne Inc. A comparison between the two types of IDCs and the impact of IDC geometry is given in Chapter 5. Each type of IDC will now be discussed.

#### 3.3.1 Large Geometry IDCs

The geometry of these IDCs were as follows:

- $W = 20 \mu\text{m}$  (digit width)
- $s = 10 \mu\text{m}$  (digit separation)
- $L = 5 \text{ mm}$  (digit length)
- $x = 5 \text{ mm}$  (IDC width)
- $A = 25 \text{ mm}^2$  (planar area)

These values were chosen by surveying the literature where IDCs with digit widths and separations in the 10's of micrometres range are commonly utilized for humidity sensing applications [28,35,36,38,47,54,114,115]. The relatively large dimensions of these IDCs made it possible to fabricate them using standard photolithography techniques. The following fabrication procedure was developed at the University of Alberta NanoFab: A 30 nm thick chrome adhesion layer was sputtered onto borofloat glass substrates followed by a 150 nm gold deposition. The substrates were then spin coated with HPR 504 photoresist, exposed through a shadow mask with the IDC patterns, and developed. Following a gold then chrome wet chemical etch, substrates were cut into die using a diamond dicing saw where each die contained one IDC. The photoresist was removed prior to GLAD film deposition by soaking the die in an acetone bath.

#### 3.3.2 Counter-Sunk Electrode IDCs

In Chapter 5 it will be shown that planarizing the surface of an IDC by counter sinking the electrodes as well as reducing both digit width and separation offer several

**Table 3.1.** IDCs used for thesis research. IDC-25-20-10 substrates were fabricated using standard photolithography techniques. All other IDCs were fabricated by Micralyne, Inc.

IDC Reference Name	Planar Area $A$ (mm <sup>2</sup> )	Digit Width $W$ (μm)	Digit Separation $s$ (μm)	Number of Digits
IDC-25-20-10	25	20	10	167
IDC-25-3-5	25	3	5	625
IDC-25-3-3	25	3	3	833
IDC-100-3-5	100	3	5	1250
IDC-100-3-3	100	3	3	1667

advantages in terms of sensor performance and fabrication. Figure 3.6 illustrates the cross section of CSE-IDCs developed by Micralyne, Inc. where gold electrodes are coplanar with a silicon dioxide layer on a silicon die. Figure 3.7 shows a photograph of a CSE-IDC.

A number of CSE-IDCs were developed with various dimensions. Table 3.1 lists the IDCs used for the research presented in this thesis. The following naming system will be used to reference IDCs: IDC- $A$ - $W$ - $s$  where the units of  $A$  is mm<sup>2</sup> and  $W$  and  $s$  are in micrometres. The planar area for all IDCs were square, thus  $A = 25 \text{ mm}^2$  implies  $L = 5 \text{ mm}$  and  $x = 5 \text{ mm}$ .

### 3.4 Thin Film Deposition

Thin film depositions were performed under high vacuum conditions (base pressures in the  $10^{-7}$  to  $10^{-6}$  Torr range) using an electron beam evaporation system (Kurt J. Lesker AXXIS system). Aluminum oxide (corundum, 99.99% purity), silicon dioxide (fused silica, 99.99% purity), and titanium dioxide (rutile, 99.9% purity) source materials were purchased from Cerac Inc. During a typical Al<sub>2</sub>O<sub>3</sub> deposition, the pressure initially increases to approximately  $3 \times 10^{-5}$  Torr as a result of oxygen outgassing from the source material. With time, the pressure drops to the mid  $10^{-6}$  Torr range as the oxygen is pumped away. Typical deposition pressures



### 3.4. Thin Film Deposition

---

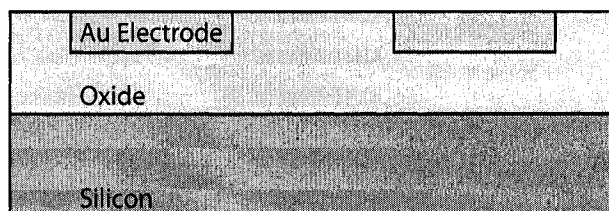


*Figure 3.6. Cross-sectional illustration of Micralyne Inc. fabricated CSE-IDC. Not to scale.*

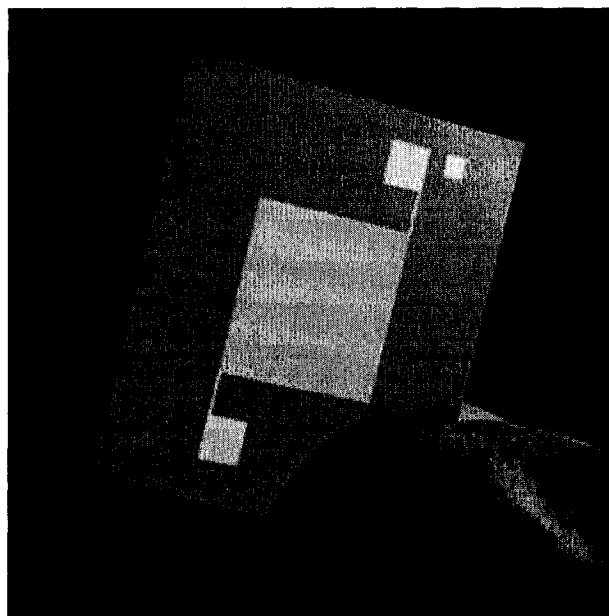


*Figure 3.7. Photograph of a CSE-IDC. The dimensions of the die are roughly  $2 \times 2$  cm.*

during SiO<sub>2</sub> depositions were  $3 \times 10^{-6}$  Torr. The deposition pressure during titania depositions was maintained between  $6 \times 10^{-5}$  and  $8 \times 10^{-5}$  Torr through the addition of oxygen gas (Praxair ultra high purity 99.993%) to promote the growth of stoichiometric films [116]. All films used for the capacitive humidity sensors in this thesis were of the vertical post type (Figure 3.3(d)) grown at constant  $\alpha$  and  $\phi$  rotation rates continually adjusted (via software) to maintain a film growth rate (in substrate normal direction) of 5 nm per 360° revolution of the substrate. Deposition rates along the substrate normal were maintained between 5–7 Å/s (via emission current) resulting in  $\phi$  rotation rates of 6–8.4 RPM. The deposition angle and film thickness were varied (Chapter 6 discusses their effect on sensor performance), however, typical values were  $\alpha = 81^\circ$  and 1.5  $\mu\text{m}$ .

### 3.5 Summary

Capacitive based humidity sensors were fabricated by coating IDCs with highly porous, nanostructured, hydrophilic, metal oxide thin films deposited by GLAD. Figure 3.8 shows a cross-sectional SEM image of a sensor fabricated from an IDC-100-3-5 coated with a 1.5  $\mu\text{m}$  thick vertical post aluminum oxide GLAD film deposited at a deposition angle of  $\alpha = 81^\circ$ . The ability of GLAD to control film morphology on the 10 nm scale for a variety of source materials makes it an ideal platform for studying humidity sensors as the composition and morphology of the sensing medium plays a critical role in device performance. Capacitive humidity sensors were chosen for study due to their dominance of the market and advantageous properties. IDCs were utilized instead of parallel plate capacitor structures due to their faster response to humidity changes and their compatibility with the GLAD process.

In the next chapter, the experimental methodology used to characterize the sensors is discussed.

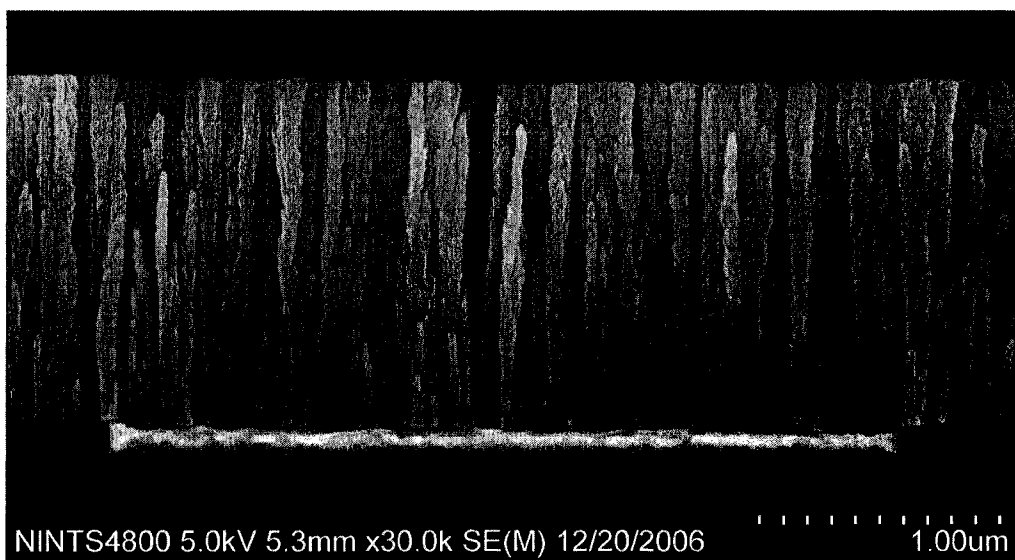


*Figure 3.8. Cross-sectional SEM image of a single digit from an IDC-100-3-5 coated with a 1.5  $\mu\text{m}$  thick  $\text{Al}_2\text{O}_3$  vertical post GLAD film deposited at  $\alpha = 81^\circ$ .*

## Chapter 4

# Experimental Methodology

In this chapter the experimental methodology used in this thesis is presented. The following will be discussed:

1. Humidity generation and control
2. Capacitance measurement and calibration
3. Resistance measurement and calibration
4. Relative humidity measurement calibration
5. Response time measurement
6. Commercial humidity sensor testing

### 4.1 Humidity Generation and Control

A humidity control chamber was constructed using a bubbler system where dry nitrogen was mixed with moist air at different ratios by varying the flow rate of each gas prior to mixing. Figure 4.1 illustrates the humidity control setup. To vary the flow, mass flow controllers (MKS M100B) with a maximum flow rate of 500 standard cubic centimetres per minute (sccm) and a resolution of 0.5 sccm were used. Briglin and Lewis have shown that saturated vapour from a similar bubbler system

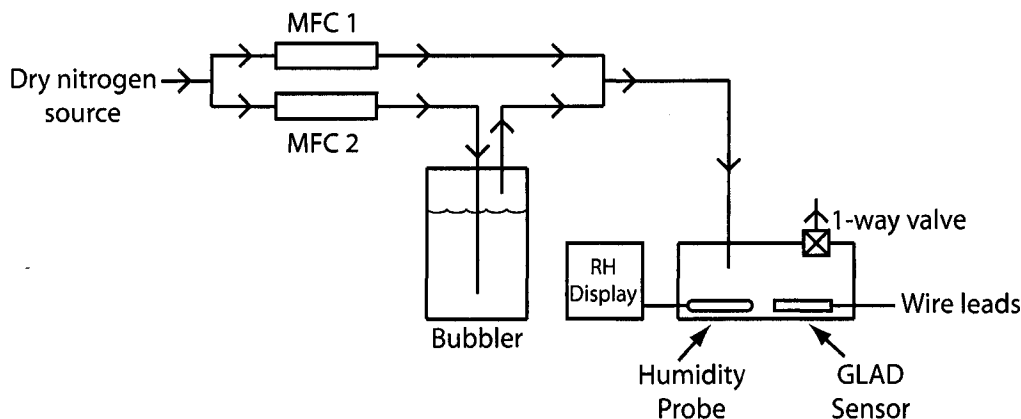


**Figure 4.1.** Humidity control setup. The flow through the mass flow controllers (MFCs) is varied to set the mixing ratio of dry nitrogen and moist air. The mixed gas enters the testing chamber where the humidity is monitored by a commercial humidity probe. Atmospheric pressure is maintained with a 1-way valve.

is produced with flow rates  $\leq 500$  sccm [46]. The moist air was obtained by submerging a nitrogen line into a sealed water reservoir. The saturated air above the water is forced out of the reservoir where it mixes with the dry nitrogen. The mixed air was delivered to a sealed sample chamber (350 mL volume) where the humidity was monitored with a commercial relative humidity probe (Vaisala HMP100). To maintain atmospheric pressure a one way valve was implemented to exhaust excess gas out of the sample chamber. The wire leads (No. 32 AWG solid) of the sensor under test were fed through two  $\frac{1}{64}$  inch drilled holes and connected to a LCR meter (QuadTech 1715 Digibridge) to monitor the capacitance.

#### 4.1.1 Automated Capacitive Response Measurements using LabVIEW

LabVIEW (version 7.0) was used to automate the process for varying the humidity and collecting capacitance data (programming by Sumudu Fernando). The commercial humidity probe is packaged with a transmitter (Vaisala HMT100) that provides a voltage signal linearly proportional to the measured relative humidity with a responsivity of 10 mV per %RH. This voltage signal was sent to a differential analog input channel of a data acquisition board (National Instruments PCI-6024E) for

#### 4.1. Humidity Generation and Control

---

use in LabVIEW.

A two channel power supply and readout (MKS Instruments PR-4000-F) was used to control the flow setpoints of the two MFCs. Both the readout and LCR meter have RS232 terminals for communication with a computer. LabVIEW drivers for both instruments are available from their respective manufacturer website.

During a typical capacitive response measurement, the user selects the start RH setpoint ( $RH_i$ ), the end RH setpoint ( $RH_f$ ), the incremental / decremental RH value between setpoints ( $\Delta RH$ ), the wait time at each setpoint ( $T_{wait}$ ), and the number of times to perform a complete increasing and decreasing humidity cycle ( $N$ ). The flow rates of the the MFCs were set to achieve the desired RH setpoint with the total flow held constant at 500 sccm. A RH setpoint of 50% will set the flow rates of both MFCs to 250 sccm, whereas a setpoint of 25% RH will set the flow rate of the nitrogen MFC to 375 sccm and the saturated water vapour MFC to 125 sccm. Thus, for a given set of input parameters the program will:

1. Set MFC flow rates to achieve  $RH_i$
2. Wait  $T_{wait}$
3. Record capacitance from LCR meter and RH from commercial probe and write to file
4. Increment RH setpoint by  $\Delta RH$
5. Repeat steps 2 to 4 until  $RH_f$  is reached and measurements logged
6. Decrement RH setpoint by  $\Delta RH$
7. Wait  $T_{wait}$
8. Record capacitance and RH and write to file
9. Repeat steps 6 to 8 until  $RH_i$  is reached
10. Repeat steps 1 to 9 until total number of completed cycles equals  $N$

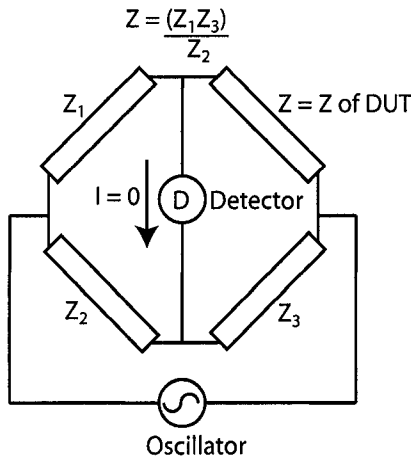


**Figure 4.2.** Nulling type bridge circuit used in LCR meter. When the current through the detector equals zero, the impedance of the DUT can be calculated based on bridge elements  $Z_1$ ,  $Z_2$ , and  $Z_3$ . The QuadTech meter utilizes different combinations of inductive, capacitive, and resistive bridge elements, depending on the measured quantity.

As a general guideline the setpoint wait time was set to at least 3 minutes since at 500 sccm the 350 mL chamber will be exchanged roughly 5 times per setpoint, ensuring equilibrium of chamber humidity.

## 4.2 Capacitance Measurement and Calibration

The LCR meter used to measure sensor capacitance is a digital meter that uses a nulling type bridge circuit to calculate impedance parameters of a device under test (DUT). This basic concept is shown in Figure 4.2.

The LCR meter uses 4-terminal connections to a DUT where one set of terminals applies an AC current and the other measures the resulting open-circuit voltage. This eliminates measurement errors from lead inductance and lead resistance (including contact resistance) in series with the device and stray capacitance between the two leads. Measurement of the current, voltage, and their phase angle difference provides the meter with all the necessary information to calculate a number of impedance parameters using either a series or parallel equivalent circuit model.

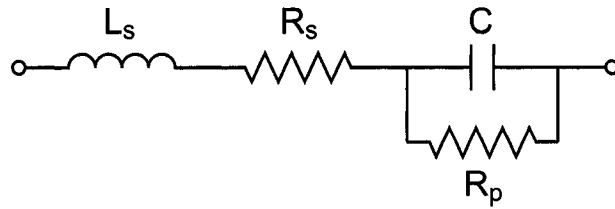


Figure 4.3. Equivalent circuit for a capacitor.

For series equivalent circuit measurements the meter models the DUT as a resistance ( $R_s$  = equivalent series resistance, ESR) in series with either a capacitance ( $C_s$ ) or inductance ( $L_s$ ). The parallel setting models the DUT as a resistance ( $R_p$  = equivalent parallel resistance, EPR) in parallel with a capacitance ( $C_p$ ) or inductance ( $L_p$ ). To decide which equivalent circuit model most accurately represents the DUT, it is necessary to look at the relative magnitude of the reactance and EPR. Since the work presented in this thesis involves capacitive based sensors, only the situation for capacitive elements will be discussed.

A real capacitor can be modeled by the circuit shown in Figure 4.3 with an inductance,  $L_s$ , in series with a resistance,  $R_s$ , in series with a parallel combination of a capacitance,  $C$ , and resistance,  $R_p$  [117]. Every circuit element has an inductance which is represented by  $L_s$ . However, for most capacitive elements this inductance can be safely ignored unless particularly high frequencies are used where self resonant characteristics become an issue [117]. The series resistance,  $R_s$ , represents the effects of conductor resistance and dielectric losses. The parallel resistance,  $R_p$ , represents the effects of leakage current through the electrodes of the capacitor.

The LCR meter models a capacitor with either  $R_s$  or  $R_p$ . Thus, it is necessary to look at the reactance of the capacitor,  $X_C$  to decide which is more appropriate. If  $X_C$  is small relative to  $R_p$ , then the parallel combination of  $X_C$  and  $R_p$  is dominated by  $X_C$  and it is therefore more appropriate to use the series model ( $C = C_s$ ). Similarly, if  $X_C$  is large relative to  $R_p$ , then  $R_p$  should not be ignored and the parallel model should be used ( $C = C_p$ ).



In addition to selecting either series or parallel measurement mode, the meter has 4 frequency settings (100 Hz, 120 Hz, 1 kHz, 10 kHz), two voltage level settings ( $0.25 V_{\text{rms}}$  and  $1.0 V_{\text{rms}}$ ), and three voltage integration times (slow, medium, and fast). The slow integration time provides 2 measurements per second and is the most accurate setting. If measurement speed is an issue (e.g., during response time measurements) then the fast setting can provide 25 measurements per second.

### 4.2.1 Capacitance Calibration

To obtain an estimate of the absolute error of the LCR meter capacitance measurements, it is necessary to assess accuracy error and precision error. A method for using multiple poor standards as an ensemble to provide a high quality calibration is developed.

#### 4.2.1.1 Capacitance Accuracy Error

The LCR meter is shipped with a NIST traceable calibration certificate. The quoted measurement accuracy is 0.2% at 1 kHz and  $1 V_{\text{rms}}$ .

Meter accuracy was tested using ceramic capacitors with nominal values ranging from 1 pF to 2.2  $\mu\text{F}$ . For these measurements, a voltage of  $1 V_{\text{rms}}$  and a frequency of 1 kHz were used. Both the series and parallel capacitance were measured and found to be similar (difference much less than meter accuracy error) for the range of values previously mentioned. The measured capacitance will be denoted as  $C_{\text{meas}}$  and the nominal capacitance as  $C_{\text{nom}}$ .

It can be argued that an ensemble of uncorrelated poor standards when taken together, results in an excellent near perfect standard, assuming that the errors between the different standards are uncorrelated. In this manner, the distribution of the errors will be centered around zero, yielding an ensemble standard with near perfect accuracy [118]. For the calibration presented here, uncorrelated error between the capacitors was ensured by choosing a large number of capacitors of

## 4.2. Capacitance Measurement and Calibration

---

different values and from different manufacturers. This frees the standard set from any bias resulting from systematic errors by a particular manufacturer, or from a particular batch of capacitors. For the LCR meter capacitance calibration, four sets of capacitors (125 in total) from more than ten different manufacturers were measured.

Figure 4.4 shows a plot of the nominal capacitance versus measured values. The data from the QuadTech calibration certificate has been included for comparison.

The data sets shown in Figure 4.4 span five orders of magnitude, thus simple least squares regression analysis will be dominated by the large capacitance values. To eliminate this dominance, an analytic fitting technique was derived on the basis of fitting the logarithm of the capacitance and calculating accuracy error using error propagation. This technique is described in Appendix A.

Table 4.1 shows the fit values of the 4 sets of capacitance measurements and the QuadTech calibration certificate data using the technique described in Appendix A.

The mean slope (excluding QuadTech data) was calculated to be:

$$\bar{m} = 1.0134 \pm 0.0063 \quad (4.1)$$

with a standard deviation of:

$$\sigma_m = 0.0125 \quad (4.2)$$

Thus, the relative uncertainty of the slope is:

$$\frac{\sigma_m}{\bar{m}} = 0.012 = 1.2\% \quad (4.3)$$

It is this value that is taken as the LCR meter accuracy error for capacitance measurements ( $\epsilon_{C,acc}$ ) as it represents the experimental uncertainty of slope values, which in turn translates to an uncertainty in  $C_{nom}$  for a given measured capacitance

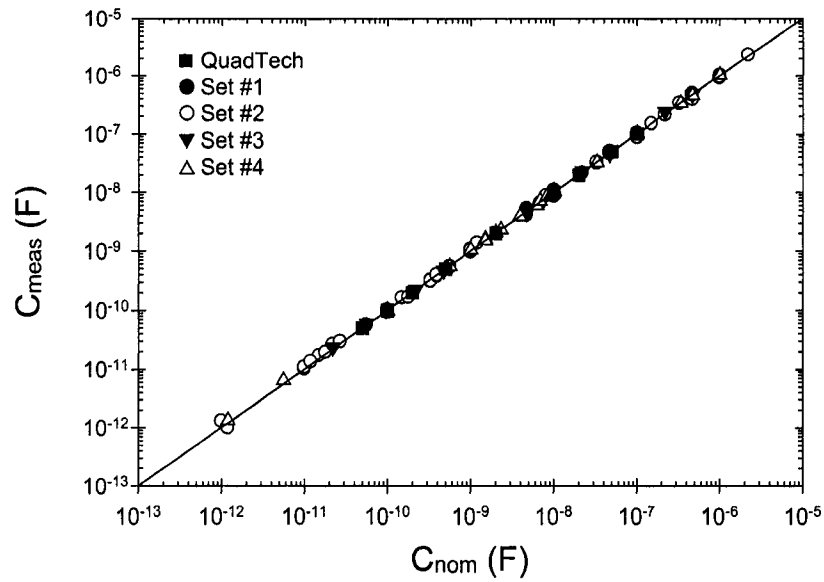


**Figure 4.4.** Nominal versus measured capacitance from QuadTech calibration certificate and 4 sets of capacitors (125 in total) from various manufacturers.

**Table 4.1.** Fit values ( $C_{meas} = mC_{nom}$ ) for the 4 sets of capacitance measurements and the QuadTech calibration certificate.

Data Set	Slope $m$	Slope Error $\delta_m$	$\delta_m/m$ [%]
QuadTech	0.9992	0.0005	0.05
#1	0.9973	0.0135	1.35
#2	1.0103	0.0155	1.53
#3	1.0260	0.0153	1.49
#4	1.0199	0.0099	0.97

## 4.2. Capacitance Measurement and Calibration

---

$C_{meas}$  via error propagation. Thus,

$$\epsilon_{C,acc} = 1.2\% \quad (4.4)$$

Equation 4.3 is representative of the LCR meter accuracy error only because of the previous argument that an ensemble of uncorrelated poor standards can be taken together and used as an accurate standard [118]. Fitting all of the capacitance measurements (using technique in Appendix A) and observing the relative residuals provides support for this argument. Figure 4.5 shows a histogram of the relative residuals and a 3-parameter Gauss distribution fit provided from SigmaPlot (version 10.0), which uses the Marquardt-Levenberg fitting algorithm. The following Gauss fit parameters were obtained:

$$x_0 = 0.2 \pm 0.4\% \quad (4.5)$$

$$\sigma = 5.4 \pm 0.4\% \quad (4.6)$$

$$R^2 = 0.940 \quad (4.7)$$

The excellent correlation coefficient and the fact that  $x_0$  is within error of zero provides evidence that the errors governing the deviation of true capacitance values from nominal capacitance values are indeed random and uncorrelated, supporting the assumption of the previous ensemble argument.

### 4.2.1.2 Capacitance Precision Error

Estimates of precision error were obtained by recording a minimum of 200 successive capacitance measurements for a variety of capacitors with nominal values ranging from 0.5 pF to 3.3  $\mu$ F. The LCR frequency and voltage was set to 1 kHz and 1  $V_{rms}$ , respectively. Two sets of data were collected; one using the fast and one using the slow integration time setting. There was no significant difference

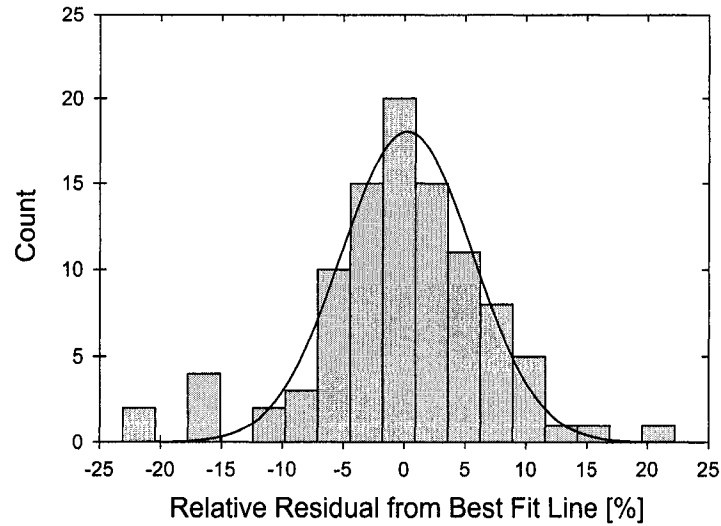


*Figure 4.5. Histogram of relative residuals of measured capacitance values from best fit line and corresponding Gaussian fit from SigmaPlot version 10.0 (Marquardt-Levenberg algorithm). Gaussian parameters were  $x_0 = 0.2 \pm 0.4\%$  and  $\sigma = 5.4 \pm 0.4\%$  with a correlation coefficient of  $R^2 = 0.940$ . The good fit to a Gauss distribution indicates that the relative residuals are normally distributed and that the capacitors used are uncorrelated.*

of measured capacitance between series and parallel measurement mode for the range of capacitance values used. The relative standard deviation (RSD) of those measurements are plotted in Figure 4.6. Some RSD values have been omitted from Figure 4.6 based on Chauvenet's Criterion [118].

The fit shown in Figure 4.6 was obtained using both the fast and slow data sets and the following equation as a model:

$$RSD = \frac{\sigma_{meas}}{C_{nom}} \quad (4.8)$$

where  $\sigma_{meas}$  is the standard deviation of the 200 measurements and  $C_{nom}$  is the nominal capacitance value in Farads. The value of  $\sigma_{meas}$  is dependent on the precision error ( $\sigma_{prec}$ ) as well as the noise introduced by the LCR meter ( $\sigma_{noise}$ ). Thus,  $\sigma_{meas}$  can be written as:

$$\sigma_{meas}^2 = \sigma_{prec}^2 + \sigma_{noise}^2 \quad (4.9)$$

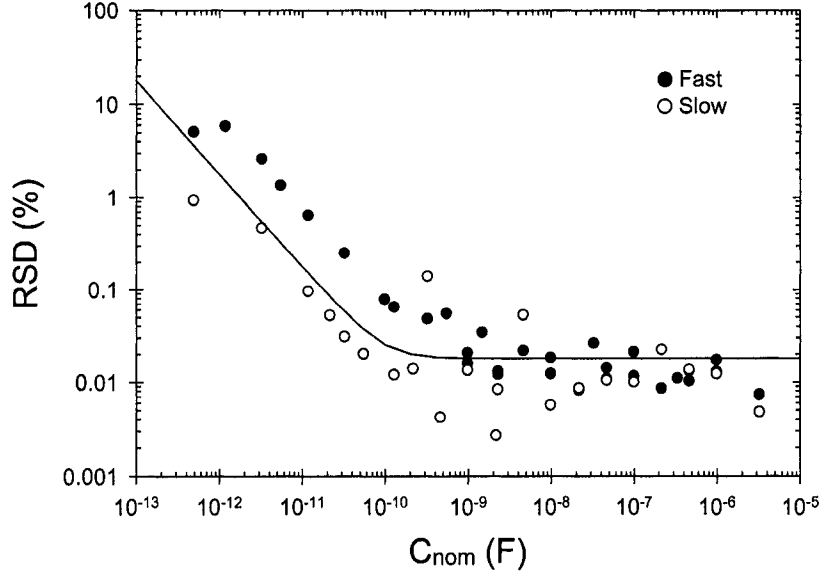


**Figure 4.6.** Relative standard deviation of a minimum 200 capacitance measurements using the fast and slow integration time setting on the LCR meter. The fit was obtained using Equation 4.10.

It is assumed that the relative precision error,  $\frac{\sigma_{prec}}{C_{nom}}$ , and the meter noise are constant and are therefore taken to be fit parameters. Thus, for fitting, Equation 4.8 is taken as:

$$RSD = \frac{\sigma_{meas}}{C_{nom}} = \sqrt{\left(\frac{\sigma_{prec}}{C_{nom}}\right)^2 + \left(\frac{\sigma_{noise}}{C_{nom}}\right)^2} = \sqrt{a^2 + \frac{b^2}{C_{nom}^2}} \quad (4.10)$$

where  $a$  and  $b$  are the fit parameters. For the data shown in Figure 4.6,  $a$  and  $b$  were calculated to be 0.018 [%] and  $1.78 \times 10^{-12}$  [%F], respectively.

The fit shown in Figure 4.6 was used as a basis to reject data based on Chauvenet's criterion [118]. Since all capacitive based sensors presented in this thesis have capacitance values greater than 100 pF, the LCR meter capacitance precision error can be taken as  $a$  from the fit using Equation 4.10. Thus, the precision error for capacitance measurements was taken as:

$$\epsilon_{C,pre} = 0.02\% \quad (4.11)$$

### 4.2.1.3 Capacitance Absolute Error

The absolute error for capacitance measurements ( $\epsilon_C$ ) was calculated by adding the accuracy error ( $\epsilon_{C,acc}$ ) and precision error ( $\epsilon_{C,pre}$ ) in quadrature:

$$\epsilon_C^2 = \epsilon_{C,acc}^2 + \epsilon_{C,pre}^2 \quad (4.12)$$

Inserting the values from equations 4.4 and 4.11:

$$\epsilon_C = \sqrt{0.012^2 + 0.0002^2} = 0.012 \quad (4.13)$$

Thus, the absolute error for capacitance measurements was taken to be:

$$\boxed{\epsilon_C = 1.2\% \text{ (68\% confidence)}} \quad (4.14)$$

## 4.3 Resistance Measurement and Calibration

The LCR meter measures the resistance of a device under test the using the same method previously described for capacitance (Section 4.2). The same guide lines for selecting the series or parallel equivalent circuit model for capacitance measurements can be applied to resistance measurements. For manufactured resistors, however, the series and parallel resistance will be equivalent ( $R_s = R_p$ ).

### 4.3.1 Resistance Calibration

Calibration of the LCR meter resistance measurements were performed in the same manner as capacitance calibration. Accuracy error was estimated by measuring multiple sets of manufactured resistors and calculating the deviation in the slope for each set of measurements. Precision error was estimated by measuring various resistors many times. Finally, absolute error was estimated based on adding in quadrature the accuracy and precision errors.

#### 4.3.1.1 Resistance Accuracy Error

Figure 4.7 shows a plot of nominal resistance ( $R_{nom}$ ) versus measured resistance ( $R_{meas}$ ) for three sets of resistors (86 in total). The LCR meter settings were 1 kHz frequency, 1 V<sub>rms</sub> voltage, and slow integraton time. The data presented in Figure 4.7 was collected with the series equivalent circuit setting, however, as previously mentioned  $R_s = R_p$  for manufactured resistors so the resistance is simply reported as  $R_{meas}$ . Sets #1 and #2 contained resistors from more than four manufacturers all with a tolerance of 5%. Set #3 resistors were from a single manufacturer and had a tolerance of 2%. Nominal resistance values ranged from 5.6  $\Omega$  to 10 M $\Omega$ . The data from the QuadTech calibration certificate has also been included in Figure 4.7 for comparison.

Table 4.2 shows the fit values of the 3 sets of resistance measurements and the QuadTech calibration certificate data using the technique described in Appendix A.

The mean slope (excluding QuadTech data) was calculated to be:

$$\bar{m} = 0.9911 \pm 0.0024 \quad (4.15)$$

with a standard deviation of:

$$\sigma_m = 0.0042 \quad (4.16)$$

Thus, the relative uncertainty of the slope is:

$$\frac{\sigma_m}{\bar{m}} = 0.004 = 0.4\% \quad (4.17)$$

As with the capacitance calibration data, the relative uncertainty in the slope is taken as the accuracy error. Thus for resistance measurements the accuracy error ( $\epsilon_{R,acc}$ ) was calculated to be:

$$\epsilon_{R,acc} = 0.4\% \quad (4.18)$$

Figure 4.8 shows a histogram of the relative residuals resulting from fitting all



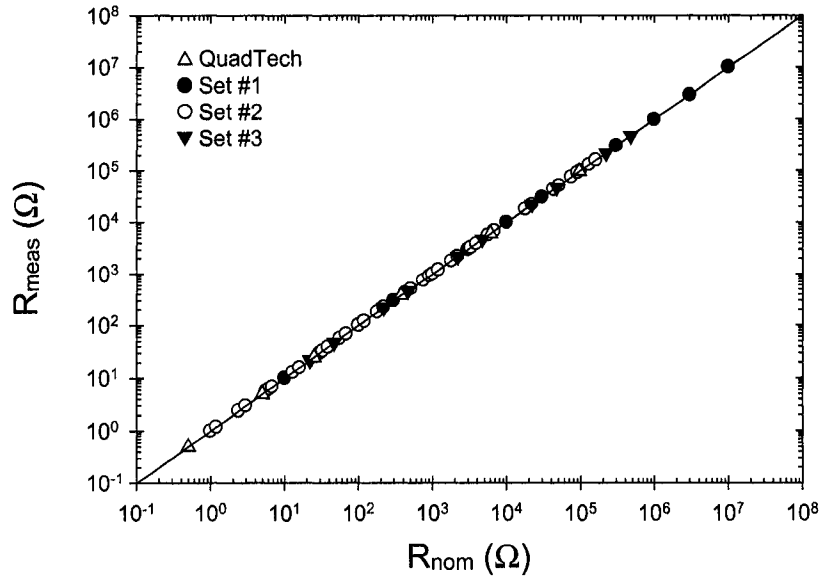


**Figure 4.7.** Nominal versus measured resistance from QuadTech calibration certificate and 3 sets of resistors (86 in total).

**Table 4.2.** Fit values ( $R_{meas} = mR_{nom}$ ) for the 3 sets of resistance measurements and the QuadTech calibration certificate.

Data Set	Slope $m$	Slope Error $\delta_m$	$\delta_m/m[\%]$
QuadTech	0.9983	0.0011	0.11
#1	0.9874	0.0010	0.10
#2	0.9903	0.0007	0.07
#3	0.9956	0.0006	0.06

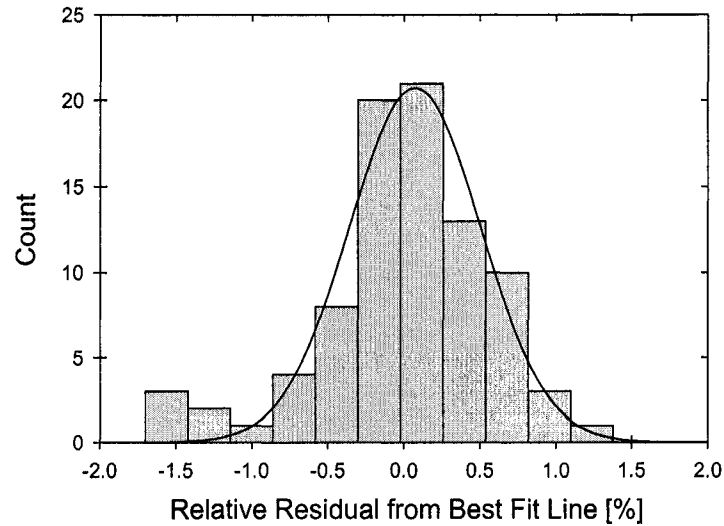


*Figure 4.8. Histogram of relative residuals of measured resistance values from best fit line and corresponding Gaussian fit from SigmaPlot. Gaussian parameters were  $x_0 = 0.07 \pm 0.04\%$  and  $\sigma = 0.4 \pm 0.04\%$  with a correlation coefficient of  $R^2 = 0.937$ . The good fit to a Gauss distribution indicates that the relative residuals are normally distributed and that the resistors used are uncorrelated.*

resistance measurements together. The following Gauss fit parameters (3 parameter fit from SigmaPlot) were obtained:

$$x_0 = 0.07 \pm 0.04\% \quad (4.19)$$

$$\sigma = 0.4 \pm 0.04\% \quad (4.20)$$

$$R^2 = 0.937 \quad (4.21)$$

The excellent correlation coefficient and the fact that  $x_0$  is close to zero provides evidence of a random error process governing the resistance calibration measurements. As with the capacitance calibration, it is essential that the ensemble of resistors be uncorrelated and that the deviation of true resistance values from nominal values be random, which Figure 4.8 supports.

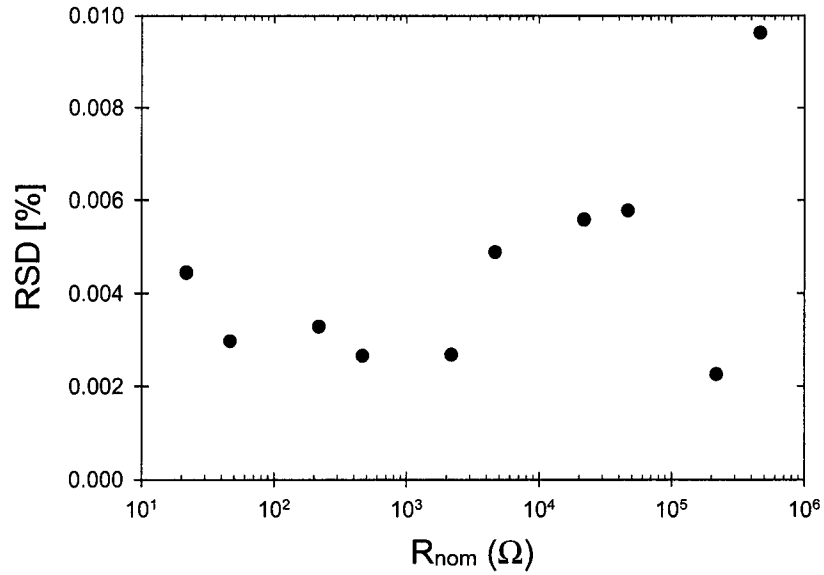


*Figure 4.9. Relative standard deviation of a minimum 100 resistance measurements on resistors with different nominal values.*

#### 4.3.1.2 Resistance Precision Error

Precision error estimates were obtained by recording a minimum of 100 subsequent resistance measurements for a variety of resistors with nominal values ranging from 22  $\Omega$  to 470 k $\Omega$ . The RSD values for these measurements are reported in Figure 4.9. Unlike the precision data for capacitance measurements shown in Figure 4.6, there is no increase in RSD for the smaller  $R_{nom}$  values. This is a result of the LCR meter being capable of reporting resistances in the m $\Omega$  range, thus the noise contribution from LCR meter for the range of  $R_{nom}$  values used in the precision measurements is minimal.

The average RSD value for the data shown in Figure 4.9 was calculated to be 0.004%, which is taken as an estimate of the precision error for resistance measurements. Thus,

$$\epsilon_{R,pre} = 0.004\% \quad (4.22)$$

Comparing Equation 4.22 to Equation 4.18 reveals that accuracy error will dominate

#### 4.4. Vaisala Relative Humidity Probe Calibration

---

the calculation for absolute error for resistance measurements. Thus, even if the largest calculated RSD value (0.01% for  $R_{nom} = 470k\Omega$ ) were used as an estimate of the precision error, the absolute error would not change.

##### 4.3.1.3 Resistance Absolute Error

The absolute error for resistance measurements ( $\epsilon_R$ ) was calculated by adding the accuracy and precision errors in quadrature as shown by Equation 4.23.

$$\epsilon_R^2 = \epsilon_{R,acc}^2 + \epsilon_{R,pre}^2 \quad (4.23)$$

Inserting the results from equations 4.18 and 4.22 gives:

$$\epsilon_R = \sqrt{0.004^2 + 0.00004^2} = 0.004 \quad (4.24)$$

Thus, the absolute error for resistance measurements was taken to be:

$$\boxed{\epsilon_R = 0.4\% \text{ (68\% confidence)}} \quad (4.25)$$

## 4.4 Vaisala Relative Humidity Probe Calibration

Vaisala HMP100 relative humidity probes are delivered with a NIST traceable calibration certificate. The quoted uncertainty (95% confidence level) is  $\pm 1.0\%$  RH for RH levels between 0% and 15%, and  $\pm 1.5\%$  RH for RH levels between 15% and 78%, both at a temperature of  $23 \pm 1$  °C.

The calibration certificates are really only a check that three different humidity measurements are within a pre-specified tolerance level ( $\pm 1.7\%$  RH), which is stated in the user manual as device uncertainty. It is desirable to confirm the limited calibration with in house calibration experiments.

Saturated salt solutions are commonly used to calibrate humidity sensors [119].

**Table 4.3.** Polynomial fit constants  $A_i$  and RH at 25°C with 99.7% confidence level uncertainty for lithium chloride, magnesium chloride, sodium chloride, and potassium sulfate. [3]

Salt	$A_0$ [%]	$A_1$ [%/°C]	$A_2$ [%/°C <sup>2</sup> ]	$A_3$ [%/°C <sup>3</sup> ]	RH(25°C) [%]
LiCl	11.23	$+8.24 \times 10^{-3}$	$-2.15 \times 10^{-4}$	0	$11.30 \pm 0.27$
MgCl <sub>2</sub>	33.67	$-7.97 \times 10^{-3}$	$-1.09 \times 10^{-3}$	0	$32.78 \pm 0.16$
NaCl	75.52	$+3.98 \times 10^{-2}$	$-2.65 \times 10^{-3}$	$+2.85 \times 10^{-5}$	$75.29 \pm 0.12$
K <sub>2</sub> SO <sub>4</sub>	98.78	$-5.91 \times 10^{-2}$	0	0	$97.30 \pm 0.45$

The technique has been known since the early 1900's and is still used today by many leading laboratories [3, 119]. It is well known that adding solute to a solvent reduces the saturation vapour pressure of the pure solvent. The saturation vapour pressure of the solution depends on the amount of solute added, the nature of the solute-solvent interactions (e.g., solubility limit), and the temperature. Saturated solutions of water and various salts generate known humidities in the air above them [3]. Based on these values, humidity sensors can be calibrated.

In 1977, Greenspan performed least squares regression analysis on the relative humidity at various temperatures for a number of saturated salt solutions [3]. He fit the data to a third order polynomial shown as Equation 4.26 here.

$$RH = A_0 + A_1T + A_2T^2 + A_3T^3 \quad (4.26)$$

where  $T$  is the temperature of the air in °C and  $RH$  is in percent.

The Vaisala HMP100 relative humidity probes were calibrated from saturated aqueous solutions of lithium chloride, magnesium chloride, sodium chloride, and potassium sulfate (Fischer Scientific, laboratory grade salts). The  $A_i$  constants for these salt solutions and their RH at 25°C are listed in table 4.3. The 99.7% confidence level ( $3\sigma$ ) uncertainty of the RH values shown in table 4.3 was calculated by Greenspan based on the residual standard deviation using three different weighting methods.

During a calibration experiment, a Vaisala humidity probe was held above a sat-

urated salt solution in a sealed chamber where the temperature was monitored by a 20 gauge type-k thermocouple (Omega). The voltage signals from the Vaisala transmitter (recall that the transmitter provides a voltage signal linearly proportional to the measured humidity) and the thermocouple were sent to an oscilloscope (Fluke 190 Series ScopeMeter) equipped with an RS232 output and computer software for data logging. The temperature and relative humidity were logged every 60 seconds for a minimum of 22 hours to ensure equilibrium had been reached.

Two Vaisala humidity probes were calibrated. Probe #1 was calibrated once (RH and temperature logged once for each of the four saturated salt solutions), whereas probe #2 was calibrated three times. New saturated salt solutions were prepared for every calibration experiment. The data from all calibration experiments are plotted in Figure 4.10. The data from the Vaisala calibration certificates have also been included for comparison.

##### 4.4.1 Vaisala RH Accuracy Error

Weighted least squares regression with error in both  $x$  ( $RH_{ref}$ ) and  $y$  ( $RH_{meas}$ ) was used to fit the data in Figure 4.10. For the error in  $RH_{ref}$  the Greenspan uncertainties were added in quadrature with the RH error due to the thermocouple temperature error, which was calculated using error propagation of Equation 4.26 and a temperature uncertainty of 2.2°C (Omega specification for type-K thermocouple). An uncertainty of 0.5% RH was used for the reference humidity values from the Vaisala calibration certificates, which was estimated from a private communication with the Vaisala Measurement Standard Laboratory. Table 4.4 lists the parameters obtained from the regression analysis for all data sets.

The average and standard deviation of the slope and intercept values listed in table 4.4 (excluding Vaisala data) were calculated to be:

$$\bar{m} = 0.9950 \tag{4.27}$$

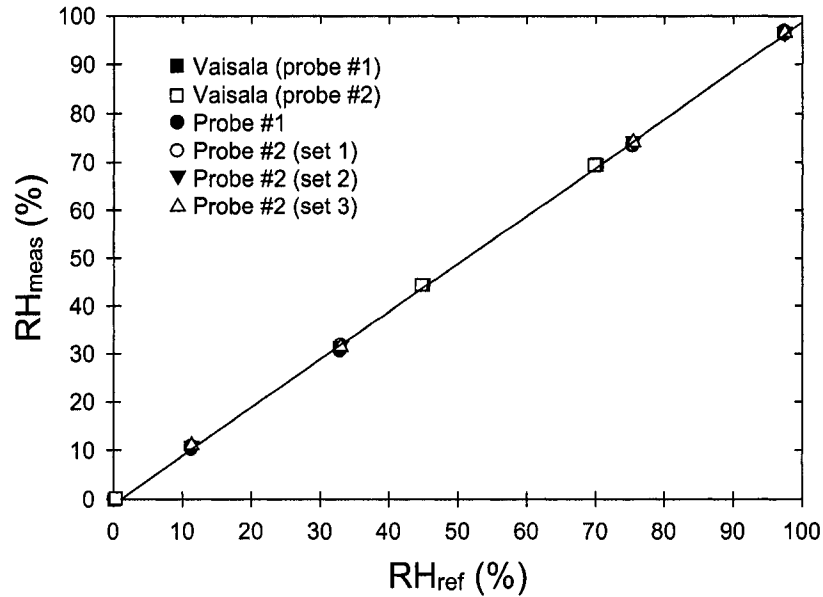


**Figure 4.10.** Reference RH versus measured RH for Vaisala humidity probe calibration experiments. The data from the Vaisala calibration certificates for both probes have been included for comparison. The line was obtained from fitting all data sets together using weighted least squares regression.

**Table 4.4.** Weighted least squares regression analysis ( $y = mx + b$ ) for data plotted in Figure 4.10.

Data Set	$m$	$b$ [% RH]
Vaisala (probe #1)	$0.9924 \pm 0.0100$	$-0.1410 \pm 0.4795$
Vaisala (probe #2)	$0.9957 \pm 0.0100$	$-0.1007 \pm 0.4807$
Probe #1	$0.9995 \pm 0.0012$	$-1.8894 \pm 0.0834$
Probe #2 (set 1)	$0.9861 \pm 0.0012$	$-0.7200 \pm 0.0835$
Probe #2 (set 2)	$0.9979 \pm 0.0012$	$-0.9612 \pm 0.0835$
Probe #2 (set 3)	$0.9965 \pm 0.0012$	$-1.0530 \pm 0.0835$

#### 4.4. Vaisala Relative Humidity Probe Calibration

---

$$\sigma_m = 0.0061 \quad (4.28)$$

$$\bar{b} = -1.1559 \quad (4.29)$$

$$\sigma_b = 0.5088 \quad (4.30)$$

An estimate for the accuracy error for RH measurements ( $\epsilon_{RH,acc}$ ) was obtained using error propagation of the equation:

$$x = \frac{y - b}{m} \quad (4.31)$$

For a given RH measurement  $y$ , there are a range of reference RH values  $x$ , that correspond to that measured value as a result of the errors in both slope ( $\delta m = \sigma_m$ ) and intercept ( $\delta b = \sigma_b$ ). Thus the accuracy error can be approximated as the error in  $x$  ( $\delta x$ ):

$$\delta x = \sqrt{\left(\frac{\delta b}{m}\right)^2 + \left(x \frac{\delta m}{m}\right)^2} \quad (4.32)$$

Substituting Equation 4.31 into Equation 4.32 shows that the accuracy error for RH measurements depends on the measured humidity  $y$ . This is in contrast to the accuracy error calculations for capacitance and resistance measurements shown in Sections 4.2.1.1 and 4.3.1.1. For those calculations the accuracy error was estimated as the relative slope error, which is relevant for the analytic fitting described in Appendix A, since there is no intercept or intercept error to account for. Setting  $b$  and  $\delta b$  equal to zero in Equation 4.32 shows that in such a situation the relative error in  $x$  is equal to the relative slope error.

Substituting Equation 4.31 and entering the values for  $b$ ,  $\delta b$ ,  $m$ , and  $\delta m$  in Equation 4.32 gives:

$$\epsilon_{RH,acc} \approx \sqrt{(3.8 \times 10^{-5})y^2 + (8.7 \times 10^{-5})y + 0.26} \quad (4.33)$$



#### 4.4.2 Vaisala RH Precision Error

For precision error, an estimate was obtained by analyzing the last 100 RH measurements (1 minute apart) from the saturated salt solutions calibration experiments. The temperature fluctuation during these measurements was less than 0.1°C. Table 4.5 lists the results of the precision experiment.

The average RSD of the values in table 4.5 was calculated to be 0.2%, which was used as an estimate of the precision error for RH measurements ( $\epsilon_{RH,pre}$ ). Thus,

$$\epsilon_{RH,pre} = 0.2\% \quad (4.34)$$

#### 4.4.3 Vaisala RH Absolute Error

The absolute error of the Vaisala RH probe ( $\epsilon_{RH}$ ) was calculated by adding the accuracy error and precision error in quadrature:

$$\epsilon_{RH} = \sqrt{\epsilon_{RH,acc}^2 + \epsilon_{RH,pre}^2} = \sqrt{(4.2 \times 10^{-5})y^2 + (8.7 \times 10^{-5})y + 0.26} \quad (4.35)$$

The absolute error given by Equation 4.35 is the 68% confidence level uncertainty ( $1\sigma$ ), doubling this value gives the 95% confidence level ( $2\sigma$ ) absolute error, which is plotted in Figure 4.11. The factory calibration uncertainty (95% confidence level) is specified in the Vaisala HMP100 User's Guide and is equal to  $\pm 1.0\%$  RH for humidity values in the range of 0-15% RH, and  $\pm 1.5\%$  RH for the 15-78% RH range. The data in Figure 4.11 is consistent with these numbers and therefore supports our calibration methodology and analysis. Thus, the absolute error (95% confidence) for RH measurements reported in this thesis is given by:

$$\epsilon_{RH} = \sqrt{(1.7 \times 10^{-4})RH^2 + (3.5 \times 10^{-4})RH + 1.04} \text{ [% RH]} \quad (4.36)$$

where  $RH$  is the relative humidity in percent.

#### 4.4. Vaisala Relative Humidity Probe Calibration

**Table 4.5.** Precision data from last 100 RH measurements of saturated salt solutions calibration experiments. The relative standard deviation (RSD) is calculated by dividing the standard deviation ( $\sigma$ ) by the mean value ( $RH_{mean}$ ).

Probe #	Set #	Salt	$RH_{mean}$ [% RH]	$\sigma$ [% RH]	RSD [%]
1	1	LiCl	10.2	0.01	0.10
2	1	LiCl	10.6	0.05	0.45
2	2	LiCl	10.6	0.02	0.23
2	3	LiCl	10.6	0.04	0.37
1	1	MgCl <sub>2</sub>	30.6	0.04	0.13
2	1	MgCl <sub>2</sub>	31.3	0.04	0.12
2	2	MgCl <sub>2</sub>	31.2	0.09	0.29
2	3	MgCl <sub>2</sub>	31.3	0.07	0.23
1	1	NaCl	73.2	0.03	0.04
2	1	NaCl	73.6	0.06	0.09
2	2	NaCl	74.0	0.10	0.13
2	3	NaCl	73.9	0.07	0.10
1	1	K <sub>2</sub> SO <sub>4</sub>	96.7	0.14	0.14
2	1	K <sub>2</sub> SO <sub>4</sub>	96.3	0.07	0.07
2	2	K <sub>2</sub> SO <sub>4</sub>	96.5	0.05	0.05
2	3	K <sub>2</sub> SO <sub>4</sub>	97.0	0.04	0.04

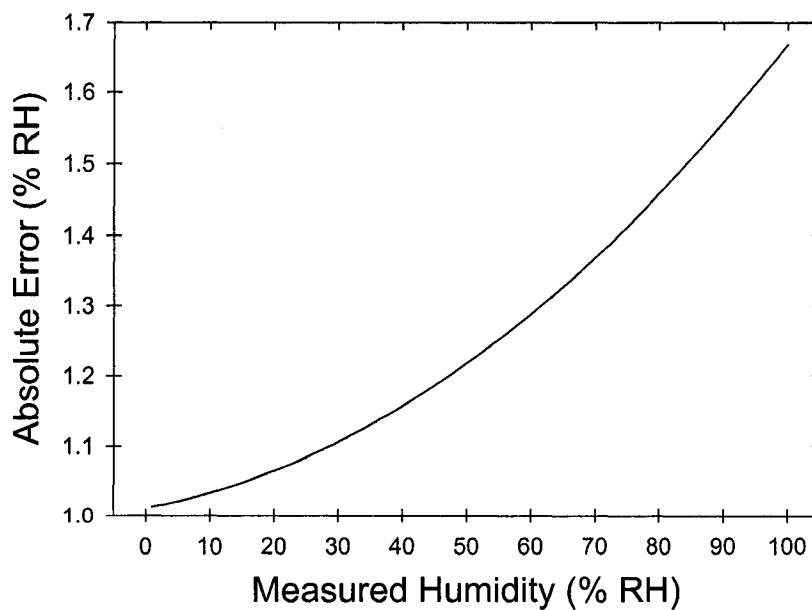


**Figure 4.11.** 95% confidence level ( $2\sigma$ ) absolute error for RH measurements.

## 4.5 Sensor Response Time Measurement

In order to give a correct definition of sensor response time consider the case of a sensor recording a change in gas concentration from  $c_1$  to  $c_2$  over a period of time,  $T$ . The concentration measured by the sensor,  $c$ , can be defined as a function of time,  $t$ :

$$c \equiv c(t) \quad (4.37)$$

If at time  $t = 0$  the measured concentration begins to change,  $c_1$  and  $c_2$  can be defined as:

$$c(t \leq 0) = c_1 \quad (4.38)$$

$$c(T) = c_2 \quad (4.39)$$

The response time is defined as the time required for the sensor to measure a certain percentage of the change  $|c_2 - c_1|$  [120]. This percentage is typically 90%, where the response time is denoted  $t_{90}$ . With the above definitions the 90% response time can be defined as the time when Equation 4.40 is satisfied:

$$c(t_{90}) = c_1 + 0.9(c_2 - c_1) \quad (4.40)$$

If  $c_2$  is less than  $c_1$ , the response time is sometimes referred to as recovery time. The terms rise time and fall time have also been used to denote the response times for increasing and decreasing concentrations, respectively. To be clear, the remainder of this thesis will adopt the use of adsorption response time when referring to the 90% response time for increasing humidity ( $c_2 > c_1$ ), desorption response time when referring to the 90% response time for decreasing humidity ( $c_2 < c_1$ ), and response time as a general term for either situation.

To obtain an accurate measurement of sensor response time, it is necessary to construct a testing system that can rapidly change the gas concentration surround-

#### *4.5. Sensor Response Time Measurement*

---

ing the sensor. It is crucial that the time taken to change the gas concentration be less than the sensor response time to minimize the effects of experimental conditions on the measured values. Various techniques have been reported to achieve a rapid gas exchange. Tobias et al. constructed a stage with two side-by-side gas outlets that pointed towards the sensor under test [121]. Rapidly oscillating the stage back and forth allowed them to change the gas surrounding the sensor between that from one outlet to the other within milliseconds (they used oxygen and hydrogen in their study, but this could easily be adopted for air at two different humidities). Tetelin et al. fabricated a cylinder with a piston at one end and a one way valve at the other [37]. The cylinder chamber was filled with moist and dry air at different ratios to generate a desired humidity level. The piston was moved at a preset velocity towards the one way valve, causing the gas in the chamber to exit at a rate of 1 litre per minute (LPM) towards a sensor held 3 cm in front of the outlet. They were able to change the humidity at the sensor from ambient RH to the RH in the chamber within 80 ms. Briglin and Lewis used a rotating disk with a section missing to alternate the gas flowing over a sensor between two streams of different concentration [46]. Using flow rates of 6 LPM and a specially constructed chamber they were able to change the gas concentration in less than 5 ms. Another technique for rapid gas exchange uses solenoid valves to divert gas flow onto a sensor between the different input gases of the solenoid valves [47, 54, 120]. This is the technique used for the research presented in this thesis.

Two diverting solenoid valves (Evolutionary Concepts Inc.) were used to alternate the flow onto the sensor under test between dry nitrogen (<1% RH) and moist air (variable RH). Figure 4.12 depicts the response time setup where the output of the two diverting valves were connected and directed towards the sensor under test, which was housed in a small, unsealed chamber (600 mL). The input gases for the solenoid valves were dry nitrogen and moist air. The actuation time of the solenoid valves is between 2 and 3 ms and the volume of air to be exchanged per

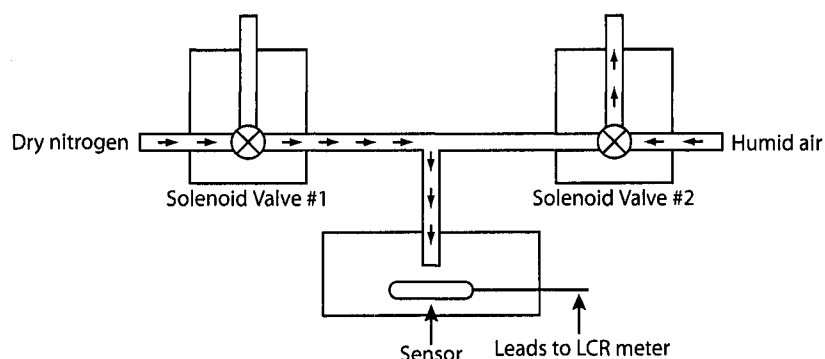


**Figure 4.12.** Response time setup using diverting solenoid valves. Description is depicted here where solenoid #1 is energized causing dry nitrogen to flow onto the sensor while the humid air in solenoid #2 (de-energized) is diverted.

adsorption/desorption event was calculated to be 2.0-2.5 mL. Thus, for a 2.5 LPM flow rate the gas exchange will occur in 50-60 ms, assuming no mixing (see Chapter 5 Section 5.5 for a more detailed investigation). Flow rates were typically held at 2.5 LPM during response time measurements using flowmeters (Cole Parmer FF-32004-10).

The sensor capacitance (or other impedance parameter) during response time measurements was monitored by the LCR meter and recorded by a computer. A simple Visual Basic program (see Appendix B) was written to allow the user to select the impedance parameter to record during a response time event, what frequency/voltage to use, and to time stamp and log the measurements. The integration time on the QuadTech meter was set to fast, providing a measurement every 40 ms (25 Hz).

The timing circuit shown in Figure 4.13 was used to alternate the actuation of the diverting solenoid valves in the response time setup. The 555 timer (LMC 555CN) was in an astable configuration, which provides a voltage waveform (square wave with low voltage  $V_L = 0$  and high voltage  $V_H = V_s$ ) with the time at high voltage,  $t_H$ , and the time at low voltage,  $t_L$ , given by:

$$t_H = \ln(2)(R_A + R_B)C \quad (4.41)$$

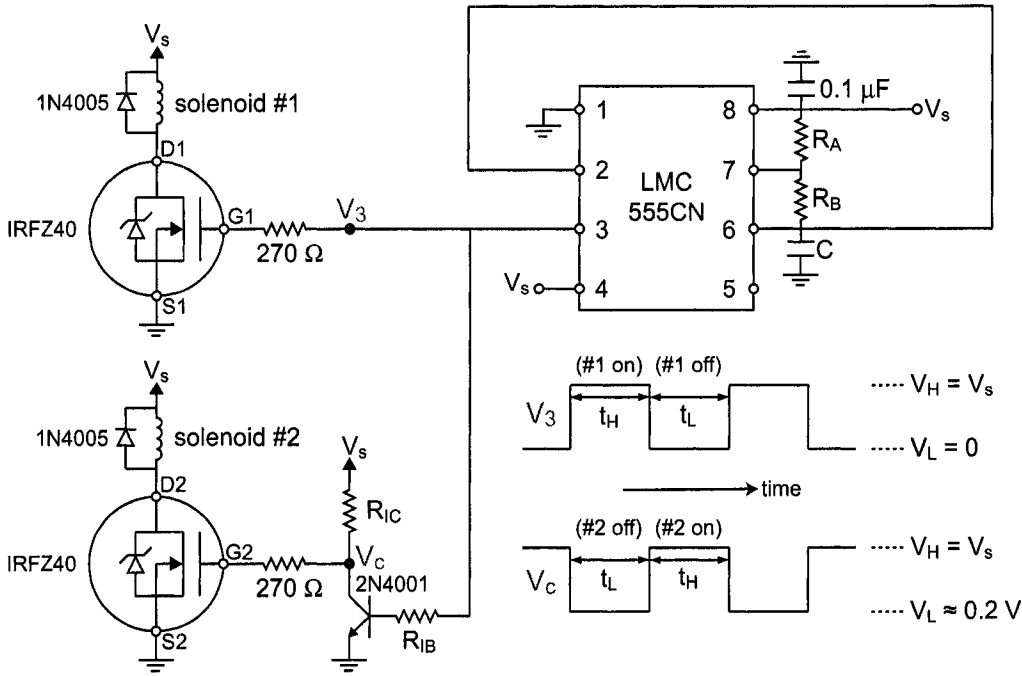


Figure 4.13. Timing circuitry for astatable switching of solenoid valves.

$$t_L = \ln(2)(R_B)C \quad (4.42)$$

where  $t_H + t_L = T =$  waveform period. For all measurements reported in this thesis, a 50% duty cycle was used. A capacitance of  $10 \mu\text{F}$  was used for  $C$ , and a resistance of  $1 \text{ k}\Omega$  was used for  $R_A$  (want RC time constants on the order of solenoid actuation time).  $R_B$  values were varied depending on the desired pulse width ( $t_H$ ) with typical values ranging from  $500 \text{ k}\Omega$  to  $3 \text{ M}\Omega$  for pulse widths of  $5 \text{ s}$  to  $30 \text{ s}$ . The high voltage,  $V_H$ , was set by the voltage  $V_s$ , which was set to the actuation voltage of the solenoid valves ( $12 V_{DC}$ ).

The solenoid valves (represented by inductors in Figure 4.13) were placed in the drain branch of a power MOSFET (IRFZ40) operating as a switch. The MOSFETs were necessary to provide sufficient current to the solenoids since the 555 timer is rated for a maximum output current of  $100 \text{ mA}$  and the solenoid valves require  $500 \text{ mA}$  when energized.

A  $270 \Omega$  gate resistance was used to reduce voltage ringing at the gate and to

provide a safety factor for FET punch through. The resistance value  $270\ \Omega$  was selected to ensure a sub-millisecond RC time constant (FET parasitic capacitances are in the 100 pF range).

When the voltage at the gate of the FETs is high, the FET is driven into saturation and current flows through the inductor and sinks into the FET. Thus, when a high voltage is present at the gate, the solenoid valves are in the energized state. When the gate voltage is low, the FET is off and the solenoid valves will be in the de-energized state.

Diodes (1N4005) were placed in parallel with the solenoid valves to act as free wheeling diodes. This is standard practice when driving inductive loads since the current through an inductor can not instantaneously change. Thus, when the FET toggles between the off and saturation states, current will circle around the diode-inductor loop until the steady-state current through the inductor is reached.

A BJT (2N4001) in switch configuration was used to invert the 555 timer signal prior to the FET driving solenoid #2. In this way, when solenoid #1 is in the energized state, solenoid #2 will be in the de-energized state and visa versa. To ensure that the BJT enters saturation, it is necessary that  $R_{IB} \leq \beta R_{IC}$ , since  $\beta$  varies with temperature and for different BJTs, it is common to select  $R_{IB} = 10R_{IC}$ . Since  $\beta$  will almost certainly be greater than 10. A  $1\ \text{k}\Omega$  resistance for  $R_{IC}$  is sufficient to ensure that the power dissipated by  $R_{IC}$  is less than the rated 250 mW, and to minimize its contribution to the FET RC time constant. Thus,  $R_{IC} = 1\ \text{k}\Omega$  and  $R_{IB} = 10\ \text{k}\Omega$ .

## 4.6 Commercial Sensor Testing

Commercial humidity sensors were purchased, tested, and compared to specifications to evaluate the humidity control chamber and response time setup.

The G-CAP2 humidity sensor from General Electric (GE) is a polymer capacitive based sensor with excellent documentation on the capacitive response and response

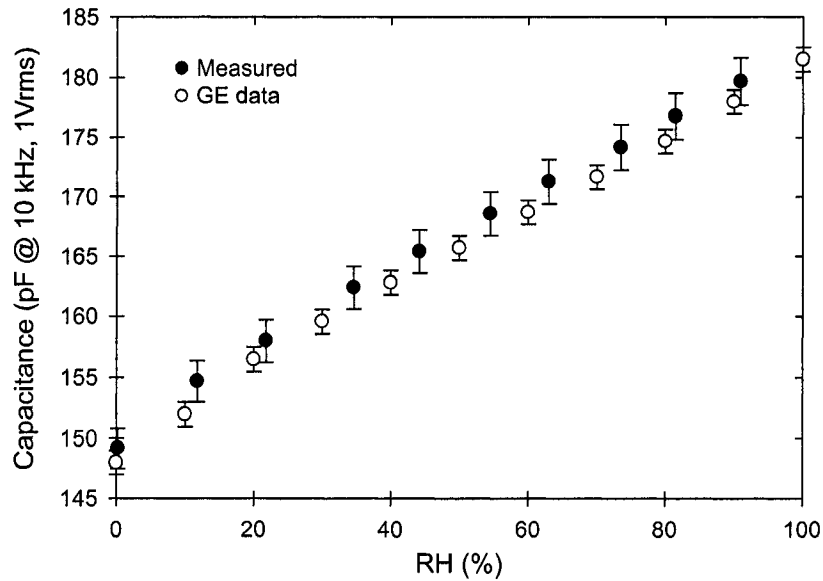


**Figure 4.14.** GE G-CAP2 capacitive humidity sensor response. The close agreement between the measured data and the data provided by GE indicates the ability to accurately obtain the capacitive response of humidity sensors.

time. The G-CAP2 is a capacitive element (no external circuitry) that is factory calibrated to within  $\pm 1$  pF, which results in interchangeability better than 3% RH. Tabulated data on the capacitance (at 10 kHz, 1.0  $V_{\text{rms}}$ ) at various RH levels is given by GE. Response time data is also given for a flow rate of 150 linear feet per minute (LFM). The typical adsorption response time is 75 seconds for a 25% to 75% RH step change. A maximum response time of 120 seconds is also given.

Figure 4.14 shows the capacitive response of the G-CAP2 sensor. The typical response data on the specification sheet has also been included for comparison. The error bars of the measured data are from the analysis in Section 4.2.1 (i.e., Equation 4.14). No hysteresis of the capacitive response was observed. The good agreement between the measured data and the data provided by GE indicates the ability of the humidity control chamber and the QuadTech LCR meter to accurately obtain the capacitive response of a humidity sensor.

Figure 4.15 shows the response time data of the G-CAP2 sensor obtained from the response time setup discussed in Section 4.5. The capacitive response in Fig-



ure 4.14 (measured data) was fit to a sigmoidal function in SigmaPlot and used to convert the response time capacitance measurements to their corresponding relative humidity value, resulting in the RH vs. time data shown in Figure 4.15.

The specification sheet for the G-CAP2 sensor gives the response time at a flow rate of 150 LFM, which corresponds to a flow rate of  $\sim 1$  LPM for the inner diameters of the fittings used in the response time setup ( $\sim 0.2''$ ). The response time data in Figure 4.15 was generated with a flow rate of 1.0 LPM. SigmaPlot was used to fit the adsorption and desorption response time curves to exponential functions, and the response times were found by solving Equation 4.40. The adsorption and desorption response times were calculated to be  $81 \pm 3$  s and  $111 \pm 2$  s, respectively. Both of these values are within the 75 s typical and 120 s maximum response times on the specification sheet. The 75 s typical response time is for an adsorption event between 25% and 75% RH, whereas the adsorption response time data shown in Figure 4.15 was for a 1% to 85% RH change, and so it was expected that this response time be slightly larger than the quoted 75 s. No typical desorption response time was stated on the specification sheet, however, the 111 s desorption response time is within the specified 120 s maximum. Thus, it appears that the response time setup provides a sufficient measurement of humidity sensor response time.

The result that desorption appears to be slower than adsorption is not unusual as the majority of humidity sensors reported in the literature have this same characteristic. It is usually quoted that this is a result of desorption kinetics being different than adsorption kinetics (e.g., desorption is endothermic) [28, 120]. This topic is rather complex and will not be discussed here.

The response time of the G-CAP2 sensor is relatively slow and so additional testing of the response time setup with a faster sensor was desired. The Vaisala MultiMeterMate RHT probe is a polymer capacitive-based sensor similar to the G-CAP2, however, the specified response time of the MultiMeterMate is only 15 seconds.

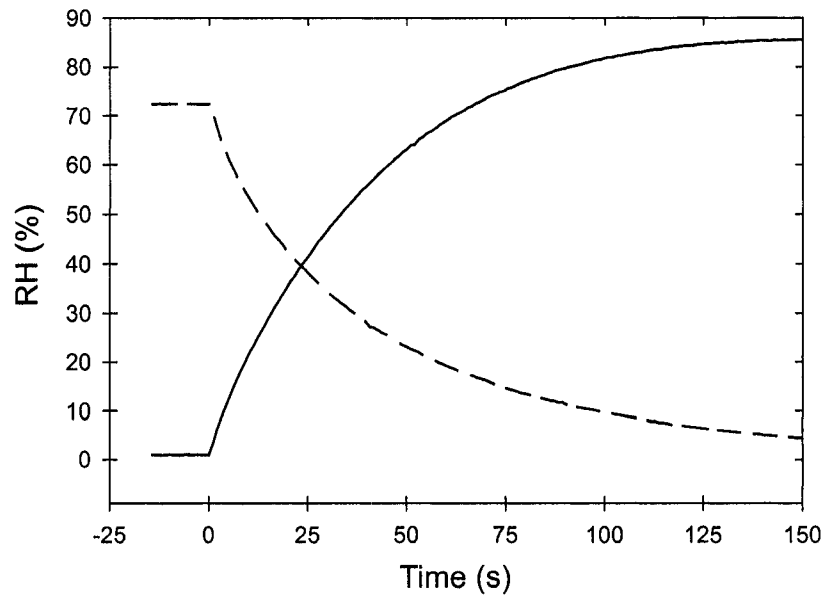


**Figure 4.15.** GE G-CAP2 response time data for 1 LPM flow rates. Adsorption and desorption response times were calculated to be  $81 \pm 3$  s and  $111 \pm 2$  s, respectively, from exponential fitting with SigmaPlot.

The sensing element of the MultiMeterMate comes attached to a probe with internal circuitry to provide an output voltage dependent on the relative humidity (1 mV per %RH). The sensing element can easily be removed for replacement of elements that require calibration.

The capacitive response of the MultiMeterMate element is shown in Figure 4.16. As with the G-CAP2 sensor, no appreciable hysteresis is present in the capacitive response and only the data collected during increasing humidity is shown. Unfortunately, Vaisala does not provide capacitance data of their sensing elements, so no comparison can be made. However, this data was used to convert the capacitance values obtained during response time measurements to their corresponding relative humidity values by fitting the capacitive response to a sigmoidal function with SigmaPlot.

Figure 4.17 shows the response time data of the MultiMeterMate element for 1 LPM flow rates. The short response time allowed multiple adsorption and des-

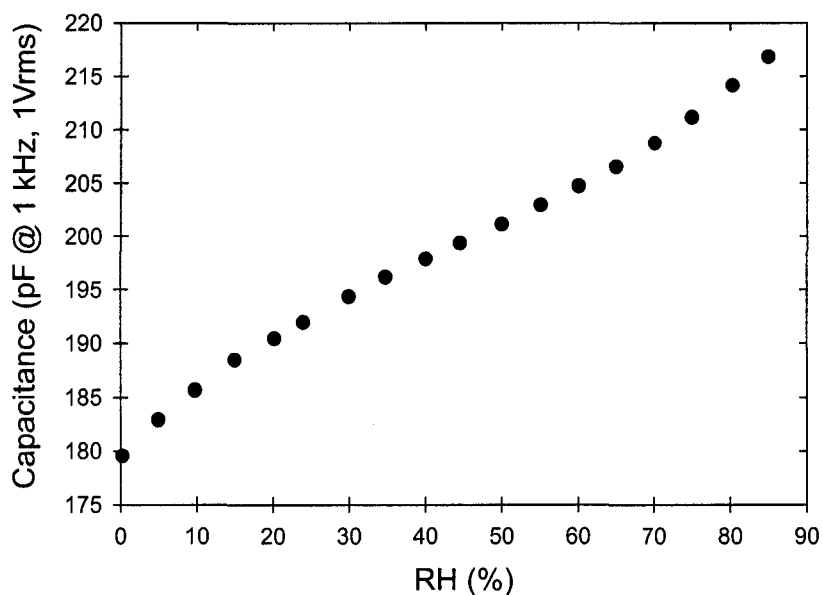


*Figure 4.16. Vaisala MultiMeterMate RHT probe capacitive humidity sensor response.*

orption measurements to be continuously recorded. Calculations of response times using exponential fitting revealed an average adsorption response time of  $1.3 \pm 0.1$  s, and an average desorption response time of  $2.5 \pm 0.1$  s. Although these values are significantly less than the specified 15 s, the difference can be attributed to the methodology used by Vaisala to measure sensor response time. Vaisala measures the response time in “still air”, meaning the testers physically move the sensor from a chamber at one humidity, to another chamber at a different humidity and recorded the response time. Although this method provides useful information, it does not provide any indication of sensor response time where air flow is involved. Thus, the measured adsorption and desorption response time values can not be compared to the specified 15 s response time. Nonetheless, this data provides insight on the ability of the response time setup to obtain measurements from fast humidity sensors.

To test the limits of the response time setup, it is necessary to test a sensor with response times in the millisecond range. To the authors knowledge, no mass

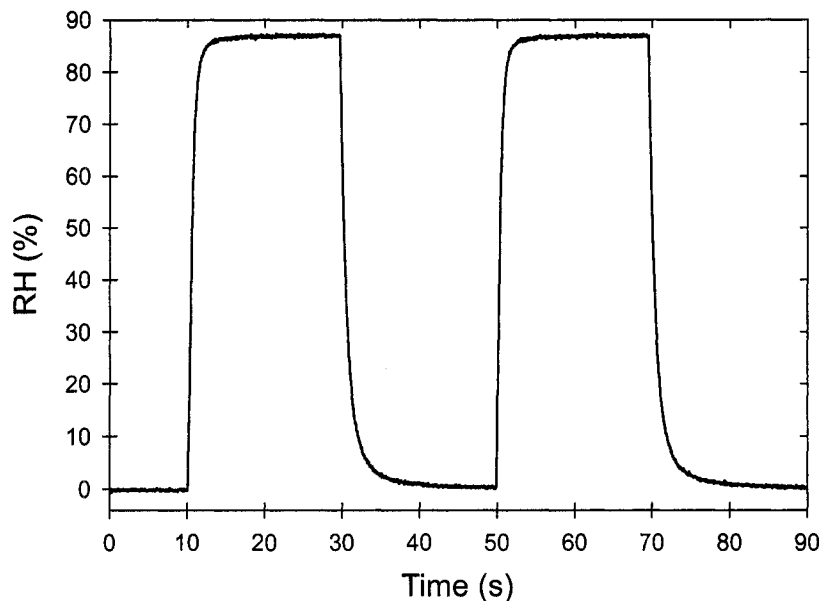


*Figure 4.17. Vaisala MultiMeterMate RHT probe response time data for 1 LPM flow rates. The average adsorption and desorption response times were calculated to be  $1.3 \pm 0.1$  s and  $2.5 \pm 0.1$  s, respectively, from a best fit exponential.*

produced commercial sensors with response times in the millisecond range were available during the time this research was conducted. However, a select few research groups have reported the fabrication of humidity sensors with millisecond response times. Kuban et al. described a microfabricated humidity sensor made of interdigitated rhodium electrodes on a silicon substrate coated with a humidity sensitive Nafion perfluorosulfonate ionomer [47]. The Nafion coating exhibits ionic conduction dependent on the ambient humidity, thus the sensor is a resistive-based humidity sensor. The adsorption and desorption response times were reported to be between 30 and 50 ms.

A similar sensor was fabricated using a CSE-IDC described in Chapter 3. Nafion solution (5% w/v in alcohols, Sigma) was spun onto an IDC-100-3-3 at 4000 RPM for 30 s and baked at 120°C for 30 min. The thickness of the Nafion film was measured with contact profilometry (Tencor Alphastep 200 Profilometer) and spectroscopic ellipsometry (J.A. Woollam DUV Spectroscopic Ellipsometer) and found to

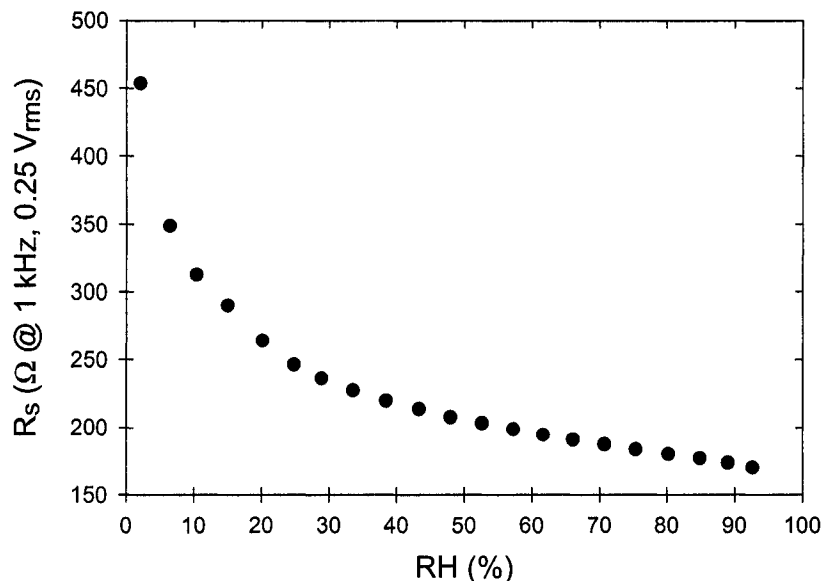


Figure 4.18. Nafion coated IDC resistive humidity sensor response.

be  $\sim 230$  nm thick. Kuban et al. reported a Nafion thickness of  $\sim 200$  nm for their fastest sensors (response time dependent on thickness).

The resistance response of the IDC Nafion coated sensor is shown in Figure 4.18. No significant hysteresis was measured and the data in Figure 4.18 pertains to increasing humidity.

The response time data is presented in Figure 4.19. Discrete data points have been included to show that this data is near the limit of the response time setup in terms of sampling time. Exponential fits revealed an adsorption and desorption response time of  $37 \pm 3$  ms and  $153 \pm 4$  ms, respectively.

The discrepancy between the 153 ms measured desorption response time and the 30 to 50 ms range reported by Kuban et al. may be attributed to the differences in sensor fabrication and characterization. The IDC structure of Kuban's sensor is quite different, but perhaps more importantly, instead of a LCR meter Kuban used custom circuitry to apply a constant DC voltage ( $> 2V$ ) and translate the current through the sensor into a voltage output signal. The sensing mechanism of Kuban's DC sensor is substantially different than the sensor presented here in that at DC

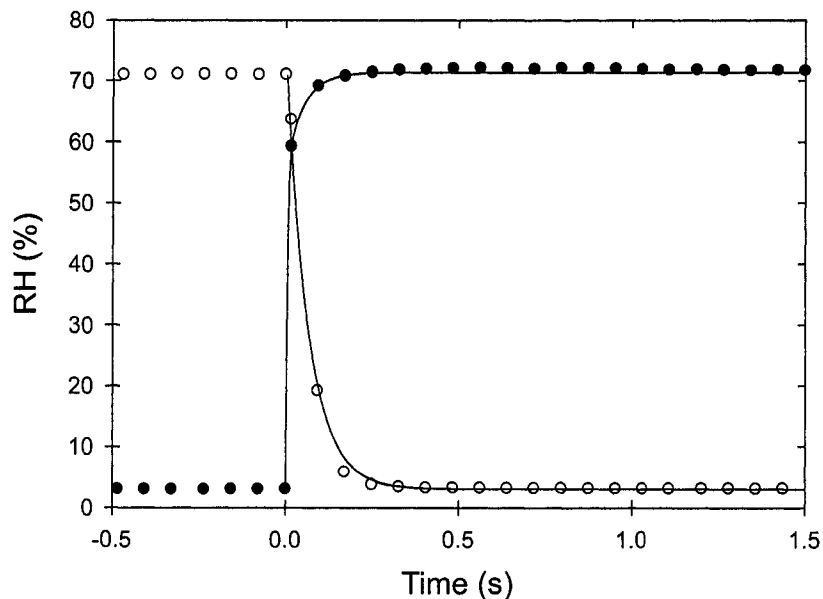


*Figure 4.19.* Nafion coated IDC resistive sensor response time data for 2.5 LPM flow rates. The adsorption and desorption response times were  $37 \pm 3$  ms and  $153 \pm 4$  ms, from best fits to an exponential.

voltages exceeding  $\sim 2V$  electrolysis occurs in the sensing medium [47].

Regardless of the desorption response time discrepancy, the results are a valid indication of the ability of the response time setup to obtain response time measurements in the 10's of milliseconds range.

## 4.7 Conclusions

The experimental methodology used to characterize humidity sensors was presented. Calibration studies on the QuadTech 1715 LCR meter revealed an absolute error for capacitance and resistance measurements of 1.2% and 0.4% (68% confidence level), respectively. Relative humidity measurement error for the Vaisala HMP100 humidity probe was found to be dependent on RH (Equation 4.36, pg. 64) and ranged from  $\pm 1.0\%$  RH to  $\pm 1.7\%$  RH (95% confidence level) over the entire RH range. Commercial sensor testing demonstrated the ability to obtain accurate capacitive response, and response time data. A resistive humidity sensor utilizing

a 230 nm thick Nafion film was fabricated and tested to reveal the capability of measuring response times on the 10's of milliseconds time scale.

In the next chapter the first experimental results of GLAD based humidity sensors will be presented with a discussion on sensor characterization.

## Chapter 5

# Sensor Characterization <sup>1</sup>

The objective of this chapter is to establish a framework for meaningful interpretation of the data obtained from GLAD produced capacitive based humidity sensors (herein denoted as sensors). The following will be discussed:

1. Impedance parameters obtained from LCR meter
2. Sensor hysteresis
3. Sensor ageing
4. IDC geometry
5. Effect of flow rate on response time measurement

### 5.1 Impedance Parameters

In Chapter 4, a discussion of the LCR meter used to obtain impedance parameters of the sensors was given. The LCR meter measures complex impedance and from that data provides capacitance (or resistance, inductance, etc.) values depending on the equivalent circuit used to model the device under test (DUT). The equivalent circuit models used by the LCR meter are shown in Figure 5.1. The impedance

---

<sup>1</sup>Part of this chapter has been published in: J.J. Steele, G.A. Fitzpatrick, and M.J. Brett. Capacitive humidity sensors with high sensitivity and subsecond response times. *IEEE Sensors Journal*, 7(6):955-956, June 2007. [122]



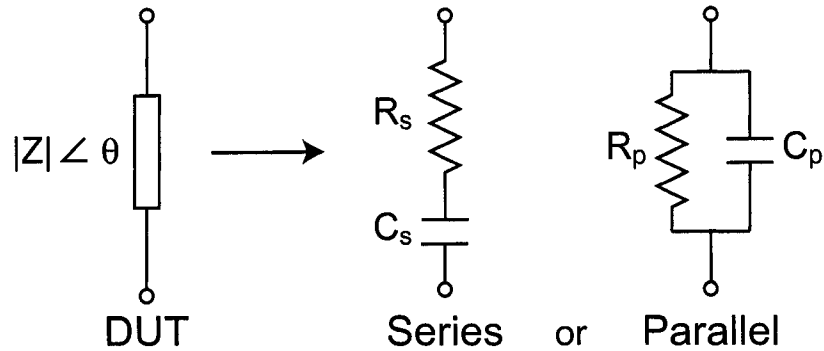


**Figure 5.1.** The DUT is modeled by the LCR meter as either a series or parallel equivalent circuit. For inductive circuits the capacitors  $C_s$  and  $C_p$  are replaced by inductors  $L_s$  and  $L_p$ , respectively.

properties of most two port devices and components can be modeled using these simple circuits, however, in some instances more complicated configurations of resistors and capacitors are required [63,123].

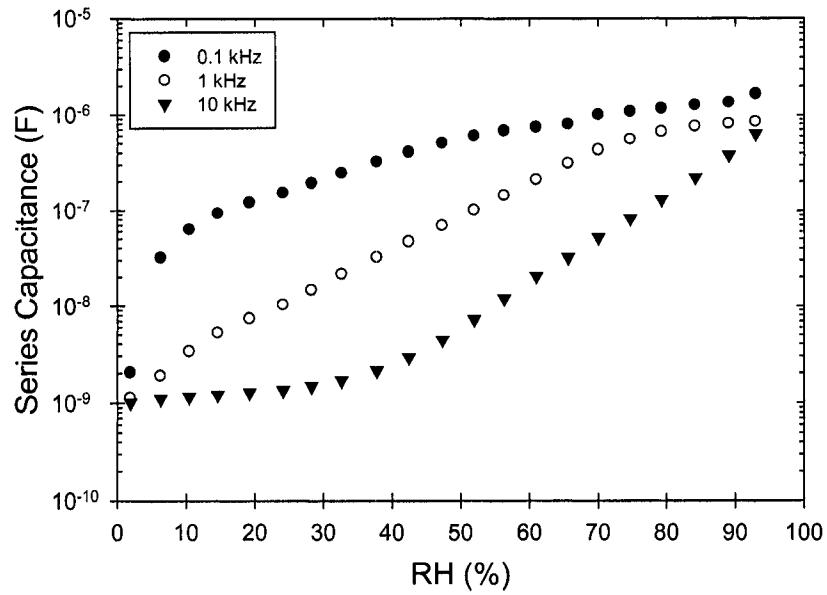
The series capacitance ( $C_s$ ) measured at a frequency of 1 kHz and a voltage of 1 V<sub>rms</sub> was used to characterize the humidity response of the sensors reported in this thesis. The primary reason for this is that the capacitance response (as opposed to impedance/resistance) facilitates direct comparison with the literature and commercial devices, therefore either the series capacitance ( $C_s$ ) or the parallel capacitance ( $C_p$ ) should be used to characterize the sensors. Figure 5.2 shows the series and parallel capacitance response at three frequencies for a sensor comprised of a 1.5  $\mu\text{m}$  thick TiO<sub>2</sub> vertical post GLAD film deposited onto a IDC-100-3-5 substrate at a deposition angle of  $\alpha = 81^\circ$ . The capacitance response data shown in Figure 5.2 are not universal for all sensors, however, the data set was amongst the best obtained in terms of sensitivity over the entire humidity range and therefore serves to identify an appropriate frequency and capacitance (series or parallel) for sensor characterization. Figure 5.2 reveals that both the  $C_s$  at 1 kHz and the  $C_p$  at 0.1 kHz responses are good candidates for sensor characterization as they have a simple functional form (near exponential) compared to the other responses and can therefore be summarized with fewer parameters. In the capacitive humidity sen-

sor literature, a measurement frequency of 1 kHz is commonly used [28, 124–127], therefore for the remainder of this thesis, the capacitive response of the GLAD produced humidity sensors will denote the series capacitance response measured at a frequency of 1 kHz, unless otherwise stated.

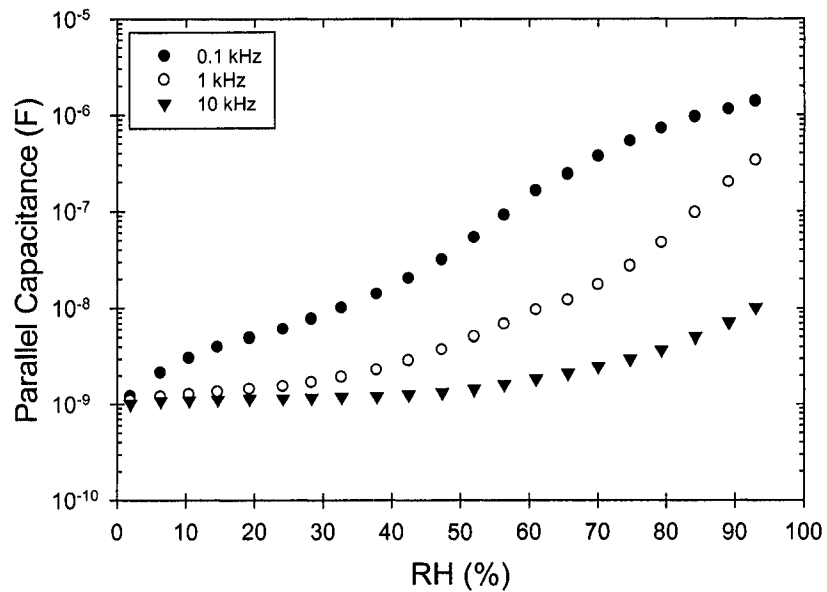
## 5.2 Hysteresis

Water vapour adsorption–desorption hysteresis can be a major problem for humidity sensors resulting in reduced accuracy and limited applications [128]. Several mechanisms have been proposed for the cause of hysteresis in both polymers and porous ceramics and the topic is controversial [21, 128–133]. Attempts to reduce hysteresis include pore widening [129], operating at raised temperatures [129], increasing hydrophobicity [129], polymer cross-linking [20], illumination with infrared radiation [130], and complex artificial neural network signal conditioning software [134, 135].

Figure 5.3 shows the capacitance response of the first two scans for a 1.5  $\mu\text{m}$  thick  $\text{TiO}_2$  vertical post film deposited at  $\alpha = 81^\circ$  onto a IDC-100-3-5. A scan is defined as one complete cycle from the low RH setpoint to the high RH setpoint and back down to the low RH setpoint. Significant hysteresis ( $\sim 15\text{--}20\%$  RH) was present in the first scan, whereas there was minimal hysteresis in the second scan. In addition, the data of the second scan nearly overlaps that of the desorption branch in the first scan. The hysteresis in the first scan was likely a result of a surface modification process occurring when the sensor was initially exposed to high humidity conditions. It is possible that the film surface was not fully hydroxylated (covered with a monolayer of hydroxyl groups) until exposure to the high humidity conditions of the first scan. Al-Abadleh and Grassian used Fourier transform infrared spectroscopy to show that water vapour adsorption hysteresis on aluminum oxide surfaces is a result of the formation of a hydroxylated layer during the first



(a)



(b)

**Figure 5.2.** Series capacitance (a) and parallel capacitance (b) response of a sensor comprised of a  $1.5 \mu\text{m}$  thick  $\text{TiO}_2$  vertical post GLAD film deposited onto a IDC-100-3-5.

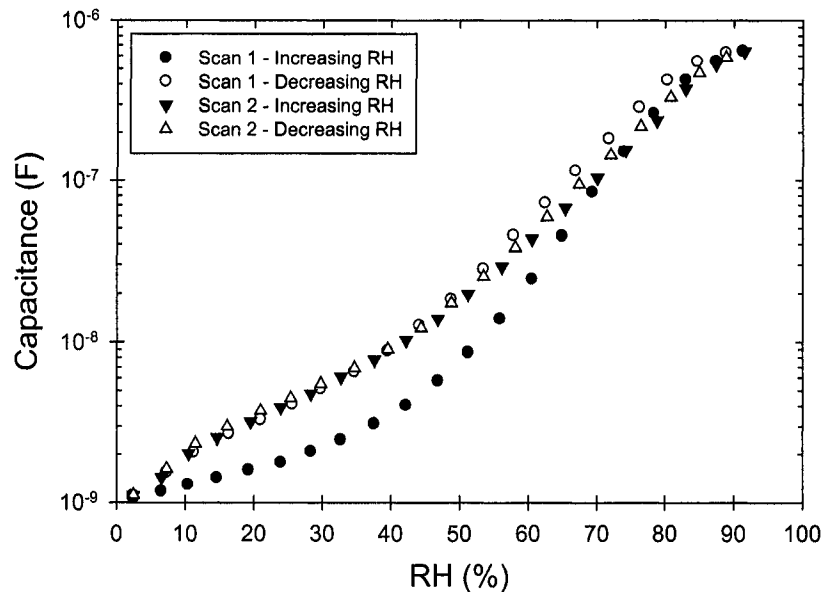


*Figure 5.3. First and second scan capacitive response for 1.5  $\mu\text{m}$  thick  $\text{TiO}_2$  vertical post film deposited at  $\alpha = 81^\circ$  onto a IDC-100-3-5. Hysteresis is substantially reduced after initial exposure to high humidity.*

adsorption isotherm [60]. It is also possible that due to the relatively slow nature of dissociative chemisorption of water vapour [2] that insufficient time had passed for complete hydroxylation prior to the first scan. The sensor that generated the data in Figure 5.3 was tested approximately 12 hours after film deposition. Sensors reported in this thesis were tested within the first 24 hours after film deposition, which may be insufficient for complete hydroxylation. Further study is required to identify the cause of hysteresis in the first scan. A proposed study will be given in Chapter 8.

To evaluate multi-scan hysteresis and repeatability characteristics of the capacitive response, the previously described sensor was tested for a total of eight scans. All eight scans had the same low RH setpoint (2%) but different high RH setpoints. The measured high RH values of the eight scans are listed in Table 5.1.

The data from the first and second scans were shown in Figure 5.3. Figure 5.4 shows the fourth scan, Figure 5.5 the sixth scan, and Figure 5.6 the eighth scan. The

data from scans 3, 5, and 7 have been omitted for clarity. The data from all eight scans show that after the first scan the capacitive response is highly repeatable, does not depend on the high RH setpoint, and exhibits minimal hysteresis.

To account for the difference of the first scan capacitive response compared to subsequent scans, all sensor response data reported in this thesis corresponds to the increasing humidity data of the second scan, unless otherwise stated.

### 5.3 Ageing

The degradation/drift of a humidity sensors response is critical to evaluating performance and potential applications [7, 8]. Most humidity sensors require re-calibration at some point in time [119]. Degradation of sensor response is typically a result of contamination from dust, dirt, oil, smoke, alcohol, and other solvents. Porous materials are especially sensitive to contamination and typically require periodic regeneration by heating to hundreds of degrees Celcius to outgas impurities [16, 18, 19].

Figure 5.7 shows the capacitive response over several days for a 1.5  $\mu\text{m}$  thick  $\text{TiO}_2$  vertical post film deposited at  $\alpha = 81^\circ$  onto a IDC-100-3-5. After only one day the sensor response was noticeably different. After one week the capacitive response had significantly degraded, becoming much less sensitive to relative humidity levels below  $\sim 40\%$ . Continued ageing further diminished sensor performance and increased the relative humidity where the sensor becomes exponentially responsive. The degradation of the capacitive response is expected to be from contamination common to porous materials as mentioned above. For example, van den Brand et al. have shown that the surface of evaporated thin films of amorphous aluminum oxide are highly reactive to organic contamination where chemisorption of carboxylates (via air-borne contaminants such as acetic and formic acid) occurs after only one hour of ageing in ambient conditions [136]. Additional ageing resulted

**Table 5.1.** Measured high RH values of eight scans with different high RH setpoints, but the same low RH setpoint (2%) used to test sensor hysteresis and repeatability.

Scan	High RH (%)
1 & 2	92
3	20
4	38
5	56
6	74
7	83
8	92

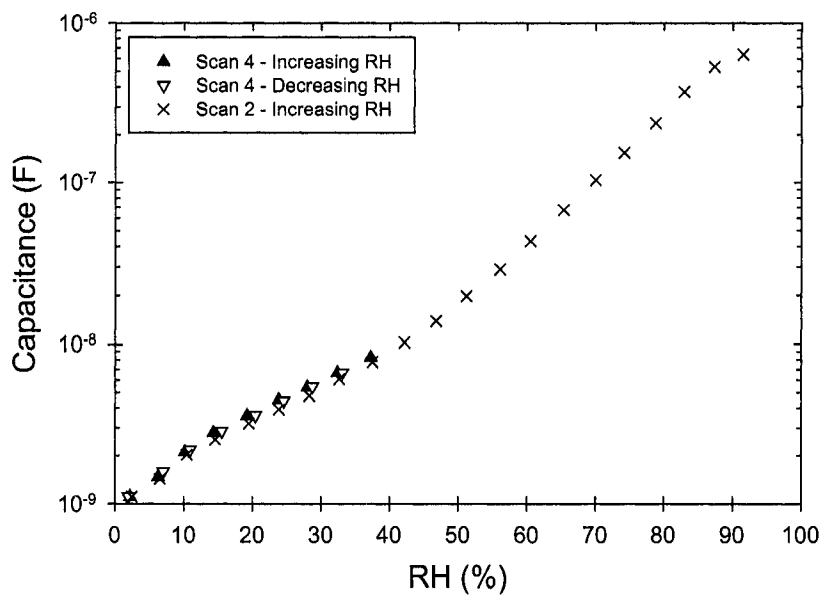


**Figure 5.4.** Fourth scan capacitive response for 1.5 μm thick TiO<sub>2</sub> vertical post film deposited at  $\alpha = 81^\circ$  onto a IDC-100-3-5.

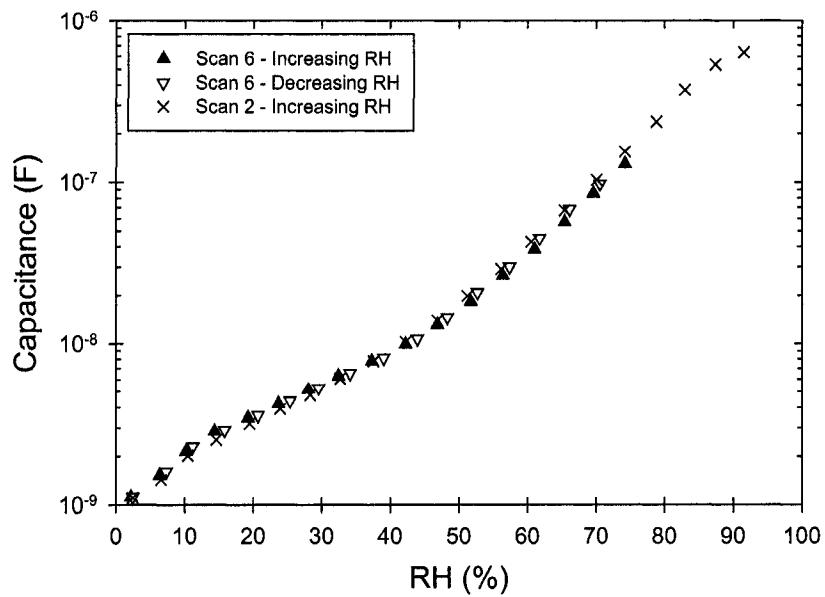


Figure 5.5. Sixth scan capacitive response for 1.5  $\mu\text{m}$  thick  $\text{TiO}_2$  vertical post film deposited at  $\alpha = 81^\circ$  onto a IDC-100-3-5.

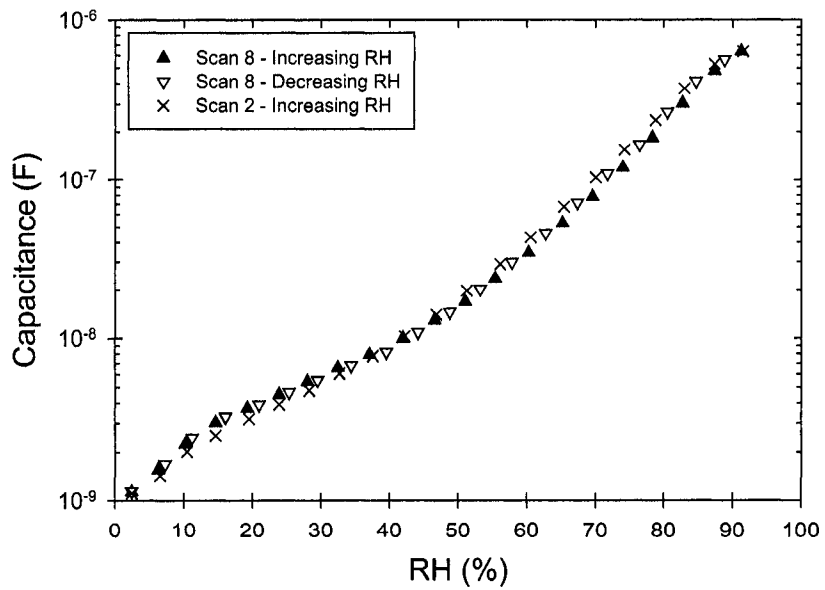


Figure 5.6. Eighth scan capacitive response for 1.5  $\mu\text{m}$  thick  $\text{TiO}_2$  vertical post film deposited at  $\alpha = 81^\circ$  onto a IDC-100-3-5.

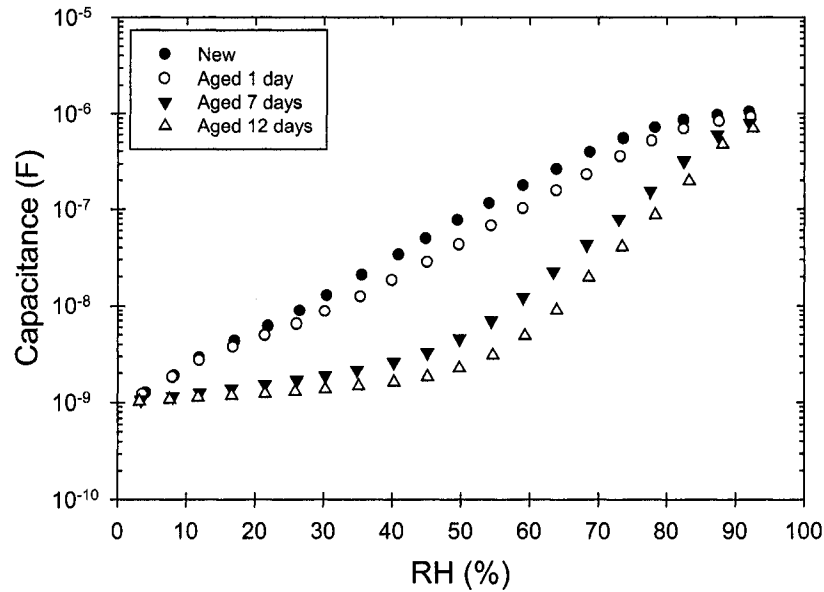


Figure 5.7. Capacitive response over several days for a 1.5  $\mu\text{m}$  thick  $\text{TiO}_2$  vertical post film deposited at  $\alpha = 81^\circ$  onto a IDC-100-3-5.

in short-chained aliphatic contamination where after 20 hours of ageing the bonding capacity of the surface decreased by  $\sim 60\%$ . Chapter 8 proposes ageing studies to confirm the degradation mechanism of GLAD produced humidity sensors.

Attempts to regenerate the capacitive response were conducted using the following heat treatments:

- 110°C for 20 hours
- 200°C for 1 hour
- 300°C for 1 hour and 5 hours
- 400°C for 5 min, 15 min, 30 min, 1 hour, and 3 hours
- 500°C for 5 min, and 30 min
- 700°C for 2 hours.

The most effective heat treatment was 400°C for 1 hour. Figure 5.8 shows the impact of such a treatment to a 17 day old sensor comprised of a 1.5  $\mu\text{m}$  thick  $\text{TiO}_2$  vertical



post film deposited at  $\alpha = 81^\circ$  onto a IDC-100-3-3. The heat treatment did not completely restore the capacitive response, which is likely a result of smoothing and/or crystallization of the columns. Smoothing reduces the surface area available for water vapour adsorption and is expected to reduce sensitivity. Crystallization of the columns will affect the capacitive response as several works have shown that the crystal phase and plane at the surface influence the water vapour adsorption capacity and hydrophilicity of the surface [137–140]. Figure 5.9 shows X-ray diffraction patterns (as deposited and after  $400^\circ\text{C}$  1 hour heat treatment) for a  $1.5\ \mu\text{m}$  thick  $\text{TiO}_2$  vertical post film deposited at  $\alpha = 81^\circ$  onto a standard boron doped p-type silicon (100) test wafer. The lack of discernable peaks in the as deposited diffraction pattern indicates an amorphous phase of the titania film. Following a  $400^\circ\text{C}$  1 hour heat treatment the X-ray pattern contained characteristic peaks of the anatase crystal phase. Using Scherrer's equation the average grain size was calculated to be  $21 \pm 2\ \text{nm}$  from the XRD data in Figure 5.9, which is similar to previously reported values [141]. Although temperatures in the  $400\text{--}500^\circ\text{C}$  range are required to desorb surface hydroxyl groups — which may explain the ineffectiveness of lower temperature heat treatments — the reduction of surface area and crystallization of the columns at these temperatures will prevent the capacitive response from regenerating to an as deposited state. While heat treatments may not be a viable option, other regenerative techniques such as oxygen plasma and chemical solution based cleaning might prove more effective.

## 5.4 IDC Geometry

The geometry of an IDC (e.g., digit width, separation, area) determines the electric field profile within the sensing medium and therefore plays an important role in sensor performance [31, 32, 110, 112, 113]. Initial studies of IDC based GLAD humidity sensors used large geometry IDCs (IDC-25-20-10 described in Chapter 3

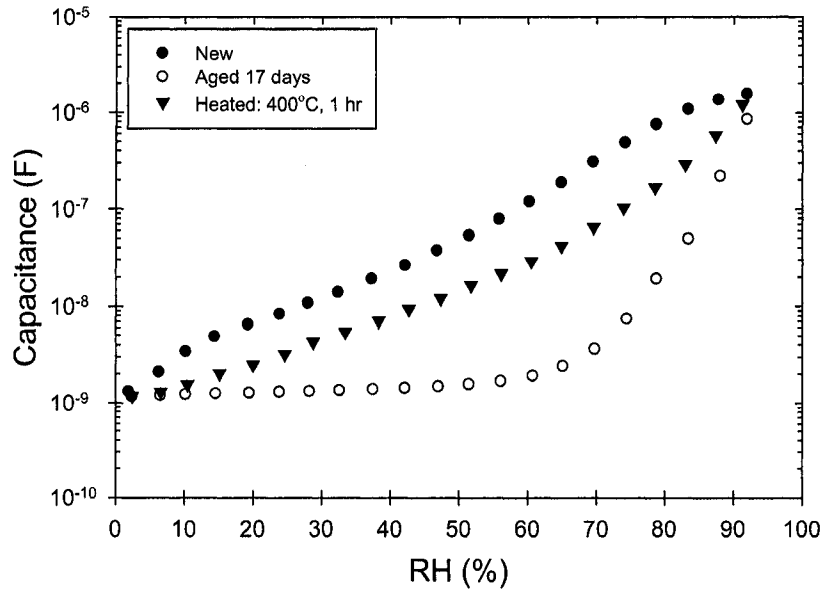


Figure 5.8. Regeneration attempt using 400°C 1 hour heat treatment for a 1.5  $\mu\text{m}$  thick  $\text{TiO}_2$  vertical post film deposited at  $\alpha = 81^\circ$  onto a IDC-100-3-3.

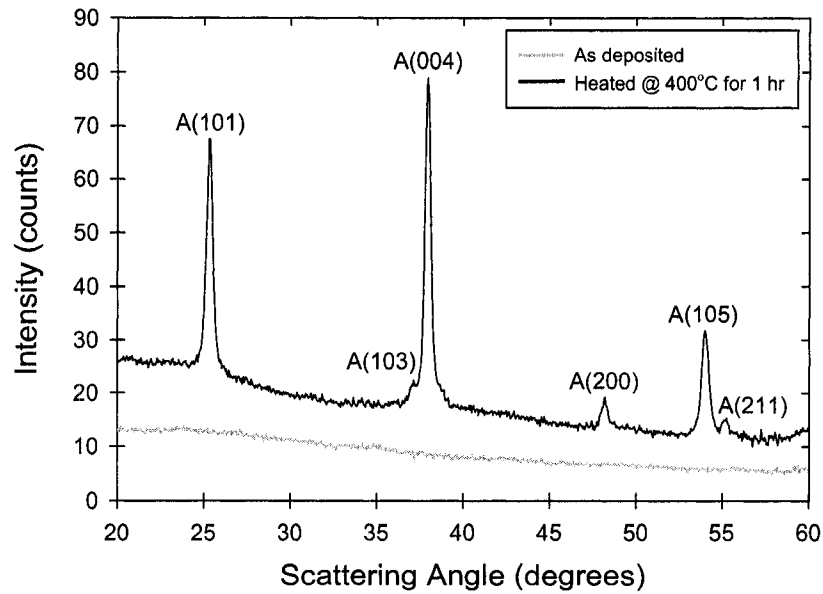
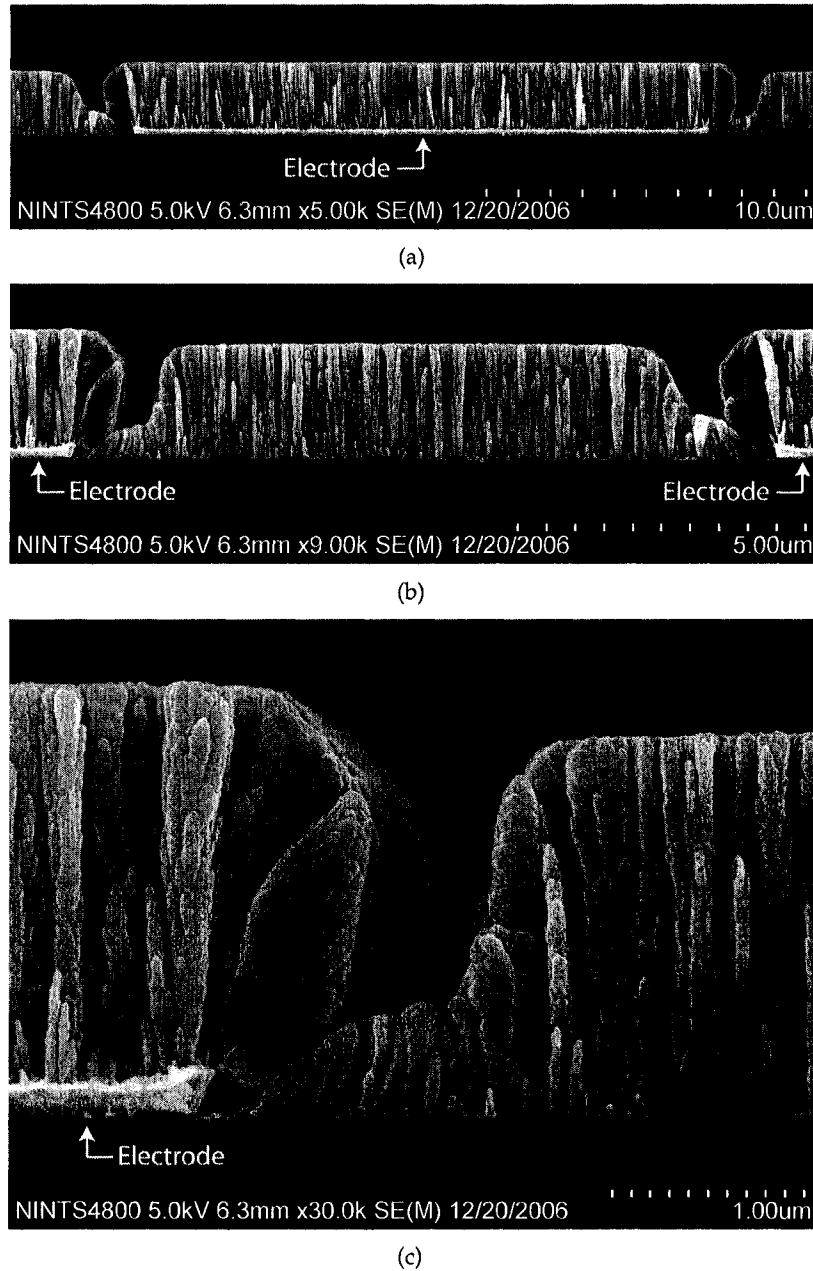


Figure 5.9. X-ray diffraction patterns for a 1.5  $\mu\text{m}$  thick  $\text{TiO}_2$  vertical post film deposited at  $\alpha = 81^\circ$  onto a standard boron doped p-type silicon (100) test wafer. As deposited, the film is amorphous, however, after heating at 400°C for 1 hour the film exhibits crystalline properties of the anatase (A) phase. The average grain size was calculated to be  $21 \pm 2$  nm.

Section 3.3.1) due to their ease of fabrication. Although they were sensitive to humidity changes, several works suggested that reducing the digit period (width + spacing) of the IDCs could enhance the sensitivity. Simulations of IDC structures have shown that approximately 95% of the electric field is contained in a distance perpendicular to the IDC surface equal to half the electrode period [31, 32, 113]. Thus, the electric field for the large geometry IDC-25-20-10 IDCs, which have a 30  $\mu\text{m}$  digit period, is essentially contained 15  $\mu\text{m}$  above the IDC surface. For GLAD films a few microns thick much of the electric field extends past the films and is not fully utilized. It was therefore desirable to reduce the digit period of the IDCs as opposed to growing films with a thickness on the order of 10's of microns for several reasons including shorter deposition times (less chance of deposition errors and therefore greater reproducibility), reduced film stress, and suppression of adverse growth effects (e.g., column broadening and extinction) which are more predominant in thicker films [72]. However, the topography of IDCs fabricated using standard photolithography techniques combined with deposition vapour flux arriving at highly oblique incidence angles during GLAD, resulted in shadowed regions on the substrate/IDC during film growth which limited the effectiveness of reducing the digit period to enhance sensitivity. This shadowing effect is demonstrated in Figure 5.10 where cross-sectional SEM images of an IDC-25-20-10 coated with a 2  $\mu\text{m}$  thick titanium dioxide vertical post film deposited at  $\alpha = 81^\circ$  are shown. The film irregularity at the electrode boundaries is a direct result of electrode induced substrate shadowing during film growth. Figure 5.10(c) shows that the film irregularity extends a distance perpendicular to the electrodes on the order of a couple microns; thus, if the digit/electrode separation were reduced to  $\sim 4 \mu\text{m}$  the entire region between the electrodes would be shadowed during deposition. The shadowing and resulting film irregularity diminishes the surface area available for water vapour adsorption and is therefore expected to reduce the sensitivity. To circumvent this problem Micralyne, Inc. developed a fabrication technique to pro-



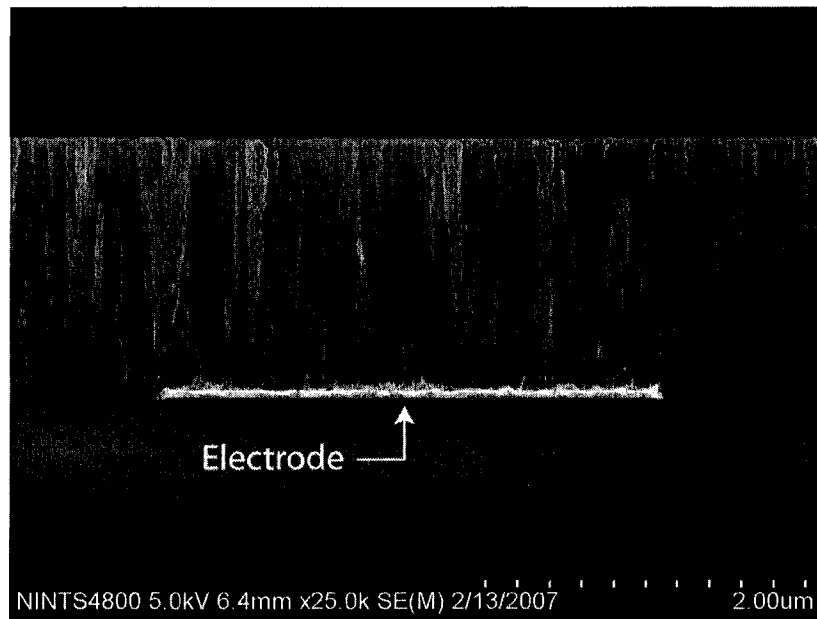
*Figure 5.10.* IDC-25-20-10 coated with a 2  $\mu\text{m}$  thick  $\text{TiO}_2$  film deposited at  $\alpha = 81^\circ$ . Substrate shadowing at electrode boundaries results in film irregularities, which reduces surface area available for water vapour adsorption.

duce the CSE-IDs described in Chapter 3 Section 3.3.2. The CSE-IDs eliminate electrode induced substrate shadowing by counter sinking the electrodes resulting in a planar surface. Figure 5.11 shows cross-sectional SEM images of a CSE-IDC (IDC-100-3-5) coated with a 1.5  $\mu\text{m}$  thick  $\text{TiO}_2$  film deposited at  $\alpha = 81^\circ$ . The elimination of film irregularity at the electrode boundaries is clearly evident. Thus, the CSE-IDs offer the advantages of uniform GLAD film coatings with larger surface area, and digit periods in the several micrometre range. These advantages facilitate the fabrication of highly sensitive sensors utilizing GLAD films of only a few microns thick.

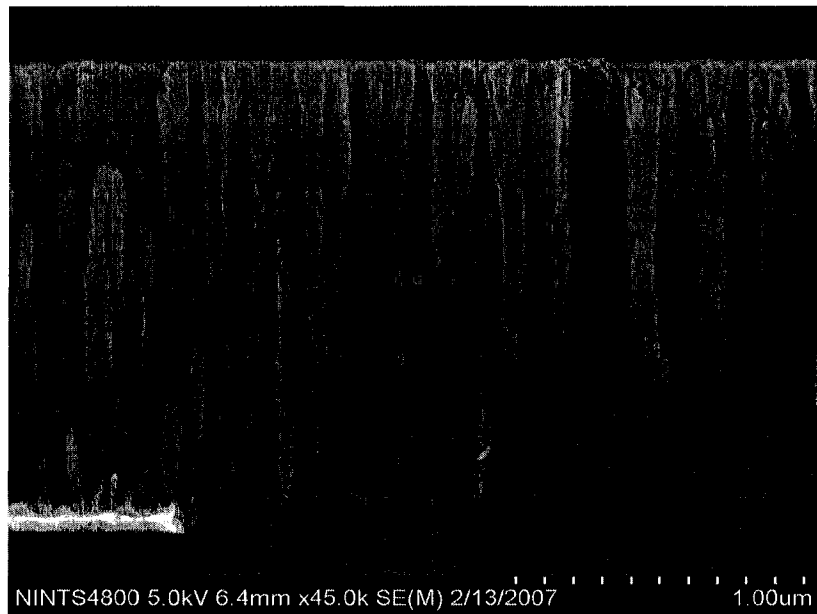
Figure 5.12 shows the capacitive response of a IDC-25-20-10 (large geometry IDC) and a IDC-25-3-3 (CSE-IDC) both coated with a 2  $\mu\text{m}$  thick  $\text{TiO}_2$  vertical post film deposited at  $\alpha = 81^\circ$ . Both sensors had the same digit area (25  $\text{mm}^2$ ) but with different digit periods (30  $\mu\text{m}$  for IDC-25-20-10 and 6  $\mu\text{m}$  for IDC-25-3-3). The topography of the IDC-25-20-10 was also different as previously discussed. The sensitivity ( $S = \text{nF} / \%RH$ ) of the sensor utilizing the IDC-25-3-3 substrate increased from 0.04  $\text{nF} / \%RH$  at low humidity to 9.7  $\text{nF} / \%RH$  at high humidity (due to exponential response), whereas the IDC-25-20-10 based sensor had a minimum and maximum sensitivity of only 0.002  $\text{nF} / \%RH$  and 0.3  $\text{nF} / \%RH$ , respectively.

Figure 5.13 further illustrates the impact of IDC geometry on the capacitive response. The minimum and maximum sensitivity of the data sets in Figure 5.13 are listed in Table 5.2. Comparing the sensitivity range for the IDC-100-3-5 and IDC-100-3-3 based sensors, which have the same digit area of 100  $\text{mm}^2$ , shows that reducing the digit period by as little as 2  $\mu\text{m}$  from 8  $\mu\text{m}$  (IDC-100-3-5) to 6  $\mu\text{m}$  (IDC-100-3-3) can enhance sensitivity. Increasing the digit area has a similar effect as shown by the IDC-25-3-3 and IDC-100-3-3 sensitivity ranges shown in Table 5.2. The increased sensitivity for the 100  $\text{mm}^2$  IDC-100-3-3 is a result of increased film surface area within the electric field.

The remainder of this thesis presents data obtained from sensors utilizing CSE-



(a)



(b)

**Figure 5.11.**  $1.5 \mu\text{m}$  thick  $\text{TiO}_2$  film ( $\alpha = 81^\circ$ ) deposited onto a CSE-IDC (IDC-100-3-5). Elimination of film irregularity at electrode boundary facilitates the use IDCs with reduced digit periods and therefore thinner GLAD films.

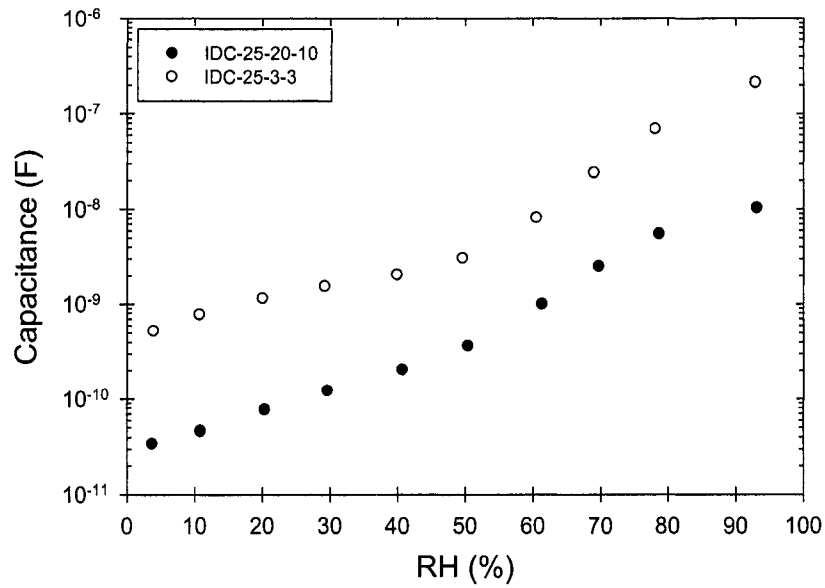


**Figure 5.12.** Capacitive response comparison between IDC-25-20-10 (large geometry IDC) and IDC-25-3-3 (CSE-IDC) both coated with a 2  $\mu\text{m}$  thick  $\text{TiO}_2$  vertical post film deposited at  $\alpha = 81^\circ$ .

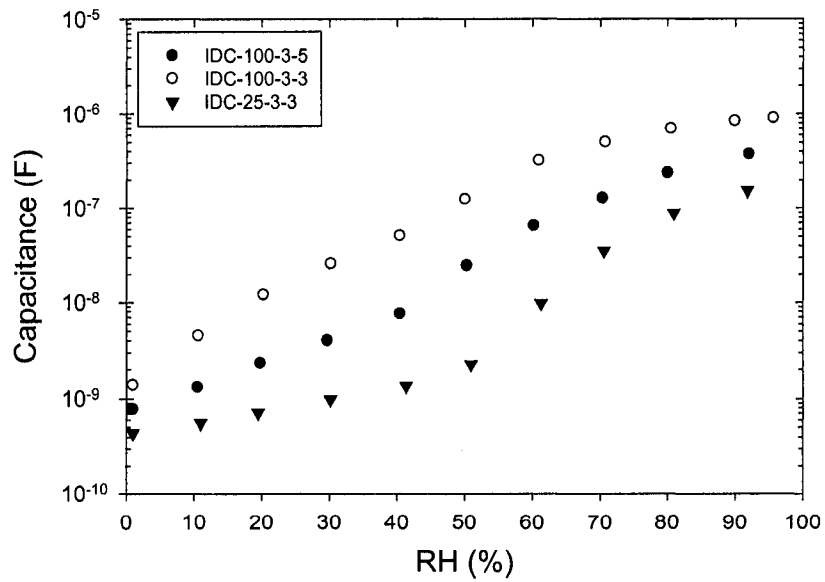


**Figure 5.13.** Effect of varying IDC geometry on capacitive response. All IDCs were coated with a 1.5  $\mu\text{m}$  thick  $\text{TiO}_2$  vertical post film deposited at  $\alpha = 81^\circ$ .

**Table 5.2.** Minimum and maximum sensitivity,  $S$ , of the sensors that produced the capacitive responses shown in Figure 5.13.

IDC	$S_{min}$ (nF / %RH)	$S_{max}$ (nF / %RH)
IDC-25-3-3	0.01	6
IDC-100-3-5	0.06	11
IDC-100-3-3	0.3	19

IDCs due to their enhanced sensitivity and uniform GLAD film coatings. The exact geometry of the IDCs varies; however, for a given study all IDCs had the same geometry.

## 5.5 Effect of Flow Rate on Response Time

In Chapter 4 Section 4.5, the setup used to measure sensor response time was described. It was stated that flow rates of 2.5 LPM were typically used during measurements to rapidly exchange the 2.0–2.5 mL volume between the solenoid valve outputs and the sensor surface. A more detailed discussion will now be given.

Figure 5.14 shows response time data obtained at three different flow rates (0.5, 1.0, 2.5 LPM) collected during a 13.5 s pulse (low RH to high RH to low RH) for a sensor comprised of a IDC-100-3-5 coated with a 1.5  $\mu\text{m}$  thick  $\text{TiO}_2$  vertical post film deposited at  $\alpha = 81^\circ$ . In Table 5.3, the calculated response times for the three different flow rates are given. The response times (adsorption and desorption) obtained at 0.5 LPM are  $\sim 2.3$  times longer than those obtained at 2.5 LPM. Similarly, the response times for 1.0 LPM are  $\sim 1.4$  times longer. M enil et al. considered a gas sensors response time as a sum of extrinsic and intrinsic components where the extrinsic component is due to the gas delivery system and the intrinsic is due to sensor properties and is independent of the experimental setup [120]. The longer response times for the smaller flow rates are a direct result of longer extrinsic times required to change the humidity at the sensor surface since the same sensor was used to obtain all measurements.



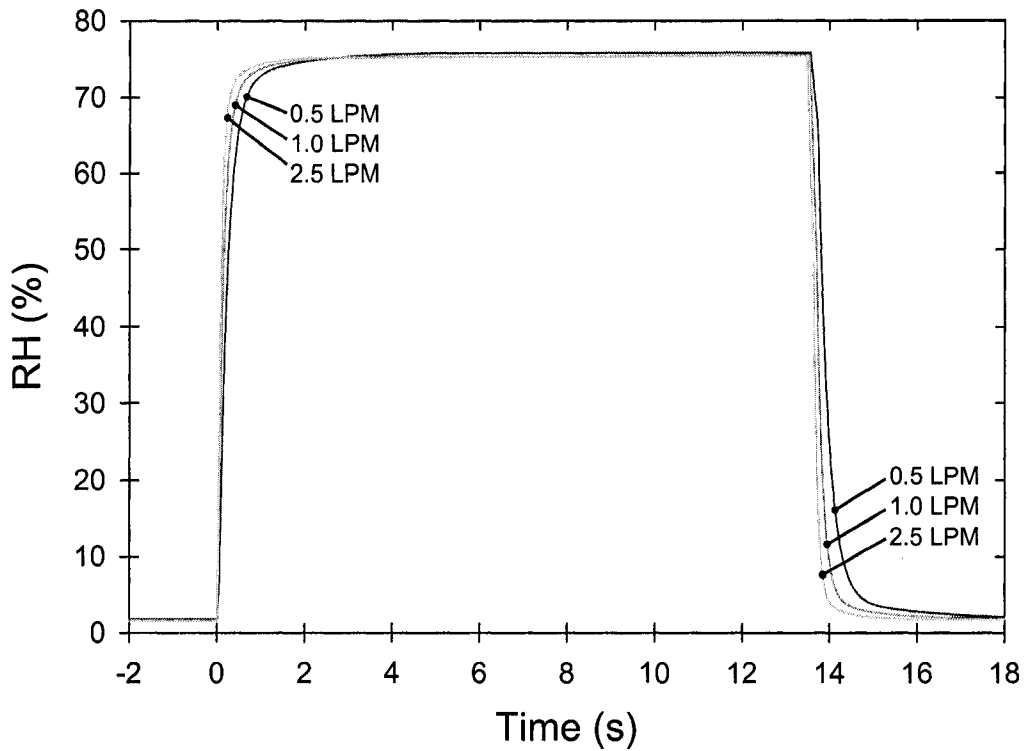


**Figure 5.14.** Effect of flow rate on response time measurement. A large contribution of the observed response times for 0.5 and 1.0 LPM are from air mixing and the gas delivery system.

**Table 5.3.** Response times for the data shown in Figure 5.14 calculated using exponential fitting with SigmaPlot.

Flow Rate (LPM)	Adsorption Response Time (ms)	Desorption Response Time (ms)
0.5	590 ± 36	775 ± 25
1.0	375 ± 4	426 ± 10
2.5	243 ± 3	336 ± 2

### 5.5. Effect of Flow Rate on Response Time

---

Several works have shown that a first order approximation of the transient concentration,  $c(t)$ , of target species (in this case water vapour) in a test cell can be obtained from the well-stirred tank model [120, 142, 143]. If at time  $t \leq 0$  the concentration in the test cell is  $c_1$  and at time  $t = 0$  gas of concentration  $c_2$  flows into the cell at a rate of  $f$ , then assuming the gas is always homogeneous in the test cell and that the total pressure remains constant, the transient concentration is given by:

$$c(t) = c_2 - (c_2 - c_1) \exp\left(\frac{-t}{\tau}\right) \quad (5.1)$$

where  $\tau = V/f$  with  $V$  the exchange volume. Thus, Equation 5.1 can be used to estimate the extrinsic response time if the exchange volume is known. Since an accurate value of the exchange volume is difficult to calculate (2.0–2.5 mL was a rough estimate) the total response time (extrinsic + intrinsic) data listed in Table 5.3 was used to estimate the extrinsic and intrinsic response times. Response times are typically defined by the time it takes for 90% of the change to occur, thus the extrinsic response time ( $t_{ex}$ ) calculated from Equation 5.1 is:

$$t_{ex} = -\tau \ln(0.1) \approx 2.3 \left(\frac{V}{f}\right) \quad (5.2)$$

since the exchange volume is constant the extrinsic response time can be defined as a function of flow rate:

$$t_{ex} \equiv t_{ex}(f) \quad (5.3)$$

Thus, the following equations hold true:

$$t_{ex}(0.5 \text{ LPM}) = 5t_{ex}(2.5 \text{ LPM}) \quad (5.4)$$

$$t_{ex}(1.0 \text{ LPM}) = 2.5t_{ex}(2.5 \text{ LPM}) \quad (5.5)$$

From the data in Table 5.3 the following six equations were obtained:

$$t_{ex}(0.5 \text{ LPM}) + t_{in,ads} = 590 \text{ ms} \quad (5.6)$$

$$t_{ex}(1.0 \text{ LPM}) + t_{in,ads} = 375 \text{ ms} \quad (5.7)$$

$$t_{ex}(2.5 \text{ LPM}) + t_{in,ads} = 243 \text{ ms} \quad (5.8)$$

$$t_{ex}(0.5 \text{ LPM}) + t_{in,des} = 775 \text{ ms} \quad (5.9)$$

$$t_{ex}(1.0 \text{ LPM}) + t_{in,des} = 426 \text{ ms} \quad (5.10)$$

$$t_{ex}(2.5 \text{ LPM}) + t_{in,des} = 336 \text{ ms} \quad (5.11)$$

where  $t_{in,ads}$  and  $t_{in,des}$  are the intrinsic response times (independent of flow rate) for adsorption and desorption, respectively. Solving the above sets of equations (5.4–5.11) yields:

$$t_{in,ads} = \{155, 156\} = 156 \text{ ms (average)} \quad (5.12)$$

$$t_{in,des} = \{226, 276\} = 251 \text{ ms (average)} \quad (5.13)$$

$$t_{ex}(2.5 \text{ LPM}) = \{85, 88\} = 87 \text{ ms (average)} \quad (5.14)$$

To minimize the extrinsic contribution to the response time, a flow rate of 2.5 LPM (maximum on flowmeters used in response time setup) was used throughout this thesis, unless otherwise stated. The reader is asked to keep in mind that the reported response times encompass a  $\sim 90$  ms contribution from the experimental setup. Direct comparisons are meaningful for all values obtained at the same flow rate.

## 5.6 Summary

The following were used to characterize the capacitive humidity sensors reported in this thesis:

1. The series capacitance measured at 1 kHz and 1 V<sub>rms</sub> was used to characterize the sensor response as a function of relative humidity.
2. Capacitive response data corresponds to the second scan during increasing humidity.
3. Sensors were tested within the first 24 hours after film deposition.
4. Several CSE-IDs with different geometries were used.
5. 2.5 LPM flow rates were used to measure sensor response time.

In the next chapter the effects GLAD film composition and morphology on sensor performance are presented.

## Chapter 6

# GLAD Film Composition and Morphology Effects on Sensor Performance

In this chapter the impact of GLAD film composition and morphology on the capacitive response and response time are presented. In particular, the following will be discussed:

1. Comparison of  $\text{Al}_2\text{O}_3$ ,  $\text{SiO}_2$ , and  $\text{TiO}_2$  as sensing materials
2. Effect of film thickness
3. Effect of deposition angle ( $\alpha$ )

### 6.1 Sensing Material

It is well known that chemical nature, crystallinity, crystal phase, and crystal plane at the surface of metal oxides affect the reactivity towards water vapour [2, 56, 59, 137–140, 144]. The degree of coordinative unsaturation of surface metal cations and therefore the Lewis acidity of the surface are strongly dependent on these prop-

erties. For example, studies have shown that the anatase phase of  $\text{TiO}_2$  is more reactive towards water vapour (larger heat of adsorption) and has a larger water vapour adsorption capacity than rutile [137, 139, 144]. Others have shown that water vapour adsorption characteristics differ between several metal oxides including  $\text{TiO}_2$  (anatase and rutile),  $\text{SiO}_2$  (silicalite, quartz, and amorphous silica), and  $\text{Al}_2\text{O}_3$  ( $\alpha$  and  $\eta$  phases) [2].

The following presents results from an investigation on the use of as deposited  $\text{TiO}_2$ ,  $\text{SiO}_2$ , and  $\text{Al}_2\text{O}_3$  vertical post GLAD films as the humidity sensitive material in capacitive sensors. These particular oxides were selected due to their frequent use in the humidity sensor literature [17] and their suitability for the GLAD process. All films were  $1.5 \pm 0.1 \mu\text{m}$  thick and deposited at an angle of  $\alpha = 81^\circ$  onto IDC-100-3-5 substrates. See Chapter 3, Section 3.4 for information on deposition conditions.

Figure 6.1 shows XRD patterns of the as deposited metal oxide films grown on p-type silicon (100) substrates obtained using a copper  $K_\alpha$  source and an area detector (Bruker D8 Discover). The lack of discernable peaks in the patterns reveals that all three metal oxides were amorphous.

### 6.1.1 Capacitive Response

Figure 6.2 shows the capacitive responses from sensors using  $\text{TiO}_2$ ,  $\text{SiO}_2$ , and  $\text{Al}_2\text{O}_3$  GLAD films. The responses were found to be repeatable as demonstrated in Figure 6.3 for the  $\text{TiO}_2$  and  $\text{Al}_2\text{O}_3$  sensors. The sensitivity (local slope of capacitive response with units  $\text{nF} / \%\text{RH}$ ) of the sensors varies as a function of humidity due to the exponential capacitive response. Figure 6.4 shows the sensitivity of the three sensors plotted as a function of RH. The sensor utilizing  $\text{TiO}_2$  was the most sensitive over the entire RH range with a minimum and maximum sensitivity of 0.2 and 34.4  $\text{nF} / \%\text{RH}$ , respectively. Figure 6.4 shows that the maximum sensitivity occurs at approximately 78% RH for  $\text{TiO}_2$ , 80% RH for  $\text{SiO}_2$ , and 55% RH for  $\text{Al}_2\text{O}_3$ .

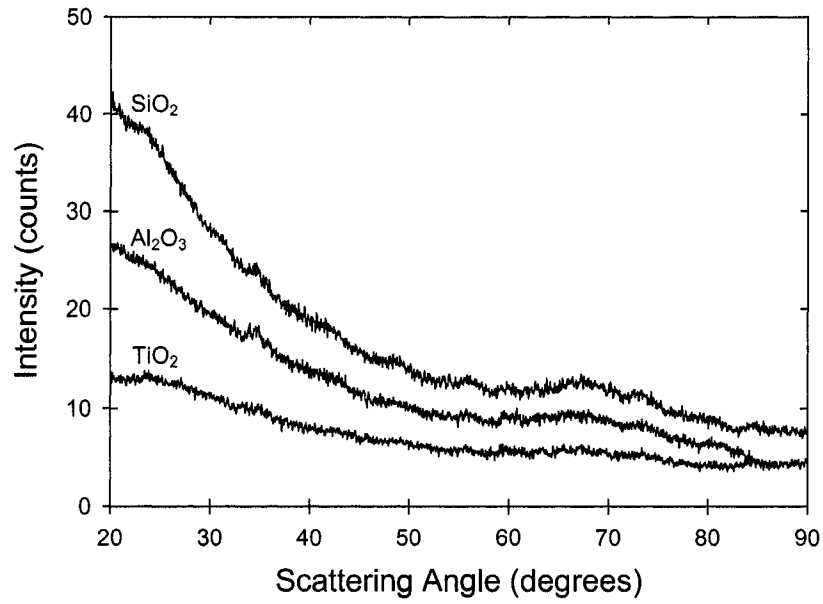


Figure 6.1. As deposited XRD patterns for 1.5  $\mu\text{m}$  thick  $\text{TiO}_2$ ,  $\text{SiO}_2$ , and  $\text{Al}_2\text{O}_3$  GLAD films deposited at an angle of  $\alpha = 81^\circ$  onto silicon wafers (100).

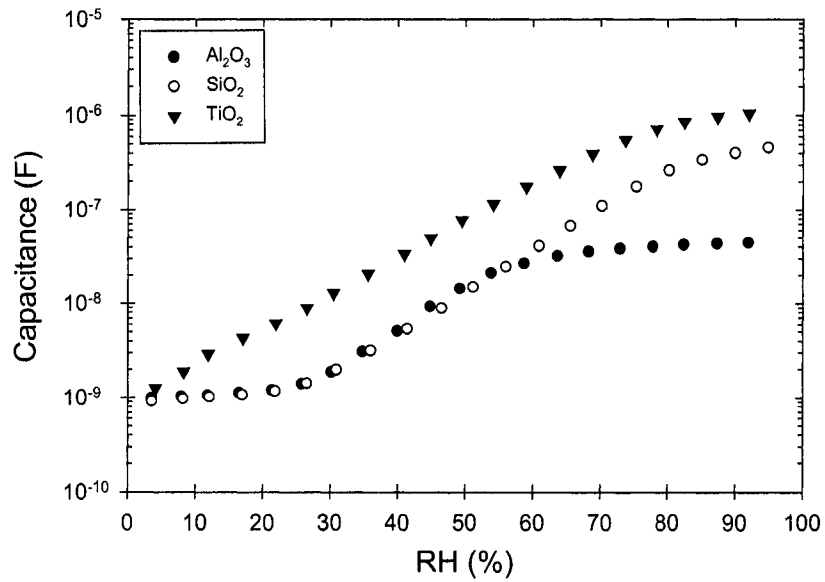
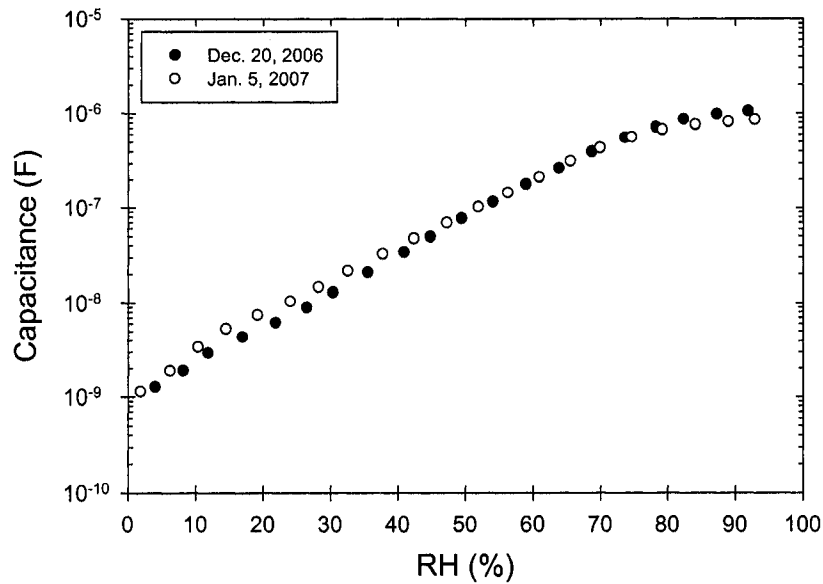
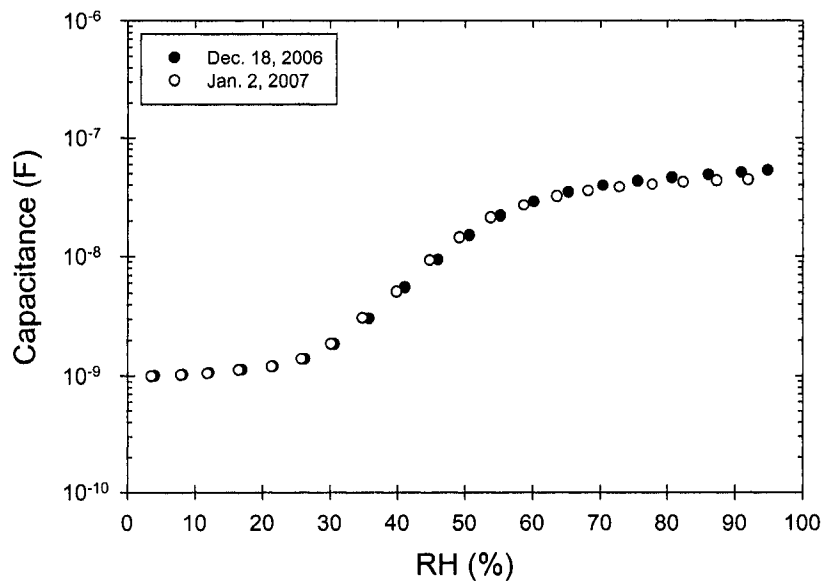
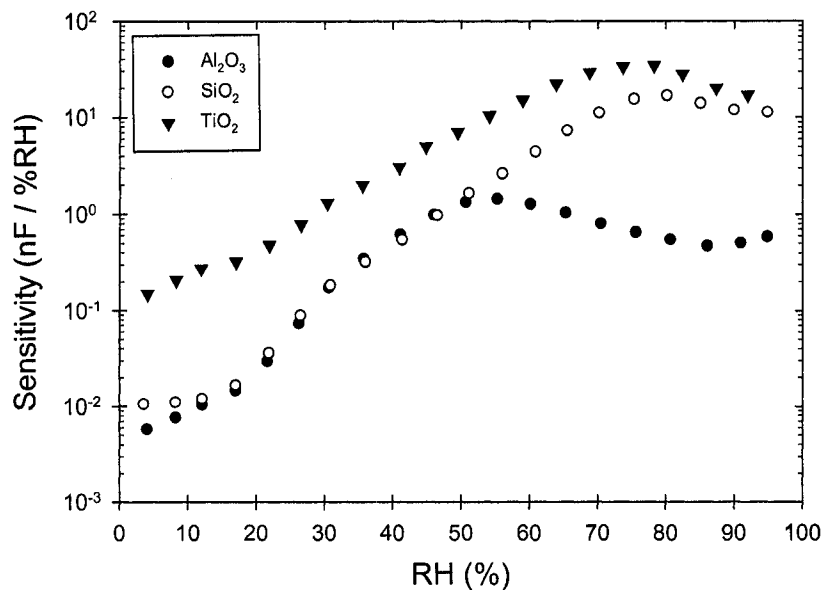


Figure 6.2. Comparison of the capacitive response for sensors made with  $\text{TiO}_2$ ,  $\text{SiO}_2$ , and  $\text{Al}_2\text{O}_3$  GLAD films. All films were  $1.5 \pm 0.1 \mu\text{m}$  thick and deposited at an angle of  $\alpha = 81^\circ$  onto IDC-100-3-5 capacitors.

(a)  $\text{TiO}_2$ (b)  $\text{Al}_2\text{O}_3$ 

**Figure 6.3.** Repeatability of capacitive response for different sensors using  $\text{TiO}_2$  and  $\text{Al}_2\text{O}_3$  GLAD films deposited on different days. All sensors were tested within 24 hours after film deposition.





**Figure 6.4.** Sensitivity plotted as a function of relative humidity for sensors made with TiO<sub>2</sub>, SiO<sub>2</sub>, and Al<sub>2</sub>O<sub>3</sub> GLAD films. The sensitivity changes with RH due to the exponential response of the sensors.

The different surface chemistry of the TiO<sub>2</sub>, SiO<sub>2</sub>, and Al<sub>2</sub>O<sub>3</sub> films will affect the capacitive response. Furthermore, morphological differences resulting from different thin film growth dynamics can also impact sensor response. Figure 6.5 shows cross-sectional and top down SEM images of the films. Figures 6.6, 6.7, and 6.8 show TEM images of the tip of a single column from the TiO<sub>2</sub>, SiO<sub>2</sub>, and Al<sub>2</sub>O<sub>3</sub> GLAD films, respectively. It is apparent that both inter- and intra-column morphology of GLAD films are dependent on the source material. Different morphologies will alter the density, porosity, surface area, and pore size distribution of the films and can therefore significantly alter sensor performance.

A significant difference in the deposition of TiO<sub>2</sub> GLAD films, as compared to SiO<sub>2</sub> and Al<sub>2</sub>O<sub>3</sub>, is the addition of oxygen gas to promote stoichiometric growth (see Chapter 3 Section 3.4 for description of deposition conditions). The addition of oxygen results in much higher deposition pressures (e.g.,  $7 \times 10^{-5}$  Torr compared to  $3 \times 10^{-6}$  Torr for SiO<sub>2</sub>). Deposition in an oxygen environment can affect

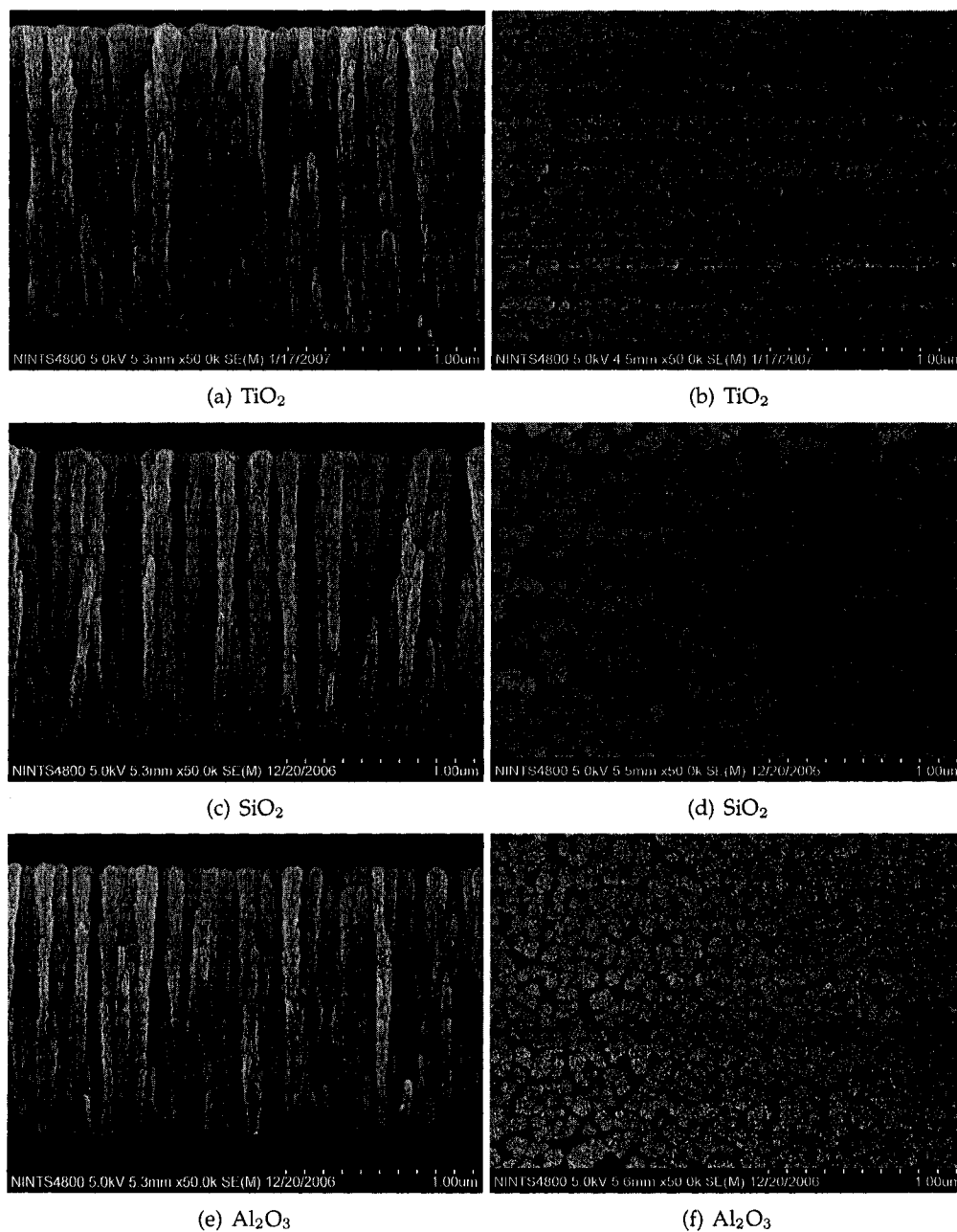


*Figure 6.5. Cross-sectional and top down SEM images of  $\text{TiO}_2$ ,  $\text{SiO}_2$ , and  $\text{Al}_2\text{O}_3$  films used in humidity sensors producing the capacitive responses shown in Figure 6.2. All images were taken at 50,000 $\times$  magnification.*



*Figure 6.6. TEM image of TiO<sub>2</sub> column.*

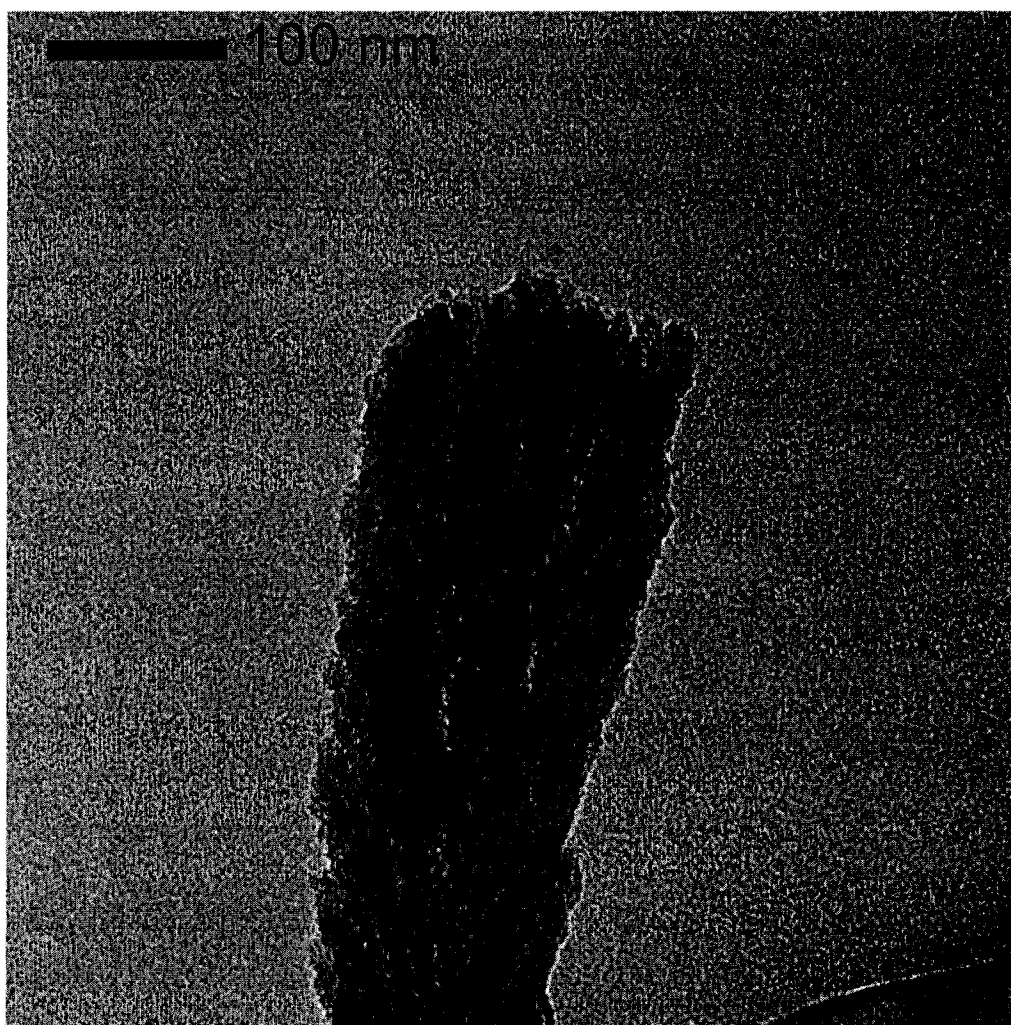


*Figure 6.7. TEM image of SiO<sub>2</sub> column.*

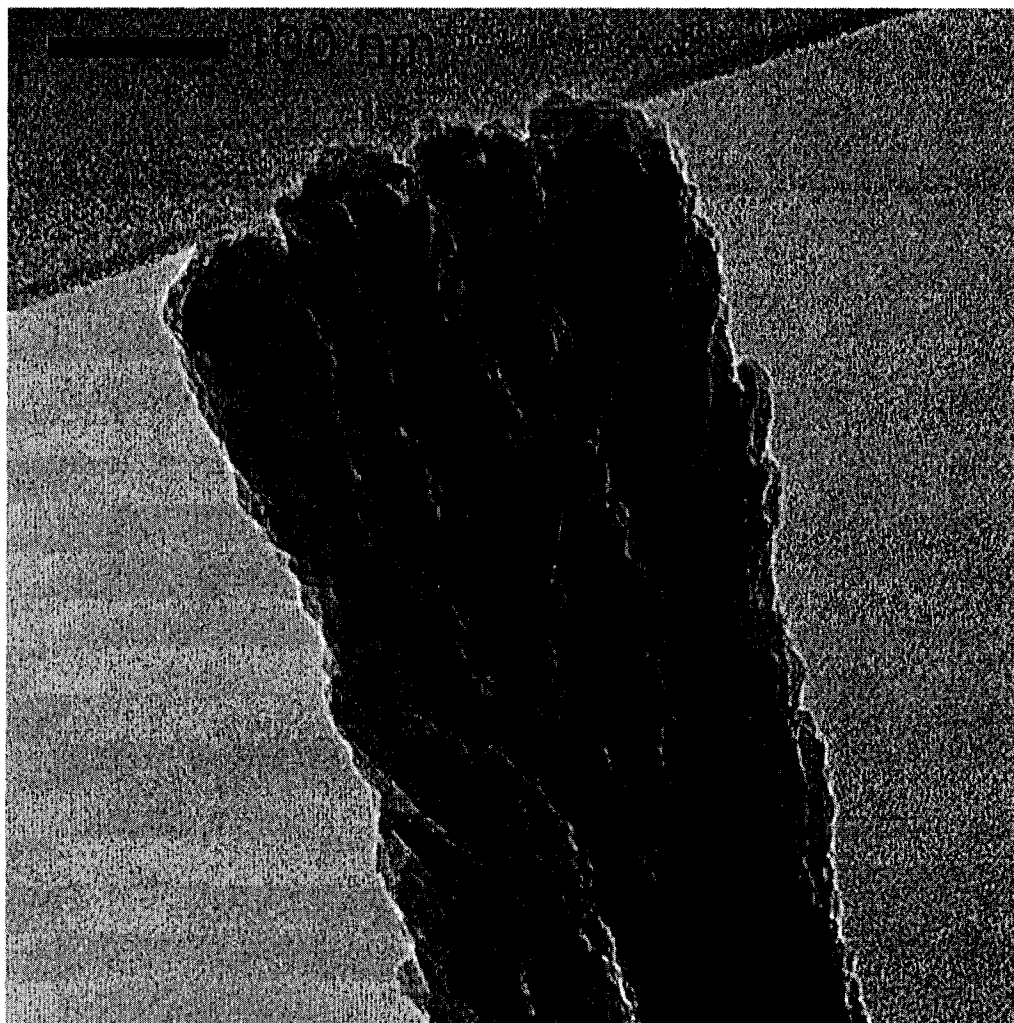


*Figure 6.8. TEM image of Al<sub>2</sub>O<sub>3</sub> column.*

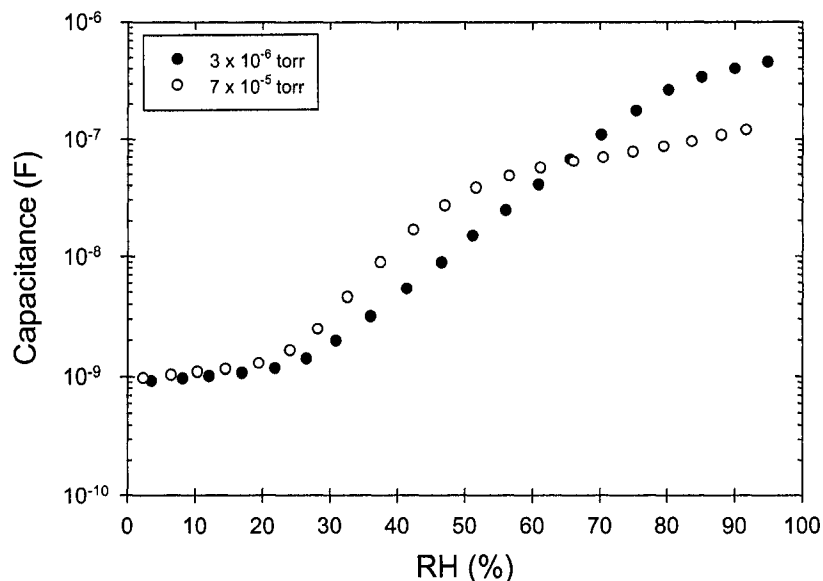


**Figure 6.9.** Effect of depositing  $\text{SiO}_2$  in high pressure oxygen environment on the capacitive response.

surface chemistry as well as growth dynamics since elevated pressures results in enhanced scattering and a larger angular distribution of the vapour flux [91]. To investigate the influence of the oxygen environment and higher deposition pressures on the capacitive response, a humidity sensor using a  $\text{SiO}_2$  GLAD film grown in an oxygen environment at  $7 \times 10^{-5}$  Torr was fabricated. With the exception of the deposition conditions, this sensor was near identical to the previously discussed  $\text{SiO}_2$  based sensor exhibiting the capacitive response shown in Figure 6.2. The capacitive response of the  $\text{SiO}_2$  sensor deposited in a high pressure oxygen environment is shown in Figure 6.9 along with the capacitive response of the previously described  $\text{SiO}_2$  sensor for comparison. The considerable difference in the capacitive response shows that the addition of oxygen gas and/or the high deposition pressures can significantly impact sensor performance as a result of surface chemistry and/or morphological changes.

Furthermore, the shape of the capacitive response for the  $\text{SiO}_2$  sensor deposited at high pressure exhibits a similar shape to that obtained from the sensor using

Al<sub>2</sub>O<sub>3</sub>. Since Al<sub>2</sub>O<sub>3</sub> films are deposited at higher pressures than SiO<sub>2</sub> films, this result suggests that film growth dynamics may play an important role in determining the capacitive response for SiO<sub>2</sub> and Al<sub>2</sub>O<sub>3</sub> films.

These results show that sensors fabricated using TiO<sub>2</sub> films offer the advantage of high sensitivity over the entire RH range, which is the primary reason why TiO<sub>2</sub> is predominantly used throughout this thesis. Characterization techniques such as gas adsorption porosimetry, vibrational surface spectroscopy, and gas adsorption calorimetry may identify the physical and chemical properties of the metal oxide films responsible for the capacitive response trends presented here.

### 6.1.2 Response Time

Response time measurements were obtained using the methodology outlined in Chapter 4 and the characterization protocol presented in Chapter 5, Section 5.5. Curves similar to those presented in Figure 5.14 on page 96 were obtained.

Figure 6.10 presents the response times of the TiO<sub>2</sub>, SiO<sub>2</sub>, and Al<sub>2</sub>O<sub>3</sub> based sensors. The response times were obtained by taking a weighted average of response times calculated using exponential fitting (using SigmaPlot version 10.0) for three adsorption and three desorption response time data sets. The average humidity change during the response time measurements was 82% RH (alternation between 2% RH and 84% RH). Although all sensors were fast compared to current commercial technology, the TiO<sub>2</sub> sensor was slowest, followed by SiO<sub>2</sub> and then Al<sub>2</sub>O<sub>3</sub>. This trend may be a result of bonding strength (more Lewis acidic materials will form stronger bonds with water vapour and thus require more energy to desorb) and/or pore size and shape distributions. The high sensitivity of TiO<sub>2</sub> towards water vapour could be a result of a finer and possibly deeper (higher aspect ratio) intra-column pore structure, which will result in a larger surface area and therefore high sensitivity; however, this would likely present a more tortuous path for water vapour adsorption/desorption, which would slow down the sensor response [145].

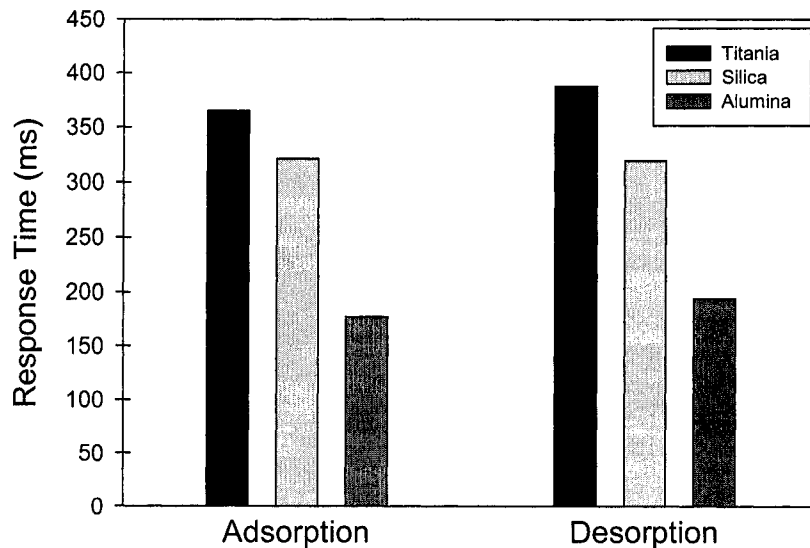


**Figure 6.10.** Response times for TiO<sub>2</sub>, SiO<sub>2</sub>, and Al<sub>2</sub>O<sub>3</sub> based sensors obtained by taking a weighted average of three adsorption and three desorption response time measurements.

## 6.2 Film Thickness

To study the effect of GLAD film thickness on sensor performance, seven sensors were fabricated using IDC-100-3-5 substrates coated with TiO<sub>2</sub> films deposited at  $\alpha = 81^\circ$ . The film thicknesses (measured from SEM images) were as follows: 0.28, 0.57, 1.1, 1.7, 3.3, 6.4, and 8.5  $\mu\text{m}$ . Cross-sectional and top down SEM images of the sensors are shown in Figures 6.11 and 6.12, respectively. Figure 6.13(a) shows the capacitive response of the sensors utilizing 0.28, 1.7, and 8.5  $\mu\text{m}$  thick films, and in Figure 6.13(b) the sensitivity is presented. The data from the other sensors were excluded for clarity, however, the following general trends in the capacitive response held true.

### 6.2.1 Low Humidity

Under low humidity ( $0\% < \text{RH} < 20\%$ ) the sensitivity was enhanced as the thickness increased from 0.28  $\mu\text{m}$  to 1.7  $\mu\text{m}$ . Films 1.7  $\mu\text{m}$  and thicker had a similar sensitivity.



## 6.2. Film Thickness

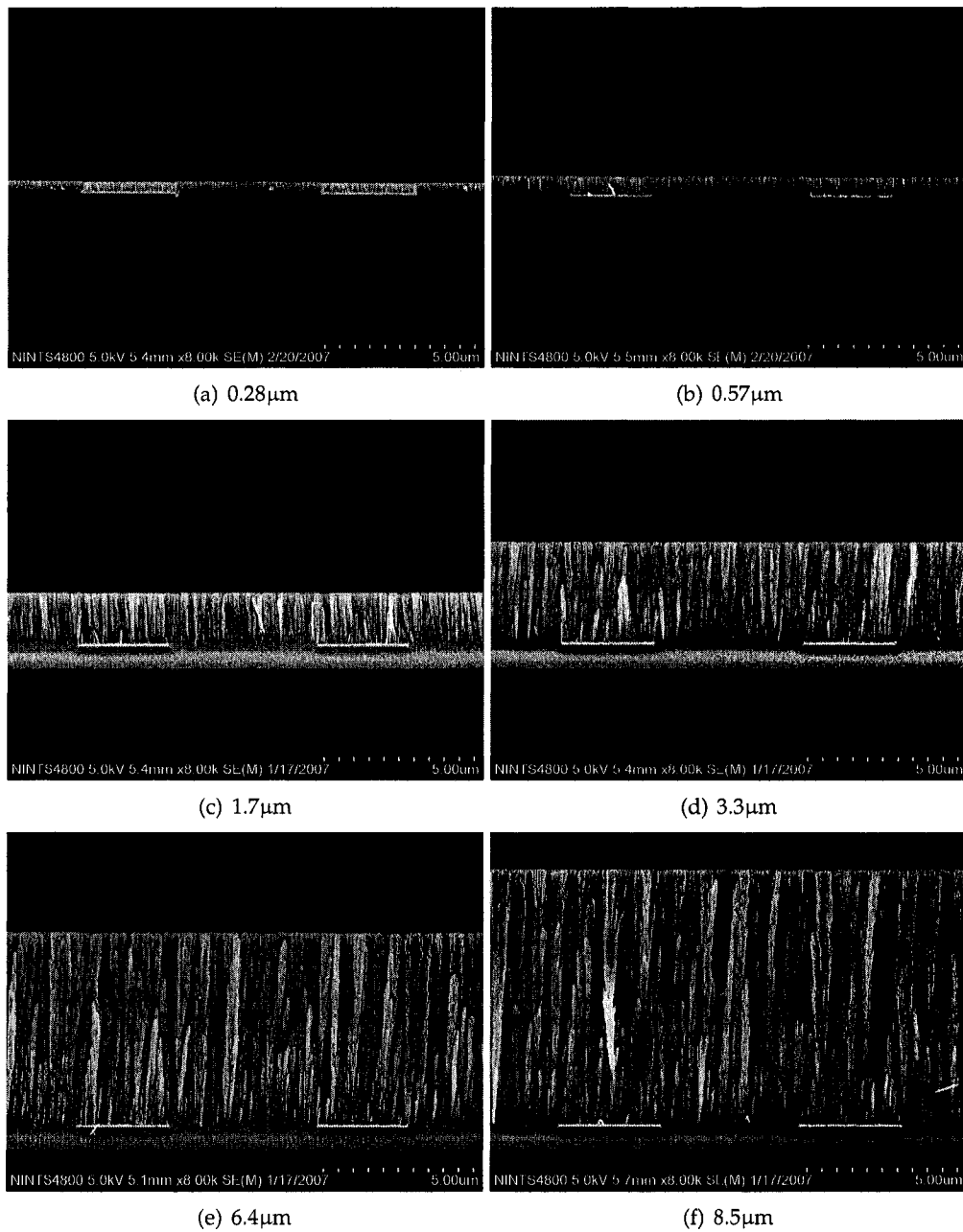


*Figure 6.11. Cross-sectional SEM images of IDC-100-3-5 substrates coated with TiO<sub>2</sub> films of varying thickness. The image of the 1.1  $\mu$ m thick film was excluded. All images were obtained at 8,000 $\times$  magnification.*

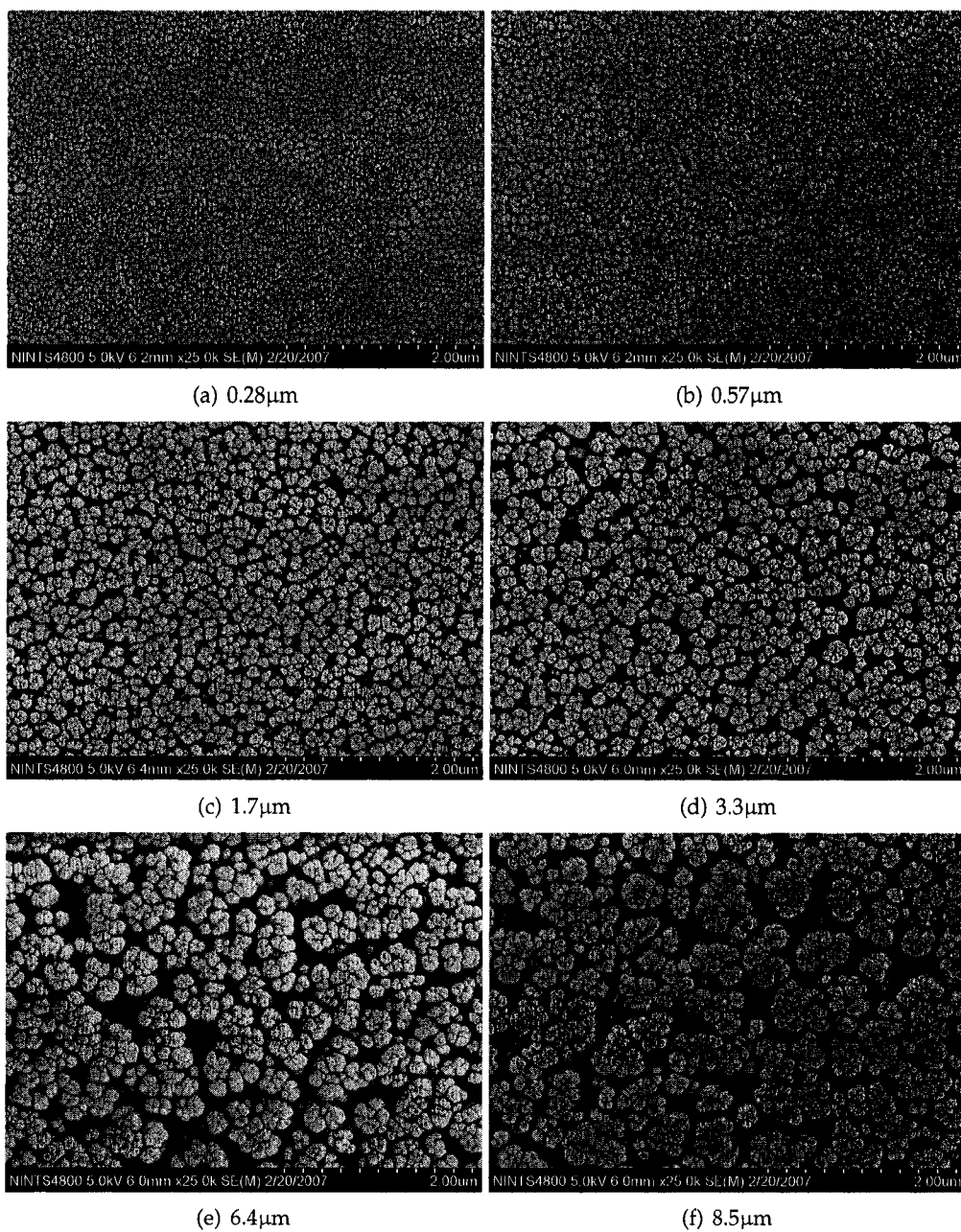


*Figure 6.12. Top down SEM images of IDC-100-3-5 substrates coated with  $\text{TiO}_2$  films of varying thickness. The image of the 1.1  $\mu\text{m}$  thick film was excluded. All images were obtained at 25,000 $\times$  magnification.*

### 6.2.2 Mid Range Humidity

For mid range humidity levels ( $20\% < RH < 70\%$ ) the sensitivity was enhanced as the thickness was increased from  $0.28\ \mu\text{m}$  to  $1.7\ \mu\text{m}$ . Between  $1.7\ \mu\text{m}$  and  $3.3\ \mu\text{m}$  the sensitivity remained constant. Above  $3.3\ \mu\text{m}$  the sensitivity began to diminish with increased thickness.

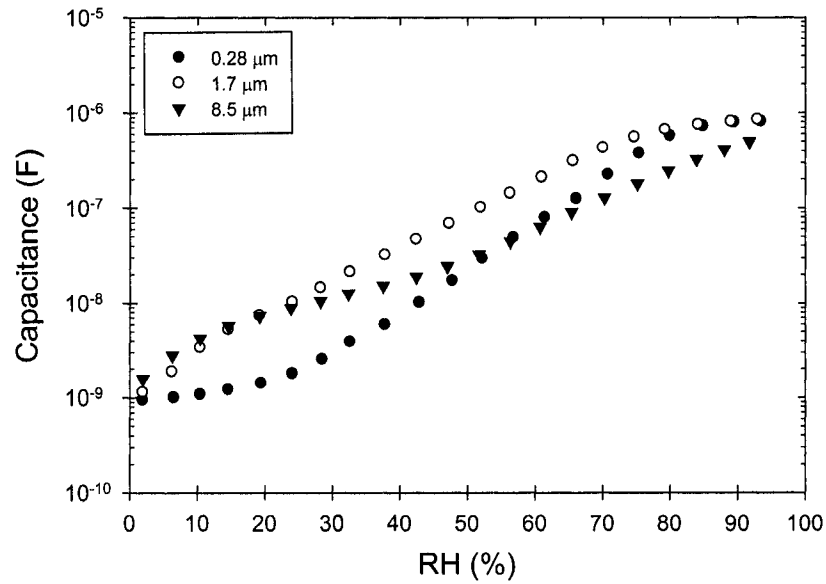
### 6.2.3 High Humidity

In the high humidity region ( $> 70\% RH$ ), the sensitivity was similar for all film thicknesses.

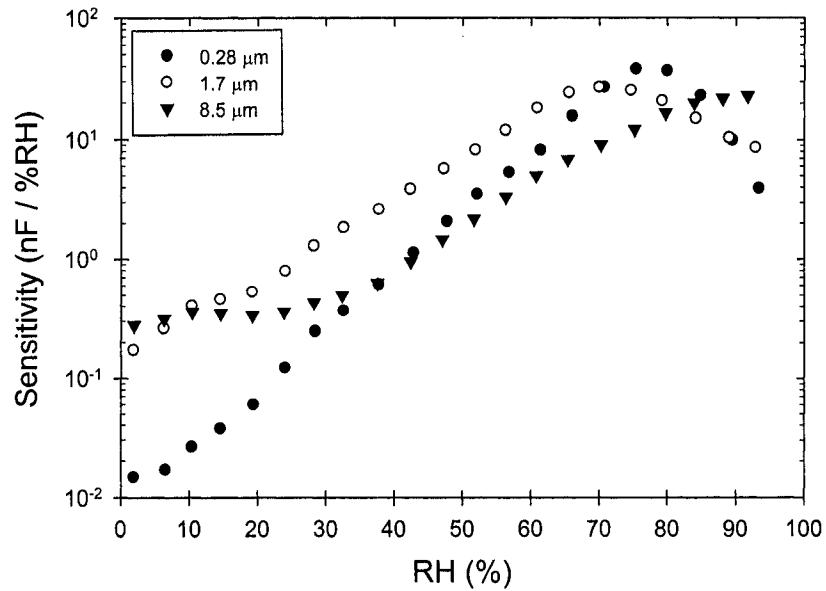
In Figure 6.14 the change in capacitance between 2–93% RH is plotted as a function of film thickness. It is apparent that the overall capacitance change is primarily a result of the first few hundred nanometres of GLAD film. Furthermore, as the film thickness is increased such that it extends past the electric field of the IDC the change in capacitance begins to diminish (recall that for IDC-100-3-5 substrates which have a digit period of  $8\ \mu\text{m}$ , 95% of the electric field is contained within  $4\ \mu\text{m}$  above the IDC surface). For these thicker films water vapour adsorption occurring near the tips of the columns which are outside the electric field will not likely result in a capacitance change and will reduce the overall change in capacitance for a given amount of adsorbed water.

### 6.2.4 Response Time

Weighted average response times were obtained using exponential fitting (Sigma-Plot) for three adsorption and three desorption response time data sets. Figure 6.15 shows the response times plotted against film thickness.  $R^2$  values for the linear fits shown in Figure 6.15 were 0.983 and 0.996 for the adsorption and desorption response time data, respectively. It is apparent that the film thickness plays a vital role in determining sensor response time. This is emphasized by observing the response times for the sensor utilizing the  $8.5\ \mu\text{m}$  thick film, which were  $1.24 \pm 0.04\ \text{s}$



(a)



(b)

**Figure 6.13.** (a) Capacitive response for IDC-100-3-5 substrates coated with TiO<sub>2</sub> films of different thickness. (b) Sensor sensitivity (capacitive response local slope) as a function of RH.

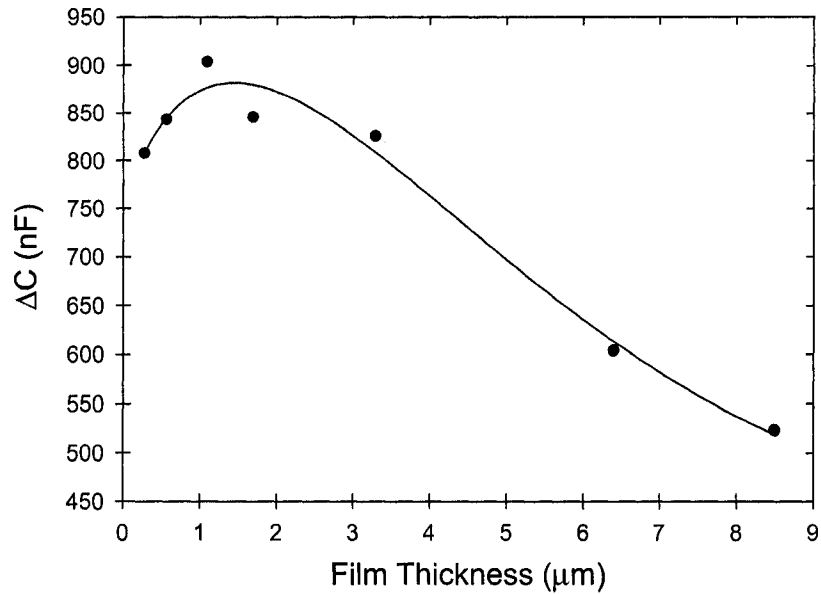


**Figure 6.14.** Change in capacitance between 2–93% RH as a function of film thickness. The line fit is a guide for the eye. This figure shows that the overall capacitance change is primarily a result of the first few hundred nanometres of GLAD film and that as the thickness of the film extends past the electric field of the IDC the change in capacitance begins to diminish.

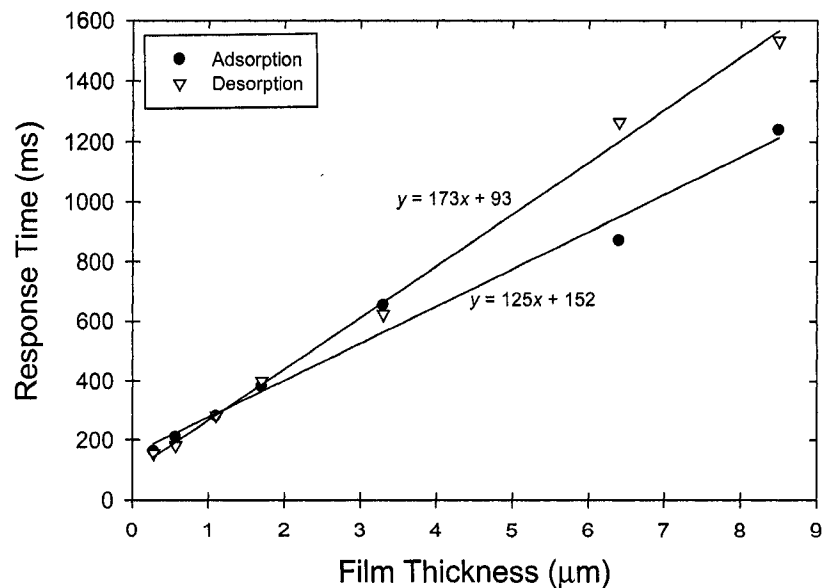


**Figure 6.15.** Weighted average response times as a function of film thickness. Linear regression  $R^2$  values were 0.983 and 0.996 for the adsorption and desorption response time data, respectively.

and  $1.53 \pm 0.02$  s for adsorption and desorption, respectively. These values are similar to those obtained from the Vaisala MultiMeterMate commercial humidity probe discussed in Chapter 4 Section 4.6, which were  $1.3 \pm 0.1$  s and  $2.5 \pm 0.1$  s for adsorption and desorption, respectively. It is likely that since the magnitude of the change in capacitance is a result of the first few hundred nanometres of film that increasing the thickness impedes water vapour access to this region of the film and therefore increases the response time.

### 6.2.5 Conclusions

The following conclusions can be drawn from the film thickness study:

1. The sensitivity can be tuned by altering film thickness.
2. The magnitude of the change in capacitance is primarily a result of the first few hundred nanometres of GLAD film.
3. The overall change in capacitance decreases as the film extends past the electric field of the IDC substrate (i.e., thickness  $\geq$  half the IDC digit period).
4. For  $\text{TiO}_2$  films deposited at  $\alpha = 81^\circ$ , a large sensitivity over the entire RH range can be obtained using films in the  $1.5 \pm 0.2 \mu\text{m}$  thickness range.
5. The response time is approximately linear with film thickness which is likely a result of impeding water vapour transfer to the initial few hundred nanometre thick sensitive layer.

## 6.3 Deposition Angle $\alpha$

It is well-known that the density/porosity of GLAD films depends on the vapour incidence angle  $\alpha$  [146]. Topographical variations due to adatom clustering and nucleation create regions of the substrate that are shadowed from the incoming vapor flux. A higher vapour incidence angle will enlarge the shadowed regions

and decrease overall film density. Inter-column pore size and growth dynamics in general are also dependent on  $\alpha$ .

To investigate the impact of  $\alpha$  on sensor performance six sensors were fabricated from IDC-25-3-5 substrates coated with 1.5  $\mu\text{m}$  thick  $\text{TiO}_2$  vertical post GLAD films. The deposition angle was different for each sensor with the following values used: 70°, 75°, 78°, 81°, 83°, and 85°. Attempts to fabricate sensors using deposition angles less than 70° were unsuccessful due to cracking and delamination of the films from internal stress. Figures 6.16 and 6.17 show cross-sectional and top down SEM images of the films used in the study, respectively.

Figure 6.18 shows the capacitive response (a) and sensitivity (b) of the sensors utilizing films grown at  $\alpha = 70^\circ, 75^\circ, 81^\circ,$  and  $85^\circ$ . The data from the  $\alpha = 78^\circ$  and  $83^\circ$  sensors were omitted for clarity. Under low humidity conditions ( $\text{RH} < \sim 20\%$ ) the sensitivity was enhanced for sensors using films deposited at lower deposition angles. This trend appears to hold true up to  $\sim 60\%$  RH, with the exception of the sensor utilizing the film grown at  $\alpha = 70^\circ$  which exhibited a reduced sensitivity. Above  $\sim 60\%$  RH the sensitivity was similar for all sensors other the  $\alpha = 70^\circ$  sensor where the relative humidity had to reach  $\sim 85\%$  before its sensitivity became similar.

The physics governing the specific shape of the capacitive response are not well understood. Although a large change in capacitance is widely reported in the literature, a fundamental understanding has not yet emerged. Further discussion on this topic will be given in Section 6.4 below.

Figure 6.19 shows the weighted average (three adsorption and three desorption measurements) response times, which were found to decrease with increasing  $\alpha$ . The influence of  $\alpha$  on response time is not nearly as strong as film thickness as even the slowest sensor ( $\alpha = 70^\circ$ ) still exhibited a  $467 \pm 3$  ms adsorption response time and a  $548 \pm 1$  ms desorption response time. It is expected that the increased response time at lower deposition angles is a result of more restricted access to the film surface due to column agglomeration and a more tortuous pore network.

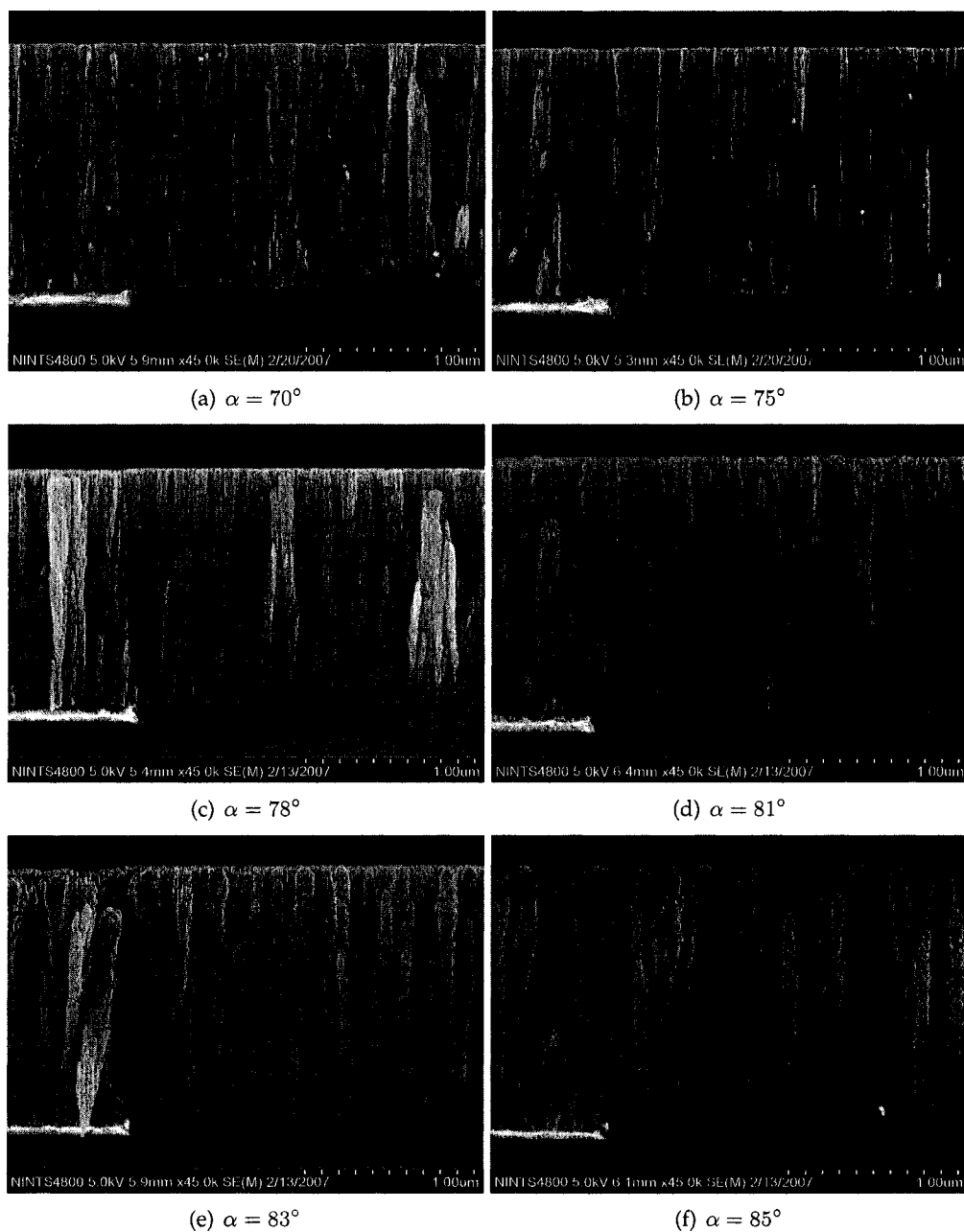


**Figure 6.16.** Cross-sectional SEM images of  $\text{TiO}_2$  films used to investigate the impact of  $\alpha$  on sensor performance. All films were deposited on IDC-25-3-5 substrates and were  $\sim 1.5 \mu\text{m}$  thick. All images were obtained using  $45,000\times$  magnification.



### 6.3. Deposition Angle $\alpha$

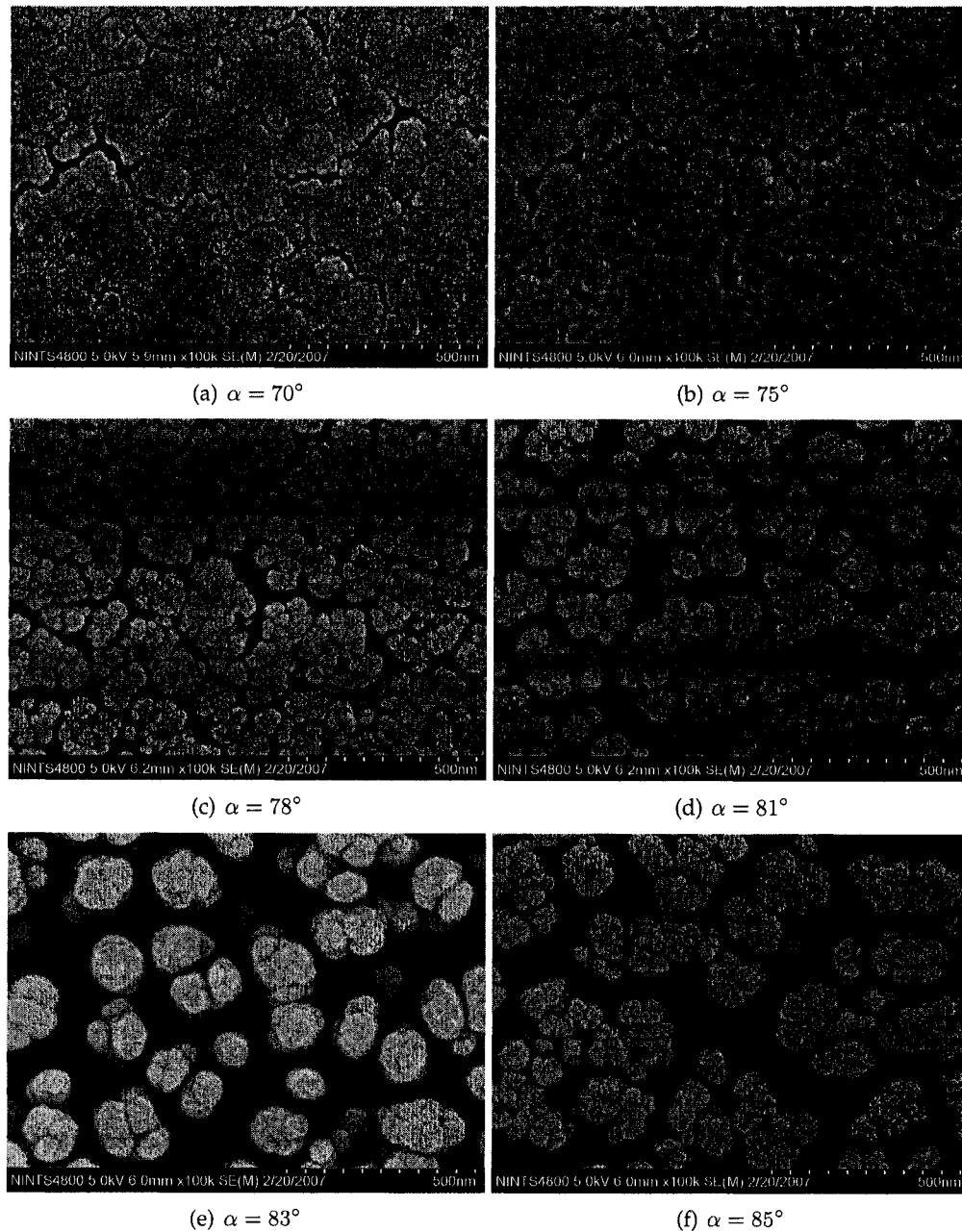
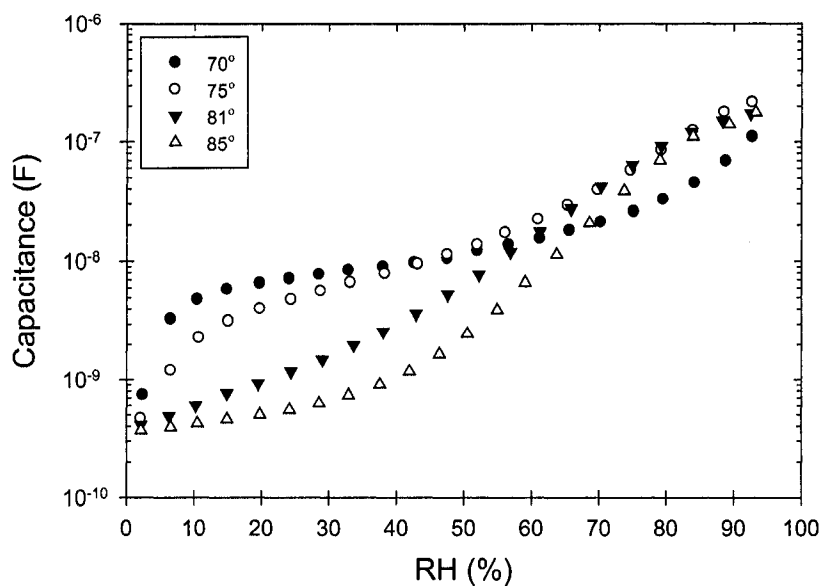
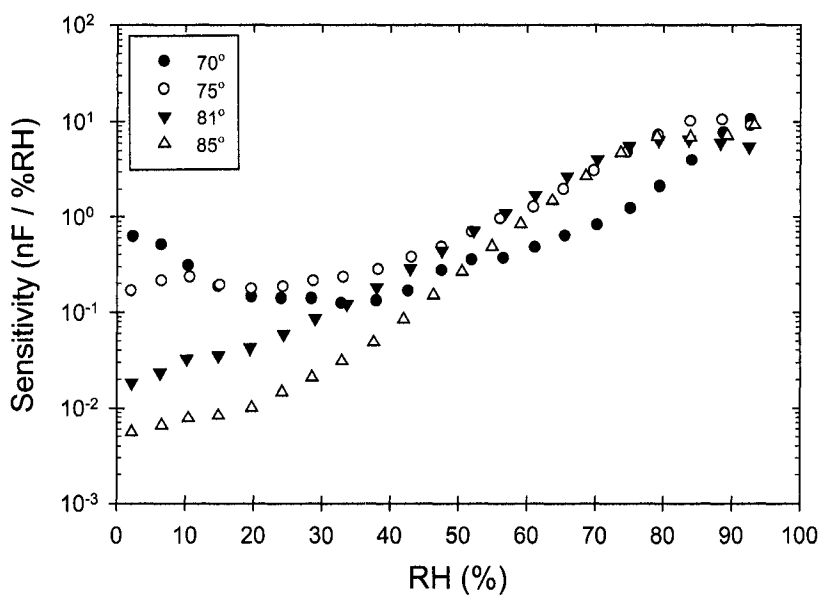


**Figure 6.17.** Top down SEM images of TiO<sub>2</sub> films used to investigate the impact of  $\alpha$  on sensor performance. All films were deposited on IDC-25-3-5 substrates and were  $\sim 1.5 \mu\text{m}$  thick. All images were obtained using  $100,000\times$  magnification.



(a)



(b)

Figure 6.18. (a) Capacitive response for IDC-25-3-5 substrates coated with 1.5 μm thick TiO<sub>2</sub> films deposited at different α. (b) Sensitivity as a function of RH.

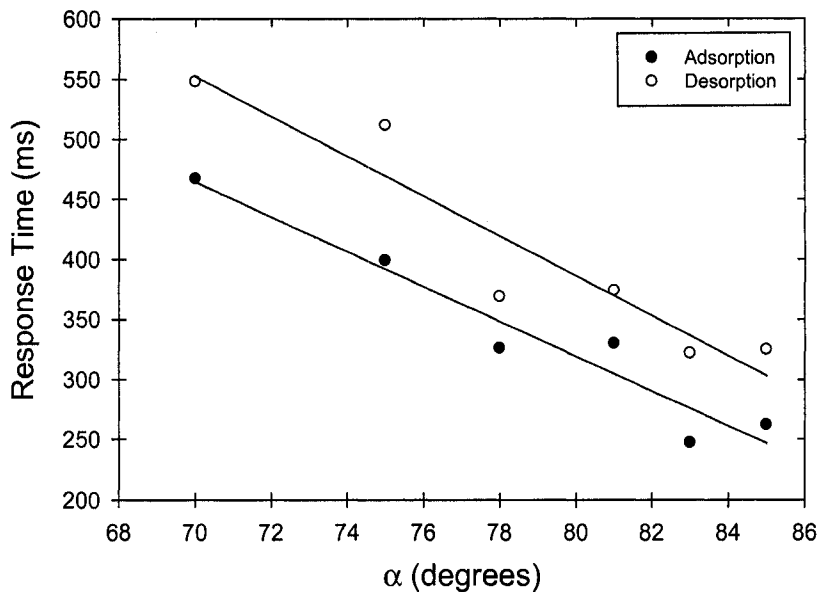


*Figure 6.19.* Weighted average response time for sensors fabricated using  $1.5 \mu\text{m}$  thick  $\text{TiO}_2$  films deposited at different  $\alpha$ . The best fit lines are a guide for the eye.

## 6.4 Discussion

It is clear from the results presented in this chapter that the device physics of capacitive humidity sensors using nanostructured porous metal oxide materials is complex. While many attempts to model the response of such sensors exist in the literature [18, 147–153], a truly fundamental understanding has not yet emerged. Orders of magnitude changes in both the capacitance and resistance are commonly reported [16, 18, 22, 28, 29, 54, 62, 122] and attributed to water vapour capillary condensing into the pores of the material [7, 22, 28, 29]. However, bulk properties of condensed water (which has a dielectric constant of roughly 80 for sub-GHz frequencies [154]) cannot account for the large changes in capacitance and resistance. Consider a humidity sensor comprised of a porous ceramic, say  $\text{TiO}_2$ , which has a dielectric constant between 86–170 (rutile) [155]. If the film porosity was 50%, then the dielectric constant (and therefore capacitance) can only increase by a factor of  $\approx 2$  as water vapour condenses and completely fills all the pores. It is apparent that

nanoscale surface interactions between the water molecules and the oxide surface play a critical role in sensor performance, a fact that is not currently discussed in the humidity sensor literature.

Morimoto et al. have measured the dielectric constant for water adsorbed on Titania (rutile) [65]. At room temperature (298 K) and a measurement frequency of 1 kHz they observed a 30 fold increase in the real component of the dielectric constant for humidity levels 0–90.5%. While this indicates an enhanced dielectric constant compared to the bulk property example given above, it is still not sufficient to explain the magnitude of the change in capacitance presented here. Furthermore, the details of the dependence of the capacitive response on composition,  $\alpha$ , and thickness are not yet understood and require a more detailed understanding of the fundamental physics on the nanometre scale.

## 6.5 Conclusions

The following conclusions can be drawn from the data presented in this chapter:

1. The composition and morphology of GLAD films have a significant impact on both the capacitive response and response time.
2. Sensors utilizing TiO<sub>2</sub> films are more sensitive than SiO<sub>2</sub> and Al<sub>2</sub>O<sub>3</sub> films.
3. The sensitivity can be tuned by altering film thickness and  $\alpha$ .
4. The overall capacitance change is primarily a result of the first few hundred nanometres of GLAD film.
5. The response time is predominantly determined by the film thickness.

In the next chapter the fabrication and characterization of an optical humidity sensor is presented and compared to capacitive based sensors.

## Chapter 7

# Optical Humidity Sensor <sup>1</sup>

In this chapter the fabrication and characterization of a GLAD titanium dioxide optical interference filter for humidity sensing is presented.

### 7.1 Introduction

Optical based humidity sensors have several advantages including immunity to electromagnetic interference, and capability of remote sensing [12]. Furthermore, they are better suited for applications where high concentrations of flammable or explosive gases are present, as electrical based sensors can act as an ignition source [157, 158]. Lee and Lee regard optical based humidity sensors as superior for low-RH applications owing to their high sensitivity under such conditions [9]. It is therefore of interest to evaluate the humidity sensitive properties of GLAD-derived optical interference coatings for sensor applications.

Optical interference filters fabricated with GLAD exploit the birefringence (linear or circular) resulting from film morphology and/or the dependence of the effective index of refraction on porosity. For example, films consisting of isolated helical columns oriented along the substrate normal exhibit a circular birefringence that

---

<sup>1</sup>This work has been published in: J.J. Steele, A.C. van Popta, M.M. Hawkeye, J.C. Sit, and M.J. Brett. Nanostructured gradient index optical filter for high-speed humidity sensing. *Sensors and Actuators B*, 120(1):213-219, December 2006. [156]

will selectively reflect either left-handed or right-handed circularly polarized light depending on the handedness of the helical columns [82].

The sensor discussed in this chapter incorporates an optical interference filter that utilizes the effective index dependence on film porosity. Periodic nanoscale porosity variations were introduced throughout the thickness of a titanium dioxide GLAD film to generate an index profile designed to yield a narrow-bandpass optical interference filter. The transmittance spectrum of the filter is sensitive to changes in humidity due to effective index changes resulting from water vapour adsorption/desorption. This design provides greater porosity and faster performance than earlier designs based on helical films [159]. The following will show that this sensor is highly sensitive, exhibits minimal hysteresis, and is extremely fast.

This work was conducted in collaboration with Andy van Popta and Matthew Hawkeye who contributed to the design, fabrication, and spectral characterization of the optical interference filter.

## 7.2 Theory

According to effective medium theory, the effective index of refraction of a medium comprised of a mixture of materials depends on the relative amounts of the constituents and the shapes of the inclusions [160]. For GLAD films, the mixture consists of film material and void (air). Also, there is a two-dimensional symmetry in the shapes of the inclusions for light at normal incidence, therefore the effective index of GLAD films is determined by film density alone [161]. A smaller deposition angle will yield a denser film with less void and a higher effective index of refraction. Conversely, a larger deposition angle will result in a film with a lower effective index of refraction. Thus, GLAD provides a means of manipulating the effective index throughout the thickness of a film through in situ adjustments of  $\alpha$

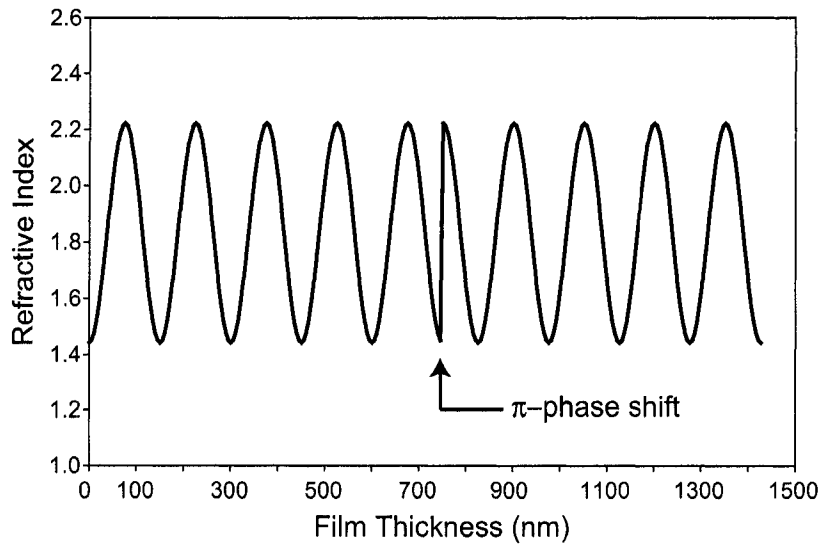


**Figure 7.1.** Refractive index profile used to obtain a narrow-bandpass optical interference filter. A  $\pi$ -phase shift is introduced after 5 periods of a 9.5 period sinusoidal oscillation of the refractive index to create the bandpass.

during deposition.

A sinusoidal variation in the refractive index of an optical medium will generate a band of frequencies in which the transmittance is strongly reduced [162,163]. The width and location of this band is dependent on the average refractive index and the period and amplitude of the index modulation. Introducing a specific defect to the index profile, such as a phase shift or a segment of constant index, produces a narrow band of frequencies within the stop band where the transmittance is substantially increased [163,164].

The GLAD technique was utilized to fabricate a porous narrow-bandpass optical interference filter for humidity sensing. The sinusoidal index profile of the filter was obtained through periodic variations of  $\alpha$  during film growth. Figure 7.1 shows the refractive index film thickness profile used for the design, where a  $\pi$ -phase shift defect is introduced after 5 periods of a 9.5 period sinusoidal index modulation to create a narrow bandpass. This design profile was used to calculate the  $\alpha$ -control algorithm used during film growth. The open pore structure and accessible surface

of the bandpass filter can interact with its environment. Adsorbed chemical species will displace the air in the pores of the film resulting in an increase of the average refractive index. However, a periodic modulation of the index will be maintained such that the bandpass will remain intact and the profile of the transmittance spectrum will not significantly degrade.

Equation 7.1 shows the dependence of the stop band centre wavelength,  $\lambda_{SB}$ , on the physical periodicity,  $\Omega$ , and the average refractive index of the film,  $n_{ave}$  [163].

$$\lambda_{SB} = 2 n_{ave} \Omega \quad (7.1)$$

For a  $\pi$ -phase shift defect the bandpass will be located near the centre of the stop band ( $\lambda_{BP} = \lambda_{SB}$ , where  $\lambda_{BP}$  is the maximum transmittance wavelength of the bandpass). Adsorption of water vapour, or other chemical species, increases the average index and red-shifts the transmittance spectrum, while desorption results in a blue-shift. This is the basis of operation for the optical humidity sensor. Selecting a hydrophilic source material to fabricate a porous narrow-bandpass optical interference filter results in a transmittance spectrum sensitive to the concentration of ambient water vapour.

### 7.3 Filter Fabrication

The bandpass interference filter consisted of a TiO<sub>2</sub> GLAD film deposited onto a Corning 7059 glass substrate. Oscillating  $\alpha$  between 30° and 80° while continuously increasing  $\phi$  at a rate of 5 RPM produced a vertical post film with nanoscale variations in post diameter. The average deposition rate was 1 nm/s. Oxygen gas was introduced during deposition to promote the formation of stoichiometric TiO<sub>2</sub> at the substrate. The oxygen flow rate was adjusted to maintain a pressure of  $5 \times 10^{-5}$  Torr. Under these growth conditions, the TiO<sub>2</sub> GLAD film will be amorphous [165].

Prior to fabrication a set of calibration films were deposited to determine the



index of refraction and the rate of film growth as a function of  $\alpha$  [166]. This information was used to calculate the  $\alpha$ -control algorithm used during the fabrication of the film in order to generate the refractive index profile shown in Figure 7.1 where the maximum and minimum effective indices of 2.22 and 1.44 correspond to deposition at  $\alpha = 30^\circ$  and  $\alpha = 80^\circ$ , respectively. A spectroscopic ellipsometer (V-VASE, J. A. Woollam Co., Inc.) and a scanning electron microscope (JSM-6301FXV, JEOL) were used to characterize the calibration films.

TiO<sub>2</sub> was chosen because it is hydrophilic, has a large bulk refractive index, and is transparent over the visible/near-IR spectrum. A large bulk index is beneficial as it results in a larger index modulation, which will produce a stop band with a larger FWHM bandwidth and a greater reflectance for a given number of index modulation periods [162]. Consequently, fewer index modulations are needed resulting in a thinner film with less internal stress and less diffuse scattering.

## 7.4 Sensor Characterization

Normal incidence transmittance spectra were obtained under varying humidity conditions using a Perkin-Elmer Lambda 900 UV/VIS/NIR spectrophotometer. To vary the humidity the bubbler system described in Chapter 4 was utilized. The humid air was delivered to the sample chamber of the spectrophotometer where the humidity was monitored with a Vaisala MultiMeterMate RH/T probe. The spectrophotometer sample chamber was sealed to prevent exposure of the internal optics to high humidity levels. To maintain atmospheric pressure a one way valve was implemented to exhaust excess gas out of the chamber.

Response time measurements were obtained using a humidity control chamber fitted with glass windows to allow light from an external laser diode (Thor Labs CPS186,  $\lambda = 668.5$  nm, 4.5 mW) to pass through the filter at normal incidence and exit the chamber where it was collected by a photodiode. The laser beam was split

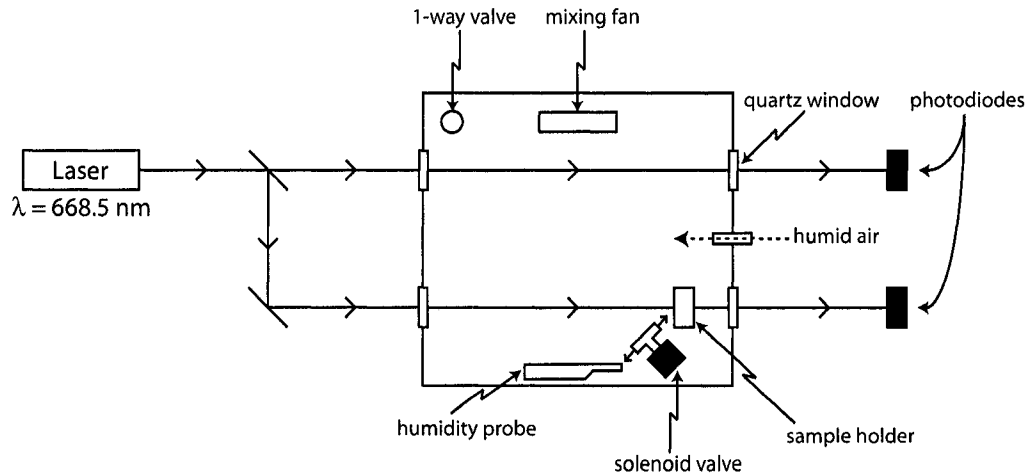


Figure 7.2. Response time setup for optical humidity sensor.

prior to entering the chamber such that one beam would pass through the filter while the other would simply pass straight through the chamber to another photodiode to monitor any fluctuations in the laser output intensity. Step-like changes in humidity were attained by electronically actuating a solenoid valve to deliver moist or dry air (from the bubbler system) to our sensor as well as a Vaisala probe for comparison. The steady-state flow of the solenoid valve was set to 28 litres per minute. Figure 7.2 illustrates the experimental setup used for response time characterization. Prior to response time measurements the filter transmittance (at the laser wavelength) as a function of relative humidity was obtained by recording the photodiode voltages under varying humidity. This data was used to translate the photodiode voltage versus time data obtained during response time measurements, to relative humidity versus time, which was used to calculate the response time. The transmittance versus relative humidity data was also used to observe sensitivity and hysteresis of the device. The transient responses of the photodiode at the filter output and the voltage signal from the Vaisala probe were recorded with a digital oscilloscope and imported to a computer for response time analysis.

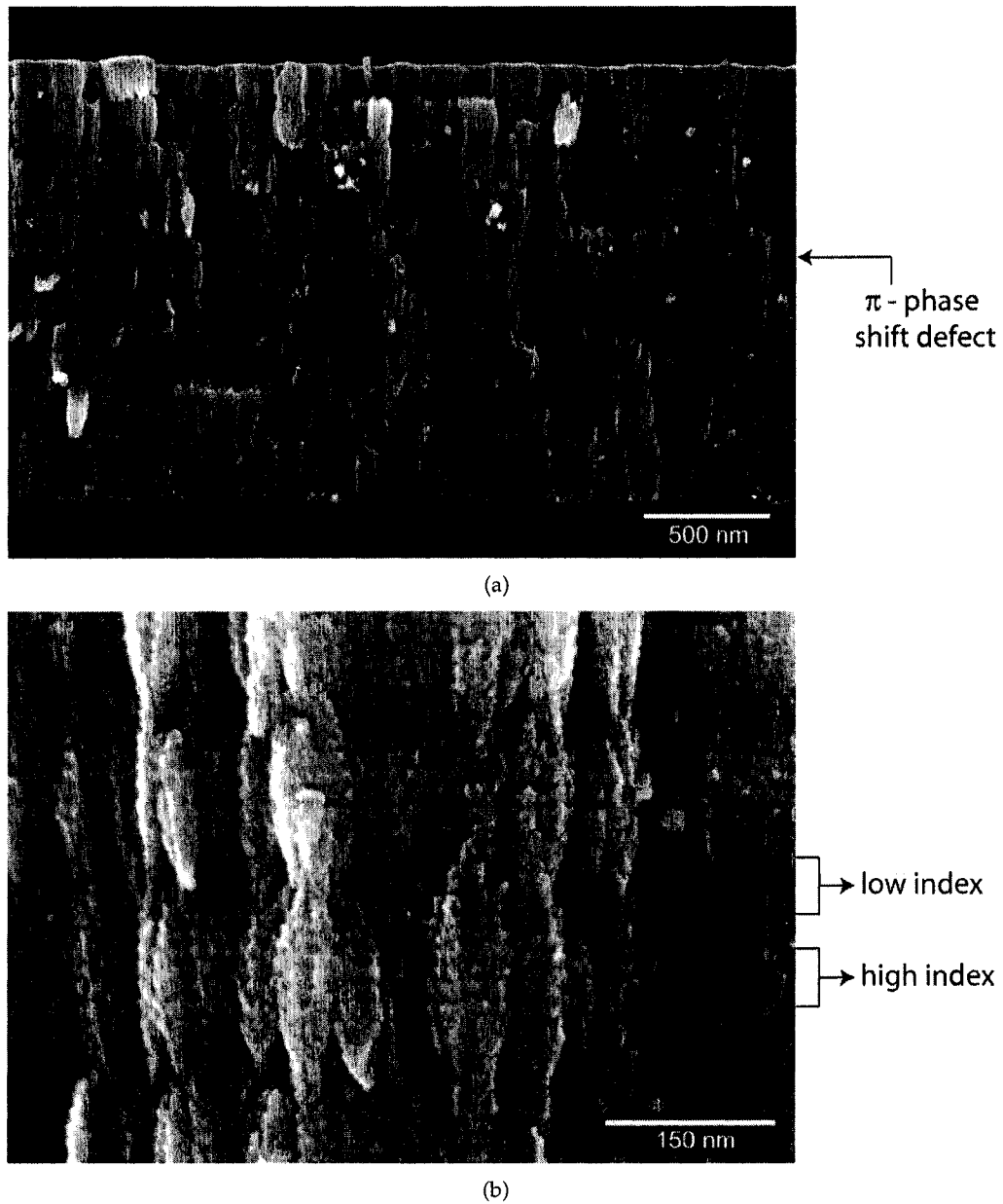
## 7.5 Results and Discussion

Figure 7.3 shows a cross-sectional SEM image of the narrow-bandpass filter. The periodic oscillation in post diameter along with the  $\pi$ -phase shift defect are clearly shown. The bright horizontal layers of the image correspond to regions of high density/index while the darker layers indicate regions of low density/index. The film thickness was measured to be 1.7  $\mu\text{m}$  with an average period thickness of  $185 \pm 10$  nm. In Figure 7.3(b) the magnification is increased showing the detailed morphology of the film and the large pores present in the low index regions.

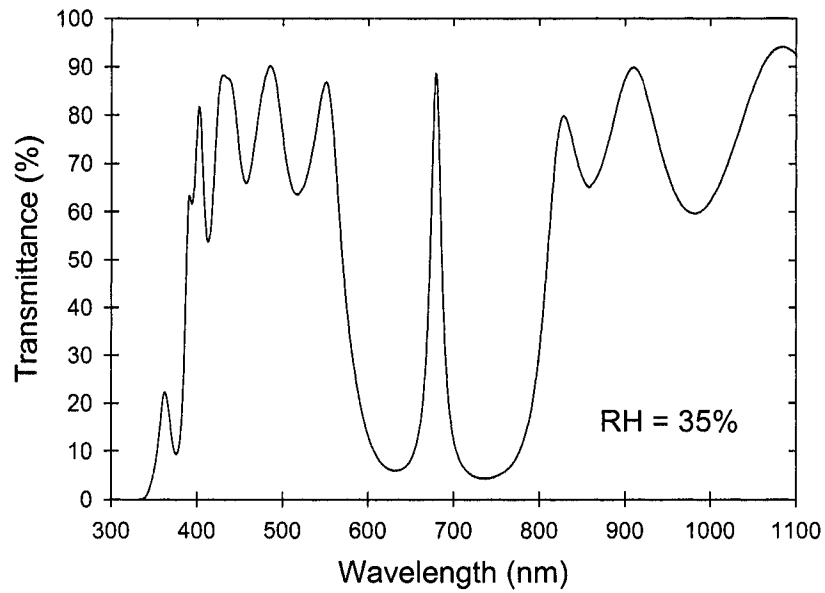
Figure 7.4(a) shows the normal incidence transmittance spectrum at 35% RH. The stop band is evident between 550 nm and 830 nm. The bandpass FWHM is 17 nm and its peak transmittance of 89% occurs at 679 nm. At shorter wavelengths, below 400 nm, the transmittance is strongly reduced due to the presence of an absorption edge of the  $\text{TiO}_2$ .

Figure 7.4(b) shows the red-shift of the bandpass at increased humidity. The bandpass shifts from 674 nm at 0.3% RH to 705 nm at 90.2% RH; an overall shift of 31 nm for a 90% change in relative humidity.

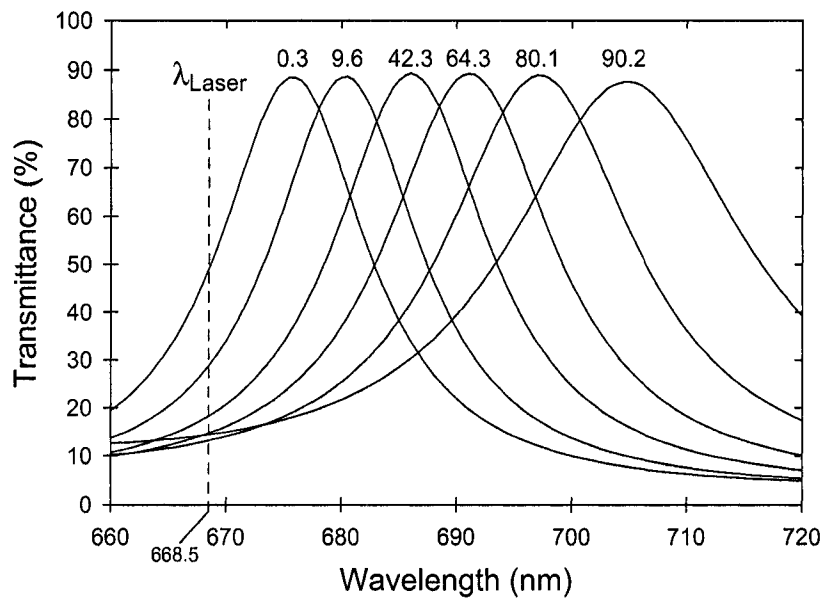
The FWHM at 90% RH is 27 nm, whereas at 0.3% RH it is 16 nm. This broadening of the bandpass at high humidity can likely be attributed to a decrease in the index modulation  $\Delta n = n_{max} - n_{min}$ , where  $n_{max}$  and  $n_{min}$  are the maximum and minimum values of the index modulation, respectively. The narrow-bandpass optical interference filter was fabricated by varying the density and therefore porosity of a titania film. High index regions of the film correspond to a dense morphology with small pores, whereas low index regions correspond to segments of the film with large pores (Figure 7.3(b)). In terms of the index profile of the filter (Figure 7.1), increasing the humidity will shift the entire profile up the refractive index axis (y-axis). At high humidity, the relative increase of  $n_{min}$  will be greater than that of  $n_{max}$  due to a greater amount of adsorbed water present in the less dense regions of the film which contain large pores. This will shift the lower index values



*Figure 7.3. Cross-sectional SEM images of narrow-bandpass filter at 40k (a) and 180k (b) magnification. The alternating bright/dark horizontal layers correspond to the regions of high/low index respectively.*



(a)



(b)

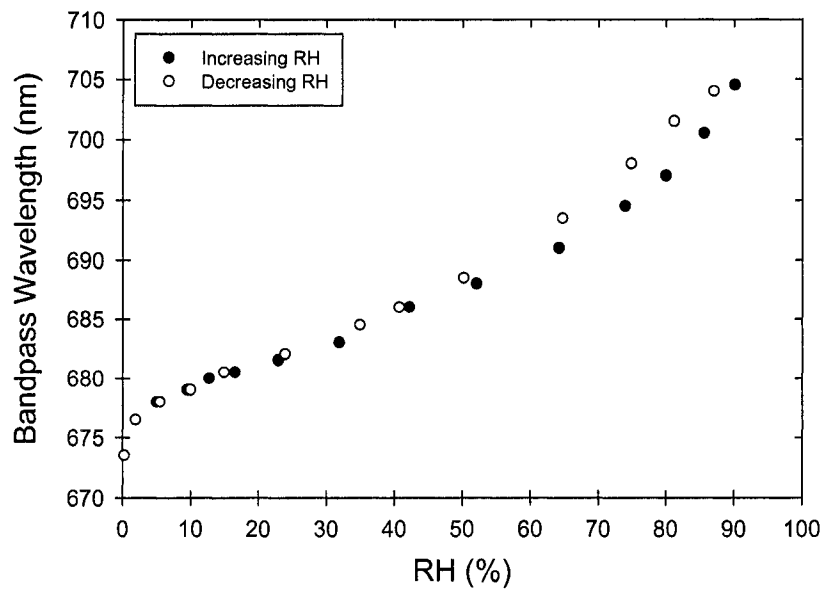
**Figure 7.4.** Normal incidence transmittance spectra of the film shown in Figure 7.3. In (a), the spectrum from 300 nm to 1100 nm is shown, revealing a bandpass located at 679 nm (peak wavelength) within the 550 nm to 830 nm stop band. In (b), the bandpass spectra obtained at different RH levels (percentages given at bandpass peaks) are shown.

of the profile towards the maximum index. The net result will be a decrease to  $\Delta n$  which will broaden the bandpass.

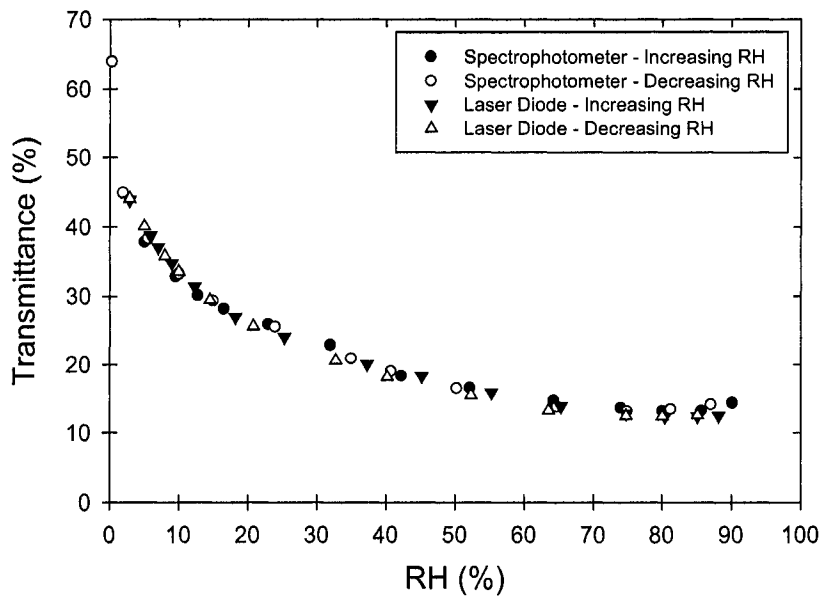
The bandpass wavelength as a function of humidity is reported in Figure 7.5(a). Hysteresis (< 8%) is evident at humidities greater than 50% RH. Below this level, the hysteresis is negligible. This data was taken during the first increasing and decreasing humidity exposure to the sensor. In Chapter 5, Section 5.2 it was shown that capacitive based humidity sensors exhibited hysteresis only during the first increasing and decreasing humidity exposure. During subsequent exposures the hysteresis was minimal. It is possible that the hysteresis observed for the optical sensor would also diminish in subsequent scans and is a topic for further study.

The transmittance data obtained from the laser diode ( $\lambda = 668.5$  nm) is reported and compared to the spectrophotometer data in Figure 7.5(b). At this wavelength a 90% change in the relative humidity results in a 51% change in transmittance. Also, there is virtually no hysteresis due to decreased sensitivity at high humidity. Figure 7.5(a) shows that hysteresis is only present above 50% RH, however, Figure 7.5(b) suggests that the sensitivity at high humidity is low enough that the difference in bandpass position for increasing and decreasing humidity does not constitute a large enough change in transmittance to be noticeable. The close agreement of the laser diode data with the spectrophotometer data shows that the setup illustrated in Figure 7.2 can accurately obtain filter transmittance data and supports its use to measure sensor response time.

Figure 7.5(b) shows that the optical sensor is highly sensitive in low to mid RH levels for 668.5 nm light. This wavelength, however, was chosen for convenience and if a different wavelength was used we would obtain a different transmittance versus relative humidity curve. The low RH sensitivity of the sensor is a result of the relative position of the laser wavelength with respect to the filter bandpass. Figure 7.4(b) shows that at 0.3% RH, 668.5 nm is to the left (lower  $\lambda$ ) of the bandpass peak and has a transmittance of about 64%. As the humidity is increased and the



(a)



(b)

Figure 7.5. (a) Bandpass location as a function of increasing and decreasing humidity. (b) Transmittance at 668.5 nm wavelength as a function of humidity obtained from the spectrophotometer and laser diode setup.

bandpass red-shifts, the transmittance at 668.5 nm strongly reduces as it traces out the left side of the narrow-bandpass. This accounts for the high sensitivity in low to mid humidity levels. As the humidity is further increased, 668.5 nm lines up near the base of the bandpass where the transmittance spectrum begins to flatten. At this point any additional red-shift to the bandpass will not change the transmittance nearly as much as a similar shift at a lower humidity. Thus, the sensitivity is reduced at high humidity.

Fortunately, this sensor architecture offers the ability to alter the performance to obtain a high sensitivity at low, mid or high RH by modifying the relative positions of the bandpass and laser wavelengths. This can be achieved by changing the laser wavelength (by selecting an appropriate laser), or the bandpass wavelength (by altering the index profile), or both. It is also possible to broaden the bandpass by decreasing the index modulation  $\Delta n$  by reducing the deposition angle range used during the fabrication of the filter (oscillating  $\alpha$  between  $60^\circ$  and  $80^\circ$  as opposed to  $30^\circ$  and  $80^\circ$  for example), or by using fewer index periods to fabricate the filter, or by selecting a different source material with a lower bulk index than  $\text{TiO}_2$ .

The adsorption and desorption response time curves for the optical sensor (solid line) and the Vaisala probe (broken line) are shown in Figure 7.6. Response times were calculated from exponential best fits provided from SigmaPlot version 10.0. The adsorption response times corresponding to a 58% RH change from 13% RH to 71% RH were  $315 \pm 35$  ms and  $2.27 \pm 0.16$  s for the optical sensor and Vaisala probe, respectively. Desorption response times for a 54% RH change from 71% RH to 17% RH were  $196 \pm 12$  ms for the optical sensor and  $2.86 \pm 0.19$  s for the Vaisala probe.

The response times of the optical sensor are similar to those obtained from capacitive sensors using  $\text{TiO}_2$  films of a similar thickness ( $1.7 \mu\text{m}$ ) when extrinsic response times due to the gas delivery system are taken into account (recall that the capacitive sensor response time measurements include a 90 ms extrinsic component for a 2.5 LPM flow rate). The extrinsic response time for the optical sensor



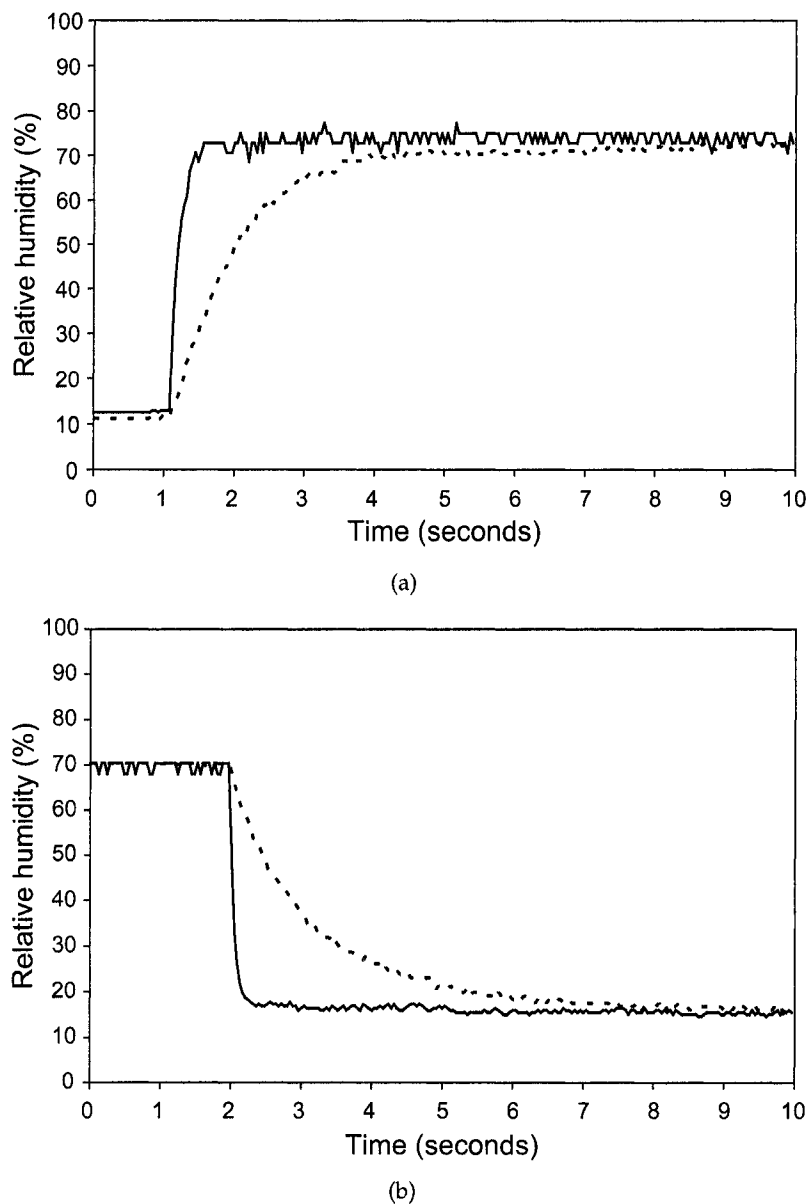


**Figure 7.6.** Adsorption (a) and desorption (b) response time data for the GLAD produced optical humidity sensor (solid line) and the Vaisala MultiMeterMate RHT probe (broken line). The humidity changed from 13% RH to 71% RH for adsorption and 71% RH to 17% RH for desorption. Response times were calculated from exponential best fits provided from SigmaPlot. For the optical sensor they were  $315 \pm 35$  ms and  $196 \pm 12$  ms for adsorption and desorption, respectively. The Vaisala probe adsorption response time was calculated to be  $2.27 \pm 0.16$  s, while desorption was  $2.86 \pm 0.19$  s.

setup was not evaluated, however, since a flow rate of 28 LPM was used it is expected that the values reported here are close to the intrinsic response times of the sensor.

## 7.6 Conclusions

The optical sensor reported in this chapter exploited spectral shifts of a porous narrow-bandpass interference filter under varying humidity conditions. A 31 nm bandpass wavelength shift was observed for a 90% change in relative humidity. At the laser diode wavelength (668.5 nm) this shift produces a transmittance change of 51%. Although this is a substantial improvement over other humidity sensors based on optical spectra shifts [12], the capacitive sensors previously reported in this thesis provide a much larger 3 orders of magnitude capacitance change. The adsorption and desorption response times were similar to those obtained from capacitive sensors using similar thickness films and were measured to be  $315 \pm 35$  ms for adsorption and  $196 \pm 12$  ms for desorption.

The optical sensor offers a high degree of control over the sensitivity through probe wavelength selection and spectral tuning. Other advantages include immunity to electromagnetic interference, capability of remote sensing, and amenability to applications where high concentrations of flammable or explosive gases are present.

## Chapter 8

# Conclusions and Future Work

### 8.1 Summary of Results

Capacitive based humidity sensors were fabricated by coating interdigitated capacitor substrates with nanostructured metal oxide thin films deposited by glancing angle deposition. Optimal performance in terms of response time, sensitivity, and operational humidity range was obtained for  $1.5 \pm 0.2 \mu\text{m}$  thick  $\text{TiO}_2$  films deposited at  $\alpha = 80^\circ \pm 2^\circ$  onto CSE-IDCs with  $\mu\text{m}$  range electrode periods (6  $\mu\text{m}$  period was smallest studied), and  $100 \text{ mm}^2$  areas (area limited by desired size of end product). These sensors exhibited a near exponential increase in capacitance from  $\sim 1 \text{ nF}$  to  $\sim 1 \mu\text{F}$  over the entire relative humidity range, and had response times on the order of 400 ms. Significant hysteresis in the capacitive response was present when the sensors were first exposed to an increasing and decreasing humidity cycle. Subsequent cycles revealed a highly repeatable capacitive response with minimal hysteresis.

Ageing studies revealed that after only one day the capacitive response was noticeably different. Further ageing continually degraded the response and diminished the sensitivity. Attempts to regenerate the capacitive response by heating the sensors revealed that a  $400^\circ\text{C}$ , 1 hour treatment was most effective. However, this

treatment was unable to completely restore the capacitive response to an as deposited state, which may be a result of crystallization of the films as identified by XRD patterns.

The geometry of the underlying IDC substrates was found to have a significant impact on the sensitivity of the sensors. Reducing the electrode period (width + spacing) as well as increasing the planar area of the IDC enhanced the sensitivity while the overall shape of the capacitive response curve remained unaffected.

Sensors fabricated from TiO<sub>2</sub> GLAD films were found to be the most sensitive in comparison to similarly fabricated sensors utilizing SiO<sub>2</sub> and Al<sub>2</sub>O<sub>3</sub> films. The response times were also affected with Al<sub>2</sub>O<sub>3</sub> being the fastest (200 ms range) followed by SiO<sub>2</sub> (300 ms range) then TiO<sub>2</sub> (400 ms range). It is expected that both surface chemistry and morphological differences were responsible for the trends observed.

The thickness of the GLAD films had a significant impact on both the capacitive response and response time of the sensors. The overall capacitance change of the sensors and the high humidity sensitivity was found to be a result of the first few hundred nanometres of film. The response time was discovered to be predominantly determined by the film thickness and ranged from a couple hundred milliseconds to over one second for TiO<sub>2</sub> films 0.28–8.5 μm thick.

The deposition angle  $\alpha$  also impacted the capacitive response and response time. Low to mid humidity sensitivity was found to increase for sensors using films deposited at lower  $\alpha$ . High humidity sensitivity was similar for all deposition angles. The response time decreased in a linear fashion with increasing  $\alpha$  over the range of 70–85°. Sensors utilizing films deposited at  $\alpha = 70^\circ$  were roughly two times slower than those using films deposited at  $\alpha = 85^\circ$ .

An optical humidity sensor was fabricated from a TiO<sub>2</sub> film with periodic nanoscale porosity variations designed to yield a narrow-bandpass optical interference filter. The transmittance spectrum of the filter shifted by 31 nm for a 90% change in

relative humidity. The adsorption and desorption response times were measured to be  $315 \pm 35$  ms and  $196 \pm 12$  ms, respectively, which is similar to the capacitive based sensors using films of similar thickness. In comparison to the capacitive based sensors the optical sensor offers the advantages of immunity to electromagnetic interference, capability of remote sensing, and amenability to sensing in flammable or explosive environments.

## **8.2 Contributions to the Field**

- A rigorous humidity sensor characterization methodology was developed. This is a significant contribution as poor practices are often observed in the humidity sensor literature. For example, breathing onto room temperature sensors is frequently used to evaluate sensor response time, which is flawed as human breath ( $\sim 37^\circ\text{C}$ ) will condense on the cooler sensor surface forming liquid water as well as introducing a variety of organic vapours and other forms of contamination from human breath. It is also common for publications to lack critical experimental information such as the frequency and circuit model used to measure capacitance/impedance as well as measurement errors.
- A thorough investigation of the performance of GLAD produced humidity sensors was performed. Several parameters and film properties which alter the performance were identified including material composition, deposition angle, film thickness, IDC geometry and the frequency of capacitance measurements.
- An optimal GLAD film for electrical based humidity sensing was discovered out of  $\text{TiO}_2$ ,  $\text{SiO}_2$ , and  $\text{Al}_2\text{O}_3$  films.
- The magnitude of the change in capacitance was shown to be a result of the

first few hundred nanometres of GLAD film.

- The sensor response time was shown to be dependant on film properties such as composition and morphology, but predominantly determined by film thickness.
- This research revealed that hysteresis was present in GLAD produced capacitive humidity sensors during the initial exposure to high humidity conditions, and that for subsequent exposures hysteresis was minimal. Several studies were identified which suggest that this is likely a result of incomplete surface hydroxylation prior to the first exposure.
- Issues with sensor ageing were identified and a heat treatment to partially restore the capacitive response was developed.
- An optical based humidity sensor that exhibited a similar high speed response as capacitive based sensors was developed. This device presents several advantages over electrical based sensors and offers a high degree of control over the sensitivity through probe wavelength selection and spectral tuning.
- The data presented in this thesis will be a strong set of test cases for future development of device physics models. This is a considerable contribution as there is a lack of understanding from a fundamental perspective of the physics governing the many orders of magnitude change in capacitance and resistance. This work provides further insight into the physics governing the response from electrical based humidity sensors utilizing porous ceramic materials.

## 8.3 Proposed Future Work

### 8.3.1 Ageing

Research on the degradation of the capacitive response with time and possible regeneration methods is of prime importance. These sensors offer several advantages and have commercialization potential. However, unless the capacitive response can be stabilized, any such thoughts must be put to rest. Ageing in controlled environments, infrared spectroscopy and other surface spectroscopic techniques may be able to identify the source of contamination. Oxygen plasma and chemical cleaning treatments should be investigated as a possible means of regeneration.

### 8.3.2 Modeling

Understanding the physics governing sensor performance would be a major contribution to the field. Impedance/dielectric spectroscopy measurements of the sensors would be instrumental towards meeting this goal. The capacitive response is strongly dependent on the measurement frequency and so far only three frequencies (0.1, 1.0, 10 kHz) have been utilized.

### 8.3.3 Porosimetry Measurements

Porosimetry data on the surface area and pore size distribution of GLAD films would be valuable for sensor characterization and understanding device physics. However, obtaining such data is not a trivial task for thin films due to their relatively low cumulative surface area for small samples. For example, nitrogen gas adsorption isotherms typically require at least  $\sim 0.5 \text{ m}^2$  surface area. Krypton is frequently used for low surface area measurements, however, obtaining pore size distributions is problematic as the physical state of Krypton is not well understood at temperatures below its triple point, 115 K, and measurements are typically obtained at 77 K.

### 8.3.4 Device Fabrication

The research presented in this thesis has identified multiply avenues for the development of extremely high sensitivity devices with a linear response over the entire RH range. The use of multiple sensors on a single chip each fabricated using GLAD films of different  $\alpha$ , thickness, and material in addition to using multiple test frequencies could lead to the development of such a device. Part of this work would also include the development of a stringent fabrication protocol to achieve a high degree of interchangeability. Ideally the film deposition process would be automated and IDC cleaning procedures and quality tests developed.

### 8.3.5 Response Time

Further investigation into response time mechanisms are required. Film growth simulations coupled with porosimetry data and gas diffusion models may be an appropriate starting point.

### 8.3.6 Sensing Material

The chemical and physical properties of metal oxides which effect sensor performance could be investigated using, for example, porosimetry, surface spectroscopy, and gas adsorption calorimetry. This may lead to the identification of materials more sensitive than those already investigated and will aid in the understanding of device physics and development of sensor models.

### 8.3.7 Hysteresis

Discovering the cause of capacitive response hysteresis during initial exposure to an increasing and decreasing humidity cycle is desired. Cyclic gas adsorption isotherms using several degassing pretreatments coupled with vibrational spectroscopy could provide insight into the hysteresis mechanism.



# References

- [1] F. Rouquerol, J. Rouquerol, and K. Sing. *Adsorption by Powders and Porous Solids*. Academic Press, San Diego, CA, 1999.
- [2] Bice Fubini, Vera Bolis, Michael Bailes, and Frank S. Stone. The reactivity of oxides with water vapor. *Solid State Ionics*, 32-33:258–272, 1989.
- [3] Lewis Greenspan. Humidity fixed points of binary saturated aqueous solutions. *Journal of Research of the National Bureau of Standards - A*, 81A(1):89–96, January-February 1977.
- [4] Martin O. Jensen. *Photonic crystal engineering in glancing angle deposition thin films*. PhD thesis, University of Alberta, Edmonton, Alberta, Canada, 2005.
- [5] P. R. Wiederhold. *Water Vapor Measurement*. Marcel Dekker, New York, NY, 1997.
- [6] Ralph Fenner and Edward Zdankiewicz. Micromachined water vapor sensors: a review of sensing technologies. *IEEE Sensors Journal*, 1(4):309–317, December 2001.
- [7] Z. M. Rittersma. Recent achievements in miniaturised humidity sensors—a review of transduction techniques. *Sensors and Actuators A, Physical*, 96(2-3):196–210, February 2002.
- [8] N. Yamazoe and Y. Shimizu. Humidity sensors: principles and applications. *Sensors and Actuators*, 10:379–398, 1986.
- [9] Chia-Yen Lee and Gwo-Bin Lee. Humidity sensors: a review. *Sensor Letters*, 3:1–15, 2005.
- [10] G. Gerlach and K. Sager. A piezoresistive humidity sensor. *Sensors and Actuators A*, 43:181–184, 1994.
- [11] Francisco J. Arregui, Zuri Ciaurriz, Maria Oneca, and Ignacio R. Matias. An experimental study about hydrogels for the fabrication of optical fiber humidity sensors. *Sensors and Actuators B*, 96(1-2):165–172, November 2003.
- [12] Teck L. Yeo, Tong Sun, Kenneth T. V. Grattan, David Parry, Rob Lade, and Brian D. Powell. Polymer-coated fiber Bragg grating for relative humidity sensing. *IEEE Sensors Journal*, 5(5):1082–1089, October 2005.

- 
- [13] Francisco J. Arregui, Yanjing Liu, Ignacio R. Matias, and Richard O. Claus. Optical fiber humidity sensor using a nano FabryPerot cavity formed by the ionic self-assembly method. *Sensors and Actuators B*, 59:54–59, 1999.
- [14] M. N. Weiss, R. Srivastava, and H. Groger. Experimental investigation of a surface plasmon-based integrated-optic humidity sensor. *Electronics Letters*, 32(9):842–843, 1996.
- [15] Y. Sadakao, M. Matsugushi, and Y. Sakai. Optical-fibre and quartz type gas sensors: humidity detection by nafion film with crystal violet and related compounds. *Sensors and Actuators A*, 25-27:489–492, 1991.
- [16] Enrico Traversa. Ceramic sensors for humidity detection: the state-of-the-art and future developments. *Sensors and Actuators B*, 23:135–156, 1995.
- [17] Zhi Chen and Chi Lu. Humidity sensors: a review of materials and mechanisms. *Sensor Letters*, 3:274–295, 2005.
- [18] William J. Fleming. A physical understanding of solid state humidity sensors. *Society of Automotive Engineers Transactions Section 2*, 90:1656–1667, 1981.
- [19] Bernard M. Kulwicki. Humidity sensors. *Journal of the American Ceramic Society*, 74(4):697–708, April 1991.
- [20] Y. Sakai, Y. Sadaoka, and M. Matsuguchi. Humidity sensors based on polymer thin films. *Sensors and Actuators B*, 35:85–90, 1996.
- [21] M. Matsuguchi, S. Umeda, Y. Sadaoka, and Y. Sakai. Characterization of polymers for a capacitive-type humidity sensor based on water sorption behaviour. *Sensors and Actuators B*, 49:179–185, 1998.
- [22] Hiromichi Arai and Tetsuro Seiyama. *Humidity Sensors*, volume 3, chapter 20, pages 981–1012. VCH, 1992.
- [23] Andrea Bearzotti, Alessandra Bianco, Giampiero Montesperelli, and Enrico Traversa. Humidity sensitivity of sputtered TiO<sub>2</sub> thin films. *Sensors and Actuators B*, 19(1-3):525–528, April 1994.
- [24] Mikko Björkqvist, Jarno Salonen, and Ensio Laine. Humidity behavior of thermally carbonized porous silicon. *Applied Surface Science*, 222(1-4):269–274, January 2004.
- [25] E. J. Connolly, G. M. O’Halloran, H. T. M. Pham, P. M. Sarro, and P. J. French. Comparison of porous silicon, porous polysilicon and porous silicon carbide as materials for humidity sensing applications. *Sensors and Actuators A*, 99(1-2):25–30, April 2002.
- [26] Razat Nohria, Rajneek K. Khillan, Yi Su, Rohit Dikshit, Yuri Lvov, and Kody Varahramyan. Humidity sensor based on ultrathin polyaniline film deposited using layer-by-layer nano-assembly. *Sensors and Actuators B*, 114(1):218–222, March 2006.

- [27] Y. Y. Qiu, C. Azeredo-Leme, L. Alcacer, and J. E. Franca. Characterization of a CMOS humidity sensor using different polyimides as sensing films. *Proceedings of SPIE*, 4591:310–315, 2001.
- [28] Wenmin Qu and Jörg-Uwe Meyer. A novel thick-film ceramic humidity sensor. *Sensors and Actuators B*, 40:175–182, 1997.
- [29] Oomman K. Varghese, Dawei Gong, Maggie Paulose, Keat G. Ong, Craig A. Grimes, and Elizabeth C. Dickey. Highly ordered nanoporous alumina films: effect of pore size and uniformity on sensing performance. *Journal of Materials Research*, 17(5):1162–1171, May 2002.
- [30] Wensheng Wang and Anil V. Virkar. A conductimetric humidity sensor based on proton conducting perovskite oxides. *Sensors and Actuators B*, 98(2-3):282–290, March 2004.
- [31] Adrian M. Kummer and Andreas Hierlemann. Configurable electrodes for capacitive-type sensors and chemical sensors. *IEEE Sensors Journal*, 6(1):3–10, February 2006.
- [32] Peter van Gerwen, Wim Laureyn, Wim Laureys, Guido Huyberegts, Maaike Op De Beeck, Kris Baert, Jan Suls, Willy Sansen, P. Jacobs, Lou Hermans, and Robert Mertens. Nanoscaled interdigitated electrode arrays for biochemical sensors. *Sensors and Actuators B*, 49(1-2):73–80, June 1998.
- [33] Bozhi Yang, Burak Aksak, Qiao Lin, and Metin Sitti. Compliant and low-cost humidity nanosensors using nanoporous polymer membranes. *Sensors and Actuators B*, 114(1):254–262, March 2006.
- [34] Uksong Kang and Kensall D. Wise. A high-speed capacitive humidity sensor with on-chip thermal reset. *IEEE Transactions on Electron Devices*, 47(4):702–710, April 2000.
- [35] Céline Laville and Claude Pellet. Interdigitated humidity sensors for a portable clinical microsystem. *IEEE Transactions on Biomedical Engineering*, 49(10):1162–1167, October 2002.
- [36] Céline Laville and Claude Pellet. Comparison of three humidity sensors for a pulmonary function diagnosis microsystem. *IEEE Sensors Journal*, 2(2):96–101, April 2002.
- [37] Angie Tételin, Vincent Pouget, Jean-Luc Lachaud, and Claude Pellet. Dynamic behavior of a chemical sensor for humidity level measurement in human breath. *IEEE Transactions on Instrumentation and Measurement*, 53(4):1262–1267, August 2004.
- [38] A. Tételin, C. Pellet, C. Laville, and G. N’Kaoua. Fast response humidity sensor for a medical microsystem. *Sensors and Actuators B*, 91:211–218, 2003.

- [39] Anton F. P. van Putten, Michael J. A. M. van Putten, Maurice H. P. M. van Putten, and Pascal F. A. M. van Putten. Multisensor microsystem for pulmonary function diagnostics. *IEEE Sensors Journal*, 2(6):636–643, December 2002.
- [40] Tsuneo Tatara and Koichi Tsuzaki. An apnea monitor using a rapid-response hygrometer. *Journal of Clinical Monitoring*, 13(1):5–9, January 1997.
- [41] H. B. Valman, B. M. Wright, and C. Lawrence. Measurement of respiratory rate in the newborn. *British Medical Journal*, 286:1783–1784, June 1983.
- [42] A. Kaan Kalkan, Matthew R. Henry, Handong Li, Joseph D. Cuiffi, Daniel J. Hayes, Charles Palmer, and Stephen J. Fonash. Biomedical/analytical applications of deposited nanostructured Si films. *Nanotechnology*, 16:1383–1391, 2005.
- [43] Peter H. Breen. Fast response humidity and temperature sensor device. U.S. Patent 6 014 890, January 18, 2000.
- [44] Paul L. Kebabian, Charles E. Kolb, and Andrew Freedman. Spectroscopic water vapor sensor for rapid response measurements of humidity in the troposphere. *Journal of Geophysical Research*, 107(D23):4670, 2002.
- [45] T. Seiyama, N. Yamazoe, and H. Arai. Ceramic humidity sensors. *Sensors and Actuators*, 4:85–96, 1983.
- [46] Shawn M. Briglin and Nathan S. Lewis. Characterization of temporal response profile of carbon black-polymer composite detectors to volatile organic vapors. *The Journal of Physical Chemistry B*, 107(40):11031–11042, 2003.
- [47] Petr Kuban, Jordan M. Berg, and Purnendu K. Dasgupta. Durable microfabricated high-speed humidity sensors. *Analytical Chemistry*, 76(9):2561–2567, May 2004.
- [48] J. P. Lukaszewicz. Controlling of surface and humidity detecting properties of carbon films – selection of a precursor for carbonization. *Thin Solid Films*, 391:270–274, 2001.
- [49] Trupti Maddanimath, I. S. Mulla, S. R. Sainkar, K. Vijayamohan, K. I. Shaikh, A. S. Patil, and S. P. Vernekar. Humidity sensing properties of surface functionalised polyethylene and polypropylene films. *Sensors and Actuators B*, 81:141–151, 2002.
- [50] James G. Fagan and Vasantha R. W. Amarakoon. Humidity sensors. *American Ceramic Society Bulletin*, 72(3):119–130, March 1993.
- [51] Brian Dick and Michael J. Brett. *Nanofabrication by glancing angle deposition*, volume 6 of *Encyclopedia of Nanoscience and Nanotechnology*, page 703. American Scientific Publishers, Stevenson Ranch, CA, 2004.

- [52] Kevin Robbie and Michael J. Brett. Method of depositing shadow sculpted thin films. U.S. Patent 5 866 204, February 2, 1999.
- [53] Kenneth D. Harris, Albert Huizinga, and Michael J. Brett. High-speed porous thin film humidity sensors. *Electrochemical and Solid-State Letters*, 5(11):H27–H29, 2002.
- [54] A. Kaan Kalkan, Handong Li, Christopher J. O'Brien, and Stephen J. Fonash. A rapid-response, high-sensitivity nanophase humidity sensor for respiratory monitoring. *IEEE Electron Device Letters*, 25(8):526–528, August 2004.
- [55] A. Kaan Kalkan, Sanghoon Bae, Handong Li, Daniel J. Hayes, and Stephen J. Fonash. Nanocrystalline Si thin films with arrayed void-column network deposited by high density plasma. *Journal of Applied Physics*, 88(1):555–561, July 2000.
- [56] V. E. Henrich and P. A. Cox. *The Surface Science of Metal Oxides*. Cambridge University Press, Cambridge, England, 1994.
- [57] Martin S. Silberberg. *Principles of General Chemistry*. McGraw-Hill, New York, NY, 2007.
- [58] Tetsuo Morimoto, Mahiko Nagao, and Fujiko Tokuda. Relation between the amounts of chemisorbed and physisorbed water on metal oxides. *Journal of Physical Chemistry*, 73(1):243–248, 1969.
- [59] Michael A. Henderson. The interaction of water with solid surfaces: fundamental aspects revisited. *Surface Science Reports*, 46:1–308, 2002.
- [60] Hind A. Al-Abadleh and V. H. Grassian. FT-IR study of water adsorption on aluminum oxide surfaces. *Langmuir*, 19(2):341–347, 2003.
- [61] Qiang Fu, Thomas Wagner, and Manfred Rühle. Hydroxylated  $\alpha$ -Al<sub>2</sub>O<sub>3</sub> (0 0 0 1) surfaces and metal/ $\alpha$ -Al<sub>2</sub>O<sub>3</sub> (0 0 0 1) interfaces. *Surface Science*, 600(21):4870–4877, November 2006.
- [62] V. K. Khanna and R. K. Nahar. Surface conduction mechanisms and the electrical properties of Al<sub>2</sub>O<sub>3</sub> humidity sensor. *Applied Surface Science*, 28(3):247–264, May-June 1987.
- [63] Gorur G. Raju. *Dielectrics in Electric Fields*. Marcel Dekker, New York, NY, 2003.
- [64] Vera V. Daniel. *Dielectric Relaxation*. Academic Press, New York, NY, 1967.
- [65] Tetsuo Morimoto and Tohru Iwaki. Dielectric behaviour of adsorbed water part 1 — measurement at room temperature on TiO<sub>2</sub>. *Journal of the Chemical Society. Faraday transactions I*, 83:943–956, 1987.

- [66] Tohru Iwaki and Tetsuo Morimoto. Dielectric behaviour of adsorbed water part 2 — measurement at low temperatures on TiO<sub>2</sub>. *Journal of the Chemical Society. Faraday transactions I*, 83:957–966, 1987.
- [67] Tohru Iwaki and Tetsuo Morimoto. Dielectric behavior of adsorbed water. 3. Measurement at room temperature on ZnO. *Langmuir*, 3:282–287, 1987.
- [68] Tohru Iwaki and Tetsuo Morimoto. Dielectric behavior of adsorbed water. 4. Measurement at low temperatures on ZnO. *Langmuir*, 3:287–290, 1987.
- [69] Rika Kuwabara, Tohru Iwaki, and Tetsuo Morimoto. Dielectric behavior of adsorbed water. 5. Measurement at room temperature on  $\alpha$ -Fe<sub>2</sub>O<sub>3</sub>. *Langmuir*, 3:1059–1062, 1987.
- [70] Seiichi Kondo, Masa aki Muroya, Hirofumi Fujiwara, and Noboru Yamaguchi. The dielectric relaxation of  $\alpha$ -alumina. *Bulletin of the Chemical Society of Japan*, 46(5):1362–1365, 1973.
- [71] E. McCafferty, V. Pravdic, and A. C. Zettlemoyer. Dielectric behaviour of adsorbed water films on the  $\alpha$ -Fe<sub>2</sub>O<sub>3</sub> surface. *Transactions of the Faraday Society*, 66:1720–1731, 1970.
- [72] John J. Steele and Michael J. Brett. Nanostructure engineering in porous columnar thin films: recent advances. *Journal of Materials Science: Materials in Electronics*, 18(4):367–379, April 2007.
- [73] K. Robbie and M. J. Brett. Sculptured thin films and glancing angle deposition: growth mechanics and applications. *Journal of Vacuum Science and Technology A*, 15(3):1460–1465, 1997.
- [74] Doug Vick, Jeremy C. Sit, and Michael J. Brett. *Glancing angle deposition of thin films*, chapter 5, pages 67–94. Recent Developments in Vacuum Science and Technology, 2003. Research Signpost, Kerala, India, 2003.
- [75] M. J. Colgan and M. J. Brett. Field emission from carbon and silicon films with pillar microstructure. *Thin Solid Films*, 389(1-2):1–4, June 2001.
- [76] J. N. Broughton and M. J. Brett. Electrochemical capacitance in manganese thin films with chevron microstructure. *Electrochemical and Solid-State Letters*, 5(12):A279–A282, 2002.
- [77] G. K. Kiema, M. J. Colgan, and M. J. Brett. Dye sensitized solar cells incorporating obliquely deposited titanium oxide layers. *Solar Energy Materials and Solar Cells*, 85:321–331, 2005.
- [78] K. D. Harris, D. Vick, E. J. Gonzalez, T. Smy, K. Robbie, and M. J. Brett. Porous thin films for thermal barrier coatings. *Surface and Coatings Technology*, 138:185–191, 2001.

- [79] John J. Steele, James Gospodyn, Jeremy C. Sit, and Michael J. Brett. Impact of morphology on high-speed humidity sensor performance. *IEEE Sensors Journal*, 6(1):24–27, February 2006.
- [80] Gregory K. Kiema and Michael J. Brett. Electrochemical characterization of carbon films with porous microstructures. *Journal of the Electrochemical Society*, 150(7):E342–E347, 2003.
- [81] Peter C. P. Hruday, Kenneth L. Westra, and Michael J. Brett. Highly ordered organic Alq<sub>3</sub> chiral luminescent thin films fabricated by glancing-angle deposition. *Advanced Materials*, 18(2):224–228, 2006.
- [82] Andy C. van Popta, Jeremy C. Sit, and Michael J. Brett. Optical properties of porous helical thin films. *Applied Optics*, 43(18):3632–3639, 2004.
- [83] S. R. Kennedy, M. J. Brett, O. Toader, and S. John. Fabrication of tetragonal square spiral photonic crystals. *Nano Letters*, 2(1):59–62, 2002.
- [84] D. Vick and M. J. Brett. Conduction anisotropy in porous thin films with chevron microstructures. *Journal of Vacuum Science and Technology A*, 24(1):156–164, 2006.
- [85] A. Kundt. On the double refraction of light in metal layers which have been prepared by cathode sputtering. *Ann. Phys. Chem.*, 27:59, 1886.
- [86] L. Holland. Effect of vapor incidence on the structure of evaporated aluminum films. *Journal of the Optical Society of America*, 43(5):376–380, May 1953.
- [87] Donald O. Smith. Anisotropy in permalloy films. *Journal of Applied Physics*, 30(4):S264–S265, 1959.
- [88] T. G. Knorr and R. W. Hoffman. Dependence of geometric magnetic anisotropy in thin iron films. *Physical Review*, 113(4):1039–1046, Feb 1959.
- [89] N. O. Young and J. Kowal. Optically active fluorite films. *Nature*, 183(4654):104–105, January 1959.
- [90] J. M. Nieuwenhuizen and H. B. Haanstra. *Philips Technical Review*, 27:87, 1966.
- [91] Leon I. Maissel and Reinhard Glang, editors. *Handbook of thin film technology*. McGraw-Hill, New York, NY, 1970.
- [92] Milton Ohring. *The Materials Science of Thin Films*. Academic Press, Toronto, 2002.
- [93] Norbert Kaiser. Review of the fundamentals of thin-film growth. *Applied Optics*, 41(16):3053–3060, June 2002.
- [94] R. Messier, T. Gehrke, C. Frankel, V. C. Venugopal, W. Ota no, and A. Lakhtakia. Engineered sculptured nematic thin films. *Journal of Vacuum Science and Technology A*, 15(4):2148–2152, July 1997.

- [95] F. Liu, C. Yu, L. Shen, J. Barnard, and G. J. Mankey. The magnetic properties of cobalt films produced by glancing angle deposition. *IEEE Transactions on Magnetics*, 36(5):2939–2941, September 2000.
- [96] K. Robbie, L. J. Friedrich, S. K. Dew, T. Smy, and M. J. Brett. Fabrication of thin films with highly porous microstructures. *Journal of Vacuum Science and Technology A*, 13(3):1032–1035, May 1995.
- [97] J. C. Sit, D. Vick, K. Robbie, and M. J. Brett. Thin film microstructure control using glancing angle deposition by sputtering. *Journal of Materials Research*, 14(4):1197–1199, April 1999.
- [98] H. Konig and G. Helwig. *Optik*, 6:111, 1950.
- [99] D. O. Smith, M. S. Cohen, and G. P. Weiss. Oblique-incidence anisotropy in evaporated permalloy films. *Journal of Applied Physics*, 31(10):1755–1762, October 1960.
- [100] Tomoyoshi Motohiro and Y. Taga. Thin film retardation plate by oblique deposition. *Applied Optics*, 28(13):2466–2482, July 1989.
- [101] Kevin Robbie, Michael J. Brett, and Akhlesh Lakhtakia. First thin film realization of a helicoidal bianisotropic medium. *Journal of Vacuum Science and Technology A: Vacuum, Surfaces, and Films*, 13(6):2991–2993, 1995.
- [102] Ian Hodgkinson, Qi Hong Wu, Michael Brett, and Kevin Robbie. Vacuum deposition of biaxial films with surface-aligned principal axes and large birefringence  $\delta n$ . *Optical Interference Coatings*, 9:104–106, 1998.
- [103] Ian Hodgkinson and Qi Hong Wu. Serial bideposition of anisotropic thin films with enhanced linear birefringence. *Applied Optics*, 38(16):3621–3625, 1999.
- [104] D.-X. Ye, Y.-P. Zhao, G.-R. Yang, Y.-G. Zhao, G.-C. Wang, and T.-M. Lu. Manipulating the column tilt angles of nanocolumnar films by glancing-angle deposition. *Nanotechnology*, 13(5):615–618, October 2002.
- [105] Stephen B. Chaney, S. Shanmukh, R. A. Dluhy, and Y.-P. Zhao. Aligned silver nanorod arrays produce high sensitivity surface-enhanced Raman spectroscopy substrates. *Applied Physics Letters*, 87(3):031908, 2005.
- [106] Motofumi Suzuki, Wataru Maekita, Kazuaki Kishimoto, Satoshi Teramura, Kaoru Nakajima, Kenji Kimura, and Yasunori Taga. Direct formation of arrays of prolate Ag nanoparticles by dynamic oblique deposition. *Japanese Journal of Applied Physics*, 44(5):L193–L195, 2005.
- [107] Andy C. van Popta, Michael J. Brett, and Jeremy C. Sit. Double-handed circular Bragg phenomena in polygonal helix thin films. *Journal of Applied Physics*, 98(8):083517, 2005.



- [108] Russell Messier, Vijayakumar C. Venugopal, and Paul D. Sunal. Origin and evolution of sculptured thin films. *Journal of Vacuum Science and Technology A*, 18(4):1538–1545, 2000.
- [109] S. V. Patel, T. E. Mlsna, B. Fruhberger, E. Klaassen, S. Cemalovic, and D. R. Baselt. Chemicapacitive microsensors for volatile organic compound detection. *Sensors and Actuators B*, 96:541–553, 2003.
- [110] Adrian M. Kummer, Andreas Hierlemann, and Henry Baltes. Tuning sensitivity and selectivity of complementary metal oxide semiconductor-based capacitive chemical microsensors. *Analytical Chemistry*, 76(9):2470–2477, May 2004.
- [111] Andy T. Wu and Michael J. Brett. Sensing humidity using nanostructured SiO posts: mechanism and optimization. *Sensors and Materials*, 13(7):399–431, 2001.
- [112] M. J. Toohey. Electrodes for nanodot-based gas sensors. *Sensors and Actuators B*, 105(2):232–250, March 2005.
- [113] Rui Igreja and C. J. Dias. Dielectric response of interdigital chemocapacitors: the role of the sensitive layer thickness. *Sensors and Actuators B*, 115:69–78, 2006.
- [114] P. Fürjes, A. Kovács, Cs. Düsco, M. Ádám, B. Müller, and U. Mescheder. Porous silicon-based humidity sensor with interdigital electrodes and internal heaters. *Sensors and Actuators B*, 95:140–144, 2003.
- [115] Debdulal Saha, Kalyan Kumar Mistry, Runa Giri, Animesh Guha, and Kamalendu Sensgupta. Dependence of moisture absorption property on solgel process of transparent nano-structured  $\gamma$ -Al<sub>2</sub>O<sub>3</sub> ceramics. *Sensors and Actuators B*, 109:363–366, 2005.
- [116] Titanium oxides for optical coatings. *Cerac Technical Publications*, [www.cerac.com](http://www.cerac.com).
- [117] W. J. Sarjeant. Capacitors. *IEEE Transactions on Electrical Insulation*, 25(5):861–922, October 1990.
- [118] John R. Taylor. *An Introduction to Error Analysis*. University Science Books, Sausalito, CA, second edition, 1997.
- [119] Jan Grönblad. Easy and reliable calibration with HMK15 humidity calibrator. *Vaisala News Magazine*, 148:18–20, 1998.
- [120] Francis Ménil, Marc Susbielles, Hélène, Debéda, Claude Lucat, and Pascal Tardy. Evidence of a correlation between the non-linearity of chemical sensors and the asymmetry of their response and recovery curves. *Sensors and Actuators B*, 106:407–423, 2005.

- 
- [121] Peter Tobias, Per Mårtensson, Anders Göras, Ingemar Lundström, and Anita Lloyd Spetz. Moving gas outlets for the evaluation of fast gas sensors. *Sensors and Actuators B*, 58:389–393, 1999.
- [122] John J. Steele, Glen A. Fitzpatrick, and Michael J. Brett. Capacitive humidity sensors with high sensitivity and subsecond response times. *IEEE Sensors Journal*, 7(6):955–956, June 2007.
- [123] Evgenij Barsoukov and J. Ross Macdonald, editors. *Impedance Spectroscopy*. Wiley, Hoboken, NJ, second edition, 2005.
- [124] Mikko Björkqvist, Jarno Salonen, Jaani Paski, and Ensio Laine. Characterization of thermally carbonized porous silicon humidity sensor. *Sensors and Actuators A*, 112(2-3):244–247, May 2004.
- [125] Seong-Jeen Kim, Jae-Yoon Park, Sang-Hoon Lee, and Seung-Hwan Yi. Humidity sensors using porous silicon layer with mesa structure. *Journal of Physics D, Applied Physics*, 33(15):1781–1784, August 2000.
- [126] R. K. Nahar. Study of the performance degradation of thin film aluminum oxide sensor at high humidity. *Sensors and Actuators B*, 63(1-2):49–54, April 2000.
- [127] Yuan Yuan Xu, Xin Jian Li, Jin Tian He, Xing Hu, and Hai Yan Wang. Capacitive humidity sensing properties of hydrothermally-etched silicon nanoporous pillar array. *Sensors and Actuators B*, 105(2):219–222, March 2005.
- [128] Y. Li and M. J. Yang. A novel highly reversible humidity sensor based on poly(2-propyn-2-furoate). *Sensors and Actuators B*, 86:155–159, 2002.
- [129] Mikko Björkqvist, Jaani Paski, Jarno Salonen, and Vesa-Pekka Lehto. Studies on hysteresis reduction in thermally carbonized porous silicon humidity sensor. *IEEE Sensors Journal*, 6(3):542–547, June 2006.
- [130] Shixuan Pang, Hartmut Graßl, and Horst Jäger. An improved humidity sensor. *Journal of Atmospheric and Oceanic Technology*, 13:1110–1115, October 1996.
- [131] Matthias Thommes. *Physical adsorption characterization of ordered and amorphous mesoporous materials*, chapter 11, pages 317–364. *Nanoporous Materials: Science and Engineering*. Imperial College Press, London, 2004.
- [132] Duncan J. Shaw. *Introduction to Colloid and Surface Chemistry*. Butterworth-Heinemann, Woburn, MA, fourth edition, 1992.
- [133] Paul C. Hiemenz and Raj Rajagopalan. *Principles of Colloid and Surface Chemistry*. Marcel Dekker, New York, NY, third edition, 1997.
- [134] T. Islam, S. Ghosh, and H. Saha. ANN-based signal conditioning and its hardware implementation of a nanostructured porous silicon relative humidity sensor. *Sensors and Actuators B*, 120:130–141, 2006.

- [135] Tariqul Islam and Hiranmay Saha. Hysteresis compensation of a porous silicon relative humidity sensor using ANN technique. *Sensors and Actuators B*, 114:334–343, 2006.
- [136] J. van den Brand, S. Van Gils, P. C. J. Beentjes, H. Terryn, and J. H. W. de Wit. Ageing of aluminium oxide surfaces and their subsequent reactivity towards bonding with organic functional groups. *Applied Surface Science*, 235:465–474, 2004.
- [137] L. L. W. Chow, M. M. F. Yuen, P. C. H. Chan, and A. T. Cheung. Reactive sputtered TiO<sub>2</sub> thin film humidity sensor with negative substrate bias. *Sensors and Actuators B*, 76(1-3):310–315, June 2001.
- [138] Ulrike Diebold. The surface science of titanium dioxide. *Surface Science Reports*, 48:53–229, 2003.
- [139] Z. Ding, G. Q. Lu, and P. F. Greenfield. Role of the crystallite phase of TiO<sub>2</sub> in heterogeneous photocatalysis for phenol oxidation in water. *Journal of Physical Chemistry B*, 104(19):4815–4820, 2000.
- [140] Adil Fahmi and Christian Minot. A theoretical investigation of water adsorption on titanium dioxide surfaces. *Surface Science*, 304(3):343–359, March 1994.
- [141] A. C. van Popta, J. Cheng, J. C. Sit, and M. J. Brett. Birefringence enhancement in annealed TiO<sub>2</sub> thin films. *Journal of Applied Physics*, accepted for publication June 5, 2007.
- [142] R. Herne, J. Brocas, and E. Vander Donckt. The response time of optical sensors based on luminescence quenching. *Analytica Chimica Acta*, 364(1-3):131–141, May 1998.
- [143] R. S. Pilling, G. Bernhardt, C. S. Kim, J. Duncan, C. B. H. Crothers, D. Kleinschmidt, D. J. Frankel, R. J. Lad, and B. G. Frederick. Quantifying gas sensor and delivery system response time using GC/MS. *Sensors and Actuators B*, 96(1-2):200–214, November 2003.
- [144] Vera Bolis, Giuseppina Cerrato, Giuliana Magnacca, and Claudio Morterra. Surface acidity of metal oxides. combined microcalorimetric and IR-spectroscopic studies of variously dehydrated systems. *Thermochimica Acta*, 312:63–77, 1998.
- [145] R. E. Cunningham and R. J. J. Williams. *Diffusion in gases and porous solids*. Plenum Press, New York, NY, 1980.
- [146] R. N. Tait, T. Smy, and M. J. Brett. Modelling and characterization of columnar growth in evaporated films. *Thin Solid Films*, 226:196–201, 1993.

- [147] W. C. Chen and P. N. Sen. Dielectric enhancement due to electrochemical double layer: Thin double layer approximation. *Journal of Chemical Physics*, 77(9):4683–4693, November 1982.
- [148] T. J. Lewis. Interfaces are the dominant feature of dielectrics at the nanometric level. *IEEE Transactions on Dielectrics and Electrical Insulation*, 11:739–753, 2004.
- [149] T. J. Lewis. Interfaces: nanometric dielectrics. *Journal of Physics D: Applied Physics*, 38:202–212, 2005.
- [150] T. Kikkawa, S. Kuroki, S. Sakamoto, K. Kohmura, H. Tanaka, and N. Hatac. Influence of humidity on electrical characteristics of self-assembled porous silica low-k films. *Journal of The Electrochemical Society*, 152(7):G560–G566, 2005.
- [151] Matthijs W. den Otter. Approximate expressions for the capacitance and electrostatic potential of interdigitated electrodes. *Sensors and Actuators A*, 96:140–144, 2002.
- [152] Rui Igreja and C. J. Dias. Analytical evaluation of the interdigital electrodes capacitance for a multi-layered structure. *Sensors and Actuators A, Physical*, 112:291–301, 2004.
- [153] R. K. Nahar and V. K. Khanna. A study of capacitance and resistance characteristics of an  $\text{Al}_2\text{O}_3$  humidity sensor. *International Journal of Electronics*, 52(6):557–567, 1982.
- [154] J. B. Hasted. *Dielectric properties*, volume 1 of *Water: A comprehensive treatise*, pages 255–309. Plenum Press, New York, NY, 1972.
- [155] H. P. R. Frederikse. *Permittivity (dielectric constant) of inorganic solids*. CRC Handbook of Chemistry and Physics, Internet Version 2007. Taylor and Francis, Boca Ranton, FL, 87 edition, 2007.
- [156] John J. Steele, Andy C. van Popta, Matthew M. Hawkeye, Jeremy C. Sit, and Michael J. Brett. Nanostructured gradient index optical filter for high-speed humidity sensing. *Sensors and Actuators B*, 120(1):213–219, December 2006.
- [157] Rong Liua, Thomas A. Schmedakeb, Yang Yang Lib, Michael J. Sailorb, and Yeshaiahu Fainman. Novel porous silicon vapor sensor based on polarization interferometry. *Sensors and Actuators B*, 87(1):58–62, November 2002.
- [158] Luca De Stefano, Ivo Rendina, Luigi Moretti, and Andrea Mario Rossi. Optical sensing of flammable substances using porous silicon microcavities. *Materials Science and Engineering B*, 100(3):271–274, July 2003.
- [159] A. Lakhtakia, M. W. McCall, J. A. Sherwin, Q. H. Wu, and I. J. Hodgkinson. Sculptured-thin-film spectral holes for optical sensing of fluids. *Optics Communications*, 194:33–46, 2001.

## References

---

- [160] D. E. Aspnes. Optical properties of thin films. *Thin Solid Films*, 89(3):249–262, March 1982.
- [161] S. R. Kennedy and M. J. Brett. Porous broadband antireflection coating by glancing angle deposition. *Applied Optics*, 42:4573–4579, 2003.
- [162] W. H. Southwell. Spectral response calculations of rugate filters using coupled-wave theory. *Journal of the Optical Society of America A*, 5(9):1558–1564, September 1988.
- [163] Bertrand G. Bovard. Rugate filter theory: an overview. *Applied Optics*, 32(28):5427–5442, October 1993.
- [164] Andy C. van Popta, Matthew M. Hawkeye, Jeremy C. Sit, and Michael J. Brett. Gradient-index narrow-bandpass filter fabricated with glancing-angle deposition. *Optics Letters*, 29(21):2545–2547, November 2004.
- [165] Andy C. van Popta, Jeremy C. Sit, and Michael J. Brett. Optical properties of porous helical thin films and the effects of post-deposition annealing. *Proceedings of the SPIE - The International Society for Optical Engineering*, 5464:198–208, 2004.
- [166] K. Kaminska, T. Brown, G. Beydaghyan, and K. Robbie. Vacuum evaporated porous silicon photonic interference filters. *Applied Optics*, 42:4212–4219, 2003.

## Appendix A

# Analytic Fitting of Linear Data with Large Range

In Chapter 4, measurements of standard capacitors and resistors with nominal values extending over several orders of magnitude are used to evaluate the LCR meter accuracy error. In such cases, the data at the upper end will dominate a least squares fit of measured versus nominal values, so a more complicated approach must be used to correctly fit data. The use of nonlinear fitting methods are avoided, since an analytic expression for the error is required.

The following equation was used as a model to fit the data.

$$y = mx \tag{A.1}$$

No intercept was used for this analysis for the following reasons: (1) the data set of nominal capacitance versus measured capacitance should produce a best fit line that passes through the origin (within error), (2) for data that spans several orders of magnitude the intercept is typically insignificant and (3) dropping the intercept greatly simplifies the analysis.

To fit correctly, it is necessary to de-emphasize the data points at the large end

to keep them from dominating the fit. This is accomplished by moving to a logarithmic space, and fitting the data there. Thus, Equation A.1 is converted to:

$$\log (y) = \log (mx) \quad (\text{A.2})$$

$$\log (y) = \log (m) + \log (x) \quad (\text{A.3})$$

This equation can be re-written in a linear form by making the transformation  $Y = \log (y)$ ,  $X = \log (x)$ , and  $M = \log (m)$ :

$$Y = M + X \quad (\text{A.4})$$

To fit Equation A.4, the derivation of least squares fitting by Taylor [118] can be altered for the special case where the slope is unity. In this case, the error ( $S$ ) to be minimized is given by:

$$S = \sum_i^N (Y_i - X_i - M)^2 \quad (\text{A.5})$$

$$\frac{\partial S}{\partial M} = \sum_i^N -2(Y_i - X_i - M) \quad (\text{A.6})$$

Setting Equation A.6 to zero and solving for  $M$  yields the analytic expression for the slope parameter:

$$M = \frac{\sum Y_i - \sum X_i}{N} \quad (\text{A.7})$$

Applying error propagation to Equation A.7 gives the error in  $M$  ( $\delta_M$ ). It is assumed that the error in  $X_i$  is negligible (standard assumption with least squares fitting [118]). The error is thus restricted to  $Y_i$  values ( $\delta_{Y_i}$ ):

$$\delta_M^2 = \sum_i^N \left( \frac{\partial M}{\partial Y_i} \right)^2 \delta_{Y_i}^2 \quad (\text{A.8})$$

The partial derivative  $\partial M / \partial Y_i$  is found from Equation A.7:

$$\frac{\partial M}{\partial Y_i} = \frac{\partial}{\partial Y_i} \frac{Y_1 + Y_2 + \dots + Y_i + \dots + Y_N}{N} = \frac{1}{N}; \forall i \quad (\text{A.9})$$

Thus,

$$\delta_M^2 = \sum \left( \frac{\delta_{Y_i}^2}{N} \right)^2 \quad (\text{A.10})$$

Assuming that  $\delta_{Y_i}$  is constant with respect to data  $i$ :

$$\delta_M = \frac{\delta_{Y_i}}{\sqrt{N}} \quad (\text{A.11})$$

The error  $\delta_{Y_i}$  is the standard deviation of the  $Y_i$  residuals from the best fit line, and is calculated from [118]:

$$\delta_{Y_i} = \sqrt{\frac{1}{N-2} \sum_i^N (Y_i - M - X_i)^2} \quad (\text{A.12})$$

Thus,  $C_{nom}$  vs.  $C_{meas}$  and  $R_{nom}$  vs.  $R_{meas}$  data can be fit to Equation A.4 using Equation A.7 with error given by Equation A.11.

To convert back to the more useful Equation A.1,  $M = \log(m)$  is simply inverted to give  $m$ :

$$m = 10^M \quad (\text{A.13})$$

The error in  $m$  ( $\delta_m$ ) is found from error propagation:

$$\delta_m = \sqrt{\left( \frac{\partial m}{\partial M} \delta_M \right)^2} = \ln(10) m \delta_M \quad (\text{A.14})$$

The relative slope error:

$$\frac{\delta_m}{m} = \ln(10) \delta_M \quad (\text{A.15})$$

represents the range of "true" capacitance / resistance values,  $x$ , that correspond to a measured value,  $y$ , and is used as an estimate of the accuracy error in Chapter 4.



## Appendix B

# Visual Basic Program for Capacitance Data Logging

In this appendix the Visual Basic program used to log sensor capacitance during response time measurements is presented. This program was co-authored by Sumudu Fernando.

When the program is run a window pops up that allows the user to select (via radio button) the impedance parameter to log during response time measurements. After making the selection and clicking the start button, three successive windows pop up and ask the user to select the measurement frequency, voltage, and sample time (typically set to zero). After these selections are made the program continually collects data from the QuadTech 1715 LCR meter (progress bar identifies program is running) until the stop button is clicked, which exits the program. When impedance parameters are measured they are immediately written to a comma separated value file.

The following is a copy of the Visual Basic code.

## Appendix B. Visual Basic Program for Capacitance Data Logging

---

```
Public Class Form1
    Inherits System.Windows.Forms.Form
    Dim meter As New Rs232
    Dim File As System.IO.File
    Dim logger As System.IO.StreamWriter
    Dim clock As New System.DateTime

    Public Function request(ByVal REQ As String, Optional ByVal ret
        As Boolean = True) As String
        meter.Write(REQ & Chr(13) & Chr(10))
        If ret Then
            Dim output As String
            Dim c As Char
            System.Threading.Thread.Sleep(10) 'sample time
            Application.DoEvents()
            meter.Read(1)
            c = meter.InputStreamString.Chars(0)
            Do While c <> Chr(10)
                output = output & c
                meter.Read(1)
                c = meter.InputStreamString.Chars(0)
            Loop
            Return output
        Else
            Return ""
        End If
    End Function

#Region " Windows Form Designer generated code "

    Public Sub New()
        MyBase.New()

        'This call is required by the Windows Form Designer.
        InitializeComponent()

        'Add any initialization after the InitializeComponent() call

    End Sub

    'Form overrides dispose to clean up the component list.
    Protected Overrides Sub Dispose(ByVal disposing As Boolean)
        If disposing Then
            If Not (components Is Nothing) Then
                components.Dispose()
            End If
        End If
        MyBase.Dispose(disposing)
    End Sub

    'Required by the Windows Form Designer
    Private components As System.ComponentModel.IContainer

    'NOTE: The following procedure is required by the Windows Form Designer
    'It can be modified using the Windows Form Designer.
    'Do not modify it using the code editor.
```

## Appendix B. Visual Basic Program for Capacitance Data Logging

---

```
Friend WithEvents Label1 As System.Windows.Forms.Label
Friend WithEvents Label2 As System.Windows.Forms.Label
Friend WithEvents Label3 As System.Windows.Forms.Label
Friend WithEvents StartButton As System.Windows.Forms.Button
Friend WithEvents StopButton As System.Windows.Forms.Button
Friend WithEvents RsButton As System.Windows.Forms.RadioButton
Friend WithEvents RpButton As System.Windows.Forms.RadioButton
Friend WithEvents ZsButton As System.Windows.Forms.RadioButton
Friend WithEvents CpButton As System.Windows.Forms.RadioButton
Friend WithEvents CsButton As System.Windows.Forms.RadioButton
Friend WithEvents Label4 As System.Windows.Forms.Label
Friend WithEvents Label5 As System.Windows.Forms.Label
Friend WithEvents ProgressBar As System.Windows.Forms.ProgressBar
<System.Diagnostics.DebuggerStepThrough()>
Private Sub InitializeComponent()
    Me.Label1 = New System.Windows.Forms.Label
    Me.Label2 = New System.Windows.Forms.Label
    Me.Label3 = New System.Windows.Forms.Label
    Me.StartButton = New System.Windows.Forms.Button
    Me.StopButton = New System.Windows.Forms.Button
    Me.RsButton = New System.Windows.Forms.RadioButton
    Me.RpButton = New System.Windows.Forms.RadioButton
    Me.ZsButton = New System.Windows.Forms.RadioButton
    Me.CpButton = New System.Windows.Forms.RadioButton
    Me.CsButton = New System.Windows.Forms.RadioButton
    Me.Label4 = New System.Windows.Forms.Label
    Me.Label5 = New System.Windows.Forms.Label
    Me.ProgressBar = New System.Windows.Forms.ProgressBar
    Me.SuspendLayout()
    '
    'Label1
    '
    Me.Label1.Font = New System.Drawing.Font("Times New Roman", 18.0!,
        System.Drawing.FontStyle.Regular,
        System.Drawing.GraphicsUnit.Point, CType(0, Byte))
    Me.Label1.Location = New System.Drawing.Point(8, 8)
    Me.Label1.Name = "Label1"
    Me.Label1.Size = New System.Drawing.Size(336, 32)
    Me.Label1.TabIndex = 34
    Me.Label1.Text = "QuadTech 1715 LCR Digibridge"
    Me.Label1.TextAlign = System.Drawing.ContentAlignment.MiddleCenter
    '
    'Label2
    '
    Me.Label2.Font = New System.Drawing.Font("Times New Roman", 18.0!,
        System.Drawing.FontStyle.Regular,
        System.Drawing.GraphicsUnit.Point, CType(0, Byte))
    Me.Label2.Location = New System.Drawing.Point(8, 40)
    Me.Label2.Name = "Label2"
    Me.Label2.Size = New System.Drawing.Size(336, 32)
    Me.Label2.TabIndex = 35
    Me.Label2.Text = "Response Time Logger"
    Me.Label2.TextAlign = System.Drawing.ContentAlignment.MiddleCenter
    '
    'Label3
    '

```

## Appendix B. Visual Basic Program for Capacitance Data Logging

---

```
Me.Label3.Font = New System.Drawing.Font("Times New Roman", 12.0!,
    System.Drawing.FontStyle.Italic,
    System.Drawing.GraphicsUnit.Point, CType(0, Byte))
Me.Label3.Location = New System.Drawing.Point(8, 72)
Me.Label3.Name = "Label3"
Me.Label3.Size = New System.Drawing.Size(336, 23)
Me.Label3.TabIndex = 36
Me.Label3.Text = "By John Steele and Fernando Sumudu"
Me.Label3.TextAlign = System.Drawing.ContentAlignment.MiddleCenter
'
'StartButton
'
Me.StartButton.BackColor = System.Drawing.Color.LimeGreen
Me.StartButton.Location = New System.Drawing.Point(128, 104)
Me.StartButton.Name = "StartButton"
Me.StartButton.Size = New System.Drawing.Size(104, 32)
Me.StartButton.TabIndex = 37
Me.StartButton.Text = "START"
'
'StopButton
'
Me.StopButton.BackColor = System.Drawing.Color.Tomato
Me.StopButton.Location = New System.Drawing.Point(128, 144)
Me.StopButton.Name = "StopButton"
Me.StopButton.Size = New System.Drawing.Size(104, 32)
Me.StopButton.TabIndex = 38
Me.StopButton.Text = "STOP"
'
'RsButton
'
Me.RsButton.Location = New System.Drawing.Point(160, 216)
Me.RsButton.Name = "RsButton"
Me.RsButton.Size = New System.Drawing.Size(40, 24)
Me.RsButton.TabIndex = 39
Me.RsButton.Text = "Rs"
'
'RpButton
'
Me.RpButton.Location = New System.Drawing.Point(208, 216)
Me.RpButton.Name = "RpButton"
Me.RpButton.Size = New System.Drawing.Size(40, 24)
Me.RpButton.TabIndex = 40
Me.RpButton.Text = "Rp"
'
'ZsButton
'
Me.ZsButton.Location = New System.Drawing.Point(256, 216)
Me.ZsButton.Name = "ZsButton"
Me.ZsButton.Size = New System.Drawing.Size(40, 24)
Me.ZsButton.TabIndex = 41
Me.ZsButton.Text = "Zs"
'
'CpButton
'
Me.CpButton.Location = New System.Drawing.Point(112, 216)
Me.CpButton.Name = "CpButton"
```

## Appendix B. Visual Basic Program for Capacitance Data Logging

---

```
Me.CpButton.Size = New System.Drawing.Size(40, 24)
Me.CpButton.TabIndex = 42
Me.CpButton.Text = "Cp"
'
'CsButton
'
Me.CsButton.Checked = True
Me.CsButton.Location = New System.Drawing.Point(64, 216)
Me.CsButton.Name = "CsButton"
Me.CsButton.Size = New System.Drawing.Size(40, 24)
Me.CsButton.TabIndex = 43
Me.CsButton.TabStop = True
Me.CsButton.Text = "Cs"
'
'Label4
'
Me.Label4.Font = New System.Drawing.Font("Times New Roman", 9.75!,
    System.Drawing.FontStyle.Regular,
    System.Drawing.GraphicsUnit.Point, CType(0, Byte))
Me.Label4.Location = New System.Drawing.Point(8, 240)
Me.Label4.Name = "Label4"
Me.Label4.Size = New System.Drawing.Size(336, 23)
Me.Label4.TabIndex = 44
Me.Label4.Text = "NOTE: Program run time must be less than 1 minute"
Me.Label4.TextAlign = System.Drawing.ContentAlignment.MiddleCenter
'
'Label5
'
Me.Label5.Font = New System.Drawing.Font("Times New Roman", 9.75!,
    System.Drawing.FontStyle.Regular,
    System.Drawing.GraphicsUnit.Point, CType(0, Byte))
Me.Label5.Location = New System.Drawing.Point(8, 264)
Me.Label5.Name = "Label5"
Me.Label5.Size = New System.Drawing.Size(336, 23)
Me.Label5.TabIndex = 45
Me.Label5.Text = "Output file is located here
"C:\ResponseTimeData.txt""
Me.Label5.TextAlign = System.Drawing.ContentAlignment.MiddleCenter
'
'ProgressBar
'
Me.ProgressBar.Location = New System.Drawing.Point(56, 184)
Me.ProgressBar.Maximum = 500
Me.ProgressBar.Name = "ProgressBar"
Me.ProgressBar.Size = New System.Drawing.Size(240, 23)
Me.ProgressBar.TabIndex = 46
'
'Form1
'
Me.AutoScaleBaseSize = New System.Drawing.Size(5, 13)
Me.BackColor = System.Drawing.SystemColors.ActiveBorder
Me.ClientSize = New System.Drawing.Size(352, 294)
Me.Controls.Add(Me.ProgressBar)
Me.Controls.Add(Me.Label5)
Me.Controls.Add(Me.Label4)
Me.Controls.Add(Me.CsButton)
```

## Appendix B. Visual Basic Program for Capacitance Data Logging

---

```
Me.Controls.Add(Me.CpButton)
Me.Controls.Add(Me.ZsButton)
Me.Controls.Add(Me.RpButton)
Me.Controls.Add(Me.RsButton)
Me.Controls.Add(Me.StopButton)
Me.Controls.Add(Me.StartButton)
Me.Controls.Add(Me.Label3)
Me.Controls.Add(Me.Label2)
Me.Controls.Add(Me.Label1)
Me.Name = "Form1"
Me.Text = "Form1"
Me.ResumeLayout(False)

End Sub

#End Region

Private Sub StartButton_Click(ByVal sender
As System.Object, ByVal e As System.EventArgs) Handles
StartButton.Click

    'Open output file
    logger = File.AppendText("C:\ResponseTimeData.txt")
    logger.AutoFlush = True
    If CsButton.Checked Then
        logger.WriteLine("Cs")
        logger.WriteLine("Output format: 0, Cs, Theta, Time1 (ms),
        Time2 (ms), Time1 uses a time stamp before LCR request
        and Time 2 uses a time stamp after the LCR request")
    ElseIf CpButton.Checked Then
        logger.WriteLine("Cp")
        logger.WriteLine("Output format: 0, Cp, D, Time (ms),
        Time2 (ms), Time1 uses a time stamp before LCR request
        and Time 2 uses a time stamp after the LCR request")
    ElseIf RsButton.Checked Then
        logger.WriteLine("Rs")
        logger.WriteLine("Output format: 0, Rs, Theta, Time (ms),
        Time2 (ms), Time1 uses a time stamp before LCR request
        and Time 2 uses a time stamp after the LCR request")
    ElseIf RpButton.Checked Then
        logger.WriteLine("Rp")
        logger.WriteLine("Output format: 0, Rp, Q, Time (ms),
        Time2 (ms), Time1 uses a time stamp before LCR request
        and Time 2 uses a time stamp after the LCR request")
    ElseIf ZsButton.Checked Then
        logger.WriteLine("Zs")
        logger.WriteLine("Output format: 0, Zs, Theta, Time (ms),
        Time2 (ms), Time1 uses a time stamp before LCR request
        and Time 2 uses a time stamp after the LCR request")
    End If

    Dim readTime = 1 'incremental wait time during reading of meter

    Dim freq As String
    Dim volt As String
    'prompt user for frequency and voltage
```

## Appendix B. Visual Basic Program for Capacitance Data Logging

---

```
1:      freq = InputBox("Please choose frequency." & Chr(13) & Chr(10) &
"Enter 1 for 100 Hz" & Chr(13) & Chr(10) & "Enter 2 for 120 Hz" &
Chr(13) & Chr(10) & "Enter 3 for 1000 Hz" & Chr(13) & Chr(10) &
"Enter 4 for 10000 Hz", "Frequency", "3")
      While freq <> "1" And freq <> "2" And freq <> "3" And freq <> "4"
          GoTo 1
      End While
2:      volt = InputBox("Please choose voltage." & Chr(13) & Chr(10) &
"Enter 1 for 0.25 V" & Chr(13) & Chr(10) & "Enter 2 for 1.0 V",
"Voltage", "2")
      While volt <> "1" And volt <> "2"
          GoTo 2
      End While

      'prompt user for sample time
      Dim sampleTime As Integer
3:      sampleTime = Val(InputBox("Please enter sample time in ms." &
Chr(13) & Chr(10) & "No negative numbers, no decimal points,
no commas", "Sample Time", "0"))

      'set frequency of meter
      If freq = "1" Then
          request("source:freq 100", False)
      ElseIf freq = "2" Then
          request("source:freq 120", False)
      ElseIf freq = "3" Then
          request("source:freq 1000", False)
      ElseIf freq = "4" Then
          request("source:freq 10000", False)
      End If

      'set voltage of meter
      If volt = "1" Then
          request("source:volt 0.25", False)
      ElseIf volt = "2" Then
          request("source:volt 1.0", False)
      End If

      'query voltage and write value to file
      logger.WriteLine("Voltage = " & request("Source:volt?") & " V")

      'query frequency and write value to file
      logger.WriteLine("Frequency = " & request("Source:freq?") & " Hz")

      'set primary parameter to measure
      If CsButton.Checked Then
          request("calc1:form Cs", False)
          'set secondary parameter
          request("calc2:form Phase", False)
      ElseIf CpButton.Checked Then
          request("calc1:form Cp", False)
          'set secondary parameter
          request("calc2:form D", False)
      ElseIf RsButton.Checked Then
          request("calc1:form Rs", False)
```

## Appendix B. Visual Basic Program for Capacitance Data Logging

---

```
'set secondary parameter
request("calc2:form Phase", False)
ElseIf RpButton.Checked Then
request("calc1:form Rp", False)
'set secondary parameter
request("calc2:form Q", False)
ElseIf ZsButton.Checked Then
request("calc1:form Zs", False)
'set secondary parameter
request("calc2:form Phase", False)
End If

'startTime is a reference for time stamping the LCR samples
Dim startTime As DateTime = clock.Now

'While loop continues until STOP button is pressed
While True

    'Wait a user defined amount of time before next sample
    System.Threading.Thread.Sleep(sampleTime)

    'nowTime1 is time stamp for current sample pre LCR request
    Dim nowTime1 As DateTime = clock.Now

    'request is function to get the data from the LCR meter
    Dim out As String = request("FETCH?")

    'nowTime is time stamp for current sample (after LCR request)
    Dim nowTime2 As DateTime = clock.Now

    'log results to file
    logger.WriteLine(out & "," & (nowTime1.Hour * 3600 * 1000 +
    nowTime1.Minute * 60 * 1000 + nowTime1.Second * 1000 +
    nowTime1.Millisecond) - (startTime.Hour * 3600 * 1000 +
    startTime.Minute * 60 * 1000 + startTime.Second * 1000 +
    startTime.Millisecond) & "," & (nowTime2.Hour * 3600 *
    1000 + nowTime2.Minute * 60 * 1000 + nowTime2.Second *
    1000 + nowTime2.Millisecond) - (startTime.Hour * 3600 *
    1000 + startTime.Minute * 60 * 1000 + startTime.Second *
    1000 + startTime.Millisecond))

    'Increment progressbar
    If ProgressBar.Value = ProgressBar.Maximum Then
        ProgressBar.Value = ProgressBar.Minimum
    Else
        ProgressBar.Value += 1
    End If

End While

End Sub

Private Sub StopButton_Click(ByVal sender As System.Object, ByVal e
As System.EventArgs) Handles StopButton.Click
    logger.Close()
End
```



## Appendix B. Visual Basic Program for Capacitance Data Logging

---

```
End Sub

Private Sub Form1_Load(ByVal sender As System.Object, ByVal e As
System.EventArgs) Handles MyBase.Load
    'When application starts open the RS232 port
    meter.Open(1, 38400, 8, Rs232.DataParity.Parity_None,
        Rs232.DataStopBit.StopBit_1, 512)
    System.Threading.Thread.Sleep(100) 'wait 100 ms for port to open
    Application.DoEvents() 'while waiting let application do other
        events like refresh buttons etc.

    'set parameters of LCR meter
    meter.Write("Trigger:delay 0" & Chr(13) & Chr(10))
    'set trigger delay to 0ms
    meter.Write("Trigger:edge falling" & Chr(13) & Chr(10))
    'set trigger edge to falling
    meter.Write("Sense:FIMP:Range:Auto ON" & Chr(13) & Chr(10))
    'set ranging to automatic
    meter.Write("Sense:FIMP:APER fast" & Chr(13) & Chr(10))
    'set measure rate to fast

End Sub

End Class
```

### The following code was used for the RS232 communications.

```
Imports System.Runtime.InteropServices
Imports System.Text
Imports System.Threading

#Region "RS232"
Public Class Rs232 : Implements IDisposable
    '=====
    '
    'Module : Rs232
    'Description : Class for handling RS232 communication with VB.Net
    'Created : 10/08/2001 - 8:45:25
    'Author : Corrado Cavalli (1336@gmx.it)
    'WebSite : www.corradocavalli.cjb.net
    '
    'Notes :
    '-----
    'Revisions
    '1st Public release Beta2 (10/08/2001)
    '
    'Rev.1 (28.02.2002)
    '1. Added ResetDev, SetBreak and ClearBreak to the
    EscapeCommFunction constants
    '2. Added the overloaded Open routine.
    '3. Added the modem status routines, properties and enum.
    '4. If a read times out, it now returns a EndOfStreamException
    (instead of a simple Exception).
    '5.Compiled with VS.Net final
```

## Appendix B. Visual Basic Program for Capacitance Data Logging

---

```
'Rev.2 (01.03.2002)
'Added Async support
'
' Rev.3 (07.04.2002)
'Minor bugs fixed
'
' Rev.3 (05/05/2002)
' Fixed BuildCommDCB problem
'
' Rev.4 (24/05/2002)
' Fixed problem with ASCII Encoding truncating 8th bit
'
' Rev.5 (27/05/2002)
' Added IDisposable / Finalize implementation
'=====
'// Class Members
Private mhRS As Int32 = -1 '// Handle to Com Port
Private miPort As Integer = 1 '// Default is COM1
Private miTimeout As Int32 = 70 '// Timeout in ms
Private miBaudRate As Int32 = 9600
Private meParity As DataParity = 0
Private meStopBit As DataStopBit = 0
Private miDataBit As Int32 = 8
Private miBufferSize As Int32 = 512 '// Buffers size default 512 bytes
Private mabtrxBuf As Byte() '// Receive buffer
Private meMode As Mode '// Class working mode
Private mbWaitOnRead As Boolean
Private mbWaitOnWrite As Boolean
Private mbWriteErr As Boolean
Private muOverlapped As OVERLAPPED
Private muOverlappedW As OVERLAPPED
Private muOverlappedE As OVERLAPPED
Private mabtTmpTxBuf As Byte() '// Temporary buffer used by Async Tx
Private moThreadTx As Thread
Private moThreadRx As Thread
Private miTmpBytes2Read As Int32
Private meMask As EventMasks
Private mbDisposed As Boolean
'-----

#Region "Enums"
'// Parity Data
Public Enum DataParity
    Parity_None = 0
    Parity_Odd
    Parity_Even
    Parity_Mark
End Enum
'// StopBit Data
Public Enum DataStopBit
    StopBit_1 = 1
    StopBit_2
End Enum
Private Enum PurgeBuffers
    RXAbort = &H2
```

*Appendix B. Visual Basic Program for Capacitance Data Logging*

---

```

    RXClear = &H8
    TxAbort = &H1
    TxClear = &H4
End Enum
Private Enum Lines
    SetRts = 3
    ClearRts = 4
    SetDtr = 5
    ClearDtr = 6
    ResetDev = 7 ' // Reset device if possible
    SetBreak = 8 ' // Set the device break line.
    ClearBreak = 9 ' // Clear the device break line.
End Enum
' // Modem Status
<Flags()> Public Enum ModemStatusBits
    ClearToSendOn = &H10
    DataSetReadyOn = &H20
    RingIndicatorOn = &H40
    CarrierDetect = &H80
End Enum
' // Working mode
Public Enum Mode
    NonOverlapped
    Overlapped
End Enum
' // Comm Masks
<Flags()> Public Enum EventMasks
    RxChar = &H1
    RXFlag = &H2
    TxBufferEmpty = &H4
    ClearToSend = &H8
    DataSetReady = &H10
    ReceiveLine = &H20
    Break = &H40
    StatusError = &H80
    Ring = &H100
End Enum
#End Region
#Region "Structures"
<StructLayout(LayoutKind.Sequential, Pack:=1)> Private Structure DCB
    Public DCBlength As Int32
    Public BaudRate As Int32
    Public Bits1 As Int32
    Public wReserved As Int16
    Public XonLim As Int16
    Public XoffLim As Int16
    Public ByteSize As Byte
    Public Parity As Byte
    Public StopBits As Byte
    Public XonChar As Byte
    Public XoffChar As Byte
    Public ErrorChar As Byte
    Public EofChar As Byte
    Public EvtChar As Byte
    Public wReserved2 As Int16
End Structure
```

## Appendix B. Visual Basic Program for Capacitance Data Logging

---

```
<StructLayout(LayoutKind.Sequential, Pack:=1)> Private Structure
  COMMTIMEOUTS
    Public ReadIntervalTimeout As Int32
    Public ReadTotalTimeoutMultiplier As Int32
    Public ReadTotalTimeoutConstant As Int32
    Public WriteTotalTimeoutMultiplier As Int32
    Public WriteTotalTimeoutConstant As Int32
End Structure
<StructLayout(LayoutKind.Sequential, Pack:=1)> Private Structure
  COMMCONFIG
    Public dwSize As Int32
    Public wVersion As Int16
    Public wReserved As Int16
    Public dcbx As DCB
    Public dwProviderSubType As Int32
    Public dwProviderOffset As Int32
    Public dwProviderSize As Int32
    Public wcProviderData As Byte
End Structure
<StructLayout(LayoutKind.Sequential, Pack:=1)> Public Structure
  OVERLAPPED
    Public Internal As Int32
    Public InternalHigh As Int32
    Public Offset As Int32
    Public OffsetHigh As Int32
    Public hEvent As Int32
End Structure
#End Region
#Region "Constants"
  Private Const PURGE_RXABORT As Integer = &H2
  Private Const PURGE_RXCLEAR As Integer = &H8
  Private Const PURGE_TXABORT As Integer = &H1
  Private Const PURGE_TXCLEAR As Integer = &H4
  Private Const GENERIC_READ As Integer = &H80000000
  Private Const GENERIC_WRITE As Integer = &H40000000
  Private Const OPEN_EXISTING As Integer = 3
  Private Const INVALID_HANDLE_VALUE As Integer = -1
  Private Const IO_BUFFER_SIZE As Integer = 1024
  Private Const FILE_FLAG_OVERLAPPED As Int32 = &H40000000
  Private Const ERROR_IO_PENDING As Int32 = 997
  Private Const WAIT_OBJECT_0 As Int32 = 0
  Private Const ERROR_IO_INCOMPLETE As Int32 = 996
  Private Const WAIT_TIMEOUT As Int32 = &H102&
  Private Const INFINITE As Int32 = &HFFFFFFF
#End Region

#Region "Win32API"
  '// Win32 API
  <DllImport("kernel32.dll")> Private Shared Function SetCommState(ByVal
    hCommDev As Int32, ByRef lpDCB As DCB) As Int32
  End Function
  <DllImport("kernel32.dll")> Private Shared Function GetCommState(ByVal
```

## Appendix B. Visual Basic Program for Capacitance Data Logging

---

```
hCommDev As Int32, ByRef lpDCB As DCB) As Int32
End Function
<DllImport("kernel32.dll")> Private Shared Function BuildCommDCB(ByVal
lpDef As String, ByRef lpDCB As DCB) As Int32
End Function
<DllImport("kernel32.dll")> Private Shared Function SetupComm(ByVal
hFile As Int32, ByVal dwInQueue As Int32, ByVal dwOutQueue As Int32)
As Int32
End Function
<DllImport("kernel32.dll")> Private Shared Function SetCommTimeouts
(ByVal hFile As Int32, ByRef lpCommTimeouts As COMMTIMEOUTS) As Int32
End Function
<DllImport("kernel32.dll")> Private Shared Function GetCommTimeouts
(ByVal hFile As Int32, ByRef lpCommTimeouts As COMMTIMEOUTS) As Int32
End Function
<DllImport("kernel32.dll")> Private Shared Function ClearCommError
(ByVal hFile As Int32, ByVal lpErrors As Int32, ByVal l As Int32) As Int32
End Function
<DllImport("kernel32.dll")> Private Shared Function PurgeComm(ByVal
hFile As Int32, ByVal dwFlags As Int32) As Int32
End Function
<DllImport("kernel32.dll")> Private Shared Function EscapeCommFunction
(ByVal hFile As Integer, ByVal ifunc As Long) As Boolean
End Function
<DllImport("kernel32.dll")> Private Shared Function WaitCommEvent
(ByVal hFile As Integer, ByRef Mask As EventMasks, ByRef lpOverlap As
OVERLAPPED) As Int32
End Function
<DllImport("kernel32.dll")> Private Shared Function WriteFile(ByVal
hFile As Integer, ByVal Buffer As Byte(), ByVal nNumberOfBytesToWrite
As Integer, ByRef lpNumberOfBytesWritten As Integer, ByRef
lpOverlapped As OVERLAPPED) As Integer
End Function
<DllImport("kernel32.dll")> Private Shared Function ReadFile(ByVal
hFile As Integer, ByVal Buffer As Byte(), ByVal nNumberOfBytesToRead
As Integer, ByRef lpNumberOfBytesRead As Integer, ByRef lpOverlapped
As OVERLAPPED) As Integer
End Function
<DllImport("kernel32.dll")> Private Shared Function CreateFile
(<MarshalAs(UnmanagedType.LPStr)> ByVal lpFileName As String, ByVal
dwDesiredAccess As Integer, ByVal dwShareMode As Integer, ByVal
lpSecurityAttributes As Integer, ByVal dwCreationDisposition As
Integer, ByVal dwFlagsAndAttributes As Integer, ByVal hTemplateFile
As Integer) As Integer
End Function
<DllImport("kernel32.dll")> Private Shared Function CloseHandle(ByVal
hObject As Integer) As Integer
End Function
<DllImport("kernel32.dll")> Private Shared Function FormatMessage
(ByVal dwFlags As Integer, ByVal lpSource As Integer, ByVal
dwMessageId As Integer, ByVal dwLanguageId As Integer, <MarshalAs
(UnmanagedType.LPStr)> ByVal lpBuffer As String, ByVal nSize As
Integer, ByVal Arguments As Integer) As Integer
End Function
<DllImport("kernel32.dll")> Public Shared Function GetCommModemStatus
(ByVal hFile As Int32, ByRef lpModemStatus As Int32) As Boolean
```

## Appendix B. Visual Basic Program for Capacitance Data Logging

---

```
End Function
<DllImport("kernel32.dll")> Private Shared Function CreateEvent
    (ByVal lpEventAttributes As Int32, ByVal bManualReset As Int32, ByVal
    bInitialState As Int32, <MarshalAs(UnmanagedType.LPStr)> ByVal lpName
    As String) As Int32

End Function
<DllImport("kernel32.dll")> Private Shared Function GetLastError() As
Int32
End Function
<DllImport("kernel32.dll")> Private Shared Function
WaitForSingleObject(ByVal hHandle As Int32, ByVal dwMilliseconds As
Int32) As Int32
End Function
<DllImport("kernel32.dll")> Private Shared Function
GetOverlappedResult(ByVal hFile As Int32, ByRef lpOverlapped As
OVERLAPPED, ByRef lpNumberOfBytesTransferred As Int32, ByVal bWait
As Int32) As Int32

End Function
<DllImport("kernel32.dll")> Private Shared Function SetCommMask(ByVal
hFile As Int32, ByVal lpEvtMask As Int32) As Int32
End Function

Private Declare Function FormatMessage Lib "kernel32" Alias _
    "FormatMessageA" (ByVal dwFlags As Int32, ByVal lpSource As Int32, _
    ByVal dwMessageId As Int32, ByVal dwLanguageId As Int32, _
    ByVal lpBuffer As StringBuilder, ByVal nSize As Int32, ByVal
    Arguments As Int32) _
    As Int32

#End Region
#Region "Events"
    Public Event DataReceived(ByVal Source As Rs232, ByVal DataBuffer() As
    Byte)
    Public Event TxCompleted(ByVal Source As Rs232)
    Public Event CommEvent(ByVal Source As Rs232, ByVal Mask As EventMasks)
#End Region

Public Property Port() As Integer
    '=====
    '
    'Description : Communication Port
    'Created : 21/09/2001 - 11:25:49
    '
    '*Parameters Info*
    '
    'Notes :
    '=====
    Get
        Return miPort
    End Get
    Set(ByVal Value As Integer)
```

## Appendix B. Visual Basic Program for Capacitance Data Logging

---

```
        miPort = Value
    End Set
End Property
Public Overridable Property Timeout() As Integer
'=====
'
'Description: Communication timeout in seconds
'Created : 21/09/2001 - 11:26:50
'
'*Parameters Info*
'
'Notes :
'=====
Get
    Return miTimeout
End Get
Set (ByVal Value As Integer)
    miTimeout = CInt(IIf(Value = 0, 500, Value))
    '// If Port is open updates it on the fly
    pSetTimeout()
End Set
End Property
Public Property Parity() As DataParity
'=====
'
'Description : Communication parity
'Created : 21/09/2001 - 11:27:15
'
'*Parameters Info*
'
'Notes :
'=====
Get
    Return meParity
End Get
Set (ByVal Value As DataParity)
    meParity = Value
End Set
End Property
Public Property StopBit() As DataStopBit
'=====
'
'Description: Communication StopBit
'Created : 21/09/2001 - 11:27:37
'
'*Parameters Info*
'
'Notes :
'=====
Get
    Return meStopBit
End Get
Set (ByVal Value As DataStopBit)
    meStopBit = Value
End Set
End Property
```

*Appendix B. Visual Basic Program for Capacitance Data Logging*

---

```
Public Property BaudRate() As Integer
    '=====
    '
    'Description: Communication BaudRate
    'Created : 21/09/2001 - 11:28:00
    '
    '*Parameters Info*
    '
    'Notes :
    '=====
    Get
        Return miBaudRate
    End Get
    Set(ByVal Value As Integer)
        miBaudRate = Value
    End Set
End Property
Public Property DataBit() As Integer
    '=====
    '
    'Description : Communication DataBit
    'Created : 21/09/2001 - 11:28:20
    '
    '*Parameters Info*
    '
    'Notes :
    '=====
    Get
        Return miDataBit
    End Get
    Set(ByVal Value As Integer)
        miDataBit = Value
    End Set
End Property
Public Property BufferSize() As Integer
    '=====
    '
    'Description : Receive Buffer size
    'Created : 21/09/2001 - 11:33:05
    '
    '*Parameters Info*
    '
    'Notes :
    '=====
    Get
        Return miBufferSize
    End Get
    Set(ByVal Value As Integer)
        miBufferSize = Value
    End Set
End Property
Public Overloads Sub Open()
    '=====
    '
    'Description : Initializes and Opens communication port
    'Created : 21/09/2001 - 11:33:40
```



## Appendix B. Visual Basic Program for Capacitance Data Logging

---

```
'
'*Parameters Info*
'
'Notes :
'=====
'// Get Dcb block,Update with current data
Dim uDcb As DCB, iRc As Int32
'// Set working mode
Dim iMode As Int32 = Convert.ToInt32(IIf(meMode = Mode.Overlapped,
FILE_FLAG_OVERLAPPED, 0))
'// Initializes Com Port
If miPort > 0 Then
    Try
        '// Creates a COM Port stream handle
        mhRS = CreateFile("COM" & miPort.ToString, _
        GENERIC_READ Or GENERIC_WRITE, 0, 0, _
        OPEN_EXISTING, iMode, 0)
        If mhRS <> -1 Then
            '// Clear all communication errors
            Dim lpErrCode As Int32
            iRc = ClearCommError(mhRS, lpErrCode, 0&)
            '// Clears I/O buffers
            iRc = PurgeComm(mhRS, PurgeBuffers.RXClear Or PurgeBuffers
            .TxClear)
            '// Gets COM Settings
            iRc = GetCommState(mhRS, uDcb)
            '// Updates COM Settings
            Dim sParity As String = "NOEM"
            sParity = sParity.Substring(meParity, 1)
            '// Set DCB State
            Dim sDCBState As String = String.Format("baud={0} parity=
            {1} data={2} stop={3}", miBaudRate, sParity, miDataBit,
            CInt(meStopBit))
            iRc = BuildCommDCB(sDCBState, uDcb)
            iRc = SetCommState(mhRS, uDcb)
            If iRc = 0 Then
                Dim sErrTxt As String = pErr2Text(GetLastError())
                Throw New CIOChannelException("Unable to set COM state0"
                & sErrTxt)
            End If
            '// Setup Buffers (Rx,Tx)
            iRc = SetupComm(mhRS, miBufferSize, miBufferSize)
            '// Set Timeouts
            pSetTimeout()
        Else
            '// Raise Initialization problems
            Throw New CIOChannelException("Unable to open COM" &
            miPort.ToString)
        End If
    Catch Ex As Exception
        '// Generica error
        Throw New CIOChannelException(Ex.Message, Ex)
    End Try
Else
    '// Port not defined, cannot open
    Throw New ApplicationException("COM Port not defined,use Port
```

## Appendix B. Visual Basic Program for Capacitance Data Logging

---

```
        property to set it before invoking InitPort")
    End If
End Sub
Public Overloads Sub Open(ByVal Port As Integer, ByVal BaudRate As
Integer, ByVal DataBit As Integer, ByVal Parity As DataParity, ByVal
StopBit As DataStopBit, ByVal BufferSize As Integer)
    '=====  
    '  
    'Description: Opens communication port (Overloaded method)  
    'Created : 21/09/2001 - 11:33:40  
    '  
    '*Parameters Info*  
    '  
    'Notes :  
    '=====  
    Me.Port = Port  
    Me.BaudRate = BaudRate  
    Me.DataBit = DataBit  
    Me.Parity = Parity  
    Me.StopBit = StopBit  
    Me.BufferSize = BufferSize  
    Open()  
End Sub
Public Sub Close()  
    '=====  
    '  
    'Description: Close communication channel  
    'Created : 21/09/2001 - 11:38:00  
    '  
    '*Parameters Info*  
    '  
    'Notes :  
    '=====  
    If mhRS <> -1 Then  
        CloseHandle(mhRS)  
        mhRS = -1  
    End If  
End Sub
ReadOnly Property IsOpen() As Boolean  
    '=====  
    '  
    'Description: Returns Port Status  
    'Created : 21/09/2001 - 11:38:51  
    '  
    '*Parameters Info*  
    '  
    'Notes :  
    '=====  
    Get  
        Return CBool(mhRS <> -1)  
    End Get  
End Property
Public Overloads Sub Write(ByVal Buffer As Byte()  
    '=====  
    '  
    'Description: Transmit a stream
```

## Appendix B. Visual Basic Program for Capacitance Data Logging

---

```
'Created : 21/09/2001 - 11:39:51
'
'*Parameters Info*
'Buffer : Array of Byte() to write
'Notes :
'=====
Dim iBytesWritten, iRc As Integer
'-----
If mhRS = -1 Then
    Throw New ApplicationException("Please initialize and open port
    before using this method")
Else
    '// Transmit data to COM Port
    Try
        If meMode = Mode.Overlapped Then
            '// Overlapped write
            If pHandleOverlappedWrite(Buffer) Then
                Throw New ApplicationException("Error in overlapped
                write")
            End If
        Else
            '// Clears IO buffers
            PurgeComm(mhRS, PURGE_RXCLEAR Or PURGE_TXCLEAR)
            iRc = WriteFile(mhRS, Buffer, Buffer.Length, iBytesWritten
            , Nothing)
            If iRc = 0 Then
                Throw New ApplicationException("Write Error - Bytes
                Written " & iBytesWritten.ToString & " of " &
                Buffer.Length.ToString)
            End If
        End If
    Catch Ex As Exception
        Throw
    End Try
End If
End Sub
Public Overloads Sub Write(ByVal Buffer As String)
'=====
'
'Description : Writes a string to RS232
'Created : 04/02/2002 - 8:46:42
'
'*Parameters Info*
'
'Notes : 24/05/2002 Fixed problem with ASCII Encoding
'=====
Dim oEncoder As New System.Text.ASCIIEncoding()
Dim oEnc As Encoding = oEncoder.GetEncoding(1252)
'-----
Dim aByte() As Byte = oEnc.GetBytes(Buffer)
Me.Write(aByte)
End Sub
Public Function Read(ByVal Bytes2Read As Integer) As Integer
'=====
'
'Description: Read Bytes from Port
```

*Appendix B. Visual Basic Program for Capacitance Data Logging*

---

```
'Created : 21/09/2001 - 11:41:17
',
'*Parameters Info*
'Bytes2Read : Bytes to read from port
'Returns : Number of readed chars
',
'Notes :
'=====
Dim iReadChars, iRc As Integer
'-----
'// If Bytes2Read not specified uses BufferSize
If Bytes2Read = 0 Then Bytes2Read = miBufferSize
If mhRS = -1 Then
    Throw New ApplicationException("Please initialize and open port
    before using this method")
Else
    '// Get bytes from port
    Try
        '// Purge buffers
        'PurgeComm(mhRS, PURGE_RXCLEAR Or PURGE_TXCLEAR)
        '// Creates an event for overlapped operations
        If meMode = Mode.Overlapped Then
            pHandleOverlappedRead(Bytes2Read)
        Else
            '// Non overlapped mode
            ReDim mabtRxBuf(Bytes2Read - 1)
            iRc = ReadFile(mhRS, mabtRxBuf, Bytes2Read, iReadChars,
            Nothing)
            If iRc = 0 Then
                '// Read Error
                Throw New ApplicationException("ReadFile error " &
                iRc.ToString)
            Else
                '// Handles timeout or returns input chars
                If iReadChars = 0 Then
                    Return -1
                Else
                    mbWaitOnRead = True
                    Return (iReadChars)
                End If
            End If
        End If
    End Try
    Catch Ex As Exception
        '// Others generic erroes
        Throw New ApplicationException("Read Error: " & Ex.Message, Ex)
    End Try
End If
End Function
Overridable ReadOnly Property InputStream() As Byte()
'=====
',
'Description: Returns received data as Byte()
'Created : 21/09/2001 - 11:45:06
',
'*Parameters Info*
',
```

*Appendix B. Visual Basic Program for Capacitance Data Logging*

---

```
'Notes :
'=====
Get
    Return mabtrxBuf
End Get
End Property
Overridable ReadOnly Property InputStreamString() As String
'=====
'
'Description : Return a string containing received data
'Created : 04/02/2002 - 8:49:55
'
'*Parameters Info*
'
'Notes :
'=====
Get
    Dim oEncoder As New System.Text.ASCIIEncoding()
    '-----
    Return oEncoder.GetString(Me.InputStream)
End Get
End Property
Public Sub ClearInputBuffer()
'=====
'
'Description: Clears Input buffer
'Created : 21/09/2001 - 11:45:34
'
'*Parameters Info*
'
'Notes : Gets all character until end of buffer
'=====
If Not mhRS = -1 Then
    PurgeComm(mhRS, PURGE_RXCLEAR)
End If
End Sub
Public WriteOnly Property Rts() As Boolean
'=====
'
'Description: Set/Resets RTS Line
'Created : 21/09/2001 - 11:45:34
'
'*Parameters Info*
'
'Notes :
'=====
Set (ByVal Value As Boolean)
    If Not mhRS = -1 Then
        If Value Then
            EscapeCommFunction(mhRS, Lines.SetRts)
        Else
            EscapeCommFunction(mhRS, Lines.ClearRts)
        End If
    End If
End Set
End Property
```

*Appendix B. Visual Basic Program for Capacitance Data Logging*

---

```
Public WriteOnly Property Dtr() As Boolean
'=====  
,  
'Description: Set/Resets DTR Line  
'Created : 21/09/2001 - 11:45:34  
,  
'*Parameters Info*  
,  
'Notes :  
'=====  
Set (ByVal Value As Boolean)  
    If Not mhRS = -1 Then  
        If Value Then  
            EscapeCommFunction(mhRS, Lines.SetDtr)  
        Else  
            EscapeCommFunction(mhRS, Lines.ClearDtr)  
        End If  
    End If  
End Set  
End Property  
Public ReadOnly Property ModemStatus() As ModemStatusBits  
'=====  
,  
'Description : Gets Modem status  
'Created : 28/02/2002 - 8:58:04  
,  
'*Parameters Info*  
,  
'Notes :  
'=====  
Get  
    If mhRS = -1 Then  
        Throw New ApplicationException("Please initialize and open  
        port before using this method")  
    Else  
        '// Retrieve modem status  
        Dim lpModemStatus As Int32  
        If Not GetCommModemStatus(mhRS, lpModemStatus) Then  
            Throw New ApplicationException("Unable to get modem status")  
        Else  
            Return CType(lpModemStatus, ModemStatusBits)  
        End If  
    End If  
End Get  
End Property  
Public Function CheckLineStatus(ByVal Line As ModemStatusBits) As Boolean  
'=====  
,  
'Description : Check status of a Modem Line  
'Created : 28/02/2002 - 10:25:17  
,  
'*Parameters Info*  
,  
'Notes :  
'=====  
Return Convert.ToBoolean(ModemStatus And Line)
```

*Appendix B. Visual Basic Program for Capacitance Data Logging*

---

```
End Function
Public Property WorkingMode() As Mode
    '=====
    '
    'Description : Set working mode (Overlapped/NonOverlapped)
    'Created : 28/02/2002 - 15:01:18
    '
    '*Parameters Info*
    '
    'Notes :
    '=====
    Get
        Return meMode
    End Get
    Set (ByVal Value As Mode)
        meMode = Value
    End Set
End Property
Public Overloads Sub AsyncWrite(ByVal Buffer() As Byte)
    '=====
    '
    'Description : Write bytes using another thread, TxCompleted
    raised when done
    'Created : 01/03/2002 - 12:00:56
    '
    '*Parameters Info*
    '
    'Notes :
    '=====
    If meMode <> Mode.Overlapped Then Throw New ApplicationException
    ("Async Methods allowed only when WorkingMode=Overlapped")
    If mbWaitOnWrite = True Then Throw New ApplicationException
    ("Unable to send message because of pending transmission.")
    mabtTmpTxBuf = Buffer
    moThreadTx = New Thread(AddressOf _W)
    moThreadTx.Start()
End Sub
Public Overloads Sub AsyncWrite(ByVal Buffer As String)
    '=====
    '
    'Description : Overloaded Async Write
    'Created : 01/03/2002 - 12:00:56
    '
    '*Parameters Info*
    '
    'Notes :
    '=====
    Dim oEncoder As New System.Text.ASCIIEncoding()
    '-----
    Dim aByte() As Byte = oEncoder.GetBytes(Buffer)
    Me.AsyncWrite(aByte)
End Sub
Public Overloads Sub AsyncRead(ByVal Bytes2Read As Int32)
    '=====
    '
    'Description : Read bytes using a different thread, RxCompleted
```

*Appendix B. Visual Basic Program for Capacitance Data Logging*

---

```
raised when done
'Created : 01/03/2002 - 12:00:56
'
'*Parameters Info*
'
'Notes :
'=====
If meMode <> Mode.Overlapped Then Throw New ApplicationException
("Async Methods allowed only when WorkingMode=Overlapped")
miTmpBytes2Read = Bytes2Read
moThreadTx = New Thread(AddressOf _R)
moThreadTx.Start()
End Sub
#Region "Finalize"
Protected Overrides Sub Finalize()
'=====
'
'Description : Closes COM port if object is garbage collected
and still owns
'
'
'COM port reosurces
'
'Created : 27/05/2002 - 19:05:56
'
'*Parameters Info*
'
'Notes :
'=====
Try
If Not mbDisposed Then Close()
Finally
End Try
End Sub
#End Region

#Region "Thread related functions"
Public Sub _W()
'=====
'
'Description : Method invoked by thread to perform an async write
'Created : 01/03/2002 - 12:23:08
'
'*Parameters Info*
'
'Notes : Do not invoke this method from code
'=====
Write(mabtTmpTxBuf)
End Sub
Public Sub _R()
'=====
'
'Description : Method invoked by thread to perform an async read
'Created : 01/03/2002 - 12:23:08
'
'*Parameters Info*
'
'Notes : Do not invoke this method from code
```



*Appendix B. Visual Basic Program for Capacitance Data Logging*

---

```
'=====
Dim iRet As Int32 = Read(miTmpBytes2Read)
End Sub
#End Region

#Region "Private Routines"
Private Sub pSetTimeout()
'=====
'
'Description: Set communication timeouts
'Created : 21/09/2001 - 11:46:40
'
'*Parameters Info*
'
'Notes :
'=====
Dim uCtm As COMMTIMEOUTS
'// Set ComTimeout
If mhRS = -1 Then
Exit Sub
Else
'// Changes setup on the fly
With uCtm
.ReadIntervalTimeout = 0
.ReadTotalTimeoutMultiplier = 0
.ReadTotalTimeoutConstant = miTimeout
.WriteTotalTimeoutMultiplier = 10
.WriteTotalTimeoutConstant = 100
End With
SetCommTimeouts(mhRS, uCtm)
End If
End Sub
Private Sub pHandleOverlappedRead(ByVal Bytes2Read As Int32)
'=====
'
'Description : Handles overlapped read
'Created : 28/02/2002 - 16:03:06
'
'*Parameters Info*
'
'Notes :
'=====
Dim iReadChars, iRc, iRes, iLastErr As Int32
'-----
muOverlapped.hEvent = CreateEvent(Nothing, 1, 0, Nothing)
If muOverlapped.hEvent = 0 Then
'// Can't create event
Throw New ApplicationException("Error creating event for
overlapped read.")
Else
'// Overlapped reading
If mbWaitOnRead = False Then
ReDim mabtRxBuf(Bytes2Read - 1)
iRc = ReadFile(mhRS, mabtRxBuf, Bytes2Read, iReadChars,
muOverlapped)
If iRc = 0 Then
```

*Appendix B. Visual Basic Program for Capacitance Data Logging*

---

```

        iLastError = GetLastError()
    If iLastError <> ERROR_IO_PENDING Then
        Throw New ArgumentException("Overlapped Read Error: "
            & pErr2Text(iLastError))
    Else
        '// Set Flag
        mbWaitOnRead = True
    End If
Else
    '// Read completed successfully
    RaiseEvent DataReceived(Me, mabtRxBuf)
End If
End If
End If
End If
End Sub
Private Function pHandleOverlappedWrite(ByVal Buffer() As Byte) As Boolean
    '=====  

    '  

    'Description : Handles overlapped Write  

    'Created : 28/02/2002 - 16:03:06  

    '  

    '*Parameters Info*  

    '  

    'Notes :  

    '=====  

    Dim iBytesWritten, iRc, iLastError, iRes As Integer, bErr As Boolean
    '-----

```

```
muOverlappedW.hEvent = CreateEvent(Nothing, 1, 0, Nothing)
If muOverlappedW.hEvent = 0 Then
    '// Can't create event
    Throw New ApplicationException("Error creating event for
    overlapped write.")
Else
    '// Overlapped write
    PurgeComm(mhRS, PURGE_RXCLEAR Or PURGE_TXCLEAR)
    mbWaitOnRead = True
    iRc = WriteFile(mhRS, Buffer, Buffer.Length, iBytesWritten,
    muOverlappedW)
    If iRc = 0 Then
        iLastError = GetLastError()
        If iLastError <> ERROR_IO_PENDING Then
            Throw New ArgumentException("Overlapped Read Error: " &
            pErr2Text(iLastError))
        Else
            '// Write is pending
            iRes = WaitForSingleObject(muOverlappedW.hEvent, INFINITE)
            Select Case iRes
                Case WAIT_OBJECT_0
                    '// Object signaled, operation completed
                    If GetOverlappedResult(mhRS, muOverlappedW,
                    iBytesWritten, 0) = 0 Then
                        bErr = True
                    Else
                        '// Notifies Async tx completion, stops thread
                        mbWaitOnRead = False
                        RaiseEvent TxCompleted(Me)
                    End If
                End Select
            End If
        Else
            '// Wait operation completed immediatly
            bErr = False
        End If
    End If
    CloseHandle(muOverlappedW.hEvent)
    Return bErr
End Function
Private Function pErr2Text(ByVal lCode As Int32) As String
    '=====  
,  
'Description : Translates API Code to text  
'Created : 01/03/2002 - 11:47:46  
,  
'*Parameters Info*  
,  
'Notes :  
'=====  
Dim sRtrnCode As New StringBuilder(256)  
Dim lRet As Int32  
'-----  
lRet = FormatMessage(&H1000, 0, lCode, 0, sRtrnCode, 256, 0)  
If lRet > 0 Then  
    Return sRtrnCode.ToString
```

*Appendix B. Visual Basic Program for Capacitance Data Logging*

---

```
Else
    Return "Error not found."
End If

End Function
Private Sub pDispose() Implements IDisposable.Dispose
    '=====
    '
    'Description : Handles correct class disposing Write
    'Created : 27/05/2002 - 19:03:06
    '
    '*Parameters Info*
    '
    'Notes :
    '=====
    If Not mbDisposed AndAlso mhRS <> -1 Then
        '// Closes Com Port releasing resources
        Try
            Close()
        Finally
            mbDisposed = True
            '// Suppress unnecessary Finalize overhead
            GC.SuppressFinalize(Me)
        End Try
    End If

End Sub

#End Region
End Class
#End Region

#Region "Exceptions"
Public Class CIOChannelException : Inherits ApplicationException
    '=====
    '
    'Module : CChannellException
    'Description: Customized Channell Exception
    'Created : 17/10/2001 - 10:32:37
    '
    'Notes : This exception is raised when
    NACK error found
    '=====
    Sub New(ByVal Message As String)
        MyBase.New(Message)
    End Sub
    Sub New(ByVal Message As String, ByVal InnerException As Exception)
        MyBase.New(Message, InnerException)
    End Sub
End Class
Public Class IOTimeoutException : Inherits CIOChannelException
    '=====
    '
    'Description : Timeout customized exception
```

*Appendix B. Visual Basic Program for Capacitance Data Logging*

---

```
'Created : 28/02/2002 - 10:43:43
',
' *Parameters Info*
',
' Notes :
' =====
Sub New(ByVal Message As String)
MyBase.New(Message)
End Sub
Sub New(ByVal Message As String, ByVal InnerException As Exception)
MyBase.New(Message, InnerException)
End Sub
End Class

#End Region
```